UNIVERSITÉ DE STRASBOURG

ÉCOLE DOCTORALE DE PHYSIQUE, CHIMIE-PHYSIQUE

Institut de Physique et Chimie des Matériaux de Strasbourg

THÈSE présentée par :

Loïc MOCZKO

soutenue le : **29 mars 2023**

pour obtenir le grade de : **Docteur de l'université de Strasbourg**

Discipline / Spécialité : Physique / Nanophysique

Suspended van der Waals heterostructures: from optical spectroscopy to opto-electro-mechanics

THÈSE dirigée par :

M. BERCIAUD Stéphane	Professeur, Université de Strasbourg

RAPPORTEURS :

M. RESERBAT-PLANTEY Antoine	Chargé de recherche CNRS, CRHEA
M. CADIZ Fabian	Professeur assistant, Ecole Polytechnique

AUTRES MEMBRES DU JURY :

Mme. VOLIOTIS Valia	Professeure, INSP, Sorbonne Université
M. FAVERO Ivan	Directeur de recherche, CNRS, MPQ
M. RASTEI Mircea	Maître de conférences, Université de Strasbourg
M. WIRTZ Ludger	Professeur, Université du Luxembourg

Contents

Remerciements

Après la chute d'une table optique, une pandémie mondiale et quelques pannes de manip, nous voilà arrivés à la fin de cette thèse de doctorat qui aura été plus épique que prévu. Et comme dans chaque aventure épique, il y a une longue liste de personnes croisées en chemin sans qui je ne serais pas arrivé jusqu'ici.

Avant toute chose, je souhaite remercier Antoine Reserbat-Plantey et Fabian Cadiz pour avoir accepté d'examiner en détail ce manuscrit, ainsi que les autres membres du jury, Ivan Favero, Valia Voliotis, Mircea Rastei et enfin Ludger Wirtz (que je remercie également pour sa collaboration et son accueil au Luxembourg, aux côtés de Sven Reichardt, qui a permis de changer la dimension du chapitre 3 de ce manuscrit).

Ensuite, je souhaite remercier très chaleureusement Stéphane Berciaud, qui aura su jouer sur la corde sensible pour me convaincre de me lancer dans cette thèse, en me proposant de "jouer du nano-tambour". Trois ans et demi après (voir 4 à 5 si on compte les stages !), je suis bien content de m'être laissé séduire et te remercie pour tout ce que ta supervision m'a apporté, scientifiquement comme humainement. Un énorme Merci à toi Stéphane.

Toute personne connaissant un tant soit peu le monde de la recherche sait pertinemment que l'on ne fait pas grand-chose tout seul, et qu'une bonne équipe est primordiale pour réussir. J'ai eu la chance de faire partie d'une équipe formidable, que j'ai pu voir évoluer en en apprenant toujours plus. D'abord, je remercie Etienne, Luis et Léo pour m'avoir pris sous leurs ailes dès mes années de master, à la fois au labo et en dehors. Grâce à vous, je me suis senti dès le départ comme à la maison. I don't forget Xin, whose past notes and "dead" samples ended up being very useful. Puis de nouvelles personnes se sont ajoutées à l'aventure. En premier lieu Arnaud, dont l'enthousiasme et les nouvelles idées ont aidé à me remotiver lors des périodes plus difficiles, et Aditi[1]. I enjoyed a lot working and debating with you about random things, as well as sharpening my English with you, that is now as sharp as my cutlery (yes, I did it). Don't forget that most of the time, you are doing a better job than you think you are. Great science is ahead (and at least 2 potential Ig Nobels) ! Un peu plus tard, Joanna a rejoint l'équipe. Ce serait un affront de ne pas mentionner qu'elle faisait partie de l'aventure bien avant cela. Après tout ce temps passé à travailler, réviser, festoyer, s'enthousiasmer, râler notre désaccord, dessiner, et même jouer à la belote ensemble (nos premières heures sur les bancs de la fac, c'était il y a 9 ans et 2 mois au moment où j'écris ces lignes), je suis fier et reconnaissant d'avoir grandi (et pas que scientifiquement) à tes côtés. Finalement, je souhaite bonne chance au dernier venu, Quentin, amuse-toi bien avec tes 2D-magnets et les nouveaux jouets d'Arnaud.

[1] Meme-Master Aditi Raman Moghe

Certains n'étaient que de passage mais ont su laisser leur trace. Among them, the most courageous one is without a doubt Aditya. A few months stay in Strasbourg with the perfect timing to not miss the covid lockdown, to then learn Raman spectroscopy with the worst laser we have... You chose the hard way but you nailed it, and we had a great time in the end. Je remercie aussi les différents stagiaires avec qui j'ai travaillé, d'abord Yannis et Charles-Ambroise, qui ont contribué à mes tentatives de liquéfaction d'excitons, puis Jules, mon premier vrai padawan, dont l'aisance avec la manip m'a impressionné. Je te souhaite bonne chance pour ta thèse dans la France de l'intérieur.

Une autre des chances que j'ai eues durant ces 3 ans et demi, c'est d'avoir l'occasion de développer et monter entièrement une manip toute neuve, en partant d'une salle vide. Je recommande à tout jeune expérimentateur en ayant l'occasion de passer par cette étape. Maintenant que le super-setup de la salle 0012 est opérationnel, il est aussi temps de mettre en lumière les super-héros de l'ombre qui ont grandement contribué à sa réalisation : Michi, Jérémy, Guillaume et toute l'équipe de l'atelier de mécanique. Je n'oublie pas non plus Véronique, avec qui passer des commandes est toujours un plaisir. De même, avoir un super-setup c'est bien, avoir de supers échantillons à mettre dedans, c'est mieux. Pour cela, je remercie Sabine, Romain et Hicham de la plateforme STnano, pas un seul de mes nano-tambours n'aurait vu le jour sans leur aide.

Je remercie également les différentes personnes de l'IPCMS et plus largement de l'Université de Strasbourg qui ont rendu mon passage par ici plus agréable. Je pense par exemple aux discussions parfois philosophiques avec les collègues du bureau 1053, les pauses café (ou balades nocturnes à pédalo) avec les STMistes, les mésoscopistes ou les "clients" de la place du café 2.0, les sessions de rugby... Et bien-sûr aussi, les copains de MPA et du magistère/master : Morgane, Julia, Elisa, Camille, Camille, Rémi, Félix, Thomas, Samiul... Beaucoup d'entre eux qui se reconnaitront étant devenus bien plus que des camarades de classes malgré nos chemins différents et les (parfois très grandes) distances. En parlant de copains, il y en a un paquet qui me soutiennent dans tout ce que j'entreprends et que je souhaite remercier pour ça, qu'ils soient compères de musique, pingouins ou sauvageons de la région de Marlenheim. Big up à tous ceux qui sont passés par la coloc du Robistrot, parce qu'il n'y a pas de meilleure façon pour décompresser que d'avoir ses copains directement à la maison. Mention spéciale à Olivier, qui m'a supporté pendant l'avènement de Dark Locos, à la toute fin de la rédaction de ce manuscrit.

Enfin, un grand merci à ma famille, notamment mes parents, qui m'ont soutenu de toutes les manières possibles pendants toutes ces années à faire des choses incompréhensibles avec des lettres à la place des chiffres, des lasers et des trucs vraiment très petits.

Sur ce, afin de finaliser dignement ce manuscrit, je conclurai en deux mots : HOPLA GUT !

Introduction

It is common knowledge that the world that surrounds us is in three dimensions (3D), to a point that is so fundamental that it can seem odd to state it. However, a large amount of systems in this 3D world are perfectly described by the physics of two-dimensional (2D) systems. The spatial confinement of one of the three dimensions leads at the macroscopic scale to an obvious optimisation of the surface to volume ratio, but also to a first interesting property: a decrease in the material bending rigidity. Thin sheets of materials are thus able to be bent and depending on the material's elasticity, to come back to their equilibrium position. The thin sheet of material then behaves as a 2D mechanical oscillator whose vibrations maybe actuated by mechanical means, as for a drumhead, or by electrostatic means, as for a speaker. The same physics is at play at smaller scales, down to the µm and nm range, in micro- and nano-electromechanical systems (NEMS) [1, 2].

At smaller scales, down to the nm range, the spatial confinement leads to the creation of electronic bound states that lies at the core of the functioning principles of modern technology [3, 4]. Thanks to the development of precise growth techniques, the fabrication of nanostructures of increasingly smaller dimensions has been made possible and is now well established. In two dimensions, techniques such as molecular beam epitaxy and metal-organic chemical vapor deposition led to the fabrication of quantum wells formed of nanoscale semiconductor heterostructures, as the well known GaAs/AlGaAs quantum well, with confinement layers of a few nm [5]. The two-dimensional confinement of the electrons in quantum wells led to the creation of optical devices with greatly enhanced performances and efficiency.

Layered materials are composed of 2D layers of atoms with strong in-plane covalent bounds, stacked on top of each other by weaker van der Waals forces. One can isolate single layers from the bulk material and bring the 2D physics to its ultimate limit, down to the atomic scale, at the boundary between solid state and molecular physics. These atomically thin materials can show a large set of physical properties, from semimetal as graphene to insulator as hexagonal boron-nitride (hBN) or semiconductor as transition metal dichalcogenides (TMD). Figure 1 presents an overview of the diversity of 2D-materials. Recently, magnetic 2D-materials were isolated and completed the toolkit of atomically thin materials [7, 8]. The atomic thickness of 2D-materials also makes them highly sensitive to their environment and easily tunable.

In addition, the absence of dangling bonds on their surface allows to combine different 2D-materials in van der Waals heterostructures by precisely stacking a chosen sequence of materials on top of each other [9]. Thanks to the broad set of material's properties available, the amount of possible architectures is tremendous. When two materials are brought to

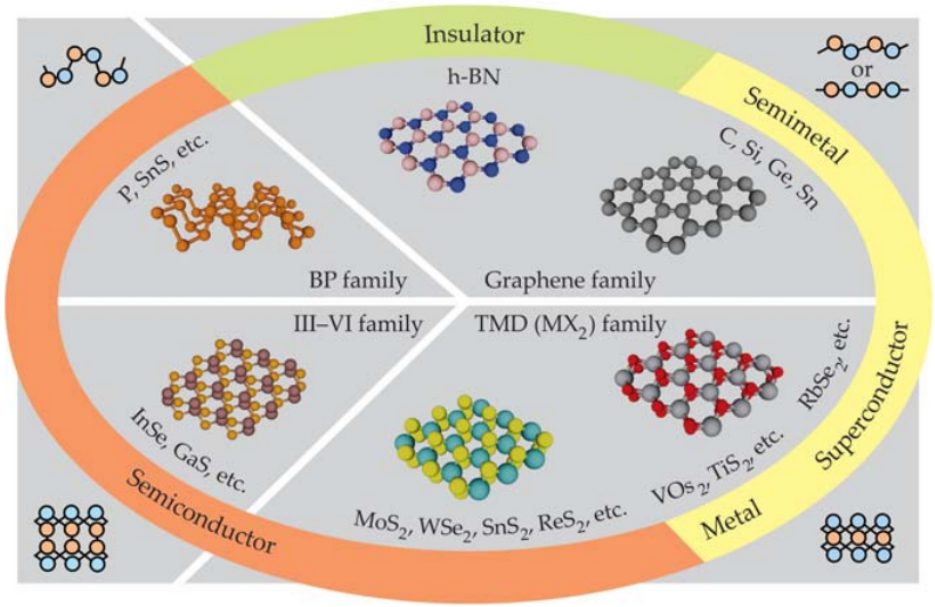

Figure 1: An overview of the 2D-materials family. Extracted from [6]

contact, near-field interlayer mechanism occur and define the resulting properties of the heterostructures.

Furthermore, contrary to conventional semiconductor quantum wells that are by definition embedded in a thicker material, the inherent 2D crystalline structure of van der Waals materials allows to build devices with suspended 2D-materials that are not in direct contact with any type of substrate or solid medium. As such, they can be employed as atomically thin vibrating membranes whose vibrations follow the same physics as the macroscopic ones [10]. This specificity gives the unique opportunity to design microscale drum-like devices with a van der Waals heterostructure as drumhead and use the mechanical degree of freedom as an additional probe of the materials properties, or inversely, as a way to tune them.

Among the promising properties of 2D-materials, their optical properties are of particular interest. For example, monolayer TMDs are direct gap semiconductors with an intense light emission. Their optical response is dominated by excitons with a binding energy that exceeds the room temperature thermal energy [11]. In practice the optical response of TMDs can be investigated by the means of optical spectroscopy, where the exciton population is created thanks to a laser excitation [12]. The exciton emission takes the form of a well defined feature in the photoluminescence (PL) spectrum and is sensitive to the material characteristics, such as its doping level or strain, as well as its environment, being its dielectric environment, the temperature, or the optical field [11].

All of these parameters that affect the exciton response may also be sensitive to the mechanical vibration of the suspended material in a drum-like sample and lead to an interplay between the optical and mechanical properties of the used van der Waals heterostructure. Furthermore, the mechanical response of the drum-like system can be measured optically with the same laser beam that is used to excite the suspended 2D-material. Indeed, the drum-like geometry may be seen as a poor Fabry-Perot interferometer where the suspended van der Waals heterostructure acts as a movable mirror. Because of this advantageous con-

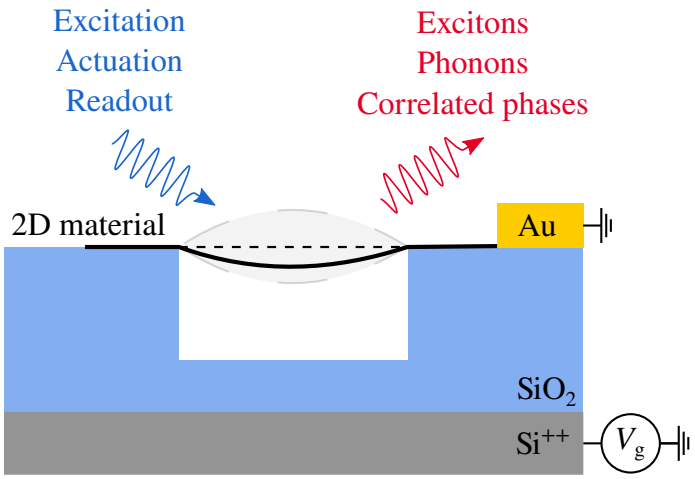

Figure 2: The drum-like sample geometry as a platform for opto-electro-mechanics.

figuration, the drum-like sample geometry is a promising platform to investigate the coupling of the optical response of suspended van der Waals heterostructures with their mechanical degree of freedom, as depicted in figure 2. It is in the framework of this emergent research field that we will refer to as *opto-electro-mechanics* that this PhD work is settled.

More specifically, the general objective of this PhD project, started in 2019, is to complete a thematic evolution in my host team at IPCMS that was initiated in 2016 following extensive work on the physics of freely suspended graphene monolayers. It consists in bringing the mechanical degree of freedom to an experimental methodology based mostly on the optical spectroscopy of 2D-materials in order to develop a state-of-the-art activity in opto-electro-mechanics. To this end, I was in charge of the development of a brand new setup dedicated to this project. It is based on a cryo-compatible confocal microscope built around a closed-cycle gas free cryostat with electrical access. It now allows a simultaneous and automated monitoring of the mechanical and optical responses of drum-like samples.

In parallel to the development of this new setup, the optical response of suspended 2D-materials was investigated at room temperature by the means of optical spectroscopy. The results presented in this PhD thesis can thus be organised in two subsets. The first one, corresponding to chapters 2 and 3 focus on physical phenomena that arises in the room temperature optical response of monolayer TMDs and monolayer graphene as their substrate or close environment is changed or removed. The second one, that corresponds to chapter 4 presents low temperature results obtained thanks to the newly developed experimental setup and couples the mechanical degree of freedom to the optical response of graphene/TMD heterostructures.

Manuscript organization

This manuscript is divided in four chapters.

Chapter 1 is dedicated to the description of the 2D-materials investigated in this work, together with their heterostructures. Notably, the general properties of graphene and TMD monolayer are discussed, with a focus on the properties useful to the understanding of the physics of graphene/TMD heterostructures, also introduced in this chapter, and the results presented in the other chapters.

Chapter 2 focuses on correlated electron-hole phases in suspended monolayer TMDs excited by the means of a strong laser excitation. The general concept of electron-hole plasma and liquid phases is presented. Room temperature results on the evolution of the PL and Raman spectrum as a function of laser power in suspended MoS_2 and suspended WS_2 are discussed in order to investigate the possibility of such a phase transition in these materials as well as the underlying processes.

Chapter 3 presents an investigation on the effect of dielectric screening on the Raman spectrum of monolayer graphene. A systematic analysis of hyperspectral Raman maps of graphene-based heterostructures is presented and supported by symmetry-based theoretical arguments in order to describe how the different symmetries of zone-center and zone-edge phonons in graphene leads to different effects on the corresponding optical phonons.

Chapter 4 compiles low temperature results on a graphene/$MoSe_2$ drum-like device. After a discussion on the technical details concerning the electrostatic actuation of the sample, an experimental way to achieve an electromechanical control of the interlayer coupling based on the results of chapter 3 is proposed. Then, static and dynamical modulation of the $MoSe_2$ exciton energy is achieved via an electromechanical modulation of the sample's strain.

Finally, a last chapter concludes this manuscript and gives an outlook.

Details on the setups, sample fabrication and experimental methods are given in appendix A, B, C and D.

CHAPTER 1

2D-materials and van der Waals heterostructures

The term of two-dimensional (2D) materials refers to a large set of solids whose crystalline structure is formed of atomically thin layers. In the plane, the atoms that forms one layer are bound by strong covalent bonds, but out of the plane each layer is attached to its neighboring one by weaker van der Waals forces. Thanks to this layered structure, it is possible to overcome the out-of-plane van der Waals force and isolate a single layer from the bulk material. Since the first experimental isolation of monolayer graphene, a broad family of layered materials covering a wide range of different properties have been discovered. Their large palette of properties forms a formidable toolkit to understand and engineer matter at the atomic scale.

In this chapter, we will introduce the basic characteristics and properties of graphene, semiconducting transition metal dichalcogenides (TMDs) and their heterostructures with a focus on their optical signatures.

1.1 Graphene

1.1.1 Crystal structure

Graphene is the first 2D-material to be experimentally isolated by K. S. Novoselov and A. K. Geim in 2004 [13], a discovery that has started the whole research field on van der Waals systems and for which they were awarded with the 2010's Nobel Prize of Physics. It is made of a single sheet of carbon atoms bound together by sp2 hybrid orbitals in a honeycomb structure that can be described as a triangular lattice with a basis of two atoms A and B, as sketched figure 1.1a. The distance between two neighboring atoms A and B is given by $a = 1.42$ Å, that is approximately equal to the mean value of simple and double carbon-carbon bond length (1.54 Å and 1.34 Å respectively [14]). The unit cell is defined by the vectors [15]

$$\boldsymbol{a}_1 = \frac{a}{2}\begin{pmatrix} 3 \\ \sqrt{3} \end{pmatrix} \text{ and } \boldsymbol{a}_2 = \frac{a}{2}\begin{pmatrix} 3 \\ -\sqrt{3} \end{pmatrix} \tag{1.1}$$

and the positions of the three A atoms neighboring a given B atom are determined by the

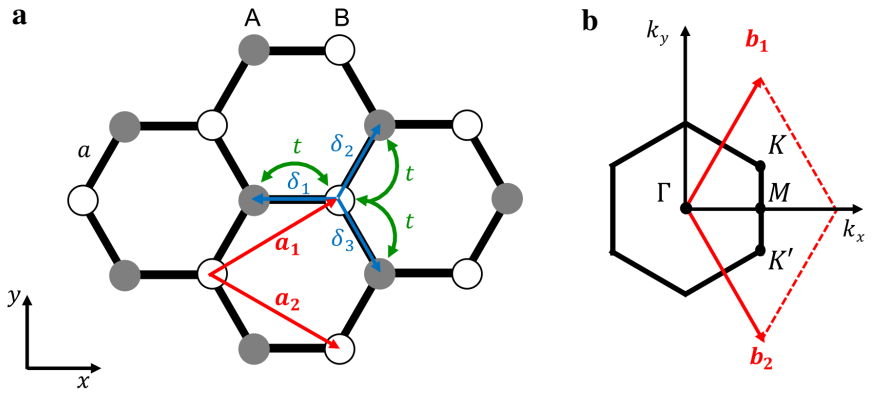

Figure 1.1: Crystal structure of Graphene. a. Sketch of the honeycomb lattice structure of graphene. A atoms are represented as grey filled circles and B atoms as black empty circles. **b.** The first Brillouin zone of graphene. Adapted from [16].

three vectors

$$\boldsymbol{\delta}_1 = \frac{a}{2}\begin{pmatrix}1\\\sqrt{3}\end{pmatrix}, \boldsymbol{\delta}_2 = \frac{a}{2}\begin{pmatrix}1\\-\sqrt{3}\end{pmatrix} \text{ and } \boldsymbol{\delta}_3 = -a\begin{pmatrix}1\\0\end{pmatrix}. \tag{1.2}$$

In the reciprocal lattice the basis vectors are

$$\boldsymbol{b}_1 = \frac{2\pi}{3a}\begin{pmatrix}1\\\sqrt{3}\end{pmatrix} \text{ and } \boldsymbol{b}_2 = \frac{2\pi}{3a}\begin{pmatrix}1\\-\sqrt{3}\end{pmatrix} \tag{1.3}$$

and the first Brillouin zone is hexagonal, characterized by the four high symmetry points Γ, M, K and K' represented figure 1.1b. Especially, the non equivalence of the K and K' points is responsible for the valley degeneracy of graphene and an important part of the peculiar physics of graphene is concentrated on these specific points.

1.1.2 Electronic properties and optical absorption

Band structure

As stated previously the carbon atoms in graphene are bound thanks to the sp2 hybrid orbitals. They are the result from the hybridization of the 2s, $2p_x$ and $2p_y$ orbitals, leaving the $2p_z$ orbitals perpendicular to the plane. Interactions between the neighbouring sp2 hybrid orbitals leads to the bonding σ and antibonding σ^* orbitals that become bands once the full graphene lattice is considered. Similarly, the out-of-plane $2p_z$ orbitals gives the π and π^* electronic bands. Energetically the σ bands are far away from the Fermi level, with a separation of more than 10 eV and can be neglected in most experiments. Thus, most of the graphene's properties can be understood by considering the electronic structure of the π and π^* bands [17].

Calculations of the π and π^* bands can be done by the means of a tight-binding-model [18, 19]. Considering only interactions with nearest neighbors and a hopping parameter $t \approx 2.7$ eV, the electronic dispersion of the π $(-)$ and π^* $(+)$ bands is given by

$$E_\pm(\boldsymbol{k}) = \pm t\sqrt{3 + f(\boldsymbol{k})} \tag{1.4}$$

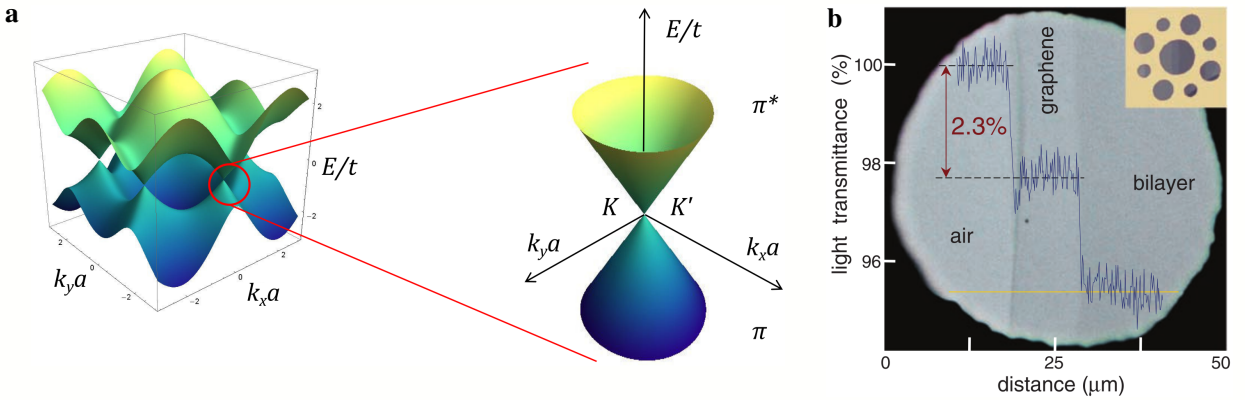

Figure 1.2: Electronic structure and optical absorption of graphene. **a.** Electronic structure of graphene-based on equation (1.4) with a zoom on the Dirac cone located at the K and K' points of the Brillouin zone. Adapted from [16]. **b.** Optical image of monolayer and bilayer graphene in a transmission microscope. The blue line gives the change of light transmittance along the yellow line, with a 2.3% drop for each added graphene layer. The inset on the top right corner is a picture of the used sample design. Adapted from [20].

with

$$f(\boldsymbol{k}) = 2\cos\left(\sqrt{3}k_y a\right) + 4\cos\left(\frac{\sqrt{3}}{2}k_y a\right)\cos\left(\frac{3}{2}k_x a\right) \tag{1.5}$$

and is represented figure 1.2a. The two bands are degenerate at the corners of the Brillouin zone, represented by the K and K' points, with the touching point being the position of the Fermi level for neutral graphene. Furthermore, one can note from figure 1.2a and equation (1.4) that the bands are symmetric with respect to the zero energy plane. This apparent symmetry is due to our nearest neighbor approximation and is not true anymore once further neighbor hopping is considered.

Dirac Cones

Since the π and π^* bands touch at the K and K' points, the low energy states with energies $E < t$ are located near those same points. Their wavevector can be expressed as $\boldsymbol{k} \approx \boldsymbol{K}^{(\prime)} + \boldsymbol{q}$ with $|\boldsymbol{q}|a \ll 1$ and their dispersion relation can be obtained from a Taylor expansion of equation (1.4). The resulting dispersion is linear and goes as

$$E_{\pm}(\boldsymbol{q}) = \pm\hbar v_{\mathrm{F}}|\boldsymbol{q}| \tag{1.6}$$

with $v_{\mathrm{F}} = 3ta/2\hbar \approx 1 \times 10^6$ m.s^{-1} the *Fermi velocity*. Equation (1.6) is similar to the energy dispersion of photons $E = \hbar ck$ with $c = v_{\mathrm{F}}$. This uncommon linear dispersion relation is what gives graphene its peculiar electronic properties. Electrons can be described as *massless Dirac fermions* and the electronic wavefunctions at the K and K' points are solutions to the relativistic Dirac equation instead of the Schrödinger equation, from which the electrons gain unique properties as the half integer quantum Hall effect or Klein tunneling [15]. Still, one should note that despite being described by relativistic equations, the electrons in graphene

are not strictly speaking relativistic particles since their speed is given by the Fermi velocity $v_F \ll c$.

Another uncommon property resulting from equation (1.6) concerns the density of states

$$g(E) = \frac{2E}{\pi(\hbar v_F)^2} \tag{1.7}$$

that scales linearly with the energy E and vanishes for $E = 0$, instead of remaining constant as it is usually the case for a 2D electron gas. Note again that all the specificities mentioned here are true only close to the K and K' points of the Brillouin Zone. For higher wavevectors $|\boldsymbol{q}|$, the cone shape deforms itself into a triangular like shape and is not anymore isotrope in momentum space. This effect is called *trigonal warping* [21, 22].

Optical absorption

The optical absorption of graphene can involve both interband and intraband transitions. For undoped graphene, since $g(0) = 0$, intraband transitions are not possible. Furthermore, in the near infrared and visible range, intraband transitions dominate the optical absorption, that is constant and independent of the Fermi velocity v_F. One can estimate its value by considering the ratio between absorbed and incident power [20]

$$\mathcal{A} = \frac{P_{abs}}{P_{in}} = \frac{\eta_a \hbar\omega}{c|\boldsymbol{\mathcal{E}}|/4\pi} \tag{1.8}$$

where photons have an energy $\hbar\omega$, $\boldsymbol{\mathcal{E}}$ is the incoming light field and η_a is the probability of absorption and can be determined by Fermi's golden rule [20]

$$\eta_a = \frac{2\pi}{\hbar}|M|^2 g(E). \tag{1.9}$$

In this expression, M represents the matrix elements of the 2D Dirac light-matter interaction Hamiltonian and can be calculated to obtain $|M|^2 = (e|\boldsymbol{\mathcal{E}}|v_F)^2/8\omega^2$. Thus, the absorbed power is given by[1] $P_{abs} = (e|\boldsymbol{\mathcal{E}}|)^2/4\hbar$ that finally leads to the optical absorption

$$\mathcal{A} = \pi\alpha \approx 2.3\% \tag{1.10}$$

with $\alpha = e^2/\hbar c$ the fine structure constant [20]. This estimation was confirmed experimentally, as presented in figure 1.2b that shows an optical image of monolayer and bilayer graphene in a transmission microscope. The blue line is showing the optical transmission along the yellow line and present drops of 2.3 % for each additional layer of graphene. While this value can seem small, it is enough to be distinguished by a well trained eye. This estimation of the absorption of a graphene monolayer can be extended to few-layer graphene as $\mathcal{A} = N\pi\alpha$ with N the number of layers and has been proven to be a good approximation up to $N \leq 4$ [20].

[1] We used there that the absorption of a photon with energy $\hbar\omega$ excites electrons of energy $E = \hbar\omega/2$

1.1.3 Vibrational properties

Phonon dispersion and Kohn anomalies

With two atoms per unit cell, graphene has six phonon branches that are represented figure 1.3a. Two of them are in-plane longitudinal modes (LA and LO), two in-plane transverse modes (TA and TO) and two out-of-plane modes (ZA and ZO). Their frequencies can vary with strain, doping or dielectric screening. Measuring their characteristics by the means, for example, of Raman spectroscopy is a common way to experimentally probe the effect of external parameters on the graphene properties.

As highlighted by the red lines in figure 1.3a, some kinks appear in the dispersion of the TO phonons at K and the two degenerate LO and TO bands at Γ. These kinks were described in 1959 by W. Kohn [23] and are since then referred to as *Kohn anomalies*. Their origin can be understood by considering the conduction electrons of a metal as a free electron gas with a Fermi wavenumber k_F. If a charge density $\rho_\mathrm{ext} = \rho_0 e^{i\boldsymbol{q}.\boldsymbol{r}}$ is present in the metal, it would then induce an electronic charge density

$$\rho_\mathrm{e} = -F(q)\rho_0 e^{i\boldsymbol{q}.\boldsymbol{r}} \tag{1.11}$$

where $F(q)$ depends on the embedded charge density wavenumber q and the Fermi wavenumber k_F. In particular, for $q \approx 2k_\mathrm{F}$,

$$F(q) \propto 1 + \frac{1}{2k_\mathrm{F}}(q - 2k_\mathrm{F}) \ln|q - 2k_\mathrm{F}| \tag{1.12}$$

that leads to the singular condition

$$\lim_{q \to 2k_\mathrm{F}} \frac{\mathrm{d}F}{\mathrm{d}q} = -\infty. \tag{1.13}$$

This result illustrates the abrupt decrease of the ability of electrons to screen effectively the embedded charge density ρ_ext for $q > 2k_\mathrm{F}$ because of the impossibility for ρ_ext to cause virtual excitations of electrons that conserve energy as soon as $q > 2k_\mathrm{F}$.

If we consider phonons, a lattice vibration with wavevector $\boldsymbol{q}$ produces a change of ionic charge density in the material of the form [23]

$$\rho_\mathrm{ion} = \sum_{\boldsymbol{Q}} A_{\boldsymbol{Q}} e^{i(\boldsymbol{q}+\boldsymbol{Q}).\boldsymbol{r}} \tag{1.14}$$

where $\boldsymbol{Q}$ stands for the reciprocal lattice vectors and $A_{\boldsymbol{Q}}$ are constant coefficients. Thus, the induced electronic charge density ρ_e has the form of equation (1.11) and abruptly diminishes when $|\boldsymbol{q} + \boldsymbol{Q}| = 2k_\mathrm{F}$ in agreement with equation (1.13). The sharp decrease of ρ_e results in a drop of the restoring force that is directly reflected in the phonon frequency in the form of an abrupt frequency softening with a divergence of the frequency gradient in momentum space $|\nabla_{\boldsymbol{q}}\omega_\mathrm{ph}(\boldsymbol{q})| = \infty$.

W. Kohn stated that the locations of these anomalies in a metal are determined solely by the Fermi surface. They are to be expected for phonon wavevectors $\boldsymbol{q}$ acting as unique link

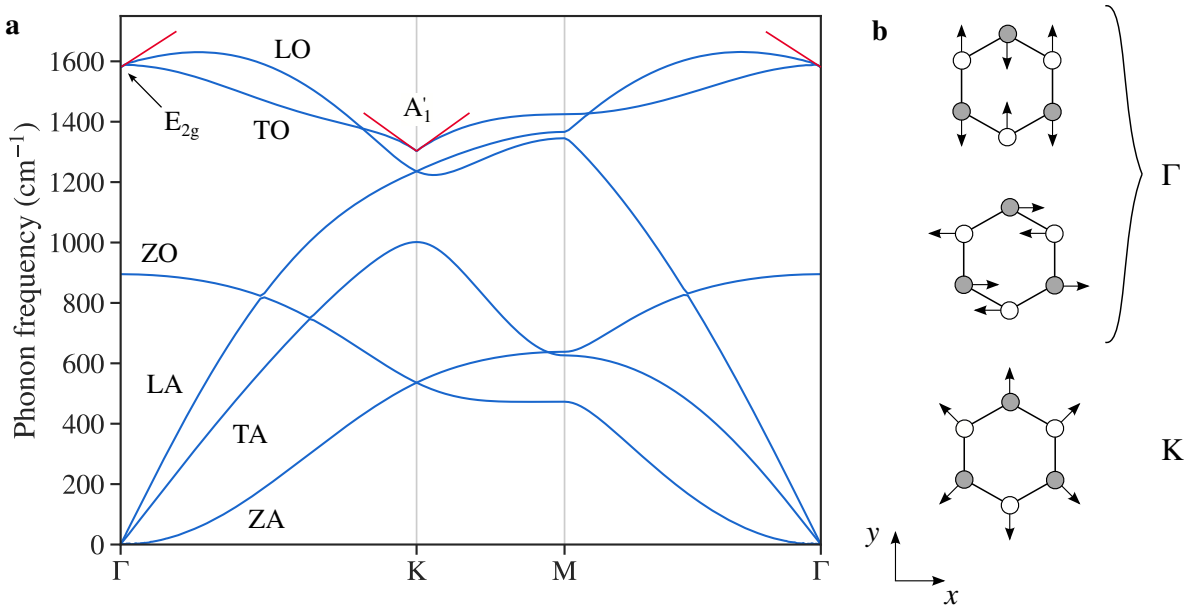

Figure 1.3: Phonons in graphene. a. Phonon dispersion in monolayer graphene. Adapted from [24]. Red lines mark the Kohn anomalies at the K and Γ points. **b.** Real space representation of the Raman active phonons in graphene, at the Γ and K points.

of two electronic states on the Fermi surface $\boldsymbol{k_1}$ and $\boldsymbol{k_2}$ such that $\boldsymbol{k_2} = \boldsymbol{k_1} + \boldsymbol{q}$ [23]. For the case of graphene, the Fermi surface is defined by 6 points at the corners of the Brillouin zone, thus leaving $\boldsymbol{q} = \boldsymbol{\Gamma}$ and $\boldsymbol{q} = \boldsymbol{K}, \boldsymbol{K'}$ as only possibilities [25, 26, 27].

Since the original description of Kohn anomalies is understood as arising from an abrupt decrease of the screening of the ionic charge density by the free electron gas, we may expect that the amplitude of a Kohn anomaly is sensitive to the dielectric environment of the considered metal. In chapter 3 we will test this hypothesis by investigating a set of graphene-based heterostructures with different dielectric environments and highlight how the different symmetries of phonons at Γ or K may change the sensitivity of the Kohn anomaly to dielectric screening.

Raman modes of Graphene

The only Raman active phonons in graphene originates from the TO and LO branches and are represented figure 1.3b. They are involved in the various peaks observed in a typical Raman spectrum of monolayer graphene as shown figure 1.4a. We will focus on the three ones labeled in figure 1.4a, being the so-called G, 2D and 2D' modes.

G-mode

The G-mode, arising at a frequency $\omega_G \approx 1580$ cm^{-1}, is the only active one-phonon mode in graphene. It results from a non-resonant process, as illustrated figure 1.4b, and involves one zone-center phonon with E_{2g} symmetry arising from the degenerate TO/LO band at Γ. As we shall see later, this mode is highly sensitive to strain and doping and is the main one

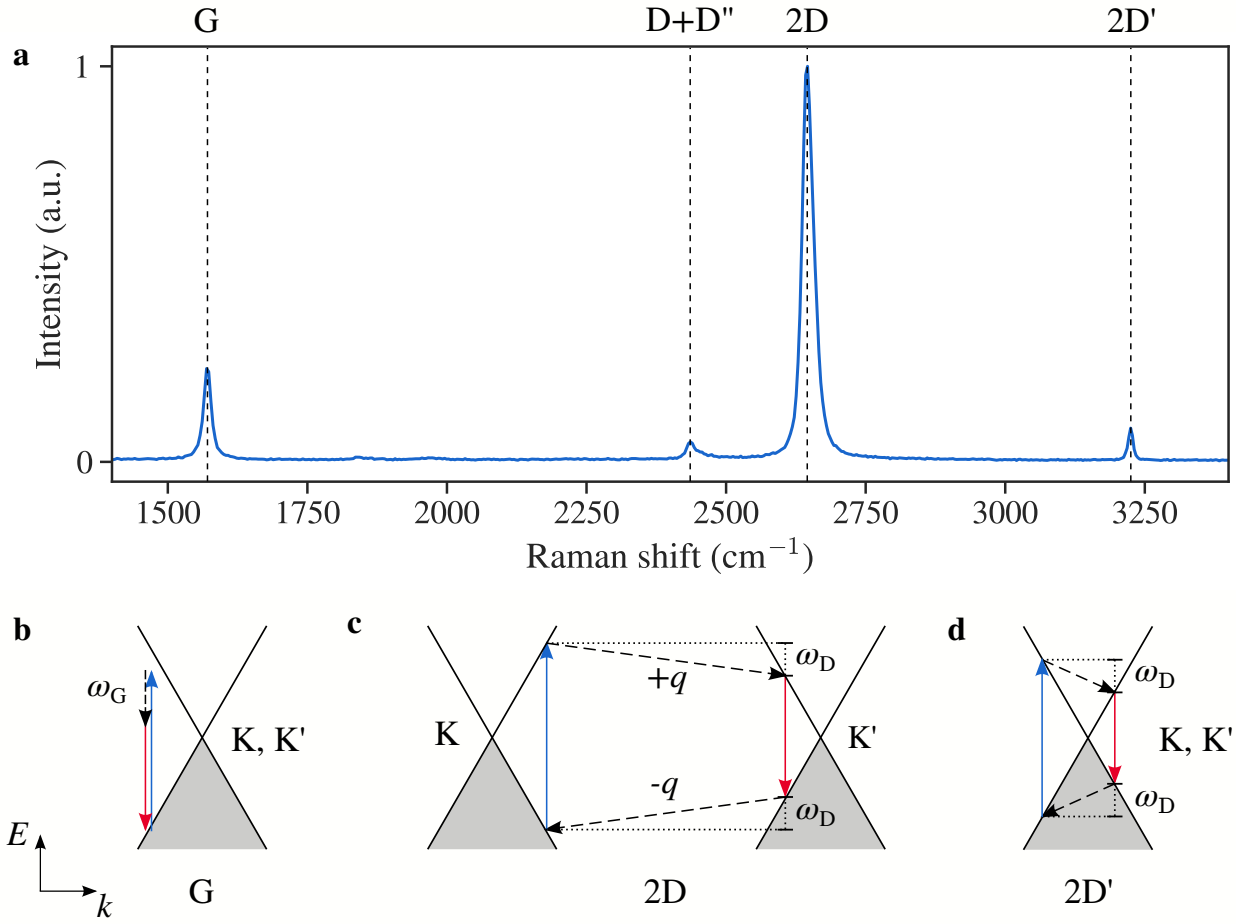

Figure 1.4: Raman modes in monolayer graphene. a. Typical Raman spectrum of monolayer graphene. **b,c,d.** One dimensional representation in energy-momentum space of of the G-mode (**b.**), 2D-mode (**c.**) and 2D'-mode scattering processes.

used for the characterisation of graphene samples [28].

2D-mode

The 2D-mode, with a frequency usually around $\omega_{2D} \approx 2600 - 2700$ cm^{-1}, results from doubly resonant processes involving two near zone-edge TO phonons with opposite momenta $\boldsymbol{q} \approx \boldsymbol{K}, \boldsymbol{K'}$, similar to the one represented figure 1.4c. It is formed by the sum of all the equivalent scattering processes and its description is far from being trivial. This character is revealed more clearly for non-monolayer graphene [28] and for undoped suspended monolayer graphene [22] as its spectral shape is not properly fitted by a single peak anymore. This effect is illustrated figure 1.5a that shows the 2D-mode spectrum of undoped suspended monolayer graphene (top) and SiO_2-supported monolayer graphene (bottom). For the SiO_2-supported case, the 2D-mode feature is well fitted by a single Voigt profile. It is true as well for doped suspended graphene [22]. In the special case of undoped suspended graphene, the asymmetric shape of the 2D-mode feature can be phenomenologically fit by a double peak profile $f(\omega) = f_+(\omega) + f_-(\omega)$ [22] where the $2D_\pm$ subfeatures are modified Lorentzian

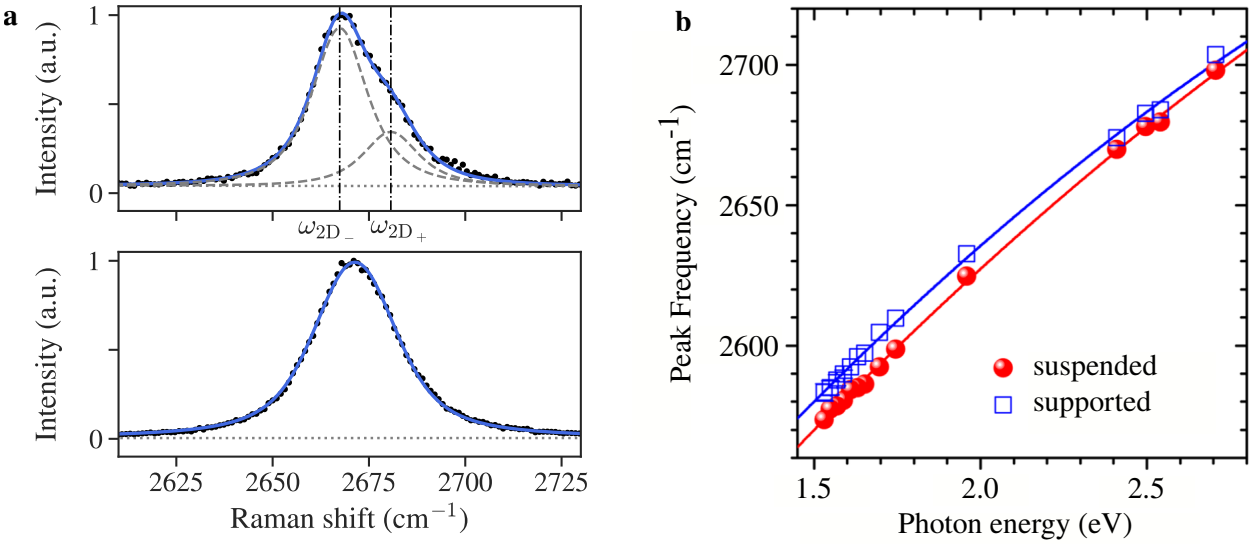

Figure 1.5: The 2D-mode in monolayer graphene a. Spectrum of the 2D-mode feature for undoped suspended graphene (top) and SiO_2-supported graphene (bottom) with their fits. The dashed grey lines in the top panel corresponds to the two $2D_\pm$ subfeatures described by equation (1.15). **b.** Dispersion of the 2D-mode frequency with the photon energy for suspended graphene (red) and supported graphene (blue). Adapted from [22].

functions [29]

$$f_\pm(\omega) \propto \left[(\omega - \omega_{2D_\pm})^2 + \frac{\gamma}{4(2^{2/3}-1)}\right]^{-3/2} \tag{1.15}$$

with γ a common parameter for the two subfeatures. Since the $2D_-$ subfeature has a much larger spectral weight, the position of the 2D-mode can be taken as $\omega_{2D} = \omega_{2D_-}$. It is important here to emphasize that the two subfeatures can not be interpreted as arising from the inner and outer loops of a same 2D-mode scattering process as the one dimensional picture remains a simplified approximation and that a complete two-dimensional model of the 2D-mode scattering process is needed to properly describe the 2D-mode feature [22]. The main purpose of this process is to obtain a good fit of the asymmetric 2D-mode lineshape with a smaller number of fitting parameters than a double Voigt fit. This procedure is the one applied in chapter 3 where we fit the 2D-mode feature of suspended graphene with a double modified Lorentzian profile and the 2D-mode feature of other sample configurations with a single Voigt profile.

Another specificity of the 2D-mode is its dispersion with the photon energy. Assuming an approximate double resonance condition [30] the 2D-mode frequency can be estimated as

$$\omega_{2D} = 2\omega_K + 2\frac{v_{TO}}{v_F}\omega_L \tag{1.16}$$

with ω_K the phonon frequency at K, $v_{TO} = d\omega(q)/dq$ the velocity of TO phonons and ω_L the incoming photon energy. Figure 1.5b shows this dispersion for suspended and SiO_2-supported graphene [22].

2D'-mode

The 2D'-mode, with a frequency $\omega_{2D'} \approx 3240$ cm^{-1}, is the intra-valley analogue of the 2D-mode and results from a resonant process involving two phonons of opposite momenta in the vicinity of the Γ point [29, 31]. Since the electron-phonon coupling at Γ is smaller than at K, the 2D'-mode feature is less intense than the 2D-mode feature [25].

Defect related modes

Non-resonant Raman modes resulting from the scattering of phonons with defects in graphene can also appear in the Raman spectrum of monolayer graphene. The so-called D-mode is often used to determine the quality of a graphene monolayer as its intensity is proportionnal to the defect density in graphene [28]. It appears between 1300 and 1400 cm^{-1} depending on the incoming laser energy. Its absence in the Raman spectrum shown figure 1.4a is a proof of the very low defect density in our mechanically exfoliated graphene monolayer.

A second defect related feature arises around 2450 cm^{-1} and corresponds to the D + D$''$ feature. It results from a non-resonant version of the 2D-mode scattering process involving a D-phonon and a phonon from the LA branch [28].

Raman spectroscopy of graphene as a versatile probe

The analysis of the Raman features in graphene provides extensive information on the interactions of graphene with its environment and can be used as a versatile probe. Especially, the combined study of the G and 2D modes features is a powerful tool that enables a precise determination of doping and strain parameters in monolayer graphene, based on a combination of theoretical and empirical modeling [28].

Doping

Doping strongly affects the Raman response of graphene and makes it the tool of choice for charge dependent studies in graphene samples. Both the G and 2D-mode features are affected and result in characteristic behaviors of the Raman parameters of these two modes. We will there summarize them following the work of G. Froehlicher *et al.* [32, 16].

A first clear behavior can be observed on the G-mode frequency ω_G. The shift $\Delta\omega_G^{(dop)} = \omega_G(E_F) - \omega_G^0$, where $\omega_G^0 = \omega_G(E_F = 0)$, arising with doping is well understood and composed of two different contributions. The first one corresponds to a phonon softening (hardening) because of additional charges in the antibonding orbitals that results from electron (hole) doping. This leads to modifications in the carbon-carbon strength. This contribution is referred to as the *adiabatic* contribution $\Delta\omega_G^A$ since it is compatible with the Born-Oppenheimer approximation. The second contribution corresponds to the renormalization of the G-mode phonon energy because of the interaction with virtual electron-hole pairs and cannot be deduced from the Born-Oppenheimer approximation. Hence, this constribution is known as the *non-adiabatic* contribution $\Delta\omega_G^{NA}$. The total shift of the G-mode due to doping can then

be expressed as

$$\Delta\omega_{\mathrm{G}}^{(\mathrm{dop})} = \Delta\omega_{\mathrm{G}}^{\mathrm{A}} + \Delta\omega_{\mathrm{G}}^{\mathrm{NA}} \tag{1.17}$$

where the adiabatic contribution can be described for finite temperatures T as a small correction that does not significantly depends on doping in the range explored in this work [33].

The non-adiabatic contribution is thus given by [33, 34]

$$\Delta\omega_{\mathrm{G}}^{\mathrm{NA}} = \frac{\lambda_{\Gamma}}{2\pi\hbar}\fint \frac{[f(E-E_{\mathrm{F}}) - f(E)]E^2\mathrm{sgn}(E)}{E^2 - (\hbar\omega_{\mathrm{G}}^0)^2/4}\mathrm{d}E \tag{1.18}$$

where $\fint$ stands for the Cauchy principal value, λ_{Γ} is a dimensionless coefficient that corresponds to the electron-phonon coupling strength at Γ [29] and $f(E) = [1+\exp(E/k_{\mathrm{B}}T)]^{-1}$ is the Fermi-Dirac distribution. Note that equation (1.18) gives two singularities when $E_F = \pm\hbar\omega_{\mathrm{G}}^0/2$ that comes from the $f(E-E_{\mathrm{F}}) - f(E)$ term. However, these singularities are smeared out at finite temperatures as the typical width of the Fermi-Dirac distribution is $k_{\mathrm{B}}T$.

The linewidth of the G-mode feature Γ_{G} is also strongly sensitive to doping and decreases as a function of $|E_{\mathrm{F}}|$ because of the spontaneous decay of G phonons into electron-hole pairs. Its variation can be obtained from the Fermi golden rule and leads to [32]

$$\Delta\Gamma_{\mathrm{G}}^{(\mathrm{dop})} = \frac{\lambda_{\Gamma}}{4}\omega_{\mathrm{G}}^0\left[f\left(-\frac{1}{2}\hbar\omega_{\mathrm{G}}^0 - E_{\mathrm{F}}\right) - f\left(\frac{1}{2}\hbar\omega_{\mathrm{G}}^0 - E_{\mathrm{F}}\right)\right] \tag{1.19}$$

that vanishes for $|E_{\mathrm{F}}| > \hbar\omega_{\mathrm{L}}/2$ because of Pauli blocking. To properly fit experimental data, both $\Delta\omega_{\mathrm{G}}^{(\mathrm{dop})}$ and $\Delta\Gamma_{\mathrm{G}}^{(\mathrm{dop})}$ need to be described as convolutions of equations (1.17) or (1.19) with a gaussian distribution with standard deviation δE_{F} to account for charge inhomogeneities, that results in random spatial fluctuations of the Fermi level E_{F} in the laser spot area [35, 36]. Figure 1.6a shows the variation with doping of ω_{G} (red) and $\Delta\Gamma_{\mathrm{G}}^{(\mathrm{dop})}$ (blue) together with their fit using equations (1.17) and (1.19) and a charge inhomogeneity parameter $\delta E_{\mathrm{F}} = 35$ meV [32].

An universal correlation between $\Delta\Gamma_{\mathrm{G}}^{(\mathrm{dop})}$ and $\Delta\omega_{\mathrm{G}}^{(\mathrm{dop})}$ can be deduced from equations (1.17) and (1.19). It is represented figure 1.6b and shows the very fast decrease of $\Delta\Gamma_{\mathrm{G}}^{(\mathrm{dop})}$ with doping, that diminishes faster than ω_{G} to reach the Pauli blocking regime. This correlation is true only for low doping ($|E_{\mathrm{F}}| \lesssim \hbar\omega_{\mathrm{G}}^0$).

Furthermore, while the intensity of the G-mode feature I_{G} is roughly constant for $|E_{\mathrm{F}}| \ll \hbar\omega_{\mathrm{L}}/2$, I_{2D} is not and decreases almost symmetrically with $|E_{\mathrm{F}}|$. Assuming fully resonant processes and neglecting trigonal warping, one gets for the integrated intensity of the 2D-mode feature that [29]

$$I_{\mathrm{2D}} \propto \left(\frac{\gamma_{\mathrm{K}}}{\gamma_{\mathrm{e-ph}} + \gamma_{\mathrm{D}} + \gamma_{\mathrm{ee}}}\right)^2 \tag{1.20}$$

where γ_{D} is the electron-defect scattering rate, γ_{ee} the electron-electron scattering rate and $\gamma_{\mathrm{e-ph}} = \gamma_{\mathrm{K}} + \gamma_{\Gamma}$ is the electron-phonon scattering rate, approximated as the sum of scattering rates for zone-center phonons γ_{Γ} and zone-edges phonons γ_{K}. γ_{D} and $\gamma_{\mathrm{e-ph}}$ are not affected

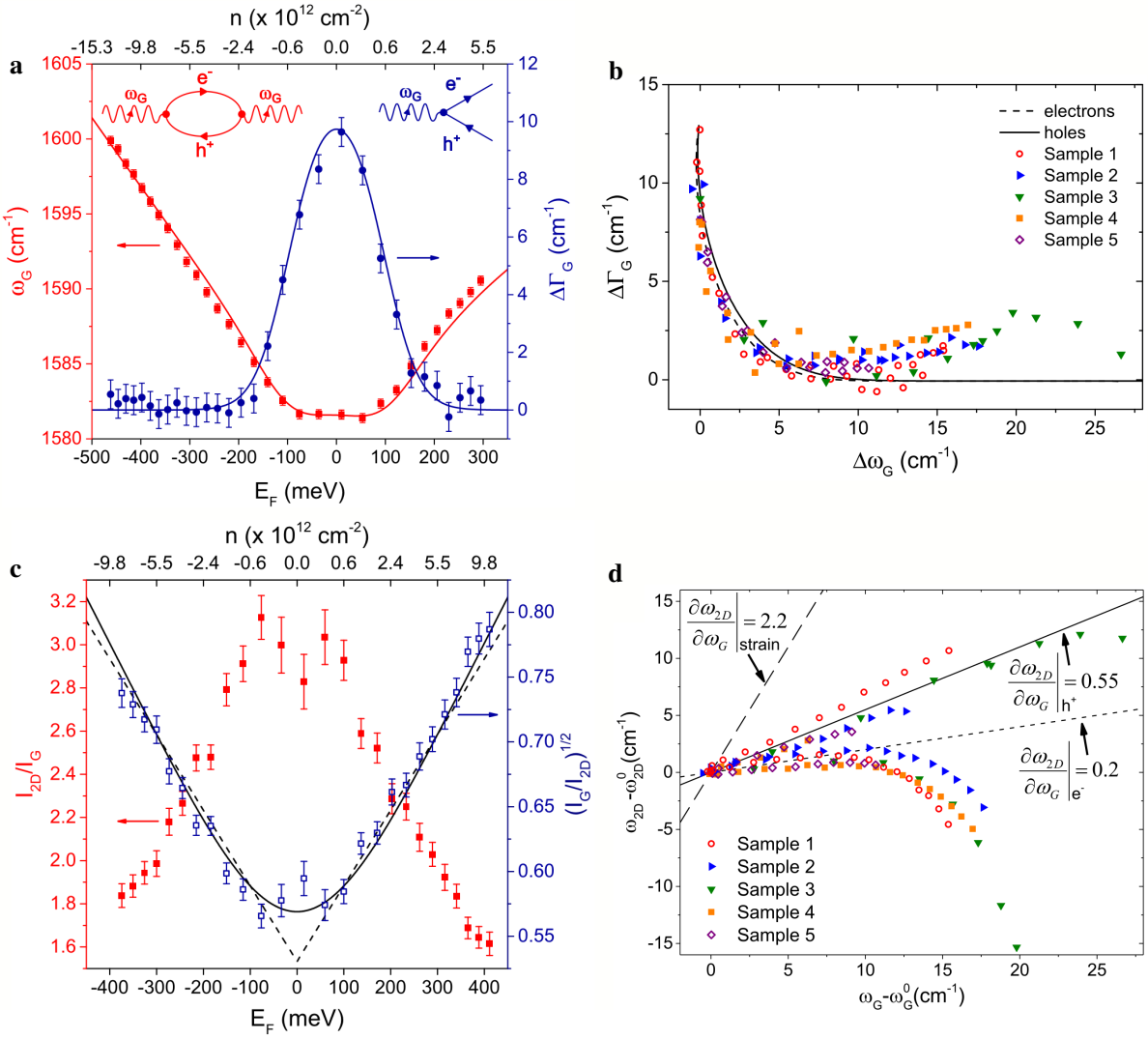

Figure 1.6: Raman spectroscopy of graphene as a probe of doping. **a.** Variation of the G-mode frequency ω_{G} (red) and relative FWHM $\Delta\Gamma_{\mathrm{G}}^{(\mathrm{dop})}$ (blue) as a function of doping. The red and blue insets represent the diagram of the two processes related to the non-adiabatic shift $\Delta\omega_{\mathrm{G}}^{\mathrm{NA}}$ and reduction of linewidth $\Delta\Gamma_{\mathrm{G}}^{(\mathrm{dop})}$ respectively. **b.** Correlation between the FWHM and the frequency of the G-mode related to doping. **c.** Variation of the intensity ratio between the 2D and G-modes as a function of doping. The red points give $I_{2\mathrm{D}}/I_{\mathrm{G}}$ and the blue points give $\sqrt{I_{\mathrm{G}}/I_{2\mathrm{D}}}$ **d.** Correlation between the G and 2D-mode frequencies related to doping or strain. The continuous lines give the expected slopes for strain ($\partial\omega_{2\mathrm{D}}/\partial\omega_{\mathrm{G}} = 2.2$), hole doping ($\partial\omega_{2\mathrm{D}}/\partial\omega_{\mathrm{G}} = 0.55$) and electron doping ($\partial\omega_{2\mathrm{D}}/\partial\omega_{\mathrm{G}} = 0.2$). All panels are adapted from [32].

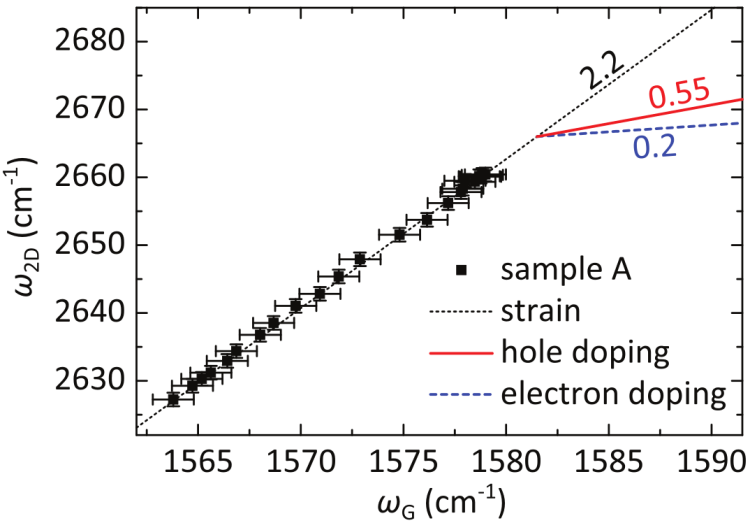

Figure 1.7: Raman spectroscopy of graphene as a probe of strain. Correlation between the G and 2D-mode frequencies related to strain. The dotted black line gives the expected slopes for strain ($\partial\omega_{2D}/\partial\omega_G = 2.2$) and is perfectly matching the experimental data obtained on a suspended graphene flake strained electromechanically. All panels are adapted from [38].

by changes in E_F but γ_{ee} scales linearly with $|E_F|$ thus leading to the diminution of the I_{2D}/I_G ratio as shown figure 1.6d.

Finally, by combining the modeled evolution of $\Delta\omega_G^{(dop)}$ with empirical studies of the doping induced shift of the 2D-mode $\Delta\omega_{2D}^{(dop)}$, universal linear correlations between the 2D-mode and G-mode frequencies can be deduced for -500 meV $\lesssim E_F \lesssim 250$ meV. The corresponding slopes are determined phenomenologically and gives $\partial\omega_{2D}/\partial\omega_G = 0.55$ for hole doping and $\partial\omega_{2D}/\partial\omega_G = 0.2$ for electron doping [37, 32]. This method has the strong advantage to give the possibility to decouple doping and strain contributions via a graphical construction, provided that the undoped and unstrained reference point is known [37].

Strain

Mechanical strain is a straightforward way to alter the lattice constant by deforming the lattice itself. That way, applying tensile strain can be seen as reducing the spring constant of the harmonic oscillator that models the lattice's vibrations, and leads to phonon softening [4]. In this work, we will focus on biaxial strain as that is the type of strain that can be applied on a circular drum. For biaxial strain ε, the change in G or 2D mode frequency is given by [39, 14]

$$\Delta\omega_i^{(strain)} = -2\gamma_i\omega_i^0\varepsilon \tag{1.21}$$

where $i = G, 2D$, γ_i is the Gruneisen parameter (with $\gamma_G = 1.8$ and $\gamma_{2D} = 2.4$), ω_i^0 is the unstrained frequency of the considered mode and ε the strain value where we take $\varepsilon > 0$ for tensile strain and $\varepsilon < 0$ for compressive strain. From equation (1.21) we can deduce the expected slope of the $\omega_G - \omega_{2D}$ correlation for strain by considering some typical values for the unstrained frequencies. For a laser energy $\hbar\omega_L = 2.33$ eV, typical values for unstrained and undoped graphene are $\omega_G^0 = 1581$ cm^{-1} and $\omega_{2D}^0 = 2667 \pm 1$ cm^{-1} [38] that lead to the

slope

$$\frac{\Delta\omega_{2D}}{\Delta\omega_G} = \frac{\gamma_{2D}\omega^0_{2D}}{\gamma_G\omega^0_G} \approx 2.2 \pm 0.1 \tag{1.22}$$

as represented by the dotted line in figure 1.7. Note that uniaxial strain can break the lattice symmetry and lead to a lifting of the LO/TO phonon branches at Γ, resulting in a splitting of the G-mode feature into two polarization dependent subfeatures [14].

1.2 Transition metal dichalcogenides

1.2.1 Crystal structure

Transition metal dichalcogenides (TMDs) refer to a vast family of van der Waals materials with formula MX_2 formed by a single plane of transition metal atoms M embedded between two planes of chalcogen atoms X. They mostly present three different crystalline phases, being the hexagonal (2Hc), octahedral (1T) and distorted octahedral (1T') phases. In this work, we will focus exclusively on the TMDs with 2Hc crystalline phase, with M = Mo, W and X = S, Se. The crystal structure of 2Hc-TMDs is shown figure 1.8a with the transition metal atoms in blue and the chalcogen atoms in orange. Viewed from the top, it presents an hexagonal structure with a basis analog to the one of graphene but with a broken inversion symmetry since the A and B sites of the honeycomb lattice are occupied by different atoms [40]. Correspondingly, the first Brillouin zone is also hexagonal with similar high symmetry points than graphene in the (k_x, k_y)-plane (see figure 1.8b) [16, 41].

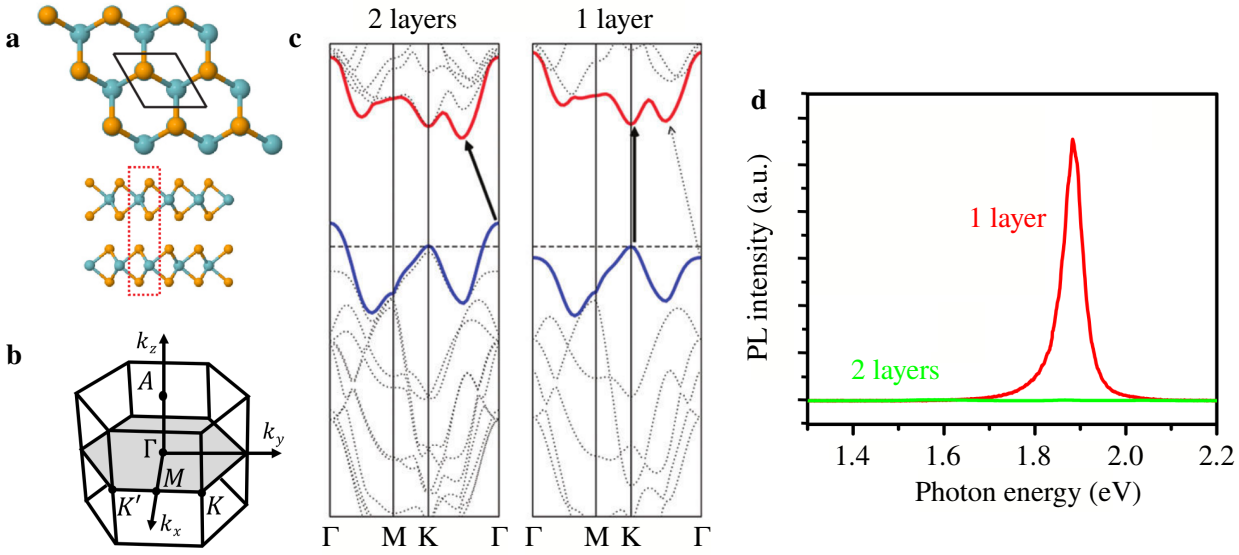

Figure 1.8: Crystalline and band structures of TMDs. **a.** Top and side view of the crystalline structure of 2Hc-TMDs. Adapted from [41]. **b.** First Brillouin zone of 2Hc-TMDs. Adapted from [16]. **c.** Calculated band structure of bilayer and monolayer MoS_2. Adapted from [42]. **d.** PL spectrum of bilayer (green) and monolayer (red) MoS_2. Adapted from [43].

1.2.2 Band structure

Indirect to direct transition

The TMDs considered in this work are semiconductors that undergo a transition from indirect to direct gap when thinned down to the monolayer limit. Figure 1.8c details it by showing the calculated band structure for bilayer and monolayer MoS_2 in the Γ-M-K-Γ axis [42]. From the bulk to the bilayer case, the maximum of the valence band is located at the Γ point while the minimum of the conduction band is in the middle of the K-Γ segment. When the number of layer is decreased, the indirect bandgap increases to finally become larger than the direct gap at K once the monolayer limit is reached.

The main consequence of the indirect to direct transition is a massive increase of the emission efficiency, as the lowest energy transition is now possible without the need to interact with a phonon in order to fulfill the condition of momentum conservation. As a result, the photoluminescence (PL) intensity of monolayer TMDs is greatly enhanced with respect to bilayer or thicker samples. This is illustrated figure 1.8d with the PL spectra of monolayer (red) and bilayer (green) MoS_2 [43]. This strong coupling to light makes monolayer TMDs a perfect candidate for photonics or optoelectronics applications [44, 11].

Spin-orbit coupling and fine structure

Since the band-edge electrons and holes originates from the d-orbitals of the heavy transition metal atoms, a strong spin-orbit coupling takes place and splits the electronic bands depending on the respective spin of the carriers [45, 46]. Because of the broken inversion symmetry of the crystalline structure, the spin-splitting is opposite between the K and K' valley and leads to chiral selection rules. Circularly polarized light can be used to excite selectively the K or K' valley using respectively σ^+ or σ^- polarized light[2].

Furthermore, while the spin-orbit coupling splitting of the valence band Δ^{v}_{SO} is always of the same sign in a given valley, the sign of the splitting of the conduction band Δ^{c}_{SO} depends on the material. For the K valley, $\Delta^{v}_{SO} > 0$ for any TMD but $\Delta^{c}_{SO} < 0$ for $MoSe_2$ and $\Delta^{c}_{SO} > 0$ for WS_2, WSe_2 and MoS_2 (see figure 1.9). As a result of the sign of Δ^{c}_{SO}, the optical transition of lowest energy is spin-allowed (spin-forbidden). Thus, we talk respectively about *bright* and *dark* TMDs.

The magnitude of the spin-orbit splitting is also different depending on the material and is about one order of magnitude higher for the valence band than the conduction band [46]. Specifically, the case of the small splitting of the conduction band of MoS_2 was only recently verified. While tight-binding and DFT calculations [47] suggest a very small positive splitting of a few meV giving a bright character to MoS_2, it was recently shown experimentally that the energy of the dark exciton is lower than the one of the bright exciton, proving that MoS_2 is a dark TMD [48].

[2] K and K' valleys are often referred to as +K and −K valleys in the literature related to valleytronics.

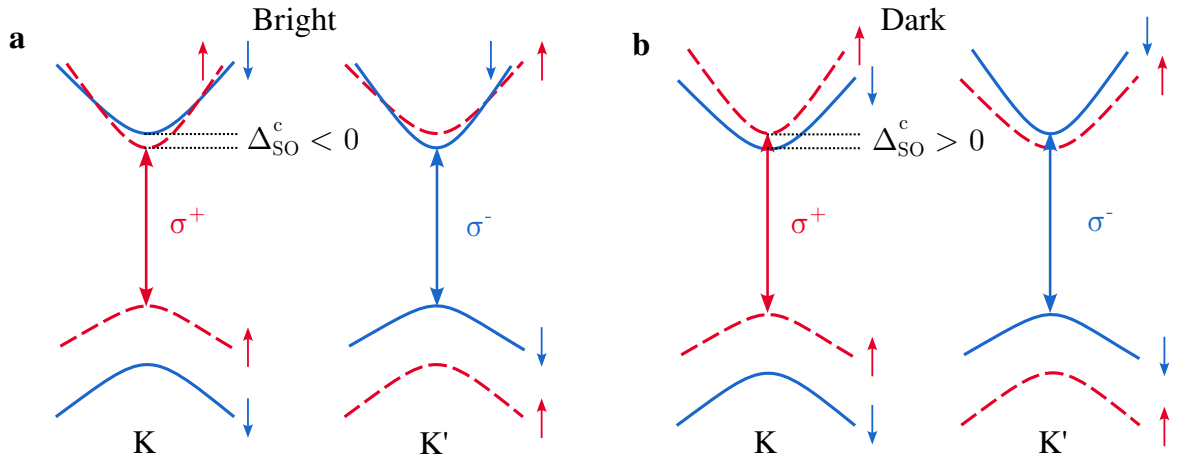

Figure 1.9: The fine structure of TMDs. a. Scheme of the fine structure at the K and K' valleys for bright TMDs. **b.** Scheme of the fine structure at the K and K' valleys for dark TMDs. Spin up bands are represented by the dashed red lines and spin down bands by the blue continuous lines. Adapted from [11].

1.2.3 Excitons in TMDs

In semiconductors, the absorption of a photon leads to the excitation of an electron-hole pair via interband electronic transitions. The excited electron and hole being of opposite charge, they interact by an attractive Coulomb interaction and form bound states lying in the electronic bandgap called *excitons* [49, 5]. Because of the fine structure of TMDs described in the previous subsection, different interband transitions lead to the formation of different excitons. Figure 1.10a schematically represents the interband electronic transitions associated with the A and B excitons in TMDs, referred respectively as X_A and X_B. In this work, we focus on the A exciton of TMDs unless specified otherwise. The important properties of excitons in TMD monolayers will be discussed below.

Binding energy and Rydberg series

In the effective mass approximation, the Coulomb interaction between electron and hole is a hydrogen-like problem with a Coulomb potential

$$V_{e-h} = \frac{-e^2}{4\pi\epsilon_0\epsilon r} \tag{1.23}$$

with $r = |\boldsymbol{r}_e - \boldsymbol{r}_h|$ and e the charge of the electron. For a direct gap semiconductor the relative motion of the hole and the electron can be separated to describe the problem by considering the motion of the center of mass. By defining the total exciton mass $M = m_e + m_h$, with $m_{e,h}$ the electron or hole effective mass, and the exciton wavevector $\boldsymbol{K}_X = \boldsymbol{k}_e + \boldsymbol{k}_h$, one obtains the dispersion relation of excitons [49]

$$E_X^{(n)} = E_g + \frac{\hbar \boldsymbol{K}_X^2}{2M} - E_b^{(n)} \tag{1.24}$$

where E_g is the electronic bandgap and $E_b^{(n)}$ the binding energy of the n-th state in the Rydberg series. In the energy-momentum space, the dispersion is thus composed of a serie of states with parabolic dispersion as represented figure 1.10b. The lowest accessible state is then at the energy $E_{1s}(\boldsymbol{K}_X = 0)$, with quantum number $n = 1$, that defines the *optical gap* with a lower energy than the electronic gap E_g.

In 2D, the electron-hole pair is spatially confined while the Coulomb interaction remains 3D and modifies simultaneously the exciton binding energy, oscillator strength and Bohr radius. Assuming a homogeneous effective dielectric constant ϵ_{eff}, one obtains for the binding energies in 2D [49]

$$E_b^{(n)} = \frac{\mathrm{Ry}^*}{(n-1/2)^2} \tag{1.25}$$

with

$$\mathrm{Ry}^* = \mathrm{Ry}\frac{\mu}{m_0}\frac{1}{\epsilon_{eff}^2} \tag{1.26}$$

where Ry is the hydrogen Rydberg constant, $\mu = m_e m_h/(m_e + m_h)$ the reduced mass of the electron-hole pair and m_0 the free electron mass. A rough estimation of the exciton binding energy in TMDs can be obtained for $\mu \approx 0.25 m_0$ and $\epsilon_{eff} \approx 5$. One then reaches an energy range $E_b^{(n=1)} \sim 500$ meV [51, 52], a value two orders of magnitude larger than for bulk GaAs (4.3 meV) and one order of magnitude larger than for AlGaAs/GaAs quantum wells (21 meV) [53]. Thus the separation between optical and electronic bandgap is enhanced as illustrated figure 1.10c that sketches the optical absorption of semiconductors in the 3D and 2D situations [50]. Another interesting point is that the binding energy of excitons in TMDs is also larger than the energy of thermal fluctuations at room temperature $k_B T \approx 26$ meV and allows the excitons to remain stable at room temperature.

Overall, the expressions for the 2D case are obtained by formally replacing n by $n - 1/2$ in the 3D case equations. One can apply such transformation to estimate the scaling of the oscillator strength $f(n)$ and the excitonic Bohr radius $a_0(n)$ and deduce that the 2D confinement of the exciton leads to stronger oscillator strengths $f(n) \propto (n-1/2)^{-3}$ and smaller Bohr radii $a_0 \propto a_B(n-1/2)$ in the 2D case [49], with a_B the hydrogen Bohr radius.

The Rydberg series of the A exciton in WS_2 where measured in 2014 by A. Chernikov *et al.* [50] by measuring its reflectance contrast (see figure 1.10d). A good agreement with the 2D-model and equation (1.25) is observed for states with $n \geq 3$. For the lowest Rydberg states, equation (1.25) systematically overestimates the binding energy. This is due to the approximation of the dielectric constant as an effective homogeneous dielectric medium, that does not properly describe the propagation of the exciton electric field along the z direction. Indeed, when n increases, so does the excitonic Bohr radius a_0 and a smaller part of the excitonic interaction field propagates in the monolayer itself. The effective dielectric constant ϵ_{eff} is thus decreasing with n. A proper description is obtained by considering a Rytova-Keldysh potential [50, 54, 55]

$$V_{e-h}(r) = -\frac{\pi e^2}{2r_0}\left[H_0\left(\frac{r}{r_0}\right) - Y_0\left(\frac{r}{r_0}\right)\right] \tag{1.27}$$

where H_0 and Y_0 are Struve and Neumann functions [54, 55]. The correction with respect to

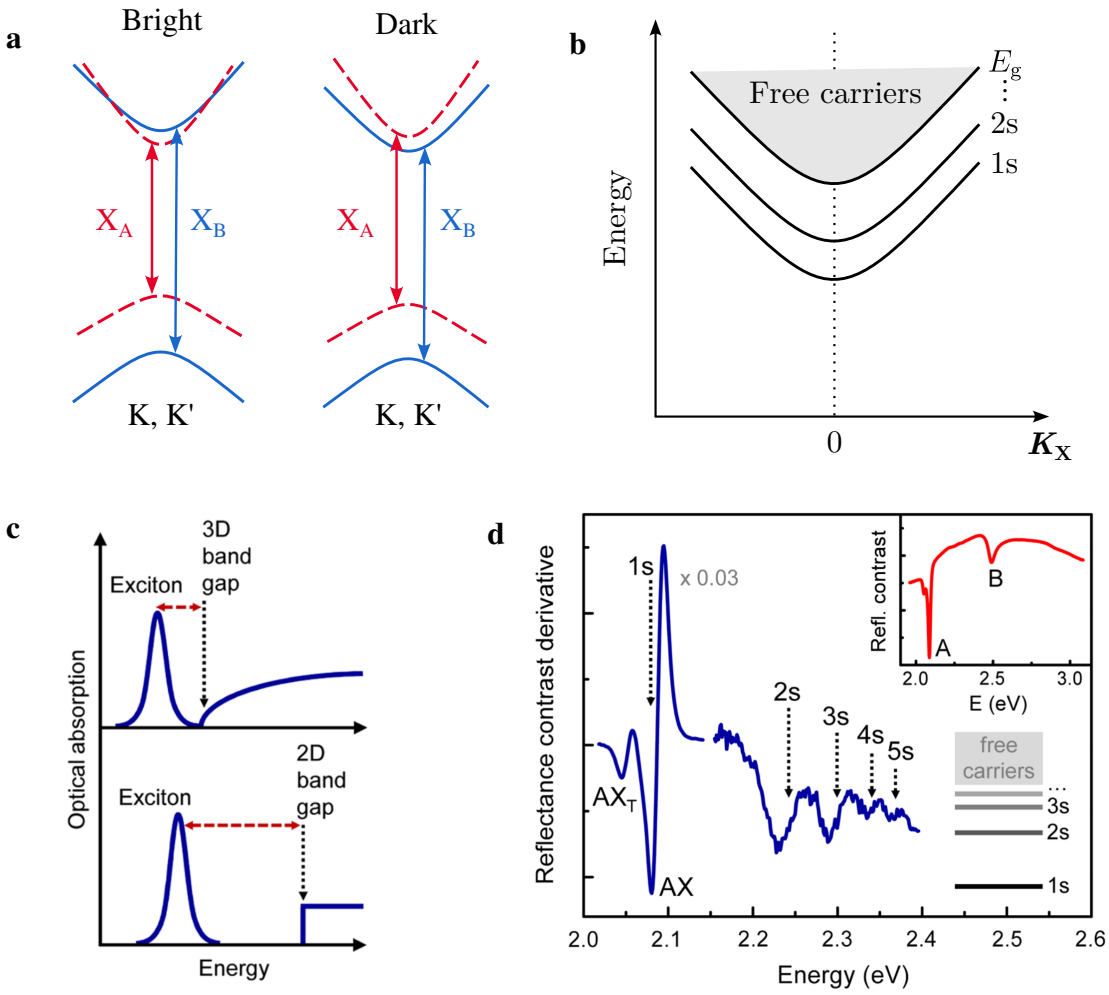

Figure 1.10: Excitons in TMDs. a. Sketch of the fine band structure of bright and dark TMDs at the K,K' points with the interband electronic transitions involved in the formation of the A and B excitons (X_A and X_B). **b.** Energy-momentum diagram of the exciton dispersion with the two first Rydberg states shown. **c.** Sketch of the optical absorption of semiconductors in the 3D case (top) and the 2D case (bottom) illustrating the increased binding energy of excitons induced by the spatial confinement. Adapted from [50]. **d.** Derivative of the reflectance contrast spectrum of monolayer WS_2 at low temperature. The absorption lines of the Rydberg states of the A exciton are marked up to $n = 5$ (5s state). The inset shows the reflectance contrast spectrum on a larger energy range to see the respective absorption peaks of the A, and B exciton 1s states. Adapted from [50].

our previous model is carried by the screening length r_0 that is related to the 2D polarizability of the monolayer TMD and acts as a typical length scale that links two different regimes of dielectric screening. The effective dielectric constant approximation is then recovered for $r \gg r_0$ with $V_{e-h}(r) \sim 1/r$, similarly to equation (1.23), while a regime of weaker interaction potential $V_{e-h}(r) \sim \ln(r)$ is found for $r \ll r_0$. The determination of the Rydberg states energies of the WS_2 monolayer using the Rytova-Keldysh potential gives an excellent agreement with the measured Rydberg series for $r_0 = 75$ Å and $E_g = 2.41$ eV [50].

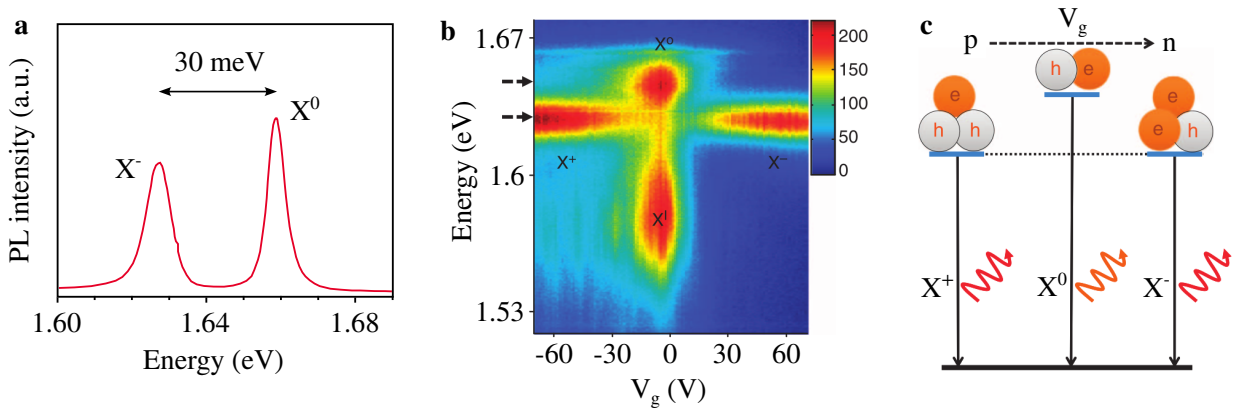

Figure 1.11: Trions in TMDs. a. Typical low temperature spectrum of monolayer $MoSe_2$ with the neutral exciton (X^0) and negatively charged trion (X^-). **b.** Charge dependent PL spectrum of monolayer $MoSe_2$ at low temperature. **c.** Sketch of the charge dependent PL emission in $MoSe_2$. All panels are adapted from [56].

Trion

In addition to excitons that are two body quasiparticles, the Coulomb interaction can form higher order excitonic states, composed of a higher number of charge carriers. The most common ones are *trions*, a three body charged quasiparticle sometimes simply called charged exciton. Similarly to excitons, trions were observed to be stable in TMDs up to room temperature with typical binding energies around 30 meV [56, 57]. Figure 1.11a shows a typical PL spectrum of monolayer $MoSe_2$ at low temperature with clear emission from the neutral exciton X^0 and the negatively charged trion X^-.

Trions are formed by the coupling of an exciton with free carriers and are thus dependent on the carrier density. Therefore their population can be monitored by a charge control of the TMD. Usually this is done with a classic field effect transistor geometry where a backgate V_g is applied to change the Fermi level of the sample. An example of such charge control in $MoSe_2$ is presented figure 1.11b where a colorplot of the evolution of the PL spectrum as a function of the backgate voltage is shown [56]. The associated diagram is sketched figure 1.11c. As the doping regime is sweeped from p to n doping, the neutral exciton features X^0 and X^I (that stands for the impurity trapped excitons) gets more prominent and overcome the emission of the positively charged trion when the neutrality point is reached. Increasing again the Fermi level leads to the opposite process with a decrease of the neutral excitons emissions and the appearing of a strong negatively charged trion feature. Note that unintentional doping in TMDs is usually a n type doping. Consequently, the trions observed in electrically floating devices are negatively charged [11].

Temperature dependent light emission

Temperature dependent PL spectrum

Despite the fact that excitons in TMDs remain stable at room temperature, their characteristics are temperature dependent and so is their emission spectrum. Figure 1.12a shows the evolution of the $MoSe_2$ PL spectrum with temperature [56]. A first observable effect concerns the energy of both the exciton and trion features that redshift with increasing temperatures. The excitonic states energies follows a standard semiconductor bandgap dependence and is well fitted by a modified Varshni equation [58, 59]

$$E_g(T) = E_g(0) - S\langle E_{ph}\rangle \left[\coth\left(\frac{\langle E_{ph}\rangle}{k_B T}\right) - 1\right] \tag{1.28}$$

where S is a dimensionless coupling constant, $\langle E_{ph}\rangle$ an average phonon energy and $E_g(0)$ the energy gap at 0 K. Applying equation (1.28) on the exciton and trion peak positions gives typical values $S \approx 2$ and $\langle E_{ph}\rangle = 15$ meV both for the exciton and trion [56] (see figure 1.12b).

The second striking effect is the drop of the trion emission around 55 K as visible in figure 1.12c that leads to negligible trion emission for $T > 150$ K . The disappearance of the trion emission with temperature can be attributed to electrons that escape the trion bound state because of thermal fluctuations [56].

Finally, homogeneous thermal broadening dominates the exciton emission even at low temperatures. For this reason the exciton emission lineshape is symmetric and the linewidth increases with temperature, going from typical values around 10 meV at low temperature to 50 meV at room temperature [56, 61]. One can note that the lineshape of the trion feature is slightly asymmetric at low temperature with a long low energy tail consistent with electron recoil effects. This effect is fully overcomed by homogeneous broadening for $T > 70$ K [56].

Temperature dependent exciton dynamics

Temperature also affects the exciton dynamics. To recombine radiatively, excitons needs to respect momentum conservation standing that only excitons with $|\boldsymbol{K}_X| \leq 2\pi/\lambda$ can recombine by emitting a photon of wavelength λ, defining the *light cone*. For a typical lattice parameter $a \sim 1$ Å, the maximum exciton momentum is 10^3 times larger than the one of a photon in the visible range. Thus, only excitons with $|\boldsymbol{K}_X| \approx 0$ can recombine radiatively[3]. When an out of equilibrium population of exciton is created, it will thermalize by the means of exciton-exciton interactions or exciton-phonon scattering. The last one can bring an exciton out of the light cone with a rate $\Gamma_{esc} = 1/\tau_{esc}$. The overall exciton decay rate can then be expressed as (see section D.1.2)

$$\Gamma_X = \Gamma_r^0 + \Gamma_{esc} \tag{1.29}$$

where $\Gamma_r^0 = 1/\tau_r^0$ is the intrinsic radiative decay rate of the exciton [60]. At low temperatures, the electron-phonon scattering is not fast enough to alter the light emission, $\Gamma_r^0 \gg \Gamma_{esc}$ and

[3] The same argument stands for one-phonon Raman spectroscopy (see section D.2)

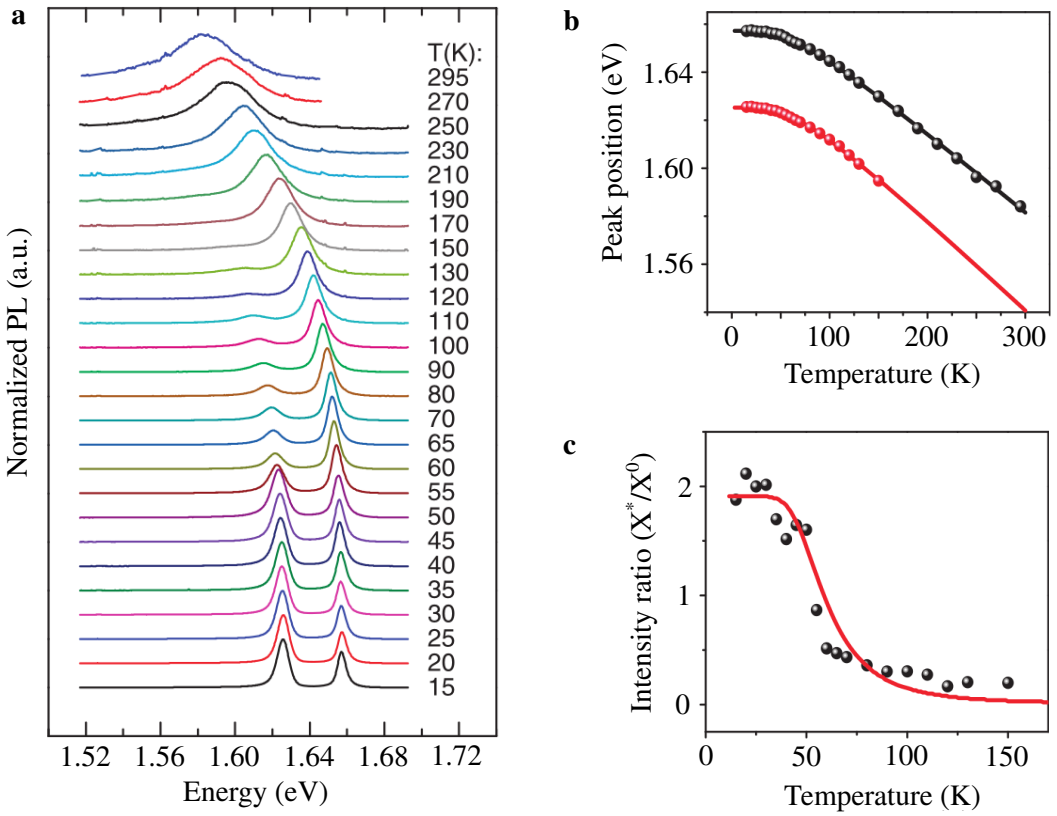

Figure 1.12: Temperature dependent PL of $MoSe_2$. a. Temperature dependent PL spectrum of monolayer $MoSe_2$. **b.** Energies of the exciton (black) and trion (red) in $MoSe_2$ as a function of temperature. The continuous lines are fit based on equation (1.28). **c.** Ratio of the trion (X^*) and exciton (X^0) PL intensity as a function of temperature. All panels are adapted from [56].

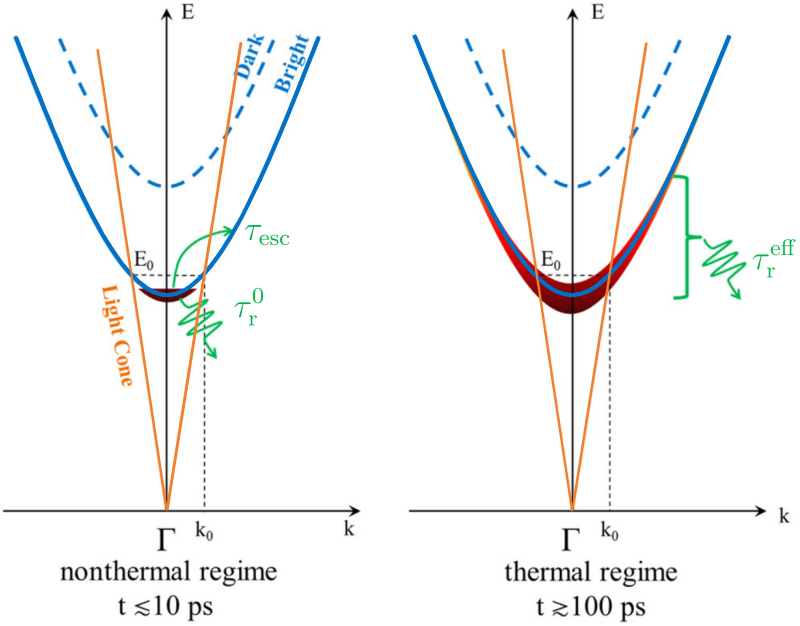

Figure 1.13: Thermal and nonthermal exciton recombination. Sketch of the nonthermal (left) and thermal (right) regimes exciton recombination processes. Adapted from [60].

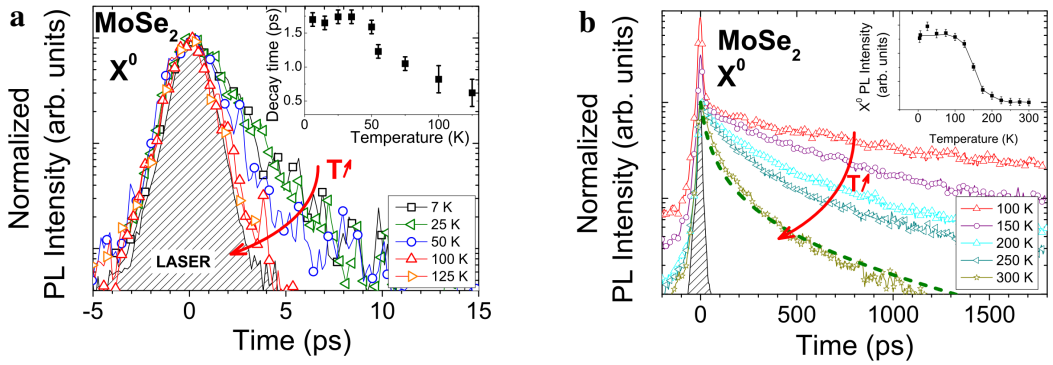

Figure 1.14: Temperature dependent exciton decay time. a. Temperature dependent time resolved PL of monolayer $MoSe_2$ showing the fast decay of the neutral exciton light emission. The inset shows the evolution of the decay time with temperature. **b.** Temperature dependent time resolved PL of monolayer $MoSe_2$ showing the slow decay of the neutral exciton light emission in the thermal regime. The inset shows the evolution of the time integrated PL intensity with temperature. Extracted from [60].

the exciton lifetime is independent of temperature and given by the intrinsic radiative lifetime τ_r^0. Figure 1.14a shows the decay of the PL emission of $MoSe_2$ that remains constant for $T < 40$ K with $\tau_r^0 \approx 1.8$ ps [60].

When the temperature increases, electron-phonon scattering events are more likely to occur and the escape rate increases leading to a diminution of the measured decay time as τ_{esc} becomes smaller than τ_r^0 and shortcuts the radiative recombination by transfering excitons out of the light cone. After a few tens of ps, the excitons extracted from the light cone by the fast electron-phonon scattering form a thermalized exciton population that starts to recombine on a longer timescale in the ns range (see figure 1.14b). The decay rate of the exciton light emission is then obtained by a thermal average of the exciton decay rate. For an exciton homogenous linewidth negligible with respect to $k_B T$, and considering that only excitons with $|\boldsymbol{K}_X| < k_0 = 2\pi/\lambda$ can recombine radiatively, the effective exciton decay time is [60]

$$\tau_r^{eff} = \frac{3}{2}\frac{k_B T}{E_0}\tau_r^0 \tag{1.30}$$

where $E_0 = (\hbar k_0)^2/2M$ (see also figure 1.13b).

As visible in figure 1.14b, for $T > 100$ K the decay time of the PL emission in $MoSe_2$ decreases with temperature while equation (1.30) tells us that it should increase linearly with temperature. This observation is correlated to a decrease of the PL intensity in continuous wave PL experiments and is explained by an increase of non-radiative recombination rates that become dominant at higher temperature [60].

Strain

Uniform strain

By applying mechanical strain, one can modify the crystal structure and alter the band structure of TMDs. The changes on the band structure directly affect the exciton states that see their energies decrease progressively with tensile strain in all TMDs, as visible in figure 1.15a that shows the evolution of the room temperature PL spectrum of monolayer MoS_2 submitted to increasing uniaxial strain from 0% to 1.5% [62]. The changes in the band structure are sketched figure 1.15b. When strain increases, both direct (KK) and indirect (ΓK) gaps decrease because of an increase of the valence band energies (see black and dark red lines in figure 1.15b), explaining the reduced excitonic energies. However, the decrease of the indirect (ΓK) gap is faster than the direct (KK) one and can lead to a direct to indirect gap transition for high strain values (see red line in figure 1.15b) [62, 63]. The differences in strain sensitivity of the different interband transitions can also be used to identify different excitonic states or bring their energies to resonance [64]. Note that biaxial strain affects the band structure the same way, the only difference being that uniaxial strain breaks the crystal symmetry and can split the exciton peak in two features that can be probed independently with linearly polarized light [65]. Interestingly since an increase in temperature leads to thermal expansion, i.e. three-directional tensile strain, the overall effect of temperature is similar and can also lead to a direct to indirect gap transition [66].

Despite the universal change of the exciton energy with strain that decreases for all TMDs, the linewidth of the excitonic state shows a different behavior with respect to strain depending on the considered material. A complete understanding of the complex interplay between excitons and phonons is needed to understand the material related differences and leads for tensile strain to a clear increase of the exciton width in MoS_2 and an overall decrease of the

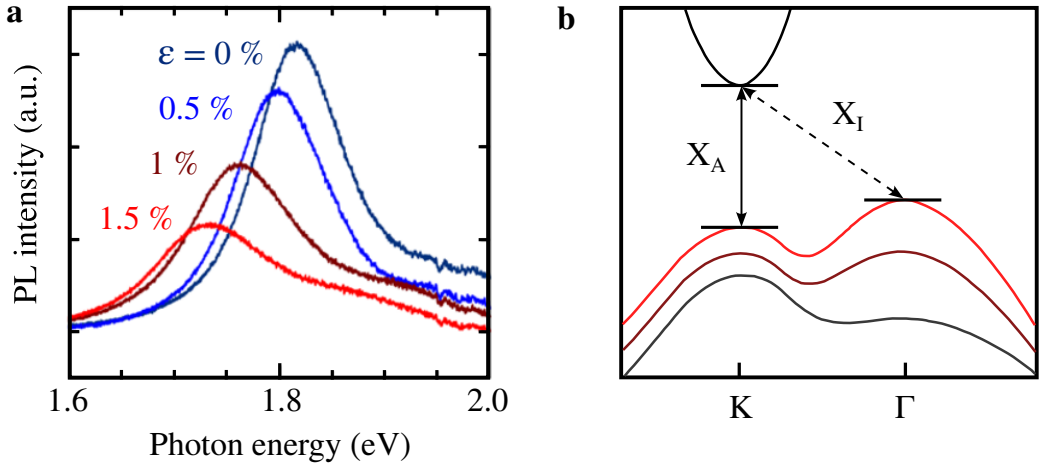

Figure 1.15: The effect of strain on MoS_2 a. Room temperature PL spectrum of monolayer MoS_2 for different values of uniaxial tensile strain. **b.** Sketch of the effect of tensile strain on the band structure of MoS_2. The depicted valance bands corresponds to uniaxial strain values around 0% (black) $\sim$ 5% (dark red) and $\sim$ 8% (red). X_A stands for the A exciton and X_I for the indirect exciton. Both panels are adapted from [62].

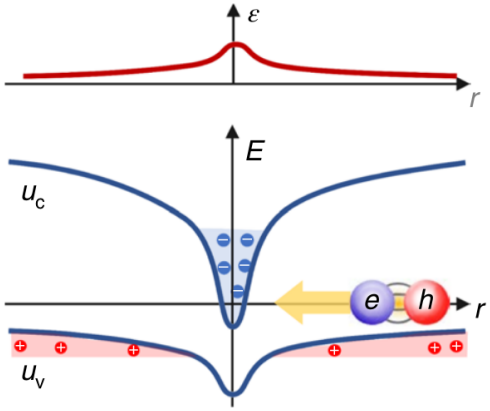

Figure 1.16: Charge funneling in a non-uniform strain profile. The non-uniform strain profile creates a local bending of the conduction and valence bands. Electrons are then funneled towards the point of maximum strain while holes are reverse funneled out of it. At the same time, the point of maximum strain also acts as an exciton trap. Adapted from [73].

exciton width in WS_2, WSe_2 and $MoSe_2$ [67, 68, 69, 62].

Non-uniform strain

Until now we did not take into account the fact that excitons in TMDs are free to move in two dimensions and can diffuse in the material before their recombination [70, 71]. While exciton diffusion can usually be neglected for the continuous wave PL experiments of this work, it is primordial when the time resolution [70] or the spatial resolution [72] is brought to a higher level.

Furthermore, strain fields can be used to direct the flow of excitons as it was done previously in AlGaAs/GaAs quantum wells [74]. Thus, a non-uniform distribution of strain will create a gradient of strain-induced bending of the electronic bands and act as a *funnel* that attracts excitons towards the point of maximum strain as depicted in figure 1.16 [75, 76]. Thanks to this effect, strain can be engineered to locally confine excitons and create quantum emitters in a deterministic way [77]. Recently, Harats *et al.* highlighted by a precise control of the non-uniform strain profile applied by an AFM tip on a suspended WS_2 monolayer that exciton funneling is accompanied by a strong redistribution of free carriers that acts as a local strain-induced doping mechanism as electrons are funneled to the point of maximum strain and holes are reverse funneled out of it. The combination of the exciton funneling and free carrier recombination leads to an extremely efficient exciton to trion conversion without electronic gating [73]. In chapter 2 we shall see that a similar effect might be at play when a suspended TMD layer is locally heated by a diffraction limited laser spot, creating a non-uniform profile of thermal dilatation in the monolayer TMD [78].

1.2.4 Vibrational properties

Phonon dispersion

With 3 atoms per unit cell (one transition metal and two chalcogens), the phonon dispersion of monolayer TMDs is composed of 9 phonon branches. Figure 1.17a shows the phonon dispersion of monolayer MoS_2 as typical example [51]. Overall the vibrational properties of TMDs are comparable to the ones of graphene but with lower phonon frequencies as a consequence of the higher mass of the atoms that compose the TMD structure.

The atomic displacement related to the four optical phonons at Γ are represented figure 1.17b as view from the side of the monolayer, with transition metal atoms in red and chalcogen atoms in blue. Among them, three are Raman active (E″, E′ and A_1') and two are infrared active (E′ and A_2''), the E′-mode being both Raman and infrared active [79]. However, in the backscattering geometry the polarization selection rule cancels the E″ contribution[4]. Thus the only one-phonon Raman features visible in the Raman spectrum of monolayer TMDs originate from the E′ and A_1' modes.

[4] In equation (D.15), $|\boldsymbol{e}_i.\bar{\boldsymbol{R}}(E').e_s| = 0$.

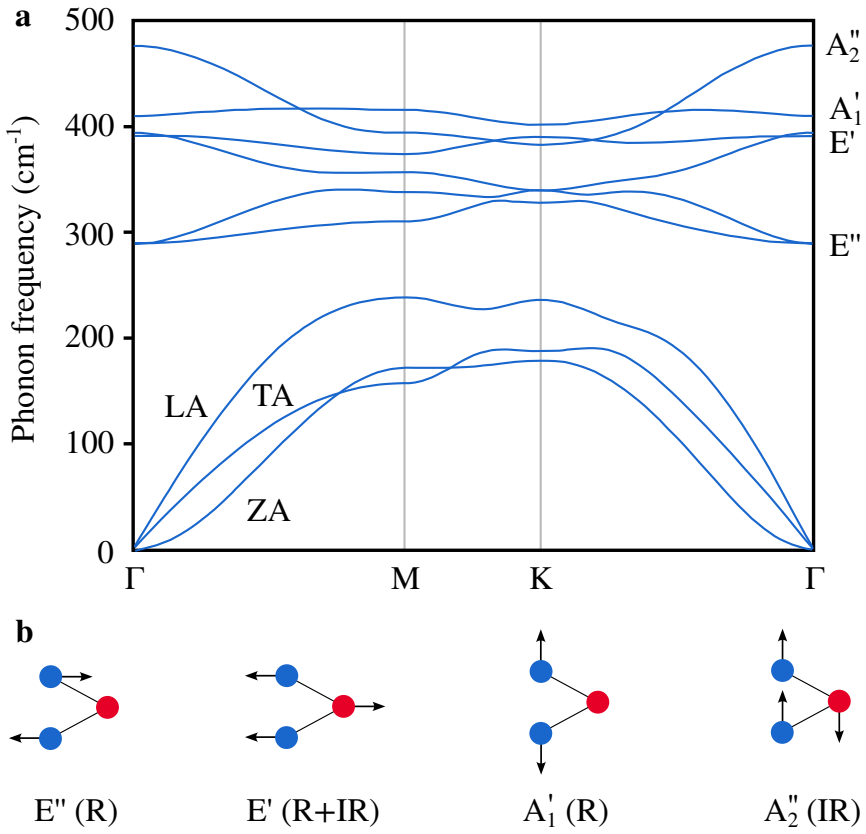

Figure 1.17: Phonons in TMDs. a. Phonon dispersion of monolayer MoS_2. Adapted from [51]. **b.** Spatial representation of the optical phonon modes at Γ for a monolayer seen from the side. The transition metal atoms are represented in red and the chalcogen atoms in blue. The activity of each mode is indicated as R for Raman active or IR for infrared active.

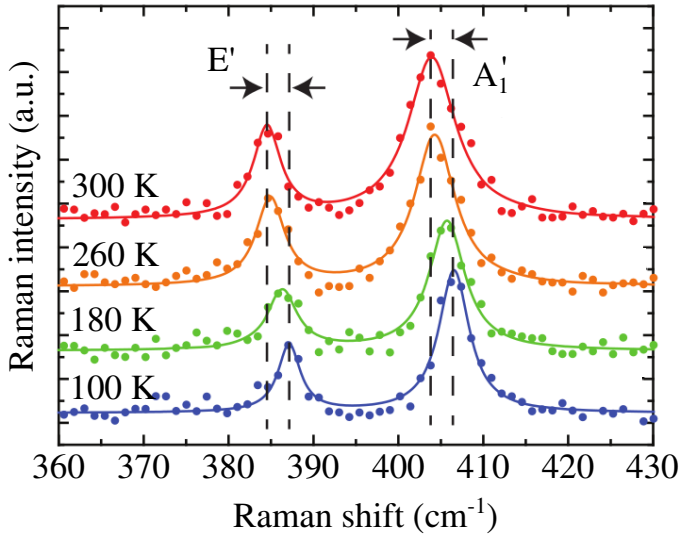

Figure 1.18: Temperature dependent Raman spectrum of suspended monolayer MoS_2. Adapted from [78].

Sensing

The E′ and A_1' modes Raman features in monolayer TMDs can be used to probe in-plane strain and doping in the sample or determine the lattice temperature of the material [79], in a similar way than the G and 2D modes in graphene (see section 1.1.3). Interestingly, the two modes do not behave similarly with respect to strain because of the perpendicular direction of their associated atomic motion. The A_1' vibration being out-of-plane, it is almost insensitive to in-plane strain (at least in the low strained case) while the E′-mode frequency redshifts linearly with tensile strain [80]. When uniaxial strain is applied, the break of the lattice symmetry leads to a splitting of the E′-mode feature in two subfeatures corresponding to the two perpendicular directions of vibration [80].

Interestingly, while the A_1'-mode is marginally sensitive to in-plane strain, the doping level of the TMD layer has a strong effect on its frequency and FWHM. On the other hand, the doping dependence of the E′-mode feature is almost negligible [81]. These two modes can thus be used as complementary probes of doping or strain.

Finally, since the frequency of Raman modes in TMDs is relatively low (typically a few hundreds of cm^{-1}), both their Stokes and Anti-Stokes features can be experimentally measured without troubles, allowing to use their intensity ratio to determine the lattice temperature (see section D.2 and equation (D.19) for more details). Furthermore, as an increase of temperature leads to thermal dilatation that affects both in-plane and out-of-plane vibrations, both the E′ and A_1' Raman modes shift as a function of temperature, giving an additional way to measure the lattice temperature (see figure 1.18) [78, 82]. This additional temperature probe will be of critical importance to determine how the laser excitation affects the lattice temperature of the suspended MoS_2 and WS_2 monolayers investigated in chapter 2.

1.3 van der Waals heterostructures

In the previous sections, we detailed some of the properties of chosen 2D-materials that owe their uncommon physics to their two-dimensional nature. Despite the fact that graphene and TMDs present astonishing properties compared to more common solid state systems, the true potential of 2D-materials is unleashed by the possibility to assemble them by a simple stack in order to tune or combine their properties. Indeed, 2D-materials such as graphene and TMDs are known as van der Waals materials, named after the type of forces that is at play to bound the monolayers together in their bulk counterparts. These same van der Waals forces that bound together the graphene planes in a bulk piece of graphite allow to bound together different types of 2D-materials with interfaces of an unprecedented quality resulting in highly efficient interlayer coupling driven by near-field interactions between the involved materials. By precisely choosing the sequence of materials one can create *van der Waals heterostructures* with predetermined properties that are engineered atomic layer by atomic layer [9] (see figure 1.19a,b).

Recently, the engineering of the properties of van der Waals heterostructures reached a new level by the introduction of experimentally controlled twist angles between two layers in a van der Waals heterostructure. For specific values of this twist angle that depend on the matching between the lattice parameters of the involved 2D-materials, *moiré patterns* can form (see figure 1.19c). It acts as a superlattice that strongly affects the interlayer coupling and can result in peculiar physical properties. For example, bilayer graphene stacked with a precise twist angle of 1.1° between the two graphene sheets can be brought to a superconducting phase [84]. In TMD/TMD bilayers, interlayer excitons can be spatially trapped in the moiré pattern or see their characteristics tuned by it [85, 86].

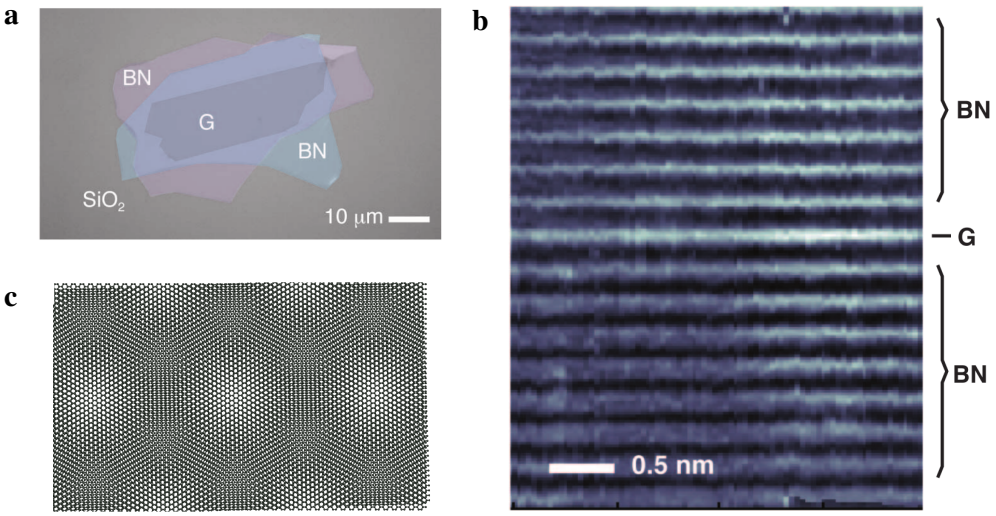

Figure 1.19: van der Waals heterostructures. a. Optical image of a hBN/graphene/hBN heterostructure. Adapted from [83]. **b.** Transmission electron microscope (TEM) image of a cross-section of a heterostructure similar to the one in a, where the atomic planes are visible. Adapted from [83]. **c.** Bilayer graphene with a 2° twist angle that forms a moiré pattern. Adapted from [40].

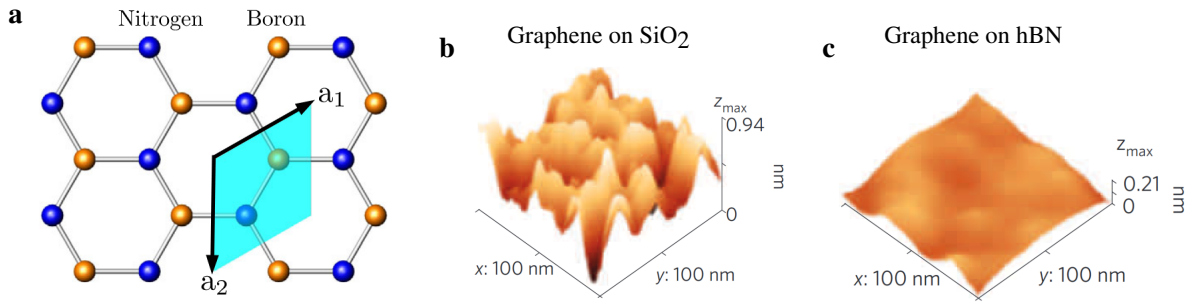

Figure 1.20: Hexagonal Boron Nitride. a. Crystal structure of monolayer hBN with Nitrogen atoms in blue and Boron atoms in orange. Adapted from [87]. **b.** Topography image of a graphene flake deposited on a SiO_2 substrate measured by Scanning Tunneling Microscopy (STM). Adapted from [88]. **c.** Topography of a graphene flake deposited on a flat bulk hBN flake measured by STM. Adapted from [88].

In this section, we will present some of the properties of selected types of van der Waals heterostructures that are important for this work.

1.3.1 Dielectric engineering with hexagonal Boron Nitride (hBN)

Hexagonal Boron Nitride

Hexagonal Boron Nitride (hBN) is the most stable form of Boron Nitride. Its crystal structure is similar to the one of graphene but with the A and B lattice sites occupied by Boron or Nitride atoms and a larger lattice parameter $a = 2.5$ Å (see figure 1.20a) [89]. It is a wide gap semiconductor with an indirect bandgap of 6 eV [90] and will be considered as an insulator in this work. Despite its very good transparency in the visible range, it is important to note that hBN can hold optically active defects in the visible and near infrared range. Such defects can behave as quantum emitters and hold great promises for quantum technologies [91, 92]. Furthermore, hBN is a good candidate as deep UV light emitter thanks to its strong excitonic emission allowed by efficient phonon assisted processes [90].

Usually, hBN is used for its very high thermal and chemical stability that makes it a good material to consider as a protecting layer. Combined with its excellent flatness and its wide bandgap character, it is often used as a dielectric layer or even as a substrate. Figure 1.20a,b shows the topography of a graphene flake deposited on a SiO_2 substrate or on bulk hBN and highlights the extreme flatness of hBN compared to more generic substrates. The effect of the enhanced flatness and inert nature of hBN plays an important role in the resulting physical properties of van der Waals heterostructures as the obtained interfaces are self-cleaning during the stacking process and shows large free of contaminants areas [46].

Dielectric homogeneity

The clean interfaces provided by the use of hBN as substrate and/or capping layer do not only prevent from the unwanted interactions of the active material of the heterostructure with contaminants that could be trapped in the asperities of a rougher substrate or adsorbed on

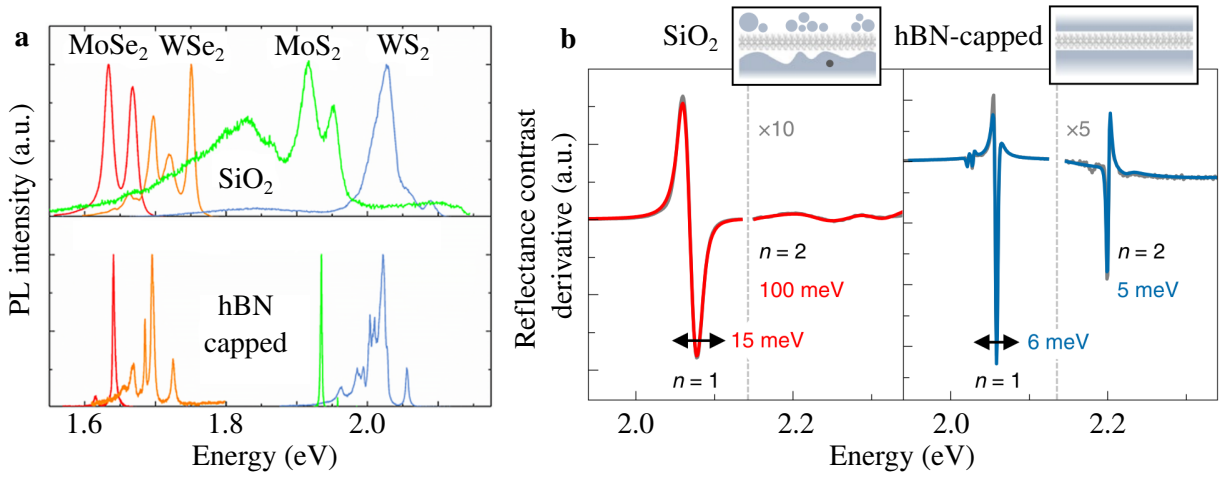

Figure 1.21: Effect of hBN-encapsulation on the optical properties of TMDs. a. PL spectra of $MoSe_2$ (red), WSe_2 (orange), MoS_2 (green) and WS_2 (blue) in the SiO_2-supported case (top) and hBN-encapsulated case (bottom). Adapted from [61]. **b.** Derivative of the reflectance constrast spectrum of SiO_2-supported WS_2 (left) and hBN-capped WS_2 (right). Adapted from [94].

an unprotected active layer, but gives an excellent way to control the dielectric environment and ensure its homogeneity. This is perfectly demonstrated by considering how the use of hBN to encapsulate a monolayer TMD affects the excitonic properties of this last one. Excitons in TMDs are strongly sensitive on their dielectric environment. An increase in dielectric screening is translated as a decrease of the quasiparticle bandgap combined with a decrease of the exciton binding energy. Although these two effects tend to compensate each others, it leads to a measurable (but small) reduction of the exciton energy when the screening increases [93].

The very good homogeneity of the interfaces between TMD monolayers and hBN implies a high homogeneity of the dielectric environment that surrounds the TMD monolayer. Thus, the spatial fluctuations in the exciton energy are greatly reduced and result in a strong sharpening of the optical features visible both in the light emission [61] and absorption spectra [94] in hBN-encapsulated TMD monolayers with respect to the ones simply deposited on bare SiO_2. Figure 1.21a presents a comparison between the SiO_2-supported and hBN-capped PL spectra at low temperature of the four TMDs considered in this manuscript. As the linewidth of the excitonic features reaches the homogeneous limit in the hBN-capped case, the fine structure of some of the excitonic features is revealed [61]. Obviously, this effect also affects the higher Rydberg states that might be hard to observe without a precisely controlled dielectric environment, as visible in figure 1.21b that shows the derivative of the reflectance contrast of monolayer WS_2 in the SiO_2-supported and hBN-capped cases [94].

Tuning the optical properties of TMDs with hBN

In addition to the reduced inhomogeneous broadening provided by hBN encapsulation, the use of hBN as a dielectric layer between an SiO_2 substrate and a TMD monolayer can tune the optical properties of the TMD monolayer. The geometry of such a sample is sketched

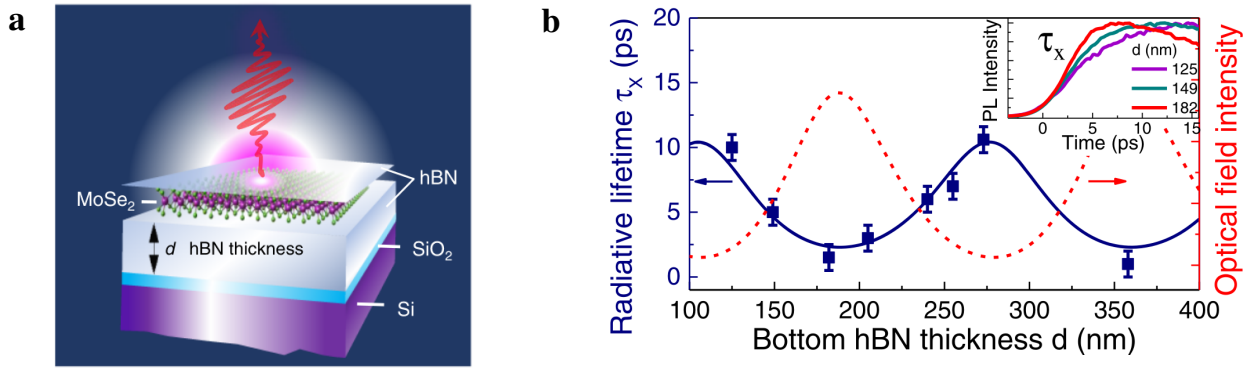

Figure 1.22: Tuning the lifetime of excitons with an hBN layer. a. Sketch of the hBN-capped sample geometry on a Si/SiO_2 substrate. **b.** Changes in the exciton radiative lifetime of monolayer $MoSe_2$ as a function of the bottom hBN thickness (blue). The corresponding optical field intensity is shown in red. The inset shows example traces of TRPL experiments for different hBN thicknesses. Both panels are extracted from [95].

figure 1.22a. Because of the multiple reflections at the various interfaces, an interference pattern is created and the density of state in the optical cavity depends on the thickness of the dielectric layer between the two mirrors. Thus, by carefully selecting the thickness of the bottom hBN layer it is possible to tune the density of available optical states at the TMD layer and tune the radiative lifetime of the exciton via a Purcell-like effect [95]. Figure 1.22b shows the evolution of the exciton radiative lifetime in $MoSe_2$ at low temperature acquired by a similar experimental procedure as the data from figure 1.14 as a function of the bottom hBN thickness together with the corresponding optical field intensity. The radiative lifetime is maximum when the optical field intensity is minimal as less states are available for the radiative recombination of the exciton, and vice versa.

1.3.2 Graphene/TMD heterostructures

We mentioned previously that the properties of van der Waals heterostructures were defined by the near field mechanisms that occur between two layers. Heterostructures made of graphene in close contact with a TMD are a perfect example to illustrate it. The potential of graphene/TMD heterostructures for optoelectronics was demonstrated early on as the strong coupling between these two materials [96] led to the realisation of highly sensitive photodetectors with tunable ps-range photoresponse [97] where graphene is used as transparent electrode and the TMD as photosensitive material. Here, we will detail the interfacial coupling in graphene/TMD heterostructures and how it affects the optical signatures of graphene and TMDs.

Charge transfer and photodoping

The first process to occur when a graphene and a TMD layer are brought together is static charge transfer. This process occurs without any illumination of the system and consists in a redistribution of the charges in the heterostructure depending on the band alignement of the

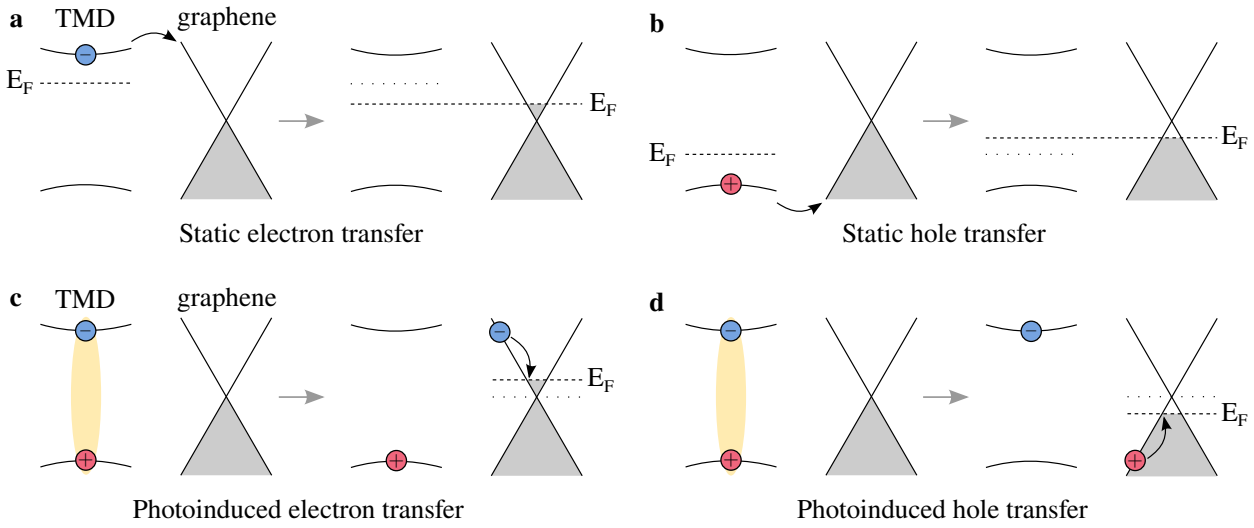

Figure 1.23: Interlayer charge transfer processes. a. Sketch of the static transfer of an electron in a TMD monolayer to graphene. **b.** Sketch of the static transfer of a hole in a TMD monolayer to graphene. **b.** Sketch of the transfer of a photoexcited electron in a TMD monolayer to graphene. **b.** Sketch of the transfer of a photoexcited hole in a TMD monolayer to graphene.

two materials. Since graphene is a semimetal with its neutrality point lying in the electronic bandgap of the TMD, the graphene layer acts as an acceptor and neutralizes the TMD layer by absorbing its excess charge carriers [46], as illustrated figure 1.23a,b. Signatures of this charge redistribution are visible when comparing the PL spectrum of a TMD/graphene heterostructure with the bare TMD one. Figure 1.24a shows the example of graphene/MoS_2 at room temperature, exhibiting a PL spectrum where the trion feature (X^*) is inexistant as the native dopants of the TMD layer are transfered to graphene [98].

A second type of charge transfer occurs upon illumination. As an electron-hole pair is created, one of the charges can tunnel to the graphene layer leading to opposite photodoping of the two layers. Sketches of the photoinduced charge transfer processes are shown figure 1.24c,d. Since this effect is photoinduced, it strongly depends on the excitation intensity and one can study it by monitoring the doping level of the two layers as a function of the laser power. Such analysis was performed previously in our research team by probing the Raman response of the graphene layer of different $MoSe_2$/graphene samples. The measured behavior is strongly dependent on the environment of the heterostructure. Figure 1.24b shows the $\Gamma_G - \omega_G$ correlation for the case of an SiO_2-supported graphene/$MoSe_2$ sample in air. For the coupled graphene/$MoSe_2$ case (red squares), the evolution of the G-mode feature parameter clearly follows the $\Gamma_G - \omega_G$ correlation expected for doping as the laser power is increased [99].

For all the probed SiO_2-supported TMD/Gr heterostructures, the measured doping of the graphene layer progressively increases to reach a saturation level around $n_{Gr} \approx 5 \times 10^{12}$ cm^{-2}, corresponding to a Fermi level $E_F \approx 300$ meV (see figure 1.24c). Once the saturation level is reached, the doping level of graphene remains constant and does not depend on the excitation intensity anymore. This situation remains stable on the minute timescale [99]. As visible on figure 1.24c this same saturation level can be reached at strongly reduced laser power when

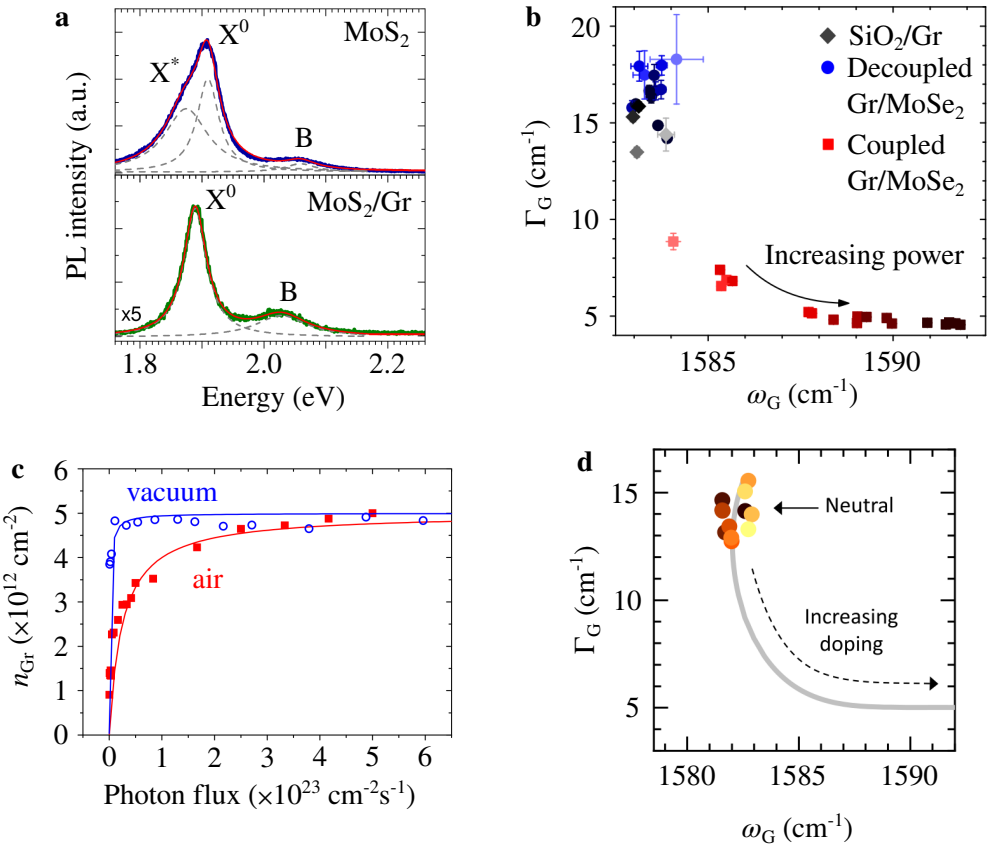

Figure 1.24: Experimental observations of interlayer charge transfer. a. Room temperature PL spectrum of MoS_2 (top) and MoS_2/graphene (bottom). Adapted from [98]. **b.** $\Gamma_G - \omega_G$ correlation with increasing laser power on an SiO_2-supported graphene/$MoSe_2$ sample. Adapted from [99]. **c.** Doping level of the graphene layer in an SiO_2-supported graphene/$MoSe_2$ sample as a function of the excitation intensity. Adapted from [16]. **d.** $\Gamma_G - \omega_G$ correlation with increasing laser power on an hBN-supported graphene/$MoSe_2$ sample. Adapted from [100].

the sample is under vacuum condition, suggesting that the observed photodoping is extrinsic in nature [99].

The complete picture is obtained by performing the same kind of analysis on hBN-supported TMD/graphene heterostructures. Figure 1.24d shows the same $\Gamma_G - \omega_G$ correlation than previously but for a hBN-supported $MoSe_2$/graphene sample. Note that the graphene layer is on top of the heterostructure on both the samples used in figures 1.24b,c and 1.24d. This time, no photodoping of the graphene layer is observed and the graphene layer remains neutral as the laser power is increased [100]. The strikingly different behavior suggests that the observed photodoping in SiO_2-supported samples is due to trapped charges. In high vacuum conditions, the adsorbed molecules that act as a leaking channel for charges are removed leaving the surface trap sites available and increasing the photodoping efficiency. On the contrary, the use of hBN as a flat substrate prevents surface traps and passivates the graphene/$MoSe_2$ heterostructure to minimize extrinsic doping [100].

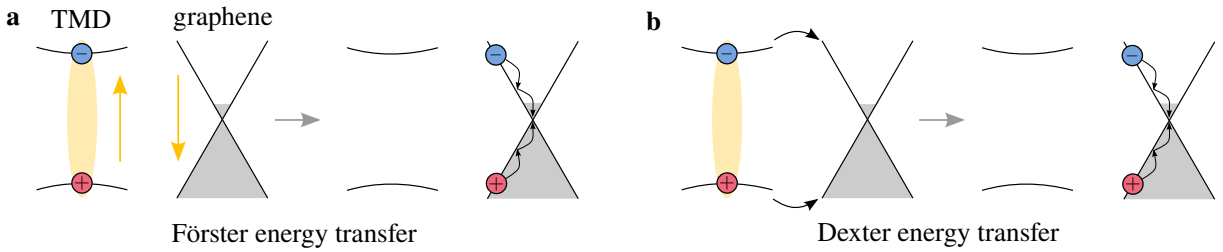

Figure 1.25: Energy transfer in TMD/graphene. a. Sketch of Förster type energy transfer. **b.** Sketch of Dexter type energy transfer.

Near field energy transfer

When light is sent on a TMD/graphene heterostructure, most of the energy that is absorbed lies on the TMD monolayer where an electron-hole pair is created. Energy transfer processes can then occur where the TMD layer plays the role of the donor and the graphene the one of the acceptor. Let us consider that the donor-acceptor energy transfer is carried by two electrons, one in the TMD (donor D) layer and the second one in the graphene (acceptor A) layer. The anti-symmetric initial excited state $|i\rangle$ (D^* excited, A unexcited) and final excited state $|f\rangle$ (D unexcited, A^* excited) are written as [101]

$$|i\rangle = \frac{1}{\sqrt{2}}\left[|D^*(1)A(2)\rangle - |D^*(2)A(1)\rangle\right] \tag{1.31}$$

and

$$|f\rangle = \frac{1}{\sqrt{2}}\left[|D(1)A^*(2)\rangle - |D(2)A^*(1)\rangle\right] \tag{1.32}$$

where 1 and 2 indicate the involved electrons. The interaction matrix element between the initial and final state are given by

$$U = \langle f|\frac{e^2}{4\pi\epsilon_0\epsilon r}|i\rangle \tag{1.33}$$

with r the distance between the two electrons and can be written as the sum of two components $U = U_\mathrm{d} + U_\mathrm{ex}$. The first contribution is know as the *Direct Coulomb interaction* and writes

$$U_\mathrm{d} = \langle D(1)A^*(2)|\frac{e^2}{4\pi\epsilon_0\epsilon r}|D^*(1)A(2)\rangle. \tag{1.34}$$

This term corresponds to a dipole-dipole interaction that leads to *Förster type energy transfer* (FRET) [102, 103], where the energy is transfered from the interaction of the exciton transition dipole in the TMD layer with delocalized transition dipoles in graphene [104, 105] (see figure 1.25a).

The second contribution is the *Exchange Coulomb interaction* given as

$$U_\mathrm{ex} = \langle D(2)A^*(1)|\frac{e^2}{4\pi\epsilon_0\epsilon r}|D^*(1)A(2)\rangle \tag{1.35}$$

that give rise to *Dexter type energy transfer* (DET) [106]. As expressed by equation (1.35) this process involves an exchange of electron that needs to tunnel from a layer to the next

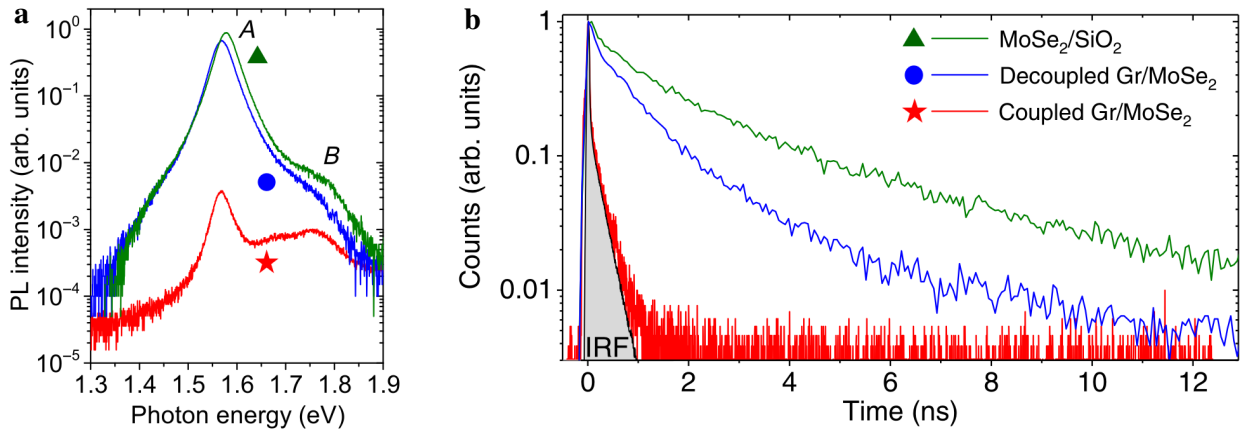

Figure 1.26: PL quenching and reduced decay time in graphene/$MoSe_2$. a. PL spectrum of $MoSe_2$ (green), decoupled graphene/$MoSe_2$ (blue) and coupled graphene/$MoSe_2$ (red) at room temperature. **b.** TRPL traces of $MoSe_2$ (green), decoupled graphene/$MoSe_2$ (blue) and coupled graphene/$MoSe_2$ (red) at room temperature. Both panels are extracted from [99].

one and depends on the overlap of the different orbitals (see figure 1.25b). Thus, DET has a shorter range than FRET [105]. For this reason, FRET is sometimes referred to as "long range" interaction while DET is referred to as "short range" interaction.

Both contributions are competing each other in TMD/graphene heterostructures and lead to a strong quenching of the A exciton PL intensity at room temperature as shown figure 1.26a for a graphene/$MoSe_2$ sample. The underlying explanation of this strong PL quenching is illustrated by the TRPL measurements shown figure 1.26b: as the radiative lifetime of the A exciton at room temperature is way larger than the typical timescale of energy transfer, adding graphene in contact to the TMD opens a fast non-radiative decay channel that bypasses the radiative recombination of the exciton and reduces the lifetime of the exciton down to the ps-range [99]. Note that the B exciton PL intensity is only marginally affected as its lifetime is notably shorter than the one of the A exciton at room temperature [99].

Filtering the PL spectrum of TMDs with graphene

At cryogenic temperature, the radiative lifetime of the neutral exciton X^0 is reduced to the same timescale as the energy transfer time giving close PL intensities for bare TMD and TMD/graphene. On the contrary, other excitonic species such as trion or biexciton shows larger radiative lifetimes (for example, $\tau_{X^*} \approx 30$ ps in SiO_2-supported $MoSe_2$ [98]) and are thus submitted to fast energy transfer that quenches their emission. Simultaneously, static charge transfer leads to a complete neutralization of the TMD flake involved in the heterostructure and avoids the formation of charged excitonic states, leading to a complete absence of both trionic emission and absorption features [98]. The combination of these two effects acts as a strong filtering of the PL spectrum of TMD monolayers when in contact to graphene, where all emission lines except the neutral exciton one are removed as shown in figure 1.27. Additionally, the non-radiative transfer of hot excitons to graphene reduces the maximum achievable density of excitons leading both to a slight quenching of the neutral exciton feature and a further reduction of the emission intensity of longer lived species [98].

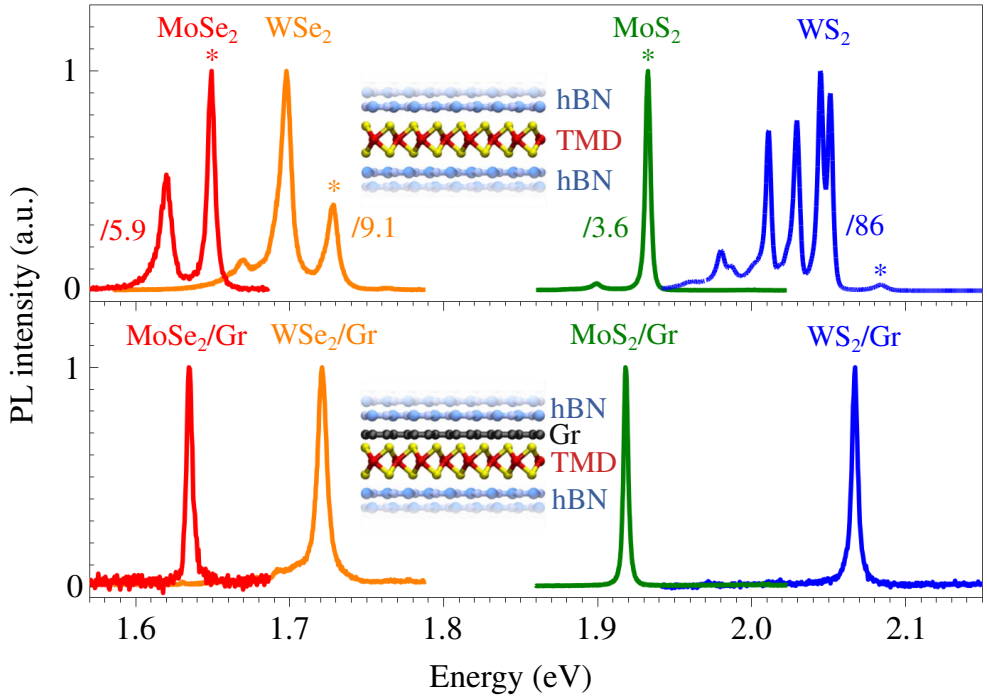

Figure 1.27: Filtering the PL spectrum of TMDs with graphene. Low temperature PL spectra of the four TMDs considered in this work when isolated (top) and when in contact to graphene (bottom). Adapted from [98].

In chapter 4 we benefit from this filtering effect that allows us to investigate the strain dependent behavior of the exciton energy of $MoSe_2$ in a suspended graphene/$MoSe_2$ heterostructure with a simplified spectrum.

1.3.3 The absence of material-substrate contact

Most of the research works on the properties of 2D-materials are done by considering samples with 2D flakes deposited on a substrate. While we saw previously that the use of hBN is a simple and efficient way to minimize extrinsic influences on the material properties and ensure an homogeneous environment, some properties remain strongly altered by the direct contact of the material of interest with a substrate. That is especially true for all types of mechanical properties in the general sense of it. Obviously, when a 2D-material is in contact with a substrate or an other 2D-material, its mechanical properties will be altered by the ones of the other material. This is also valid for the thermal response of the material, as it may not be able to expand or contract freely and give altered estimations of the thermal conductivity because of heat transfers to the substrate [78].

Fortunately the strong in-plane atomic bonds of 2D-materials make them strong enough to be freely suspended over large holes or trenches allowing to directly measure their mechanical properties with nanoindentation methods [107]. Suspending 2D-materials also gives the possibilty to use them as vibrating membranes operating in the 1-100 MHz range, opening a complete new set of possibilities that will be discussed in more details in chapter 4.

Furthermore, suspending a 2D-material to avoid direct contact with the substrate also gives the possibility to investigate its properties in a fully unscreened environment. As such, we already mentioned the specific shape of the 2D Raman mode feature in undoped and unstrained suspended graphene that cannot be reproduced in any different condition (see figure 1.5a). Importantly it has been shown that the increased electron-electron interaction in suspended graphene can lead to a breaking of the linear electronic dispersion close to the Dirac point that manifests itself as a slowly diverging of v_F at zero energy [108, 109]. As we shall see in chapter 3, such changes in the dielectric environment is also strongly affecting the optical phonons in monolayer graphene. Considering TMDs, we will see in chapter 2 that the absence of screening and the fact that suspended monolayers are free to thermally expand can lead to the formation of dense correlated electron-hole phases that cannot arise in supported monolayer TMDs [110].

Conclusion

In this chapter, the main properties of atomically thin graphene and semiconducting TMDs were introduced. Especially, we described the spectroscopic signatures that characterise their optical response and how they are sensitive to both the material's properties and their environment. We discussed the use of hBN to control more precisely the close environment of these materials as well as the proximity effects arising when graphene and TMDs are combined together in a van der Waals heterostructure and their consequences in the properties of the involved materials.

The main points introduced in this chapter can be summarized in the following take home messages:

- Graphene is an atomically thin semimetal with a peculiar linear electronic dispersion.
- Raman spectroscopy provides a versatile probe of its properties, notably related to its doping level and mechanical strain.
- Monolayer TMDs are atomically thin semiconductors with a direct band gap and a strong light emission.
- Their optical response is strongly dominated by excitons stable at room temperature, that are themselves sensitive to the material's characteristics and its environment.
- The use of hBN as dielectric allows to achieve a precise control of the environment of 2D-materials and ensures clean interfaces between the materials forming a van der Waals heterostructure.
- Interfacing a TMD monolayer with graphene opens non-radiative decay channels for excitons in TMDs and results in a filtering of the PL spectrum of the TMD.
- The combination of the 2D nature of graphene and TMDs with their remarkable mechanical properties allows to use them as vibrating membranes operating at high frequencies.

CHAPTER 2

Suspended monolayer TMDs in the strong excitation regime

In this work, our model systems are suspended 2D-materials and heterostructures that are excited optically. We mentioned in section 1.3.3 that the simple absence of an underlying substrate can have a non negligible influence on the properties of 2D-materials. Notably, suspended 2D-materials are free to expand and cannot rely on heat transfer towards a substrate to evacuate the temperature increase created by a laser illumination. In the mean time, the laser excitation creates a population of excitons with a density that directly depends on the intensity of the laser excitation. Understanding how the exciton states behave when the laser intensity is increased is both fundamentally interesting and of a critical importance for who wants to use suspended TMDs as a model system.

In this chapter, we focus our attention to the evolution of the excitonic species in suspended TMDs in the strong excitation regime. Since we are considering suspended monolayers, the effects that are observed consist of contributions from many body phenomenon and photothermal effects and allow us to achieve a better understanding of the interactions between excitons in suspended TMDs. Moreover, the formation of dense electron-hole correlated phases were reported in the literature at the beginning of this PhD, with experimental confirmation of electron-hole liquid formations in $MoTe_2$ photocells [111] and suspended MoS_2 monolayers [110, 112]. As an attempt to decorrelate those two contributions, we use a combined analysis of the photoluminescence and Raman responses versus excitation intensity on suspended MoS_2 and WS_2.

The first section of this chapter is dedicated to an overview of many particle effects in semiconductors, with a focus on the literature related to their observations in TMDs. The second section follows the work from K. Gundogdu's and L. Cao's groups on suspended MoS_2 [110, 112, 113], while the third section is dedicated to our study on suspended WS_2.

2.1 Excitonic density regimes in semiconductors

As stated in chapter 1 the optical response of semiconductors and especially TMDs is strongly dominated by excitonic states. When the density of excitons is low enough to ensure that excitons does not interact with each other (typically, for exciton densities $N \ll a_0^{-2}$ where a_0

is the exciton Bohr radius), the optical response is linear. The neutral and charged excitons are dominating the optical response and their populations dynamics can be described by the means of linear differential equations of the form of equation (D.7). When the exciton density is increased, non-linear effects need to be taken into account and can totally change the optical response. Figure 2.1 illustrates the general scenario for many-particle effects in semiconductors [49] arising when the generation rate of exciton is increased, via an increase of the excitation intensity (i.e. laser power). Experimentally, the arising of non-linear effects can be easily observed as the PL intensity is not anymore a linear function of the laser power.

2.1.1 The intermediate density regime

Exciton-exciton annihilation

When the density of exciton increases, the excitons begin to interact with each other and scattering processes occur. These scattering processes can lead to a broadening of the exciton resonance, the appearance of new luminescence features, an increase of absorption, photobleaching or even optical amplification (via stimulated emission) [49]. In TMDs, the most common exciton related scattering process is exciton-exciton annihilation (EEA). In such scattering processes, one of the exciton is either promoted to a higher excitation level or scaterred as an unbound electron-hole pair, resulting as a final state with only one exciton able to recombine radiatively at the expected energy [114, 115, 116, 117, 118]. An additional term of second order in the exciton density N_X needs to be included in the differential equation describing the exciton dynamics to model its effect on the exciton population. One obtains [114, 115]

$$\frac{\mathrm{d}N_X}{\mathrm{d}t} = G - \Gamma_X N_X - R_A N_X^2 \tag{2.1}$$

with G the exciton generation rate, Γ_X the exciton decay rate and R_A the Auger recombination rate. In continuous wave (CW) experiments, we are probing the time-averaged exciton density $\langle N_X \rangle$. In those conditions, the left hand side of equation (2.1) is null and we can express the time-averaged exciton density

$$\langle N_X \rangle = \frac{\Gamma_X}{2R_A}\left(\sqrt{1+\frac{4R_A}{\Gamma_X^2}G}-1\right). \tag{2.2}$$

Two limits are of interest here. The first one being when Auger recombination is negligible, meaning that $\Gamma_X \gg R_A$. In this situation, we recall the linear regime where $\langle N_X \rangle$ is determined by the ratio between the generation rate G and the decay rate Γ_X. The second one is a saturation regime, occuring for $\Gamma_X \ll R_A$. This situation leads to an average density with sublinear dependence on the generation rate $\langle N_X \rangle \sim G^{1/2}$.

In practice the emitted intensity is proportional to the exciton density while the generation rate can be usually assumed to be proportional to the incoming photon flux or excitation laser power. Thanks to this, power dependent PL spectroscopy is a tool of choice to study EEA and other non-linear optical phenomenons in semiconductors.

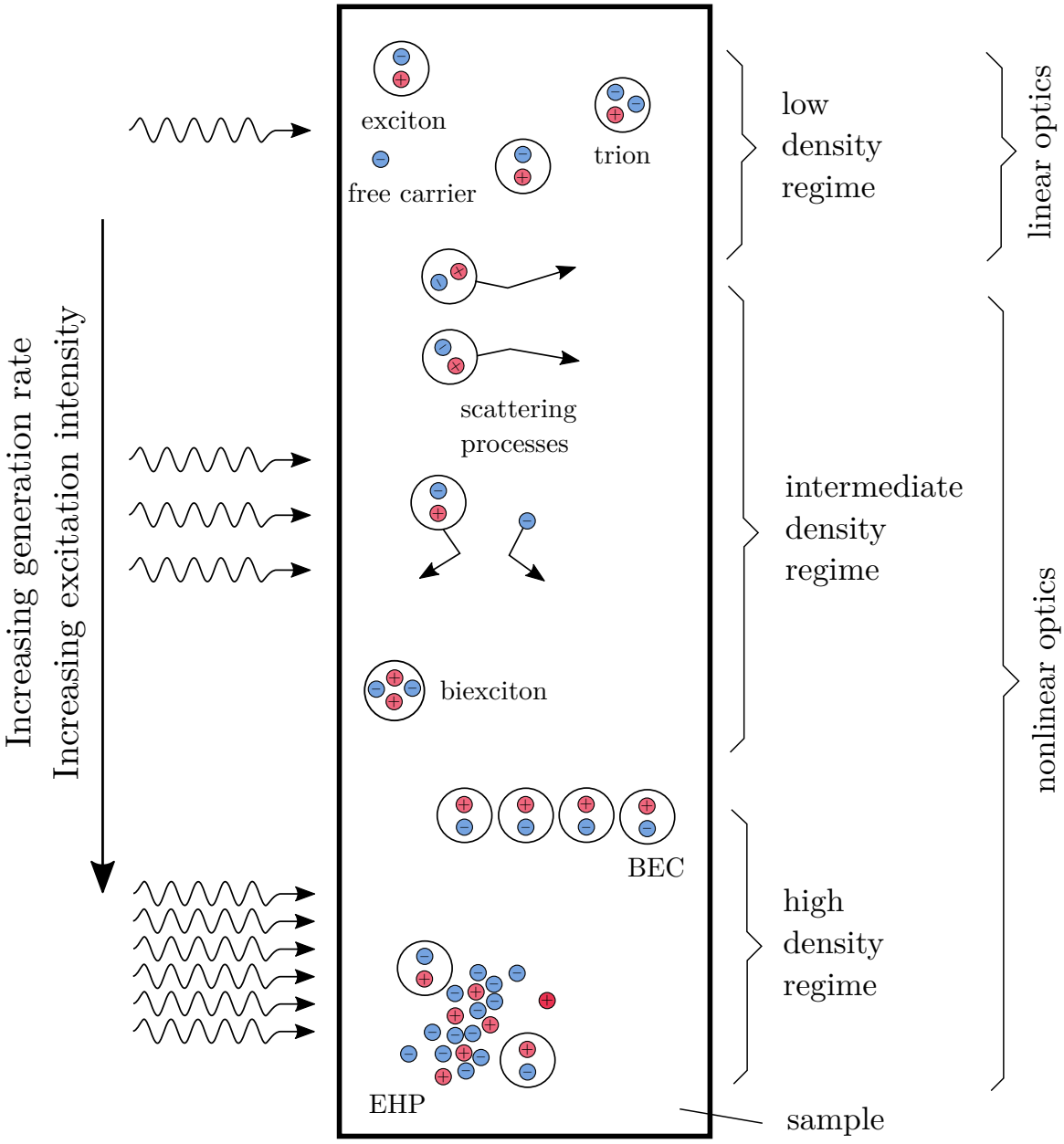

Figure 2.1: Many-particle effects in semiconductors. Adapted from [49].

Biexciton

With a high enough exciton density, more complex excitonic systems such as biexcitons can be created, formed of two excitons or an exciton and a trion. Interestingly, the dark lowest excitonic state in WX_2 (X = S, Se) gives an underlying population of dark excitons that facilitates the formation of biexcitons composed of dark and bright excitons that can then recombine radiatively [119, 120, 121]. The dynamics of biexcitons can be described by [120]

$$\frac{\mathrm{d}N_{\mathrm{XX}}}{\mathrm{d}t} = \beta N_{\mathrm{X}}^2 - \Gamma_{\mathrm{XX}} N_{\mathrm{XX}} \tag{2.3}$$

with β the biexciton formation rate from collisions of excitons and Γ_{XX} the biexciton decay rate. Similarly as before, for CW experiments we can consider a simplified differential equation for the time-averaged populations and determine that the emission intensity of a biexciton state scales as

$$\langle N_{\mathrm{XX}} \rangle = \frac{\beta}{\Gamma_{\mathrm{XX}}} \langle N_{\mathrm{X}} \rangle^2. \tag{2.4}$$

This result illustrates the characteristic supralinear behavior of the biexciton emission intensity with respect to the exciton density. Typically this is characterized by a supralinear correlation of the biexciton emission against the exciton emission intensity $I_{\mathrm{XX}} \sim I_X^{\alpha}$ (or $I_{\mathrm{XX}} \sim P^{\alpha}$ if we neglect potential EEA) with $1.2 < \alpha < 1.9$ [119, 120, 121]. The reduced value of α compared to the theoretically expected one of $\alpha = 2$ is attributed to a lack of full equilibrium between the two states [119, 120].

2.1.2 Dense electron-hole phases

Electron-hole plasma

At even higher density, we reach the so-called high density regime where excitons starts to ionize to form collective phases of electrons and holes. It is no longer possible to consider excitons as individual quasiparticles as the high density of carriers screens the Coulomb interactions and reduces the exciton binding energy to zero. The semiconductor then goes through a Mott transition from an insulating excitonic regime to an electron-hole plasma (EHP) [49, 122]. The density of electron-hole pairs in the EHP is on par with the excited volume and one can obtain a rough estimate of the critical density N_{c}, also-called *Mott density*, by considering it as reached when the average distance between excitons is comparable to the exciton Bohr radius a_0 [49]. For 2D systems this gives $N_{\mathrm{c}} \approx a_0^{-2}$ [122]. Note that this approximation is known to overestimate the Mott density by one or two orders of magnitudes [49, 122].

While the screening of the attractive Coulomb interaction between opposite charges is responsible for the disappearance of the exciton, the reduction of the repulsive Coulomb interaction between charges with the same sign leads to a reduction of the bandgap. This bandgap renormalization gets stronger as a function of the carrier density because of combined exchange and correlation effects [49]. Furthermore, the filling of the conduction and valence bands shifts the quasi-Fermi levels $E_{\mathrm{F}}^{\mathrm{e,h}}$ away and induces an inversion of the carrier

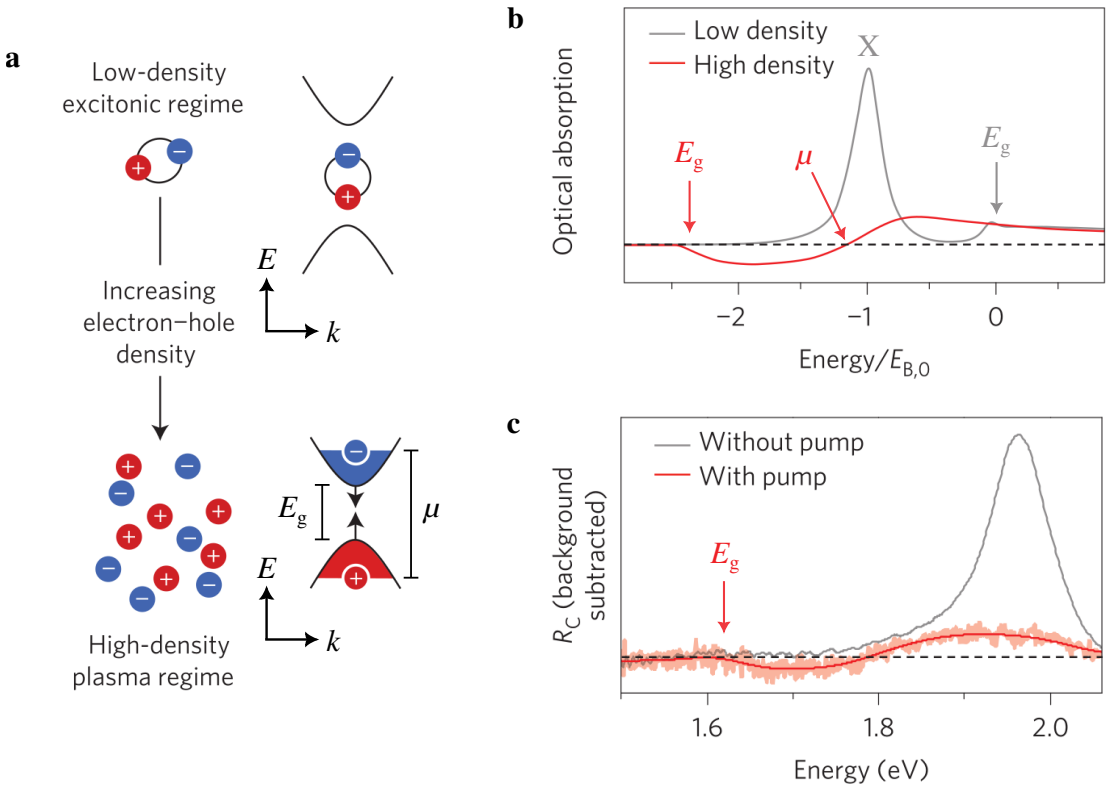

Figure 2.2: The electron-hole plasma. a. Schematic representation of the transition from a low density exciton gas to an EHP and corresponding band diagrams. **b.** Schematic representation of the optical absorption spectrum of a TMD in the low and high density regimes. The energy axis is scaled in units of the exciton binding energy at zero density. The origin is taken at the zero density energy electronic gap, indicated together with the effective chemical potential μ. **c.** Background substracted reflectance constrast spectrum of bilayer WS_2, without pump excitation (grey) and 0.4 ps after pump excitation (red). The sample temperature is T = 70 K. The pump is done with 250 fs pulses centered at 2.4 eV with an applied fluence of 840 µJ.cm^{-2}. Adapted from [122].

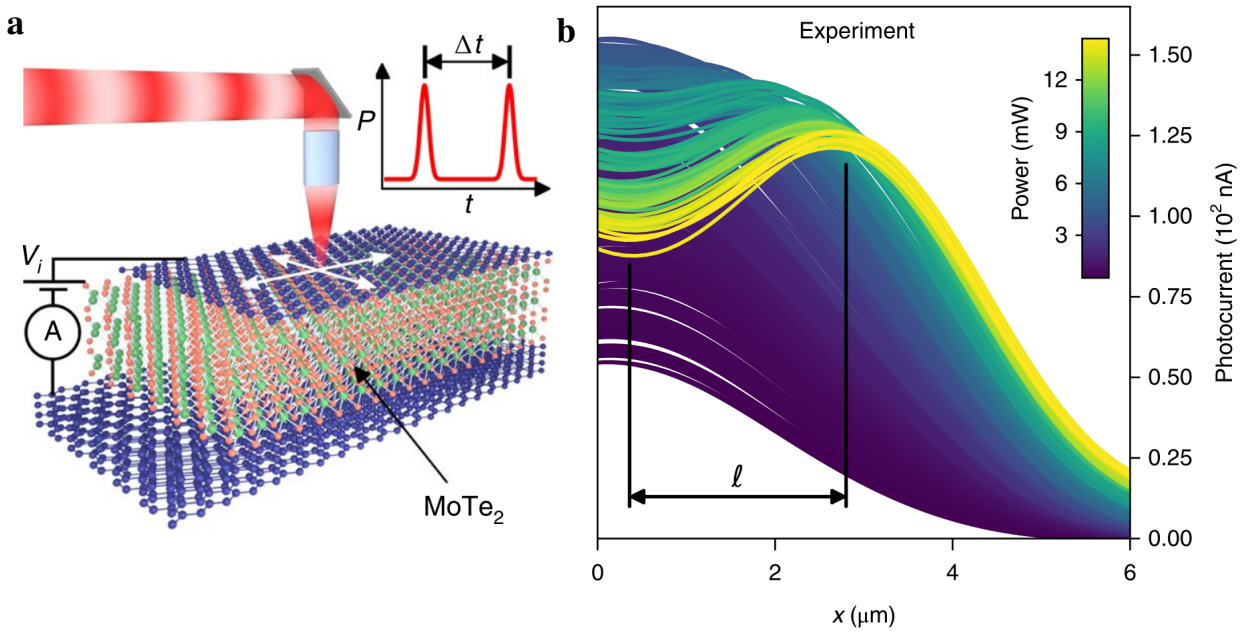

Figure 2.3: Electron-hole liquids in $MoTe_2$ photocells. a. Sketch of the dynamic photoresponse microscopy experiment. A pulsed laser beam is used to locally excite electron-hole pairs in the graphene/$MoTe_2$/graphene photocell, that generates a photocurrent detected thanks to the graphene electrode. Measuring the intensity of the photocurrent as a function of the position of the laser beam allows to reconstruct the spatial profile of the EHL droplet shown in b. **b.** Spatial profile of the photocurrent response of an EHL droplet in a graphene/$MoTe_2$/graphene photocell as a function of laser power. Data is obtained 0.2 ps after the excitation laser pulse. Adapted from [111].

population near the band edges that can be observed as a negative optical absorption, or *optical gain*, between the renormalized energy gap E_g and the effective chemical potential μ (see figure 2.2a,b) [49, 122, 110]. The appearance of a negative optical absorption window is a typical signature of the formation of an EHP and has been observed experimentally on monolayers and bilayers of WS_2 [122] and suspended MoS_2 [110]. Figure 2.2c shows the experimental observation of the optical response of an EHP formed in bilayer WS_2 using ultrafast pump-probe measurements of the reflectance contrast spectrum [122].

Electron-hole liquid

If the lifetime of the excited carriers is long enough, which can be the case for indirect gap semiconductors, the density of the EHP can be increased further and lead to a phase separation and the formation of an electron-hole liquid (EHL) droplet with a micrometer scale radius [123, 124]. The so-called liquid phase shares many properties with a classical liquid, such as the incompressibility or a high mobility of the constituent carriers, bound together by internal interactions [124]. The corresponding first order phase transition can be well described by a generalization of the classical nucleation theory [125].

Figure 2.3 shows an experimental measurement of the EHL spatial profile and size in a graphene/$MoTe_2$/graphene photocell through multi-parameter dynamic photoresponse mi-

croscopy [111]. A pulsed laser beam is used to excite electron-hole pairs in the sample, that then creates a photocurrent detected via the graphene electrodes. The photocurrent response can then be mapped as the laser beam is moved on the sample. One can see that when the laser power is increased, the spatial profile of the photocurrent response gradually increases before reaching a ring-like shape with a progressive reduction of the response at the laser spot location. The observed ring-like profile is a consequence of the incompressibility and high mobility of the EHL phase. As the carrier density cannot be increased further in the EHL droplet, an input of energy can only contribute to an expansion of the liquid phase and force highly mobile carriers towards the edges of the droplet [111]. Similar ring-like spatial profiles were observed in the photoluminescence of an EHL droplet in suspended monolayer MoS_2 [112] and µm scale EHL droplets were observed in both situations, with sample or laser spot size being the typical limiting factor.

The evolution of the room temperature PL spectrum of suspended MoS_2 through the formation of an EHL is detailed in figure 2.4. A progressive redshift up to ~ 200 meV together with a large broadening reaching FWHMs higher than 150 meV is observed when the laser power is increased. Most of these changes occur in the middle density regime and remain constant once the EHL droplet is fully formed [112]. The transition to an EHL is also marked by an explosion of the PL intensity, with a 540% increase in PL intensity for an 18% increase in excitation intensity at the critical density reported in reference [110]. As one could expect when using strong laser excitation on a suspended monolayer TMD, photothermal effects are at the core of the EHL formation process in suspended monolayer MoS_2. Indeed, characterization of the Raman response correlated with DFT calculations [110] and PL experiments with below gap excitation [113] highlighted that the EHL formation is permitted thanks to a photothermally induced direct to indirect gap transition in the monolayer MoS_2 with critical lattice temperatures $T_c \sim 500$ K.

2.2 Dense electron-hole phases in suspended monolayer MoS_2

As a first step to study suspended TMDs in the high excitation regime, we performed similar experiments on suspended monolayer MoS_2 than those reported in reference [110] consisting in power dependent PL and Raman spectroscopy at room temperature with 532 nm CW laser excitation. A few differences are to be noted between the two approaches. In our work presented below the laser spot is diffraction limited with a spot diameter around 1 µm, smaller than the suspended area. PL and Raman spectra are measured successively for each power value on our room temperature setup (see section C.3), giving a direct point to point correlation between observations in the PL and Raman spectra. For comparison, in reference [110] PL experiments are performed using a ~ 35 µm wide laser spot, larger than the suspended area while Raman spectra are obtained using a 1.6 µm spot size on holes with a diameter of 6 µm and does not allow to directly correlate the reported PL and Raman data as the power densities are not comparable. Furthermore, the heating profile is different in the two situations, with a uniformly heated membrane when a wide laser spot is used in contrary to the situation with a diffraction limited spot smaller than the suspended area.

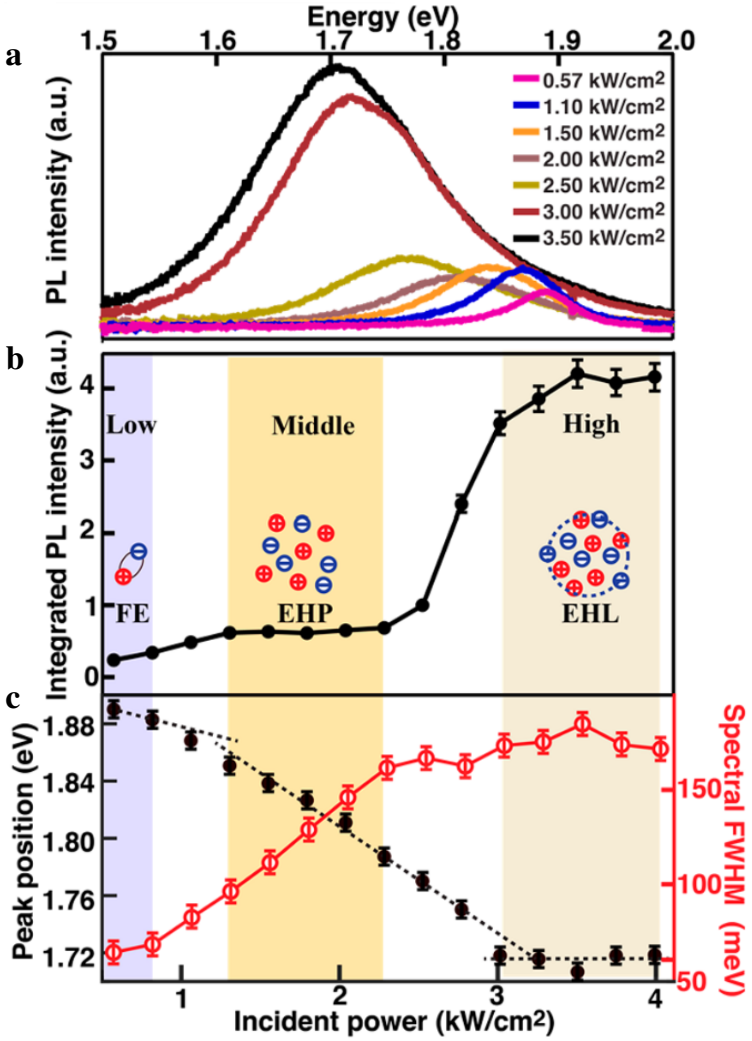

Figure 2.4: Electron-hole liquids in TMDs. a. Power dependent photoluminescence spectrum of suspended MoS_2 at room temperature. **b.** Integrated PL intensity of suspended monolayer MoS_2 versus incident power. The shaded areas define the low (free excitons), middle (EHP) and high (EHL) density regimes. **c.** Evolution of the peak position and spectral FWHM of the PL spectrum in suspended MoS_2 for increasing laser power. Extracted from [112].

Indeed, if the membrane is heated locally, a spatially gaussian heating profile will form that may affect the formation of the EHL droplet [78].

Figure 2.5a presents the power dependent PL spectra measured on a MoS_2 monolayer suspended over a 4 µm hole etched in a quartz substrate to avoid potential alterations of the broad spectra shapes by interference effects. Simple Voigt fits are performed to determine the energy of maximum intensity (E_{max}), integrated PL intensity and FWHM. As shown figure 2.5b,c an explosion of the integrated PL intensity by three orders of magnitude is observed followed by a roughly constant intensity when the laser power is increased further. A clear redshift of more than 100 meV and a broadening of the PL features are occurring together with the strong increase of the PL intensity. For the most redshifted spectra, the FWHM reaches three times the one of the low power reference. Such observations are in agreement with the reported formation of an EHL phase in suspended MoS_2 [110, 112, 113].

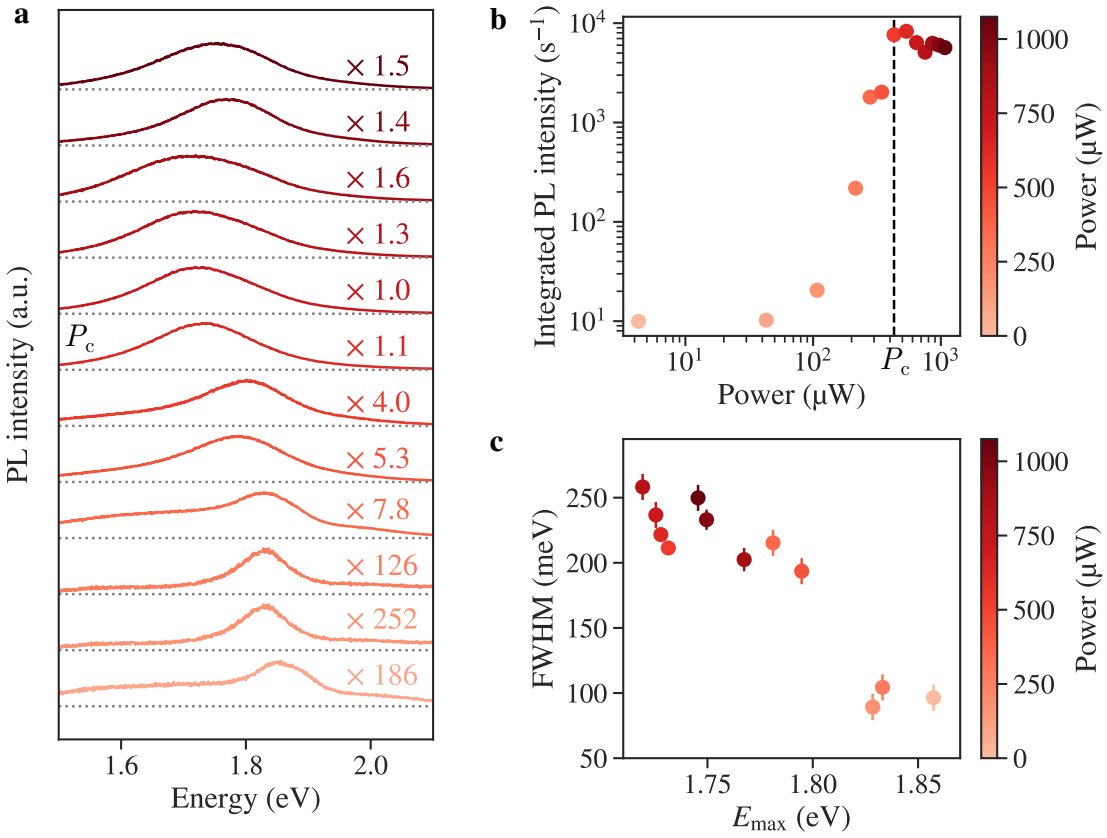

Figure 2.5: Power dependent PL spectroscopy of suspended MoS_2. a. Power dependent photoluminescence spectra of suspended MoS_2 at room temperature. P_c **b.** Integrated PL intensity of suspended monolayer MoS_2 versus incident power. The dashed vertical line refers to the critical power needed to form an EHL phase. **c.** FWHM versus energy of maximum PL intensity for increasing laser power.

We define the critical power $P_c = 430$ µW as the lowest power of the constant integrated PL intensity regime that can be interpreted as the lowest laser power needed to reach a full formation of the EHL phase (see figure 2.5). Similar spectra were obtained using Si/SiO_2 substrates with minimal changes in the overall spectral features suggesting that interference effects from the Si/SiO_2 geometry are not affecting the spectra shape in this wavelength range and might be used for future samples.

The corresponding Raman spectra are shown figure 2.6a and are used to determine the lattice temperature associated with a given input power. Thanks to the clear separation and similar intensities of E′ and A_1' modes in MoS_2 the lattice temperature can be extracted by considering either changes in the relative Stokes and Anti-Stokes intensities or changes in mode frequencies. Figure 2.6b shows the lattice temperature changes with laser power determined from the Anti-Stokes / Stokes intensity ratio of the A_1'-mode using equation (D.19) and taking the lowest power point with visible Anti-Stokes features as reference at $T_0 = 300$ K. This method gives a critical lattice temperature $T_c \approx 700$ K associated to the critical power P_c where the EHL is observed. Estimations of the lattice temperatures from the E′-mode frequency $\omega_{E'}$ and A_1'-mode frequency $\omega_{A_1'}$ are shown figure 2.6c and d. We assumed a linear temperature dependency of the mode frequencies $\omega(T) - \omega(T_0) =$

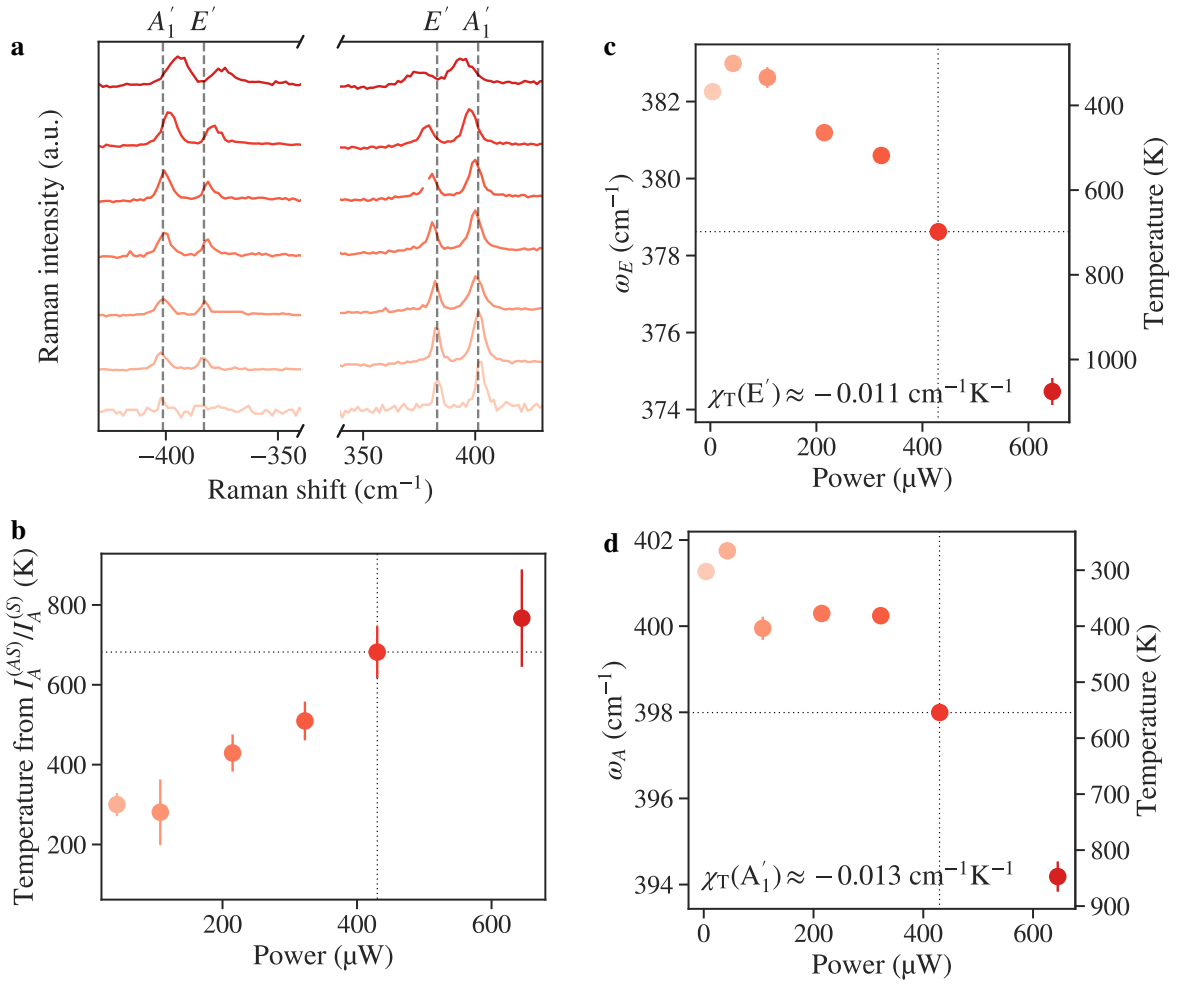

Figure 2.6: Power dependent Raman spectroscopy of suspended monolayer MoS_2. **a.** Power dependent Raman spectra of suspended MoS_2 at room temperature. **b.** Temperature estimated from the Anti-Stokes / Stokes intensity ratio of mode A_1' as a function of laser power. **c.** E′-mode frequency and corresponding temperature estimation with respect to laser power. **d.** A_1'-mode frequency and corresponding temperature estimation with respect to laser power.

$\chi_T(T - T_0)$ with linear temperature coefficients $\chi_T = -0.011$ cm^{-1}K^{-1} for the E′-mode and $\chi_T = -0.013$ cm^{-1}K^{-1} for the A_1'-mode [78], leading to respective critical temperatures $T_c \approx 700$ K from the E′-mode frequency and $T_c \approx 550$ K from the A_1'-mode frequency. Note that the higher sensitivity on in-plane strain of the E′-mode may explain the higher estimated value of T_c.

In addition, we can note that the observed phenomenon is overall reversible as long as the maximum laser power stays close to the critical value P_c. Further increase leads to a photobleaching of the exciton emission and an increase in the defect related emission. The combination of our observations confirms the reported results and interpretations in references [110, 112, 113] that claims the formation of a EHL droplet in suspended MoS_2 allowed thanks to a photothermally induced transition form direct to indirect gap in the electronic structure occuring at a critical temperature $T_c \sim 500 - 700$ K.

2.3 Suspended monolayer WS_2 in the strong excitation regime

Thanks to our observations on suspended MoS_2 we can confidently investigate potential similar formations of dense electron-hole phases in different suspended TMDs. Our candidate is suspended monolayer WS_2. The choice of WS_2 is motivated by different points. First, as described in subsection 2.1.2 observations of an EHP phase in monolayer WS_2 has already been reported in the transient regime using pump-probe optical experiments [122]. As a second point, some theoretical work suggests that WS_2 should be the TMD with lowest Mott density and strongest optical gain [126], an effect that could be enhanced when the WS_2 monolayer is suspended thanks to the reduced screening of the Coulomb interactions. Since WS_2 is a dark TMD [11] with a larger energy difference between the dark and bright exciton than MoS_2 [48] we can also expect dark excitons to form an underlying density of excitons with longer lifetime that could potentially help to reach the formation of an EHP or EHL phase.

2.3.1 Power dependent PL spectrum

The experimental methodology is the same as in the previous section and the results presented here were obtained on a WS_2 monolayer suspended over a 6 µm wide hole in a Si/SiO_2 substrate (see appendix A for more details). Power dependent PL spectra are presented in figure 2.7a and clearly shows an overall redshift and broadening of the spectrum. To understand the spectral evolution, all spectra were fit with a double Voigt model that we assign at low power to the neutral exciton X^0 (in red) and the trion X^* (in blue) based on their energy splitting at low power [127, 73]. The power dependence of the PL intensities of the two fitted peaks is shown figure 2.7b. Two regimes can be clearly identified with an abrupt transition at a critical power $P_c \approx 645$ µW and an emission spectrum right at the transition that is different in shape than any other one in the series, even for higher powers, and cannot be fitted with our double Voigt model. We will come back to this critical point later in the discussion.

For laser powers $P < P_c$, a power law fit of the PL intensity as a function of the laser power $I \sim P^\alpha$ was performed for both fitted peaks. Surprisingly, the evolution of the neutral exciton emission intensity gives $\alpha = -0.1$, meaning that the exciton density is at best constant with increasing power. At the same time, the trion PL intensity has a sublinear evolution with $\alpha = 0.6$. The combination of these evolutions leads to a fast inversion of the trion versus exciton populations with an emission ratio scaling as $I_{X^*}/I_{X^0} \sim P^{0.7}$ that suggests a highly efficient rate of exciton to trion formation, or a strongly altered exciton emission. Indeed, the trion density is usually expected to follow a linear power dependence while the exciton is expected to follow a power law with $0.5 < \alpha < 1$. This apparently surprising change in the peak intensities is accompanied by a progressive redshift and broadening of both PL features, as seen figure 2.7c.

This regime can be compared to the evolution of the PL in the SiO_2-supported case at similar laser powers presented figure 2.8. While redshift and broadening of the exciton and

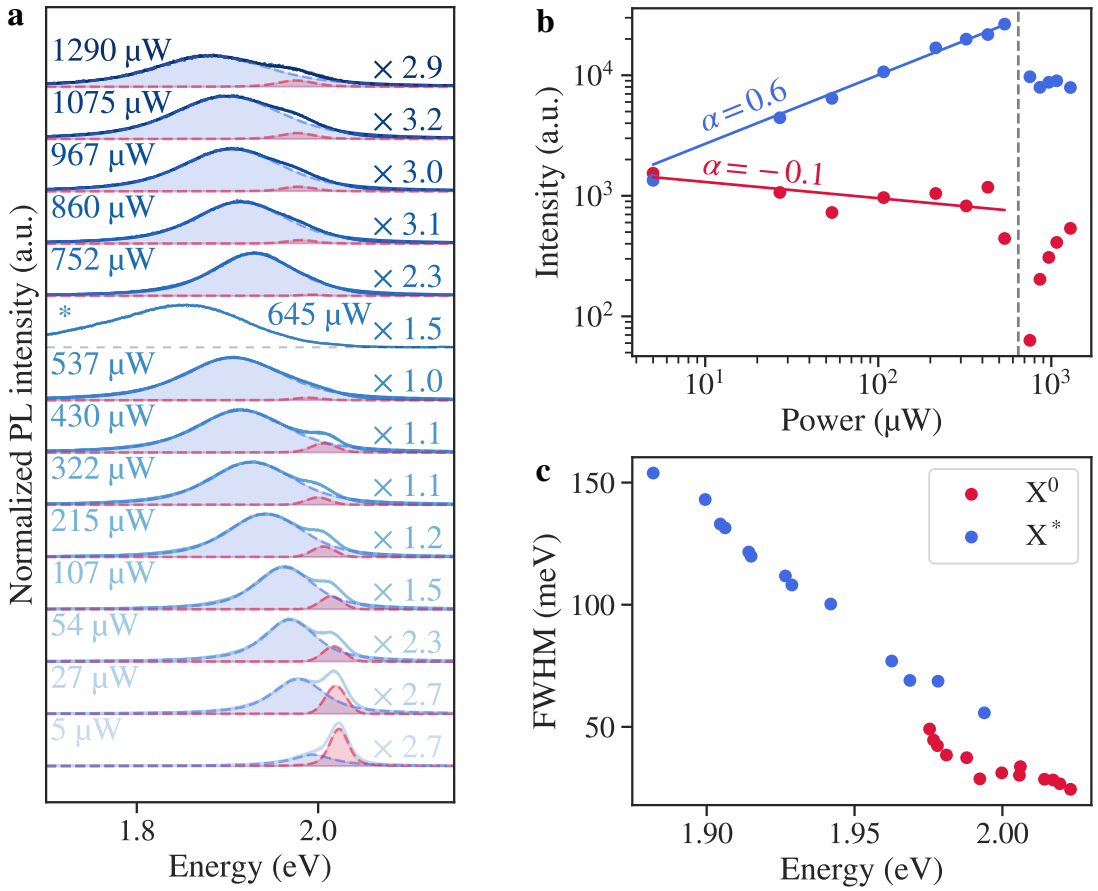

Figure 2.7: Power dependent PL of suspended monolayer WS_2. a. Power dependent PL spectra of suspended WS_2 at room temperature together with their fits. The asterisk marks the critical point. **b.** PL intensity of the neutral exciton X^0 (in red) and trion X^* (in blue) as a function of the laser power. **c.** FWHM versus energy of neutral exciton X^0 (in red) and trion X^* (in blue) peaks.

trion peaks are also seen, their amplitude are greatly reduced with respect to the suspended case (see figure 2.8c). More importantly, no anomalous evolution of the PL intensities is observed, with respective power law evolution with exponents $\alpha = 0.6$ and $\alpha = 0.8$ for exciton and trion (see figure 2.8b), suggesting an efficient exciton-exciton annihilation that is to be expected at such high excitation intensities.

2.3.2 Power dependent Raman spectrum

The power dependent Raman spectra associated with the PL ones are shown figure 2.9. As previously, a point to point correlation is ensured between PL and Raman spectra and autorizes a deeper analysis of the observed effects. Unfortunately the E′-mode of monolayer WS_2 is completely merged with the 2LA(M) phonon lines and cannot be used. We then focus ourselves on the A_1'-mode and especially its Stokes line, as the Anti-Stokes one is completely invisible at low laser power (see figure 2.9a). The first striking observation is a strong enhancement of the intensity in the A_1'-mode peaks when approching the critical

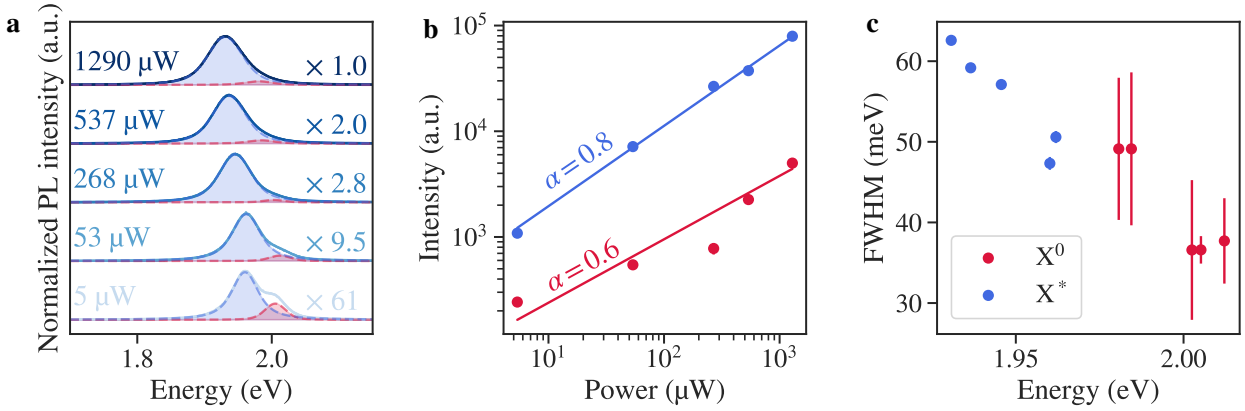

Figure 2.8: Power dependent PL of SiO_2-supported monolayer WS_2. a. Power dependent PL spectra of SiO_2-supported WS_2 at room temperature together with their fits. **b.** PL intensity of the neutral exciton X^0 (in red) and trion X^* (in blue) as a function of the laser power. **c.** FWHM versus energy of neutral exciton X^0 (in red) and trion X^* (in blue) peaks.

power P_c, as visible in figure 2.9b showing the power dependence of the Stokes A_1' intensity normalized by the intensity of the Si Raman peak (around 520 cm^{-1}, not shown here). Again, the enhancement of the A_1'-mode intensity shows a spike at the critical point and saturates at higher laser power. No effect is seen on the A_1'-mode intensity for the SiO_2-supported case.

Despite this unexpected increase in the A_1'-mode intensity, the frequency of the A_1'-mode gives information on the lattice temperature. Using the same linear approximation of the temperature dependent phonon frequencies as in the previous section, we can determine for each laser power the lattice temperature as shown figure 2.9c. The used linear temperature coefficient is $\chi_T = -0.0122$ $cm^{-1}K^{-1}$ [82]. Once again, the critical point shows an anomalously high value, with a temperature $T_c \approx 750$ K that stands out of the linear behavior observed for the other powers, including powers $P > P_c$. Note that the variation of the Raman spectrum as a function of power are fully reversible, the only exception being the critical point itself. As visible in figure 2.9c (empty black circles), a heating of the SiO_2-supported monolayer is observed but with a reduced magnitude with respect to the suspended monolayer WS_2 thanks to thermal conduction towards the SiO_2 substrate, up to a maximum temperature $T \approx 550$ K. Importantly, for suspended WS_2 a clear increase in the A_1'-mode intensity is already seen at such temperature while no effect is visible on supported WS_2. This difference is an additional indication that the observed effect is not purely due to an increased lattice temperature but involves the electronic or excitonic states.

2.3.3 Discussion

Intermediate density regime: $P < P_c$

Using the lattice temperature determined from the shift of the A_1'-mode frequency, we can evaluate the variation of the excitonic lines as a function of the lattice temperature. This is presented figure 2.10a that shows the variation of energy as a function of temperature

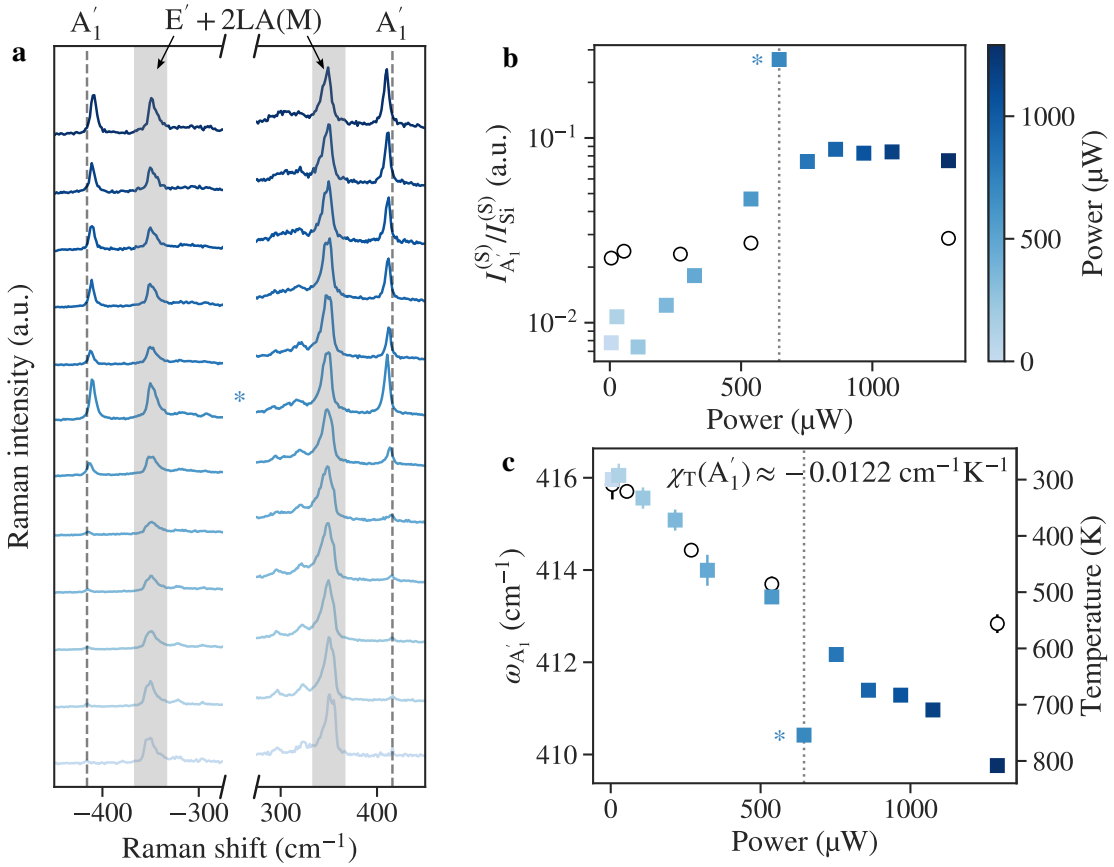

Figure 2.9: Power dependent Raman spectroscopy of monolayer WS_2. a. Power dependent Raman spectrum of suspended WS_2 at room temperature. **b.** Intensity of the Stokes A_1' peak normalized by the Si Raman peak intensity as a function of laser power. Blue squares are for suspended WS_2 and black empty circles for SiO_2-supported WS_2. The vertical dotted line refers to the critical power P_c. **c.** Evolution of the A_1'-mode frequency as a function of laser power. the right axis gives the associated lattice temperature. Blue squares are for suspended WS_2 and black empty circles for SiO_2-supported WS_2. Asterisks indicates the critical point.

for the neutral exciton X^0 (red markers) and trion X^* (blue markers) for the suspended (filled circles) and SiO_2-supported monolayer (empty squares). The filled grey area marks the points with $P > P_c$ for which the exciton-trion model may not be valid anymore. For $P < P_c$ the energy shift of the neutral exciton X^0 in both suspended and SiO_2-supported WS_2 as well as the one of the trion X^* in SiO_2-supported WS_2 follows similar linear variations with the lattice temperature, with temperature coefficients $\kappa = -145$ μeV.K^{-1}, $\kappa = -152$ μeV.K^{-1} and $\kappa = -131$ μeV.K^{-1} respectively. The dashed line in figure 2.10a gives a guide to the eye using $\kappa = -145$ μeV.K^{-1} obtained for the neutral exciton X^0 in the suspended case. The deviation of the observed shift of the trion energy is a second strong argument towards an efficient rate of exciton to trion formation and a strongly increasing trion density as the trion binding energy is known to increase with the density of free carriers [57, 73]. We believe that the scenario taking place here for $P < P_c$ is analogous to the one reported in [73] where an efficient conversion of excitons to trions is induced by non-uniform strain applied by an AFM tip on a suspended monolayer of WS_2 at room temperature. In our case, the laser spot induces a gaussian heating profile at the center of the suspended area

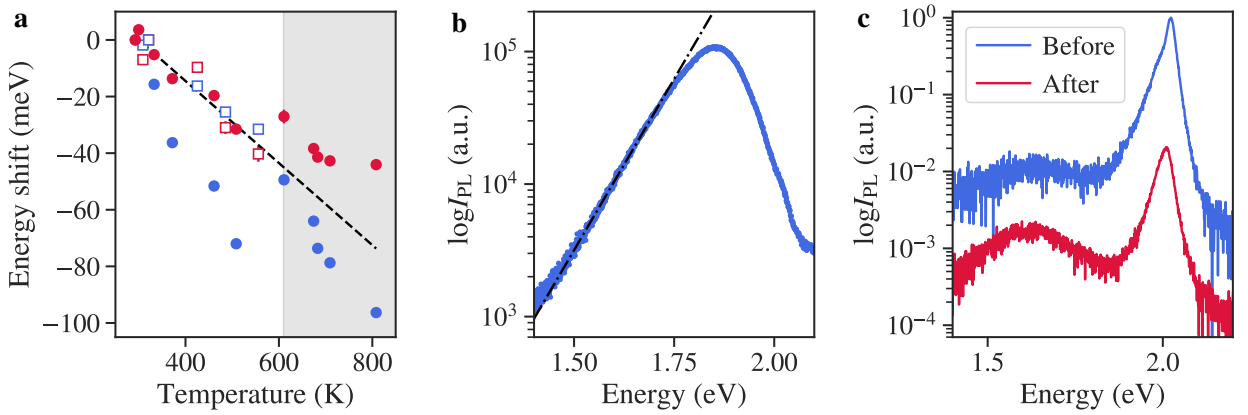

Figure 2.10: a. Energy shift of the exciton (red markers) and trion (blue markers) as a function of the lattice temperature obtained from Raman spectroscopy. Filled circles corresponds to the suspended WS_2 monolayer and empty squares to the SiO_2-supported WS_2 monolayer. The grey shaded area represent points with $P > P_c$. The dashed line results from a fit of the energy shift of the neutral exciton in the suspended case for $P < P_c$. **b.** PL spectrum of the critical point in semilog scale together with the fit of the low energy exponential tail (dash-dot line). **c.** Pl spectrum of the suspended WS_2 case at the minimal power of 5 µW taken before (blue) and after (red) the high power experiments.

[78] which leads to a non-uniform profile of thermal dilatation that favors simultaneously the funneling of carriers to the center of the laser spot and the conversion of excitons to trions, both effects that increases the density of excited carriers that is already high because of the strong laser excitation itself.

Critical point: $P = P_c$

We now focus our attention on the critical point itself. As mentioned previously the two Voigt model fails to describe the measured PL spectrum for this case. The extreme redshift and spectral broadening of this spectrum compared to the other ones together with the increased trion density that suggests our interpretations based on figure 2.10a makes the hypothesis of a transition to an EHP a viable candidate for the interpretation of the critical point. It is known from previous reports that electrons and holes in an EHP are subject to random thermal fluctuations and that their movement is the one of a Brownian motion with a kinetic energy $E_{kin} = 1.5k_BT$. Thus, the PL spectrum is expected to present an exponential band tail at low energy following $I_{PL} \propto \exp(E/E_{exp})$ with E_{exp} a fitting parameter to be determined [112, 128]. A fit of the long low energy tail of the critical PL spectrum is shown figure 2.10b and gives $E_{exp} = 84$ meV, a value slightly higher than the 65 meV observed for the EHL phase in MoS_2 [112]. This value is also close from a crude theoretical estimation assuming $E_{exp} = E_{kin} \approx 1.5k_BT_c \approx 100$ meV. The presence of a clear exponential tail at low energy is another element in favour of an interpretation based on the formation of a dense electron-hole phase in the system. Futhermore, the bandgap renormalization and occupation of the band extrema associated to an EHP and/or thermal expansion could lead to resonant effects and give a potential explanation for the increase in the A_1'-mode intensity. Indeed, the B exciton in WS_2 energy is around 2.4 eV and is expected to redshift by a similar

amount than the A exciton observed here (i.e. by a few tens of meV), which could bring it to resonance with our laser excitation at 2.33 eV [129].

However, more experiments are needed to give a clear conclusion on the nature of the critical point PL spectrum. First, a more resolved study of the PL emission close to the critical point could allow to investigate the potential formation of an EHP by a precise analysis of the evolution of E_{exp} with temperature. Indeed, it is known that E_{exp} remains constant for an EHL while it follows $E_{exp} = \gamma k_B T$ for an EHP with values of γ usually slightly higher than the 1.5 coefficient expected from the Brownian motion of carriers (values of 1.8 were reported for diamond [128] and 1.7 for suspended MoS_2 [112]). Power dependent reflectance spectra would be ideal to give complementary informations and could allow to directly measure the optical gain expected if a dense electron-hole phase is formed. Finally, the thermal motion of the suspended membrane would give an additional measurement of the temperature that could be compared to the one obtained from Raman spectroscopy to ensure that the critical temperature obtained from the shift of the A_1'-mode frequency is true around the critical point and not affected by the potential EHP phase.

Photobleaching and sample damage: $P > P_c$

One last point needs to be addressed concerning the presented set of experiments. While the general evolution of the PL and Raman spectrum seems overall reversible, we do not recall the critical point when the power is sweeped down from the maximum to the minimum values. Furthermore for higher powers, with $P > P_c$ the redshift, broadening and intensity of the PL emission seems to saturate. It is also true for the intensity of the A_1' Raman peak, while the temperature determined from the frequency shift of the A_1'-mode continue to increase. The most probable explanation of these phenomenon is obtained by comparing the PL spectra at low power (5 µW) measured before and after the power ramp (see figure 2.10c). While the overall shape of the spectrum is unchanged, the peak intensity is reduced by approximately two orders of magnitude and a more prominent defect related emission at low energy is seen after the exposition to a strong illumination. Thus, we conclude that the highest powers have damaged the suspended monolayer. Photobleaching might explain the saturation observed at high power and the absence of critical point when the power is decreased from its maximum value. Cautious care needs to be taken in future experiments to avoid such non-reversible behavior as the threshold excitation intensity leading to damages of the sample seems to be close to the critical power needed to reach the potential Mott transition.

Finally, it would be beneficial to reproduce such experiments on suspended WS_2 monolayers using a quartz substrate to ensure that there is no effect of the interference pattern created by the cavity-like geometry of the Si/SiO_2 substrate. Such effect could alter the broad shape of the critical spectrum and affect the exponential fit of the low energy tail of the PL spectrum.

Conclusion

In conclusion, we showed in this chapter preliminary results on our investigation of correlated electron-hole phases in suspended monolayers of MoS_2 and WS_2 at room temperature. Using a combination of PL and Raman spectroscopy, we confirmed the reported observation in the literature of the formation of an EHL phase in suspended monolayer MoS_2 submitted to a strong laser excitation [110, 112]. We determine the critical lattice temperature to be around $T_c = 500 - 700$ K, temperature at which the MoS_2 monolayer is expected to undergo a direct to indirect gap transition [110].

Using a similar experimental procedure, we attempted to understand the behavior of the excitonic states in monolayer WS_2 in the high density regime and evidence a potential transition to a EHP or EHL phase in the same spirit as our observations on suspended MoS_2. Our results presents the signatures of an efficient exciton to trion conversion leading to an alteration of the PL spectra that would be in agreement with the emission of an EHP. These effect on the PL spectrum are correlated with an unexpected enhancement of the A_1' Raman mode intensity. While our results could be explained by the combination of a high exciton density with a non uniform heating profile that favours exciton to trion conversion [78, 73], it is necessary to test the reproducibility of our results and the viability of the proposed interpretation with additional experiments. A first useful set of complementary result would consist into a comparison of the changes in the PL spectrum as a function of laser power in both large spot and diffraction limited spot configurations. If our interpretation based on the non uniformity of the heating profile is true, the effect should not occur when the full suspended monolayer is excited with a uniform laser excitation. In addition, it would be interesting to probe the Brownian motion of the suspended membrane (discussed in more details in chapter 4) through the potential phase transition.

Despite the need of additional experiments, we can already draw a first picture of the physics of suspended monolayer TMDs in the high density regime:

- Laser induced photoheating can lead to a direct-to-indirect gap transition in suspended MoS_2 monolayers.
- The direct-to-indirect gap transition in suspended MoS_2 allows the formation of a dense electron-hole liquid phase, that can be probed through PL spectroscopy. The signatures are an abrupt increase in the PL intensity associated to a redshift of ~ 100 meV and an increase of the FWHM of ~ 150 meV.
- In suspended monolayer WS_2, an increasing excitation intensity leads to a progressive redshift and broadening of the PL spectrum.
- An efficient exciton to trion conversion is observed before the arising of a critical point where the PL spectrum shape is strongly altered and no clear feature can be identified anymore.
- A strong enhancement of the A_1' Raman mode intensity is observed in the vicinity of the critical point.

- The effect may take its origin in the non-uniform heating profile created by the diffraction limited laser beam, in analogy to results on efficient exciton to trion conversion induced by a non uniform strain profile.
- The observed effect seem to strongly depend on the level of defects and is not observed anymore once the monolayer has been damaged.

CHAPTER 3

Symmetry dependent dielectric screening of optical phonons in graphene

In this chapter, we use monolayer graphene as a model system to investigate the behavior of optical phonons in metals with respect to dielectric screening. More specifically, we saw in section 1.1.3 that the phonon dispersion of graphene exhibits Kohn anomalies at the Γ and K, K' points of the Brillouin zone. Using Raman spectroscopy to probe phonons at the Γ and K, K' points in different types of graphene-based van der Waals heterostructures, we will explain how these Kohn anomalies are affected by changes in the dielectric environment of graphene and highlight the fundamental role of the symmetry of the involved phonons in the observed behavior. Our results will then be useful to understand the physics of suspended graphene-based heterostructures and will be used in section 4.3 as a probe of the interlayer coupling in a suspended graphene/$MoSe_2$ heterostructure.

Our investigations rely strongly on the use of hyperspectral mapping of the Raman response of our samples to ensure the statistical reliablity of our observations. Figure 3.1 presents a clear example of the phenomenon. Figure 3.1a shows an optical image of a hBN-capped graphene/WSe_2 sample, with well identified areas formed of hBN-capped graphene (**i**) and hBN-capped graphene/WSe_2 (**ii**). Hyperspectral maps of the 2D-mode and G-mode frequencies in this sample are shown figure 3.1b,c. We observe that the 2D-mode frequency is substantially increased in the hBN-capped graphene/WSe_2 area with respect to

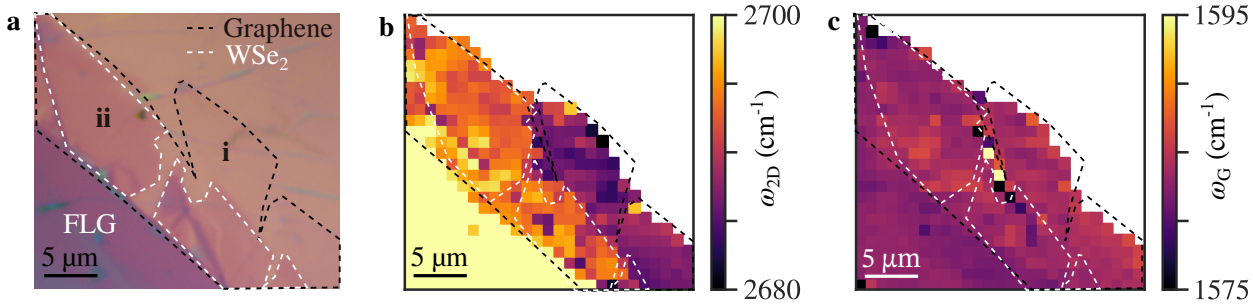

Figure 3.1: Hyperspectral Raman mapping of sample 1. a. Optical image of a hBN-capped graphene/WSe_2 sample. The contours of the relevant regions of the sample are indicated. FLG denotesa few-layer graphene flake. **b,c**. Hyperspectral Raman maps of the 2D-mode and G-mode frequencies in the sample shown in a, respectively.

the hBN-capped graphene one. The average blueshift of the observed 2D-mode frequency is $\Delta\omega_{2D} = 7.3 \pm 3$ cm^{-1}. However, the G-mode frequency remains similar in the two regions of the sample, with average frequencies $\omega_G = 1583.7 \pm 0.8$ cm^{-1} in hBN-capped graphene and $\omega_G = 1583.5 \pm 0.5$ cm^{-1} in hBN-capped graphene/WSe_2.

Such strikingly different behaviors cannot be understood by unintentional strain or doping contributions as both of them would imply a shift of the G-mode in concordance with the observed 2D-mode shift. If the blueshift of the 2D-mode was due to compressive strain, one would expect an increase of the G-mode frequency around 3 cm^{-1}, and an even stronger one in excess of 10 cm^{-1} for hole or electron doping. A more plausible origin is a different sensitivity of the Kohn anomalies at K, K' and Γ towards dielectric screening.

To elucidate the problem, we will first focus on the blueshift of the 2D-mode by considering the hypothesis of a screening induced softening of the Kohn anomaly at the K, K' point. Secondly, we will extensively use the hyperspectral mapping of the Raman response of different types of graphene-based heterostructures to understand how the different phonons are affected by the dielectric screening. Finally, we will focus on a specific sample geometry to investigate how the quality of the interfaces are themselves affecting the observed screening of the optical phonons in graphene. All measurements in this chapter were obtained at room temperature.

3.1 Dielectric screening of the Kohn anomaly at K, K'

DFT-based calculations of the phonon energies suggest that an increase of the dielectric screening in graphene implies a softening of the Kohn anomaly at the K point, as illustrated figure 3.2 [130, 31, 27]. However, the modeling of changes in the dielectric screening in such theoretical calculations remain "artificial" and a proper experimental verification is needed. To test this hypothesis experimentally, we propose to measure the dispersion of the 2D-mode frequency as a function of the laser energy described section 1.1.3 on a given sample with different types of graphene-based heterostructures. Indeed, as the laser energy increases, the

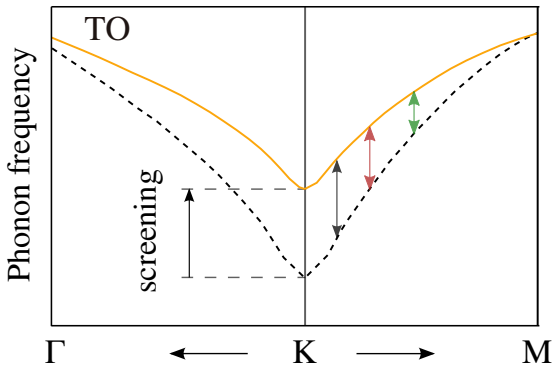

Figure 3.2: Dielectric screening of the Kohn anomaly at K. Sketch of the effect of dielectric screening of the Kohn anomaly present at the K and K' points of the TO phonon dispersion. The dark, red and green arrows represents the expected difference of screening induced shift in frequency of the phonon probed at three different laser energies.

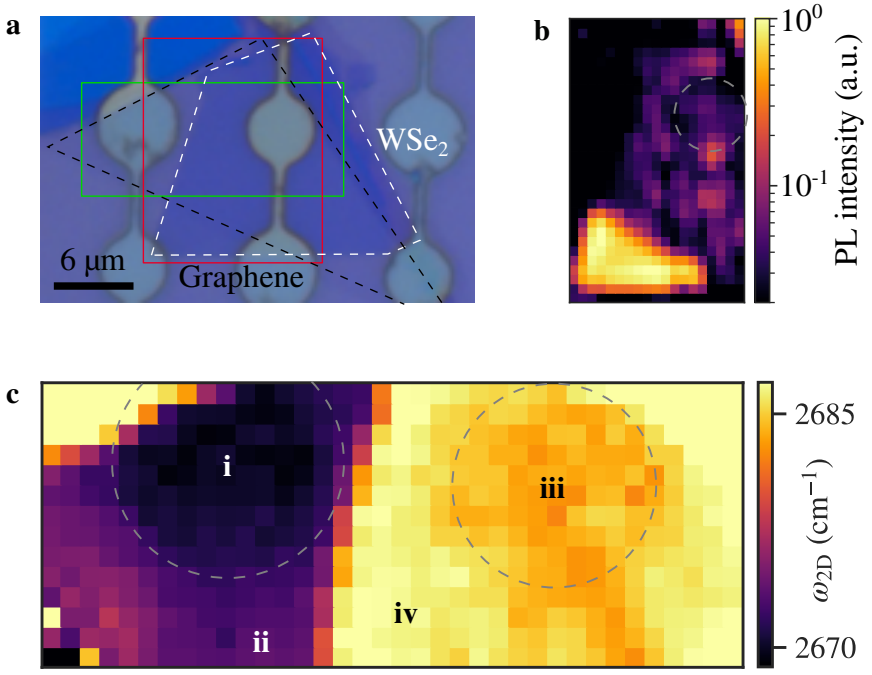

Figure 3.3: Hyperspectral mapping of sample 2. **a**. Optical image of sample 1. The monolayer graphene flake is contoured by the black dashed line and the WSe_2 one by the white dashed line. **b**. Map of the integrated PL intensity of the area defined by the red rectangle in a. **c**. hyperspectral map of the 2D-mode frequency of the area defined by the green rectangle in a. Grey dashed circles in b and c represents the holes in the substrate.

phonons involved in the 2D-mode process lies further away from the K, K' point. Thus, as the softening effect reduces with the relative distance from the K, K' point, one should expect a diminution of the screening induced blueshift of the 2D-mode as the energy of the laser increases.

Figure 3.3a shows an optical image of the considered sample. It is formed of a graphene/WSe_2 heterostructure deposited on a Si/SiO_2 substrate with prepatterned holes. The graphene and WSe_2 flakes are contoured respectively with black and white dashed lines. Both graphene alone and graphene/WSe_2 parts of the sample shows SiO_2-supported and suspended areas. A mapping of the integrated PL intensity of the sample is shown figure 3.3b. The mapping area corresponds to the red rectangle in figure 3.3a and shows that both the suspended and SiO_2-supported graphene/WSe_2 parts exhibit a quenching factor in the order of 10 compared to the SiO_2-supported monolayer WSe_2, sign of a good coupling between the two layers.

Figure 3.3c presents the hyperspectral mapping of the 2D-mode frequency of the area of sample 1 defined by the green rectangle in figure 3.3a. The four areas of interest can clearly be identified as they present different values of ω_{2D} and are marked as **i** for suspended graphene, **ii** for SiO_2-supported graphene, **iii** for suspended graphene/WSe_2 and **iv** for SiO_2-supported graphene/WSe_2. To test the hypothesis of a screening induced softening of the Kohn anomaly, we measure the Raman response of graphene in the four areas defined previously using our three available laser energies (1.58, 1.96 and 2.33 eV). The spectrum of the 2D-mode feature for each configuration and each laser energy is shown figure 3.4a together with their fits. The 2D-mode feature in each configuration except suspended graphene was

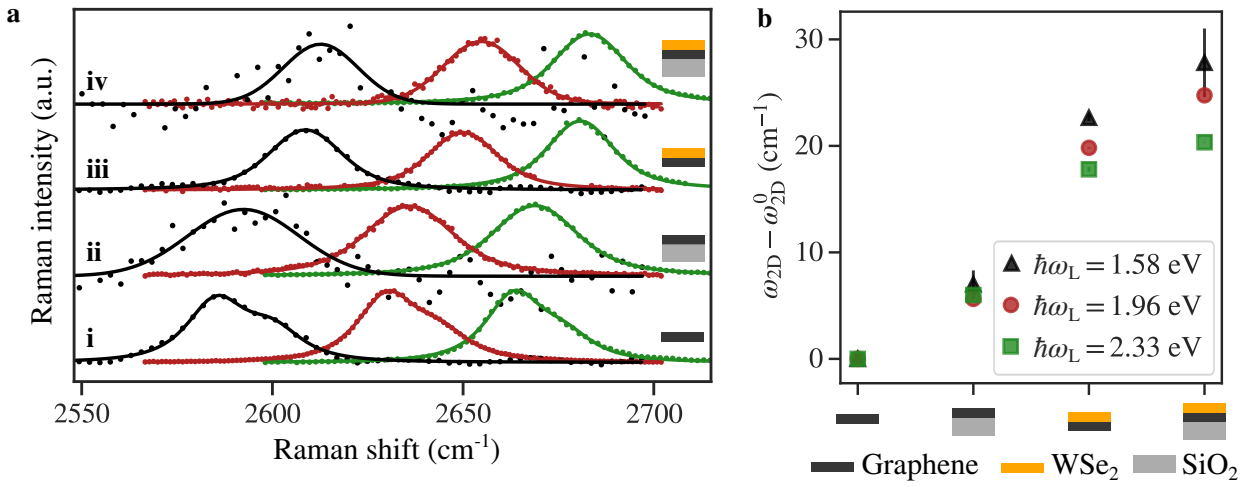

Figure 3.4: Dispersion of the 2D-mode with laser energy. **a**. Spectra of the 2D-mode figure in every given configuration and laser energy (black for 1.58 eV, red for 1.96 eV and green for 2.33 eV). **b**. 2D-mode frequency ω_{2D} in the different regions of the sample as a function of the (symbol-coded) laser photon energy. Data are shown relative to ω^0_{2D}, the value recorded on suspended graphene.

fitted with a Voigt profile. For suspended graphene, the 2D-mode feature is fitted with a double modified lorentzian profile [22, 29] as described by equation (1.15) in section 1.1.3.

To highlight the effect of dielectric screening, we order the areas of the sample by increasing expected dielectric screening and consider for each laser energy the shift $\omega_{2D} - \omega^0_{2D}$ with respect to a reference value ω^0_{2D} being the one of suspended graphene, as shown figure 3.4b. Remarkably, the upshift of the 2D-mode frequency increases in every case as a function of the laser energy. For an excitation energy of 2.33 eV the upshift increases by up to 20 cm^{-1} when moving from region **i** to region **iv** while it reaches up to 27 cm^{-1} for an excitation energy of 1.58 eV. We thus observe an overall screening induced blueshift of ω_{2D} that decreases with the excitation energy, in agreement with the hypothesis of a softening of the Kohn anomaly at K depicted before.

However, an increase in dielectric screening can also result in a decrease of the Fermi velocity v_F because of a renormalization of the electron-electron interaction and a breaking of the linear dispersion approximation close from the Dirac point [109, 108]. While such effect could translate in an upshift of ω_{2D}, as expressed in the approximate double resonant condition of equation (1.16), we do not expect it to contribute as the used excitation energies involve electronic states with energies $\hbar\omega_L/2$ that are far enough from the K, K' point to not be affect by dielectric screening [109, 131].

3.2 Graphene's Raman response in various dielectric environments

To obtain a more quantitative understanding of the observed phenomenon, we performed a systematic analysis based on the hyperspectral mapping of the Raman spectrum of a set of samples with different types of graphene-based heterostructures. The considered set is composed of the two samples presented figures 3.1 and 3.3 (respectively referred to as sample 1 and 2) and an additional sample formed of an hBN/$MoSe_2$/graphene heterostructure (see appendix E and Ref. [100]), referred as sample 3. From now on, all data presented in this chapter were acquired with a 2.33 eV excitation energy.

For all samples, the G-mode feature is fitted with a Lorentzian feature to directly extract ω_G and Γ_G. The 2D-mode feature is fitted in all samples with a single Voigt profile. Γ_{2D} is then taken to be equal to the FWHM of the Voigt profile. Except for the case of suspended graphene, ω_{2D} is taken as the central position of the Voigt profile. For the peculiar case of suspended graphene, a second fit with a double modified Lorentzian profile based on equation (1.15) is performed and we take $\omega_{2D} = \omega_{2D\_}$.

The different areas of interest are spatially determined by a combination of optical imaging and PL mapping. The Raman response of each defined area is then analysed to ensure minimal contributions from built-in strain and unintentional doping on our observations. A power dependent study of the Raman response is also performed to ensure that all the data is acquired with laser powers low enough to avoid any spurious doping of the graphene layer (typically ~ 100 µW/µm^2). Details on the preliminary determination of the interesting areas and unwanted contributions are given in appendix E.

3.2.1 G and 2D-mode frequencies

The spatially averaged values of ω_{2D} and ω_G obtained for our three samples are gathered in figure 3.5a and b, respectively. The samples are once again ordered by increasing expected dielectric screening. Errorbars are corresponding to the standard deviation of the spatially averaged values of ω_{2D} and ω_G. We observe a progressive upshift of the 2D-mode feature up to 26.1 ± 2.4 cm^{-1} reached in the fully hBN-capped graphene/WSe_2 case.

Different remarkable observations can be done from the data of figure 3.5a. First, while the upshift of ω_{2D} due to the bulk SiO_2 substrate itself is only of 5.9 ± 2.3 cm^{-1}, much larger upshifts of 14.8 ± 2.8 cm^{-1} and 16.0 ± 1.2 cm^{-1} are found when SiO_2 is replaced by van der Waals materials, respectively bulk hBN and monolayer WSe_2. In spite of their similar dielectric constants, bulk hBN leads to a much larger upshift of ω_{2D} than bulk SiO_2 [132, 133, 109]. This observation can be explained by the higher level of roughness of SiO_2 compared to layered materials [88] and suggests that graphene remains partly decoupled from SiO_2 while atomically flat substrates ensures an optimal coupling and reduced disorder. Such result also suggests that the Raman 2D-mode is highly sensitive to the nanoscale environment of graphene [134] and that the direct correspondence between the dielectric constant of a material coupled to graphene and the resulting screening induced shift of ω_{2D} is not straightforward. Furthermore, the observed upshift of ω_{2D} is slightly larger in suspended

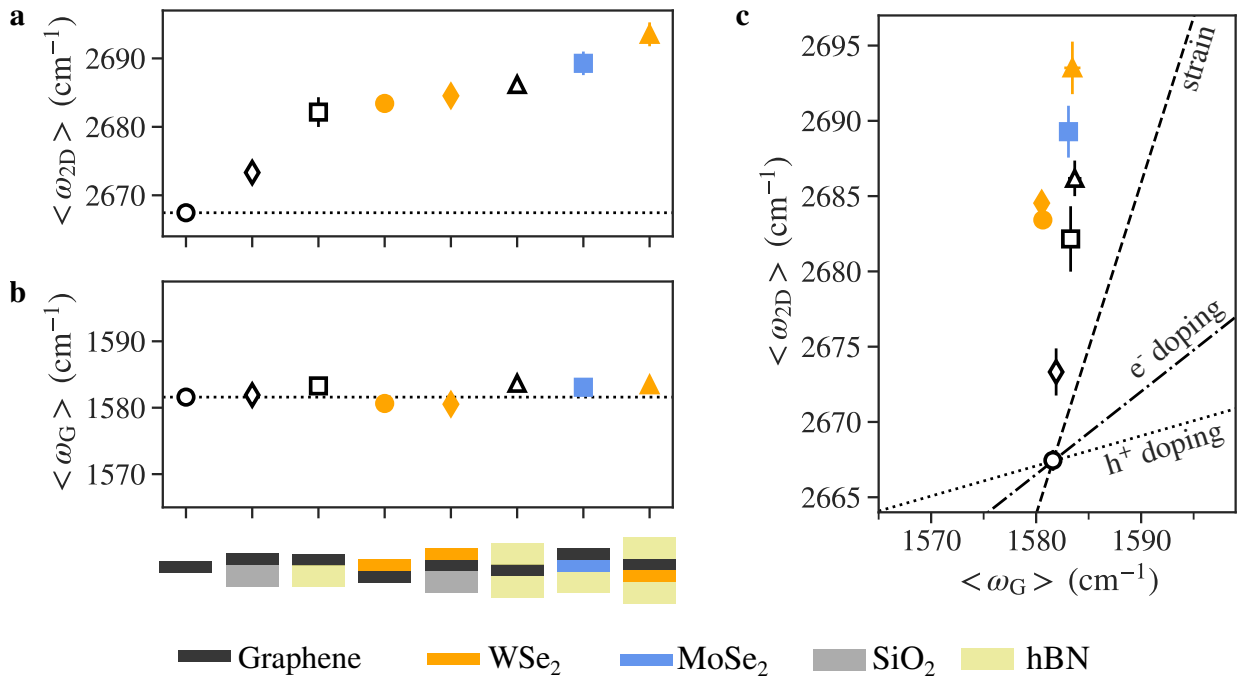

Figure 3.5: Upshift of the 2D-mode frequency and invariance of the G-mode frequency in various dielectric environments. **a**,**b**. Spatially averaged 2D-mode (a) and G-mode (b) frequencies measured on a variety of graphene-based van der Waals heterostructures (see sketches below the graphs). Samples are ordered by increasing expected dielectric screening experienced by graphene. **c**. Correlation between the spatially averaged 2D- and G-mode frequencies shown in a and b. The short dashed, dot-dashed and dotted lines correspond to the expected correlations in the presence of biaxial strain, hole and electron doping, respectively. The reference point for undoped and unstrained graphene is taken for the suspended graphene monolayer. All measurements were performed under laser excitation at 2.33 eV.

graphene/WSe_2 than in graphene on bulk hBN, illustrating the remarkably strong interaction between a TMD monolayer and graphene.

Figure 3.5b demonstrates that the contrasting behavior between 2D-mode and G-mode introduced in figure 3.1 is true even in very different dielectric environments. Indeed, in all the considered heterostructures ω_G remains constant at 1582 ± 2 cm^{-1} whereas ω_{2D} upshifts by more than 20 cm^{-1}. The ω_G invariance is further demonstrated in the $\omega_G - \omega_{2D}$ correlation plot shown figure 3.5c that also shows a clear discrepancy of our data with the expected correlation slopes for strain or doping. A linear fit of the plotted data yields a slope $\partial\omega_{2D}/\partial\omega_G$ above 10. This behavior can seem counter-intuitive since a Kohn anomaly is also present at Γ, suggesting that a sizeable upshift of ω_G could be expected when graphene is screened by another material.

3.2.2 Symmetry protected zone-center optical phonons

The observations described previously can be understood from a symmetry point of view. The following discussion is the fruit of a collaboration with Sven Reichardt and Ludger Wirtz from the University of Luxembourg, who provided the theoretical explanation detailed below.

Let us consider the contribution of the low-energy π-bands[1] to the phonon dynamical matrix D (in which the diagonal terms provide ω_{ph}^2) at Γ, and show that it is insensitive to dielectric screening. For a given phonon polarization $\lambda = \mathrm{LO}, \mathrm{TO}$, we have [24, 135]

$$D_\lambda|_{\pi\text{-bands}} = \frac{2}{M_{\mathrm{C}}} \int_{\mathrm{BZ}} \frac{\mathrm{d}^2 k}{A_{\mathrm{BZ}}} \sum_{\mathrm{spin}} \frac{\langle \pi, \boldsymbol{k} | \partial_\lambda \hat{V} | \pi^*, \boldsymbol{k} \rangle \langle \pi^*, \boldsymbol{k} | \partial_\lambda \hat{V}_{\mathrm{bare}} | \pi, \boldsymbol{k} \rangle}{\varepsilon_{\boldsymbol{k}}^{\pi^*} - \varepsilon_{\boldsymbol{k}}^{\pi}}, \tag{3.1}$$

where M_{C} is the mass of a carbon atom, A_{BZ} the area of the first Brillouin zone (BZ), $\varepsilon_{\boldsymbol{k}}^{\pi^{(*)}}$ is the energy of the $\pi^{(*)}$-band at a point $\boldsymbol{k}$ in the first Brillouin zone, and $\partial_\lambda \hat{V}_{(\mathrm{bare})}$ is the operator corresponding to a change of the screened (bare) ionic potential felt by the electrons upon displacement of the atoms according to phonon mode λ.

In the low-energy regime, relevant for the description of phonons, the symmetry of the graphene lattice dictates that the electrons can be described by the Dirac-Weyl Hamiltonian. Additionally, the zone-center optical phonons are degenerate ($\mathrm{E_{2g}}$ symmetry) and thus behave as vector-like quasiparticles. The effective screened electron-phonon interaction Hamiltonian takes the form [136, 137]

$$\hat{\mathcal{H}}_{\mathrm{elph,eff}} = \sum_{\mathrm{spin}} \int \mathrm{d}^2 r \sum_{\alpha,\beta\in\{A,B\}} \sum_{\lambda=\mathrm{LO,TO}} \sum_{i,j\in\{x,y\}} \hat{\psi}_\alpha^\dagger(\boldsymbol{r}) \sigma_{\alpha\beta}^i \hat{\psi}_\beta(\boldsymbol{r}) \Delta V \big(\mathsf{R}_z(90^\circ)_{i,j}\big) \hat{u}_\lambda^j \tag{3.2}$$

where $\hat{\psi}_\alpha(\boldsymbol{r})$ is the field operator for an electron in a p_z orbital on sublattice $\alpha = A, B$, σ^i is the i-th Pauli matrix, $\hat{u}_\lambda^i$ is the i-th Cartesian component of the "atom-relative" displacement operator (A minus B displacement) for an optical phonon at the Γ point, $\mathsf{R}_z(90^\circ)$ denotes a counterclockwise rotation by 90° in the x-y plane, and ΔV is the effective screened electron-phonon coupling constant. The effective interaction Hamiltonian $\hat{\mathcal{H}}_{\mathrm{elph,eff}}^{\mathrm{bare}}$ for the *bare* electron-phonon interaction takes on the same form as in equation (3.2), with ΔV being replaced by the effective *bare* coupling constant ΔV_{bare}.

In equation (3.1), the screened (bare) electron-phonon matrix elements are given by the matrix elements of the respective effective interaction Hamiltonian for phonon absorption

$$\langle \pi^*, \boldsymbol{k} | \partial_\lambda \hat{V}_{(\mathrm{bare})} | \pi, \boldsymbol{k} \rangle = \langle \pi^*, \boldsymbol{k} | \hat{\mathcal{H}}_{\mathrm{elph,eff}}^{(\mathrm{bare})} | \pi, \boldsymbol{k}; \lambda, \boldsymbol{q} = \boldsymbol{\Gamma} \rangle. \tag{3.3}$$

We note that the form of the interaction Hamiltonian is the same as that of the electron-photon interaction Hamiltonian in quantum electrodynamics (QED), with the phonon playing the role of the photon, the 90°-rotated displacement vector playing the role of the vector potential, and the sublattice playing the role of the spin indices. We can thus make use of all the identities that apply in QED, in particular the Ward identity. In its simplest form, it relates the exact, i.e., screened, interaction vertex to the exact electron Green's function $G(\omega, \boldsymbol{k})$ [138]. Applied to graphene, the Ward identity can be formally written

$$\Delta V \propto \frac{\partial}{\partial k} G^{-1}(\omega = 0, \boldsymbol{k}) = v_{\mathrm{F}} \tag{3.4}$$

[1] We can confidently assume that the σ bands / bonds, being much more rigid, are only insignificantly affected and it is only the dangling p_z bonds / the π bands that actually get influenced by the screening.

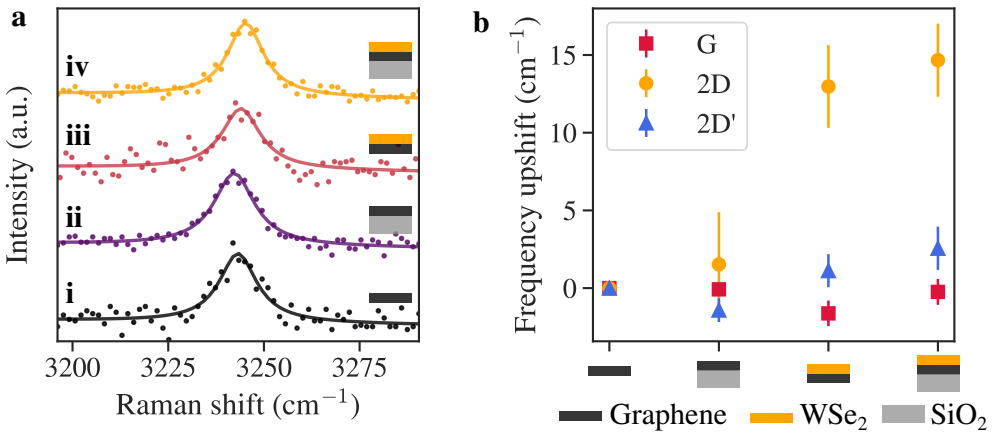

Figure 3.6: Upshift of the 2D'-mode frequency in various dielectric environments. **a**. Typical spectra of the 2D'-mode feature measured in the four different regions of sample 2 defined figure 3.3. **c**. Evolution of ω_{G} (red squares), ω_{2D} (orange circles) and $\omega_{\mathrm{2D'}}$ as a function of the different dielectric environments of sample 2. All measurements were performed under laser excitation at 2.33 eV.

and implies that the screened electron-phonon coupling is proportional to the Fermi velocity.

An important point to note is that the dielectric environment only enters in the screened electron-phonon coupling matrix elements and in the electronic band energies. A direct use of the Ward identity can then be done by observing that $\varepsilon^{\pi^*}_{\boldsymbol{k}} - \varepsilon^{\pi}_{\boldsymbol{k}} \propto v_{\mathrm{F}}$ and $\langle \pi, \boldsymbol{k} | \partial_\lambda \hat{V} | \pi^*, \boldsymbol{k} \rangle \propto \Delta V \propto v_{\mathrm{F}}$. Since the proportionality constants and all the other terms in equation (3.1) are independent from screening, the influence of the screening environment cancels exactly and rends the LO and TO phonon frequencies at Γ insensitive to changes in the dielectric environment, in agreement with the observed constant G-mode frequency.

As the A'_1 phonons at K (that are involved in the 2D-mode scattering process) are not degenerate, it behaves as a scalar quasiparticle and the mathematical structure of the effective electron-phonon Hamiltonian does not allow anymore the use of the Ward identity. There is then no symmetry-based reasoning that protects the TO phonon frequencies at K and ω_{2D} is then screening sensitive.

3.2.3 Dielectric screening of the 2D'-mode

To test further the symmetry-based argument of the protected phonon frequencies at Γ, we probe the evolution of the 2D'-mode frequency with its dielectric environment. As mentioned in section 1.1.3, the 2D'-mode process can be seen as an intravalley 2D-mode process involving phonons in the close vicinity of the Γ point. For this purpose, we consider Sample 2 and the same areas of interest as in figure 3.3, namely suspended graphene (i), SiO_2-supported graphene (ii), suspended graphene/WSe_2 (iii) and SiO_2-supported graphene/WSe_2 (iv). The results are presented figure 3.6 and compared with the measured G-mode and 2D-mode frequencies in the same areas.

In the most screened case (i.e., in this sample, SiO_2-supported graphene/WSe_2), we measure an almost negligible spatially averaged blueshift $\Delta\omega_{\mathrm{2D'}} = 2.6 \pm 1.4$ cm^{-1} with respect to

the unscreened case of suspended graphene, while, within experimental accuracy, we do not resolve any sizeable shift when comparing the other remaining cases to suspended graphene. We can thus consider that $\Delta\omega_{2D'}$ is vanishingly small and in any event more than one order of magnitude smaller than the 2D-mode upshifts $\Delta\omega_{2D}$. These results are in agreement with the theoretical discussion on the symmetry protection of the optical phonon frequency at Γ and further demonstrate that the screening of the Kohn anomaly that occurs for zone-edge TO phonons at K can be used as a uniquely sensitive probe of dielectric screening.

3.3 Fine tuning of the dielectric environment

The observations from the previous section highlight the great importance of the quality of the coupling between graphene and its environment as well as the overall homogeneity of this one. In this section, we give complementary experimental results to achieve a deeper understanding of the 2D-mode sensitivity to its dielectric environment.

3.3.1 G and 2D-mode linewidths

The FWHM of the G and 2D-mode features of graphene (Γ_G and Γ_{2D}) can serve as a useful probe of the homogeneity of the dielectric environment surrounding the graphene layer. Figure 3.7a,b shows the spatially averaged FWHM of the 2D-mode Γ_{2D} and G-mode Γ_G of graphene depending of its environment, ordered by increasing expected dielectric screening. The dataset is the same as in figure 3.5. A sharpening of the 2D-mode can be observed as screening increases. In particular, hBN-capping gives greatly reduced linewidths of the 2D-mode down to 16 ± 0.5 cm^{-1} for the sharpest spectra (see figure 3.7d). This sharpening of the 2D-mode feature points towards an increased homogeneity of the dielectric environment of graphene, when it is tightly coupled to a layered material [134, 139].

Interestingly, this reduction of Γ_{2D} is correlated to the blueshift of ω_{2D}, as visible in figure 3.7c, and highlights the strong influence of the interface quality on the overall dielectric environment of graphene as the phonon frequencies at K are more strongly shifted when the dielectric environment is more homogeneous. As expected, the G-mode FWHM Γ_G does not seem to vary significantly with the dielectric environment.

3.3.2 Proximity dependent screening

To further explore the impact of interfacial coupling on the Raman 2D-mode feature, we compare different areas of another graphene/WSe_2 sample (Sample 4) with various degrees of coupling between graphene and monolayer WSe_2 (1L-WSe_2). Figure 3.8a shows an optical image of the considered sample, where we highlight five regions of interest. These regions were identified by considering the WSe_2 PL intensity map presented in figure 3.8b. Regions 1, 2 and 3 correspond to graphene/WSe_2 heterostructures with different interlayer coupling, as illustrated by their respective PL emission spectra shown figure 3.8d (see also figure 3.9b). The energy shift visible between region 1 and regions 2 and 3 can also be seen as an effect of

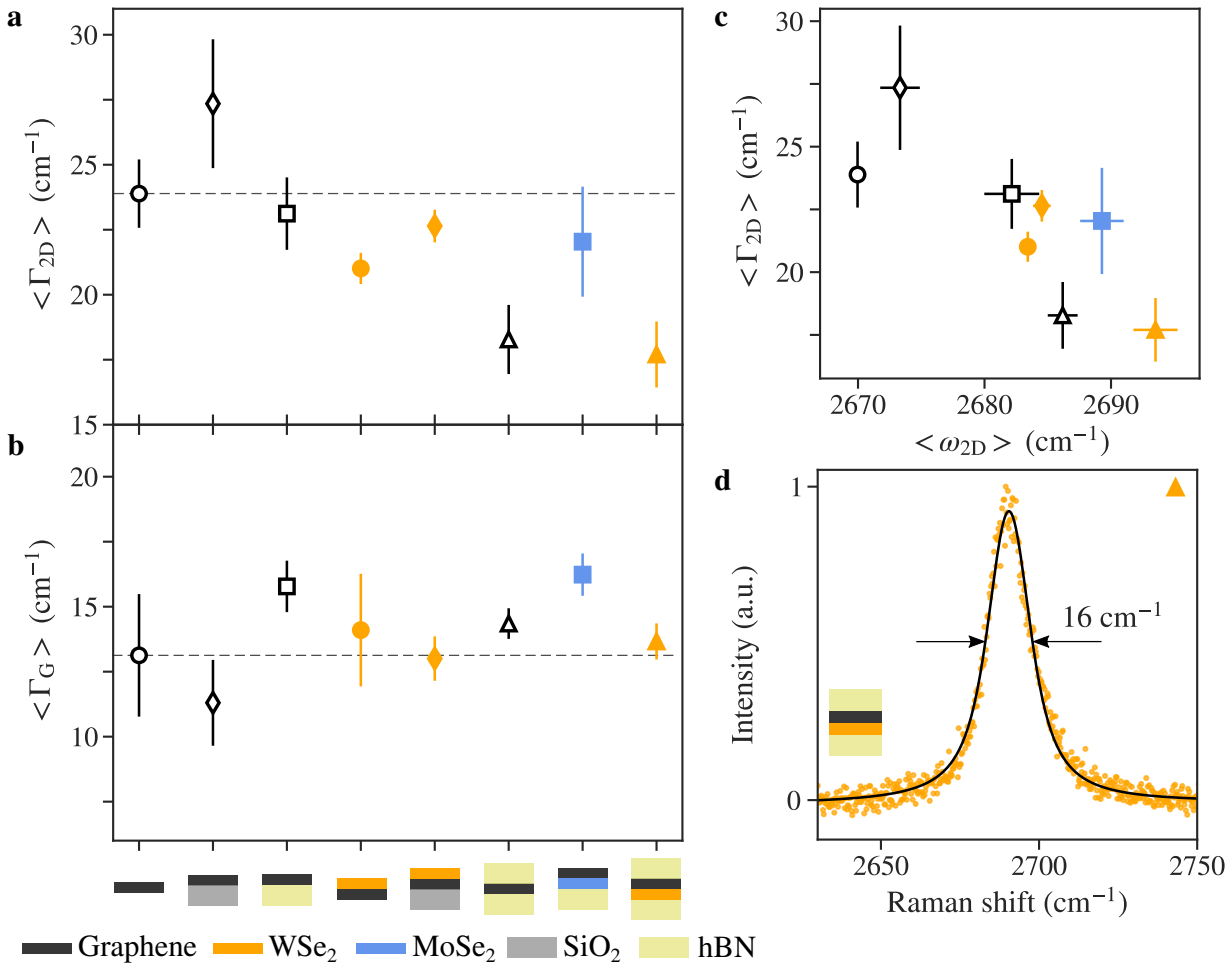

Figure 3.7: Analysis of the 2D-mode linewidth. **a**. Spatially averaged FWHM of the Raman 2D-mode of graphene depending of its dielectric environment, ordered by increasing expected dielectric screening. **b**. Spatially averaged FWHM of the Raman G-mode of graphene depending of its dielectric environment, ordered by increasing expected dielectric screening. **c**. Observed correlation between Γ_{2D} and ω_{2D}. **d**. Observation of a narrow 2D-mode feature in hBN-capped graphene/WSe_2. The solid line is a Lorentzian fit.

dielectric screening due to a smaller interlayer distance between the two layers in regions 2 and 3 with respect to region 1. Figure 3.8e and figure 3.9a prove the strong sensitivity of ω_{2D} to the coupling between the TMD layer and graphene, as ω_{2D} increases when the PL intensity diminishes. Note that in this specific sample, the graphene reference gives $\omega_{2D} \approx 2670.5 \pm 1$ cm^{-1}. The sharpening of the 2D-mode discussed previously is also observed here depending on the interlayer coupling (see figure 3.9b).

Regions 4 and 5 of the same sample are formed by bilayer WSe_2 (2L-WSe_2) interfaced with graphene and present two different levels of coupling (see figure 3.8). Note that the PL intensity of bilayer WSe_2 is lower than in the monolayer limit because of the indirect to direct bandgap transition occurring in the monolayer limit [140]. These two areas also show a coupling-dependent blueshift of ω_{2D} and reduction of Γ_{2D} (see figure 3.9c,e). More interestingly, the obtained values of ω_{2D} and Γ_{2D} for graphene/2L-WSe_2 are similar to the ones observed for graphene/1L-WSe_2 which suggests that dielectric screening essentially stems

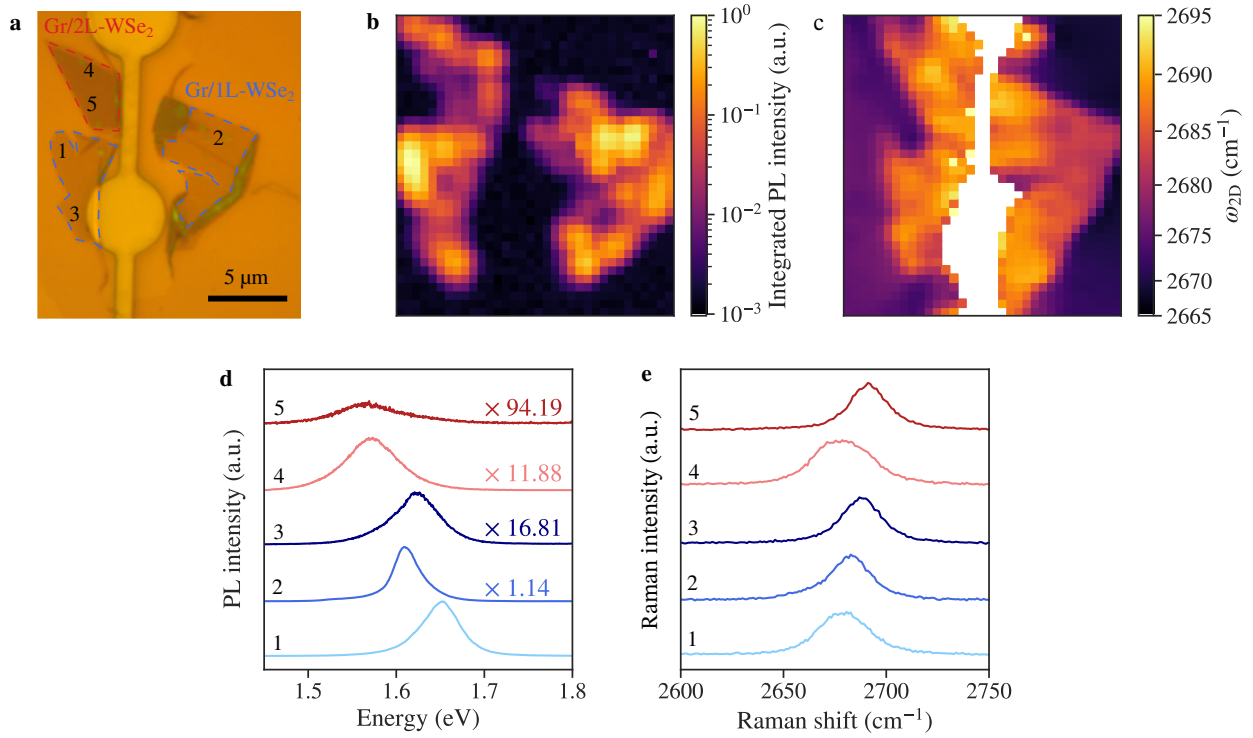

Figure 3.8: Supplementary data on a spatially inhomogeneous sample (Sample 4). a. Optical image of another graphene/WSe_2 sample on Si/SiO_2 with different regions of interest identified (Sample 4). **b, c.** Photoluminescence intensity and 2D-mode frequency maps of the sample shown in a, respectively. **d.** Typical PL spectra for each region of interest. **e.** Typical Raman 2D-mode spectra for each region of interest. Note that although the substrate is patterned with holes and venting channels, the sample is not partly suspended.

from the first layer in contact with graphene, shedding light on the short-range character of the phenomenon.

3.3.3 The influence of surface roughness

Finally, to investigate on the effect of surface roughness of the used substrate, we compare the observed upshift of the 2D-mode frequency in an additional set of graphene/TMD heterostructures deposited onto SiO_2 substrates. Figure 3.10 presents $\Delta\omega_{2D}$, the difference between the 2D-mode frequency in a graphene/TMD heterostructure and in the graphene reference of the same sample. We observe that $\Delta\omega_{2D}$ is appreciably higher when the graphene layer is *not* directly in contact with SiO_2. We understand this as originating from the thicker nature of TMDs, which may conform less than graphene to the microscopic irregularities of the SiO_2 surface. Thus, having the TMD layer in contact with SiO_2 gives a flatter surface from the view point of graphene, and balancing the dielectric environment towards a stronger contribution from the TMD than in the opposite situation.

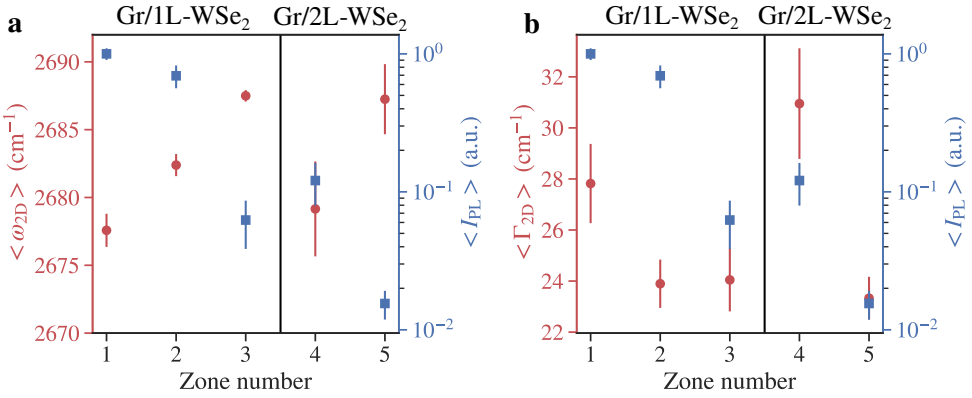

Figure 3.9: Spatially averaged parameters for Sample 4. a. Spatially averaged 2D-mode frequency $\langle\omega_{2D}\rangle$ and integrated PL intensity $\langle I_{PL}\rangle$. **b**. spatially averaged 2D-mode FWHM $\langle\Gamma_{2D}\rangle$ and integrated PL intensity $\langle I_{PL}\rangle$ for the 5 different regions of interest in Sample 4, introduced in figure 3.8.

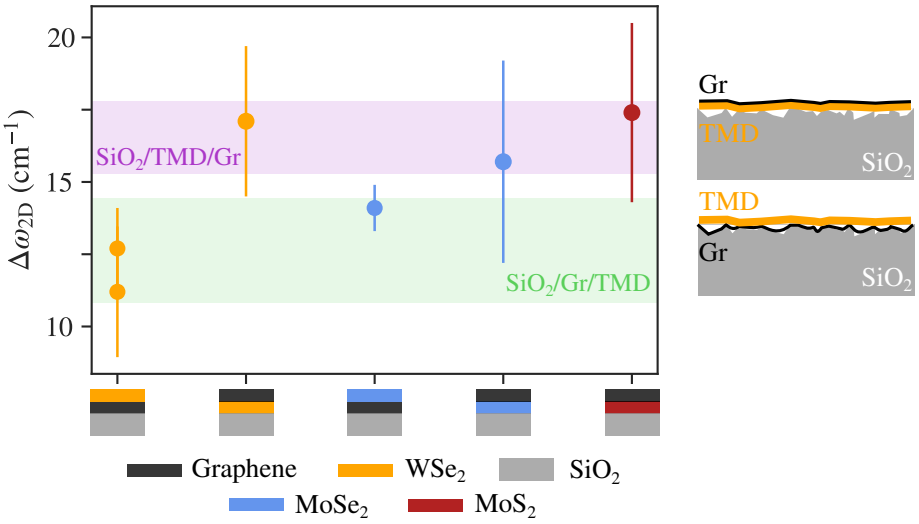

Figure 3.10: Impact of surface roughness. Spatially averaged screening-induced upshift of the 2D-mode feature in a set of graphene/TMD heterostructures deposited onto SiO_2, with the graphene layer either sandwiched between SiO_2 and the TMD or deposited on top of the SiO_2/TMD structure.

Conclusion

In conclusion, we demonstrated in this chapter that the Raman-active optical phonons in graphene are an efficient probe of dielectric screening and of the microscopic details of interlayer coupling within van der Waals heterostructures. The presence of a surrounding medium in the close proximity to a graphene monolayer screens the Kohn anomaly at the K point. The result is a sizeable upshift of the 2D-mode feature by up to 26 cm^{-1} when comparing a suspended graphene monolayer to a hBN-encapsulated graphene/TMD heterostructure.

Furthermore, the E_{2g} phonons involved in the Raman G-mode and 2D'-mode scattering process are symmetry protected from screening effects such that their frequency is invariant in all the experimental configurations examined here. Fundamentally this frequency invariance is a direct consequence of the unique symmetry properties of the low-energy Dirac Hamiltonian in graphene.

In the past years, the analysis of the G-mode and 2D-mode features has enabled quantitative and in-depth characterization of graphene-based samples, notably concerning defects, strain and doping contributions. The study from this chapter demonstrates that the observed variability in the 2D-mode frequency can also stem for a large part from dielectric screening while the G-mode is chiefly sensitive to strain and doping. These results hence provides useful guidelines to decipher hyperspectral Raman maps and better understand proximity effects in heterostructures. A first demonstration of this last point will be developed in section 4.3.

The results from this chapter can be summarized in the following take home messages:

- The phonons involved in the G and 2D Raman modes of monolayer graphene are related to the Kohn anomalies at the Γ and K points of the Brillouin Zone.
- A softening of the Kohn anomaly occurs when the dielectric screening increases, resulting in a significant upshift of the 2D-mode frequency.
- A single layer of TMD is enough to induce an upshift of ω_{2D} up to 16 cm^{-1}.
- In contrast, the G-mode frequency remains constant when the dielectric environment is changed.
- The non-sensitivity of the G-mode to screening is explained by the E_{2g} symmetry of the phonons at the Γ point that implies a protection of the zone-center phonon frequencies.
- This symmetry dependent screening of the optical phonons in graphene enlarges the versatility of the Raman spectroscopy of graphene as a characterisation tool for van der Waals heterostructures.

CHAPTER 4

Electromechanical modulation of the optical properties in graphene/TMD heterostructures

In this chapter, the capabilities of the low temperature experimental setup presented in appendix C are used to investigate the properties of graphene/TMD heterostructures by combining optical spectroscopy and nanomechanics. This setup was specifically developed towards this goal and was built entirely in the framework of this PhD work. Our approach is based on the control of strain in the suspended heterostructure thanks to the use of electrostatic actuation.

In a first section, we will describe the mechanical properties of two-dimensional membranes and give some examples of state-of-the-art results that couples the optical response of suspended 2D-materials with their mechanical degree of freedom. Secondly, we will describe the electrostatic actuation and how we optically measure the mechanical motion of our nanodrums.

Next we will focus on a static study of the Raman response in a suspended graphene/TMD heterostructure. Using the knowledge that was developed in chapter 3, we probe a potential change in the dielectric environment of graphene when the gate bias is increased and the membrane is deflected.

Finally we study the possibility to use statically and dynamically-induced strain to tune the photoluminescence of the heterostructure. A first study of the dependence of the PL characteristics of the TMD layer (integrated intensity, position and linewidth) is performed in the static regime in order to determine the strain sensitivity of the PL response. Then, by driving our device in its non-linear mechanical regime, we attempt to achieve a dynamical strain-induced modulation of the excitonic energy. All the results presented in this chapter were taken at a temperature of 4 K unless otherwise specified.

4.1 Mechanical properties and Optomechanics of suspended 2D-materials

4.1.1 Mechanical properties

In general, the mechanical behavior of a material upon deformation is described by the means of the theory of elasticity in which the considered material is described as a continuous medium. With such considerations, the deformation of a material is accounted by a position dependent displacement vector $\boldsymbol{u} = \boldsymbol{r} - \boldsymbol{r'}$ that relates the initial position of a given point $\boldsymbol{r}$ to its position after the deformation $\boldsymbol{r'}$. Once the material is deformed, the distance between each point $|\delta \boldsymbol{r}|$ changes to become [2]

$$|\delta \boldsymbol{r'}|^2 = |\delta \boldsymbol{r}|^2 + 2 \sum_{i=x,y,z} \sum_{k=x,y,z} \varepsilon_{ik} x_i x_k \tag{4.1}$$

where x_i gives the i-th component of $\boldsymbol{r}$ and ε_{ik} are the components of the *strain tensor* $\bar{\boldsymbol{\varepsilon}}$ given by

$$\varepsilon_{ik} = \frac{1}{2} \left[\frac{\partial u_i}{\partial x_k} + \frac{\partial u_k}{\partial x_i} + \sum_{l=x,y,z} \frac{\partial u_l}{\partial x_i} \frac{\partial u_l}{\partial x_k} \right]. \tag{4.2}$$

Note however that the second order term in equation (4.2) is usually neglected as strains are usually small for small deformations [2, 141]. When deformed, internal forces arises in order to bring the material back to its equilibrium configuration. These internal forces are called *internal stress* and the total resulting force can be expressed as $\boldsymbol{F} = \nabla . \bar{\boldsymbol{\sigma}}$, where $\bar{\boldsymbol{\sigma}}$ stands for the *stress tensor* [2, 141].

The stress and strain tensors are related by Hooke's law, that one can express in tensor form as

$$\bar{\boldsymbol{\sigma}} = \bar{\boldsymbol{C}} \bar{\boldsymbol{\varepsilon}} \tag{4.3}$$

where $\bar{\boldsymbol{C}}$ stands for the *elasticity tensor* which is symmetric and can be diagonalized [142]. To this stage, we still need to define some characteristic parameters that are intrinsic to the material and that shall be used to express the various components of the elasticity tensor $\bar{\boldsymbol{C}}$. Fortunately, applying normal stress to an isotropic material does not produce any angle distortion and we can thus recall a more common situation to define our fundamental parameters following the one-dimensional version of Hooke's law. Assuming an isotropic 2D-material, a normal stress σ_x along the x direction results in a unit elongation [141]

$$\varepsilon_x = \frac{\sigma_x}{E} \tag{4.4}$$

along the same axis, where we defined the *Young's modulus* E that quantifies the ability of the material to deform elastically along the stress direction, in direct analogy to a spring constant. Following the elongation along the x direction, the material will contract in the transverse direction proportionally to the longitudinal elongation as

$$\varepsilon_y = -\nu \varepsilon_x \tag{4.5}$$

defining the *Poisson's ratio* ν [141].

Freely suspended 2D-materials typically exhibit very large Young's modulus (central indentation experiments gives typical values around $E = 210 \pm 50$ GPa for monolayer MoS_2 [143] or $E = 223 \pm 16$ GPa for bilayer hBN [144]). This is especially true for suspended graphene with measured Young modulus up to $E \sim 1$ TPa in both central indentation [145] and pressure blister [146] experiments that makes graphene one of the stiffest material on Earth. Suspended 2D-materials also show extraordinary high breaking strength, with breaking stress values that approaches the theoretical limit for a brittle material where the breaking point is given by the intrinsic strength of the atomic bounds [107] ($\sigma_{\max} = 130 \pm 10$ GPa and $\sigma_{\max} = 27 \pm 6$ GPa respectively measured on exfoliated graphene and MoS_2 [147, 143]). Additionally, suspended 2D-materials tend to show reduced pre-stress values in the $\sim$ 0.01-1 GPa range with respect to more conventional membranes such as 10 to 200 nm thick silicon nitride membranes that typically exhibit pre-stresses in the 1-10 GPa range [107].

However, due to their reduced thickness h their bending rigidity $\kappa = Eh^3/12(1-\nu^2)$ remains negligible and suspended 2D-materials are still in the membrane regime. Thanks to this peculiar combination of strong in-plane stiffness and reduced out-of-plane rigidity, the use of 2D-materials as vibrating membrane in nanoelectromechanical systems (NEMS) has quickly been demonstrated to be promising, with a first demonstration of a functional NEMS based on a graphene flake reported in 2007 by S. Bunch *et al.* [148], 3 years only after the first isolation of monolayer graphene [13]. Similar vibrating systems based on TMDs [149, 150] and van der Waals heterostructures [151] were later on demonstrated together with their promising capabilities at cryogenic temperatures [152].

Because of the reduced bending rigity and mass of the suspended 2D-materials, such NEMS can show a very high frequency tunability [153] and a high force sensitivity [154] that allows them to reach non-linear regimes even at low actuation forces [155]. Combined with the high Young's modulus of 2D-materials, NEMS based on them typically operate in the 1-100 MHz range [10].

4.1.2 Dynamics of 2D membranes

In this work, we focus on circular nanoresonators that follows the description of vibrating membranes. Figure 4.1a shows a sketch of the nanodrum sample geometry, where ξ is the deflection of the membrane with respect to the horizontal case. It is the crucial parameter here that is both affected by the various external forces F_{ext} that induce the actuation of the system, and defining the interference pattern primordial to the reflective detection of the membrane's motion. In the following, we will separate the static and dynamic components of ξ by defining

$$\xi(\boldsymbol{r}, t) = \xi_0(\boldsymbol{r}) + w(\boldsymbol{r}, t) \tag{4.6}$$

where $\xi_0(\boldsymbol{r})$ is the static deflection of the membrane and $w(\boldsymbol{r}, t)$ describes its time-dependent oscillations.

This section is dedicated to the description of the dynamics of the membrane, determined by the fluctuating term $w(\boldsymbol{r}, t)$. It can be rewritten as $w(\boldsymbol{r}, t) = u(\boldsymbol{r})z(t)$ to separate the

spatial profile of the oscillations $u(\boldsymbol{r})$ and the time dependant oscillations $z(t)$ [1].

Harmonic oscillator

In the linear regime, the oscillations of the system are described as a linear damped harmonic oscillator

$$\ddot{z}(t) + \frac{\Omega_0}{Q}\dot{z}(t) + \Omega_0^2 z(t) = \frac{1}{m}F_{\text{ext}}(t) \tag{4.7}$$

with resonance frequency $\Omega_0/2\pi$ and quality factor $Q = \Omega_0/\gamma_{\text{m}}$, $\gamma_{\text{m}}/2\pi$ being the damping rate and m the oscillator's mass. We can solve this equation in Fourier space using the Fourier transform $f[\Omega] = \int f(t)e^{i\Omega t}\text{dt}$, leading to the complex solution

$$z[\Omega] = \chi_{\text{m}}[\Omega]F_{\text{ext}}[\Omega] \tag{4.8}$$

where we define the mechanical susceptibility χ_{m} as

$$\chi_{\text{m}}[\Omega] = \frac{1}{m(\Omega_0^2 - \Omega^2 - i\Omega_0\Omega/Q)}. \tag{4.9}$$

For a harmonic external force $F_{\text{ext}}(t) = F_0 e^{i\Omega t}$, the resulting solution is of the form $z(t) = z_0 e^{i\Omega t}$, with an amplitude z_0 given by the modulus of z

$$z_0 = |z(t)| = \frac{F_0/m}{\sqrt{(\Omega^2 - \Omega_0^2)^2 + (\Omega_0\Omega/Q)^2}} \tag{4.10}$$

and that describes the spectral shape of the mechanical response in the linear regime. In these conditions, the phase delay ϕ of the oscillator is given as

$$\tan\phi = \frac{\Omega\Omega_0}{mQ(\Omega_0^2 - \Omega^2)}. \tag{4.11}$$

We can note that for $Q \gg 1$, the close vicinity of the resonance (for $|\Omega - \Omega_0| \ll 1$) can be approximated by a Lorentzian profile centered at Ω_0 and with a linewidth γ_{m}. Figure 4.1b presents a typical low temperature mechanical response of device 1, a circular graphene/$MoSe_2$ resonator (see chapter 4 and appendix B), with its corresponding fit using equation (4.10).

Duffing type non-linearities

Because of the extremely reduced thickness and high aspect ratio of suspended 2D-materials, their out-of-plane flexibility is uncommonly high, a specificity that gives them a low and tunable out-of-plane stiffness and makes 2D-materials so sensitive to external forces that the non-linear regime can be reached even at low actuation forces [10, 155].

The most common non-linearities encountered in resonators are Duffing like non-linearities, that can be described by adding a cubic term in z in equation (4.7) as

$$\ddot{z}(t) + \frac{\Omega_0}{Q}\dot{z}(t) + \Omega_0^2 z(t) + \alpha_3 z^3(t) = \frac{1}{m}F_{\text{ext}}(t). \tag{4.12}$$

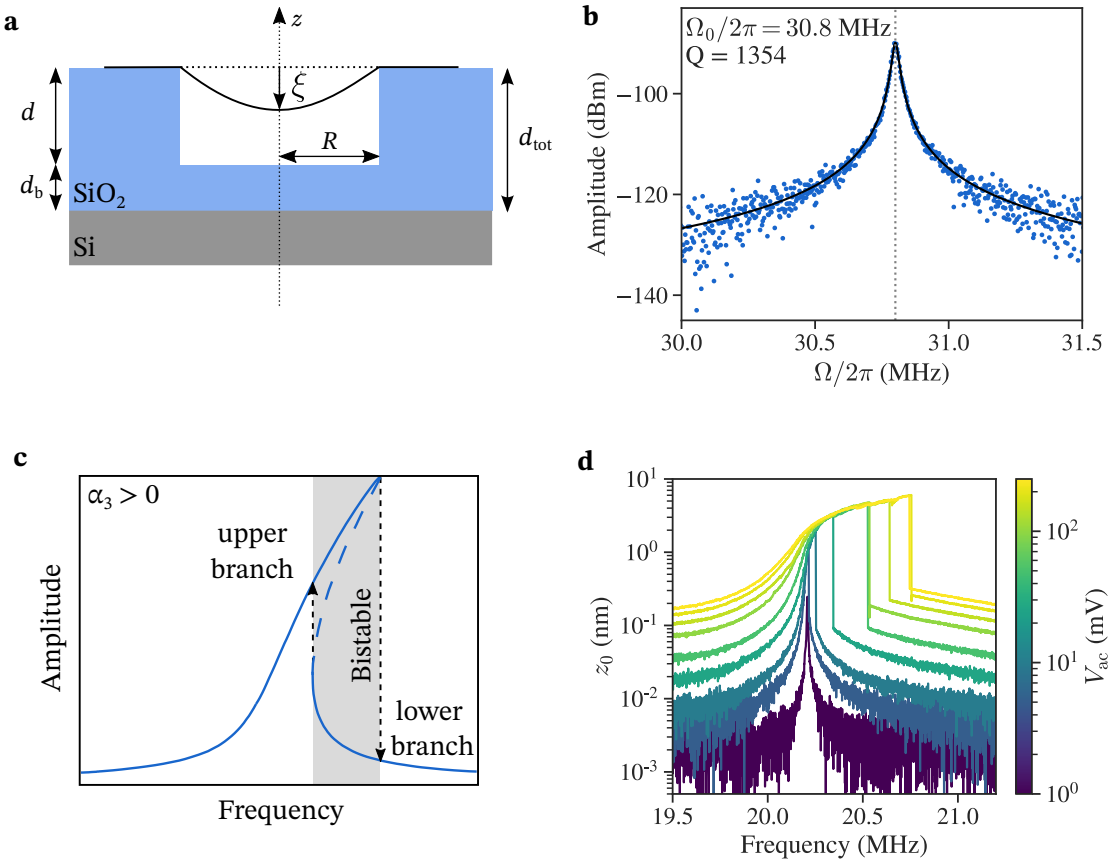

Figure 4.1: **a**. Sketch of the drumlike resonator geometry. ξ is the membrane deflection, $d_{\text{tot}} = d + d_{\text{b}}$ the total thickness of the dielectric layer. **b**. Mechanical response of device 1 formed of a circular graphene/$MoSe_2$ resonator actuated electrostatically in the linear regime at cryogenic temperature (see chapter 4 and B). **c**. Nonlinear mechanical response of a Duffing oscillator with spring hardening. Inspired from [10, 156]. **d**. Mechanical response of device 1 submitted to increasing electrostatic actuation leading to spring hardening.

The two last terms of the left hand side can be factorized by z to give a modified restoring force $F_{\text{Hooke}} = m(\Omega_0^2 + \alpha_3 z^2)z$ that expresses the effect of the non-linearity as an amplitude dependent stiffness [10]. The physical implications can be understood by considering the time-averaged stiffness giving an effective resonant frequency

$$\Omega_{\text{eff}}^2 \approx \Omega_0^2 + \alpha_3 \langle z^2 \rangle \tag{4.13}$$

that is shifting from the linear resonance frequency Ω_0 as a function of the oscillation amplitude. For $\alpha_3 > 0$ the system's resonance frequency is increasing with the oscillation amplitude and one talks about *spring hardening*. For $\alpha_3 < 0$ the opposite happens and leads to *spring softening*.

One can solve equation (4.12) for an oscillating force $F(t) = F_0 \cos(\Omega t)$ by considering an approximate solution $z(t) \approx z_0 \sin(\Omega t)$ and performing a harmonics balance to the first order terms [10] to obtain

$$z_0 \approx \frac{F_0/m}{\sqrt{(\Omega_0^2 - \Omega^2 + \frac{3}{4}\alpha_3 z_0^2)^2 + (\Omega_0 \Omega/Q)^2}} \tag{4.14}$$

after neglecting the higher order harmonics. As expected, for $\alpha_3 = 0$ equation (4.10) is recalled. For $\alpha_3 \neq 0$ the mechanical resonance bends asymmetrically in one of the two frequency directions depending on the sign of α_3, as described in figure 4.1c for $\alpha_3 > 0$. A bistable region forms with upper and lower branches inducing a hysteresis that depends on the direction of the frequency sweep. In practice, when the frequency is progressively changed accross the resonance, the amplitude will follow one of the two branches depending on the direction of the sweep and suddenly jump to the other branch when leaving the bistable region, as indicated by the dashed arrows in figure 4.1c.

The peak amplitude is reached at the frequency Ω_p that follows a parabola in terms of the oscillation's amplitude, defining the *backbone curve* [156, 39]

$$\Omega_\mathrm{p} = \Omega_0 + \frac{3\alpha_3}{8\Omega_0} z_0^2 \tag{4.15}$$

as illustrated in figure 4.1d, for a circular graphene/$MoSe_2$ drum (referred to as device 1 in appendix B) submitted to an increasing oscillating electrostatic force, showing a spring hardening.

Normal modes of a circular membrane

Up to now, we considered only a single resonance for our mechanical oscillator. In practice, the oscillations of a thin film is a sum over normal vibrational modes and each of them will present a resonance in the spectrum of the mechanical response. The profile and frequencies of the normal modes depends on its total energy $E_\mathrm{tot} = E_\mathrm{kin} + U$, where E_kin is the kinetic energy and U the total potential energy. In a general framework, the eigenfrequency of a given mode n can be estimated with the Rayleigh method [1] and gives

$$\Omega_n^2 \propto \frac{U[w_n(\boldsymbol{r},t)]}{E_\mathrm{kin}[w_n(\boldsymbol{r},t)]}. \tag{4.16}$$

This equation is true if one knows the exact mode profile. In practice, approximations are usually made to the shape of the modes and leads to theoretical values higher than the ones observed experimentally.

For a circular thin film, the energy of an oscillating-mode $w(\boldsymbol{r},t)$ is given by $E_\mathrm{tot} = E_\mathrm{kin} + U_\mathrm{b} + U_\mathrm{s}$, where the potential energy is composed of two contributions being the bending energy U_b and the stretching energy U_s. They can be calculated by integrating over the area $\mathcal{A}$ as [157, 142]

$$E_\mathrm{kin} = \frac{\rho}{2}\int_\mathcal{A} \mathrm{d}^2\boldsymbol{r} \left(\frac{\partial w(\boldsymbol{r},t)}{\partial t}\right)^2 \tag{4.17}$$

$$U_\mathrm{b} = \frac{\kappa}{2}\int_\mathcal{A} \mathrm{d}^2\boldsymbol{r} |\nabla^2 w(\boldsymbol{r},t)|^2 \tag{4.18}$$

$$U_\mathrm{s} = \frac{\sigma}{2}\int_\mathcal{A} \mathrm{d}^2\boldsymbol{r} |\nabla w(\boldsymbol{r},t)|^2 \tag{4.19}$$

with ρ the mass density of the film, $\kappa = Eh^3/12(1-\nu^2)$ the bending rigidity determined by the Young modulus E, the Poisson ratio ν and the thickness of the film h, and σ the tension

in the film. Variational minimization of the total energy leads to the differential equation of the film motion [157, 2]

$$\frac{\kappa}{h}\nabla^4 w(\boldsymbol{r},t) - \sigma\nabla^2 w(\boldsymbol{r},t) + \rho\frac{\partial^2}{\partial t^2}w(\boldsymbol{r},t) = 0. \tag{4.20}$$

Assuming an oscillating solution of the form $w(\boldsymbol{r},t) \propto u(r,\varphi)e^{i\Omega t}$, expressed in radial coordinates (r,φ) leads to the mode profiles

$$u_{mn}(r,\varphi) = A_m \cos(m\varphi) J_m\left(\frac{\alpha_{mn} r}{R}\right) \tag{4.21}$$

where A_m is a normalization constant, J_m is the Bessel function of order m, α_{mn} represent the roots of the Bessel function so that $J_m(\alpha_{mn}) = 0$, and R is the radius of the circular resonator. Figure 4.2 shows the theoretical profiles of the first modes of a circular film (lower panels) together with experimental mappings of these modes on a circular graphene drum (upper panels) [158]. Their respective eigenfrequencies can be estimated as

$$\Omega_{mn} = \alpha_{mn}\sqrt{\frac{\sigma}{\rho R^2} + \frac{\kappa\alpha_{mn}^2}{\rho h R^4}}. \tag{4.22}$$

It is worth mentioning two important particular cases here. One can categorize two-dimensional systems depending on the dominating contribution between their bending rigidity κ and tensile stress σ. 2D-materials being extremely thin, their behavior is described by the *membrane* model where the tensile stress dominates. In this case, $\sigma \gg \kappa$ and the eigenfrequencies can be approximated as

$$\Omega_{mn} \approx \alpha_{mn}\sqrt{\frac{\sigma}{\rho R^2}} \sim \frac{1}{R} \tag{4.23}$$

in opposition to *plates* dominated by the bending rigidity κ, leading to $\Omega_{mn} \sim 1/R^2$.

To complete the picture, one last parameter needs to be adressed. As each mode $w_n(\boldsymbol{r},t)$ can be seen as a specific oscillator, each of them is associated to a given *modal mass* m_n that is different than the total mass of the system m_{tot} and can be defined as [142]

$$m_n = \rho h \int \mathrm{d}^2\boldsymbol{r}\, u_n^2(\boldsymbol{r}). \tag{4.24}$$

For the fundamental (0,1) mode of a circular drum, the effective modal mass is [10]

$$m_{(0,1)} \approx 0.27 m_{\text{tot}}. \tag{4.25}$$

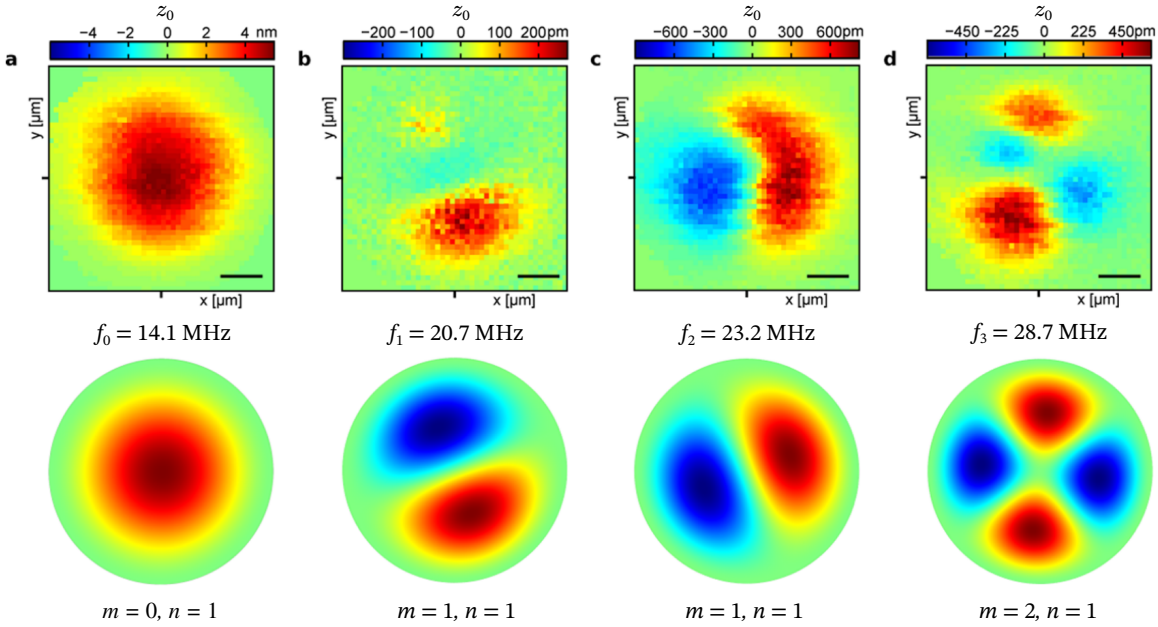

Figure 4.2: Normal modes of a circular graphene drum. Upper panels shows experimental phase resolved mappings of the four first vibrational modes of a circular graphene drum. Lower panels show the corresponding theoretical predictions. Adapted from [158].

4.1.3 Interplay between mechanical and optical properties

We discussed previously the promising character of NEMS that use 2D-materials as vibrating membranes thanks to their unique mechanical properties. It also enables new ways to study the various properties of van der Waals systems by either tuning them thanks to the addition of the mechanical degree of freedom, or use this last one as a new probe to improve or complete more common techniques. As an example, following the variations of the mechanical response has been shown to be a viable technique to probe the thermal conductance of $MoSe_2$ [159]. Since 2D-materials also present strong light-matter interactions, it is straightforward to consider the possibility to couple the mechanical and optical worlds. In this section we will briefly describe the state-of-the-art of what we will call *opto-electro-mechanics*, where 2D-NEMS are used as a platform to study how the optical response of van der Waals systems may affect the mechanical vibrations and vice-versa.

Strain engineering

In section 1.2.3 we saw that the excitonic resonances in TMDs are strain dependent. Thus, by precisely inducing strain in a TMD layer one can tune the optical response of the material in a reversible way. Previous works demonstrated that the level of strain in NEMS can be tuned efficiently by pulling electrostatically on the vibrating material thanks to a simple electrostatic backgate [160]. The same principle can be applied on 2D-materials suspended over a hole or a trench via the mean of electrostatic actuation that will be described in more details in section 4.2.2. Electrostatic gating has first been applied on suspended graphene samples. To understand the interplay between doping and strain in electrostatically deflected

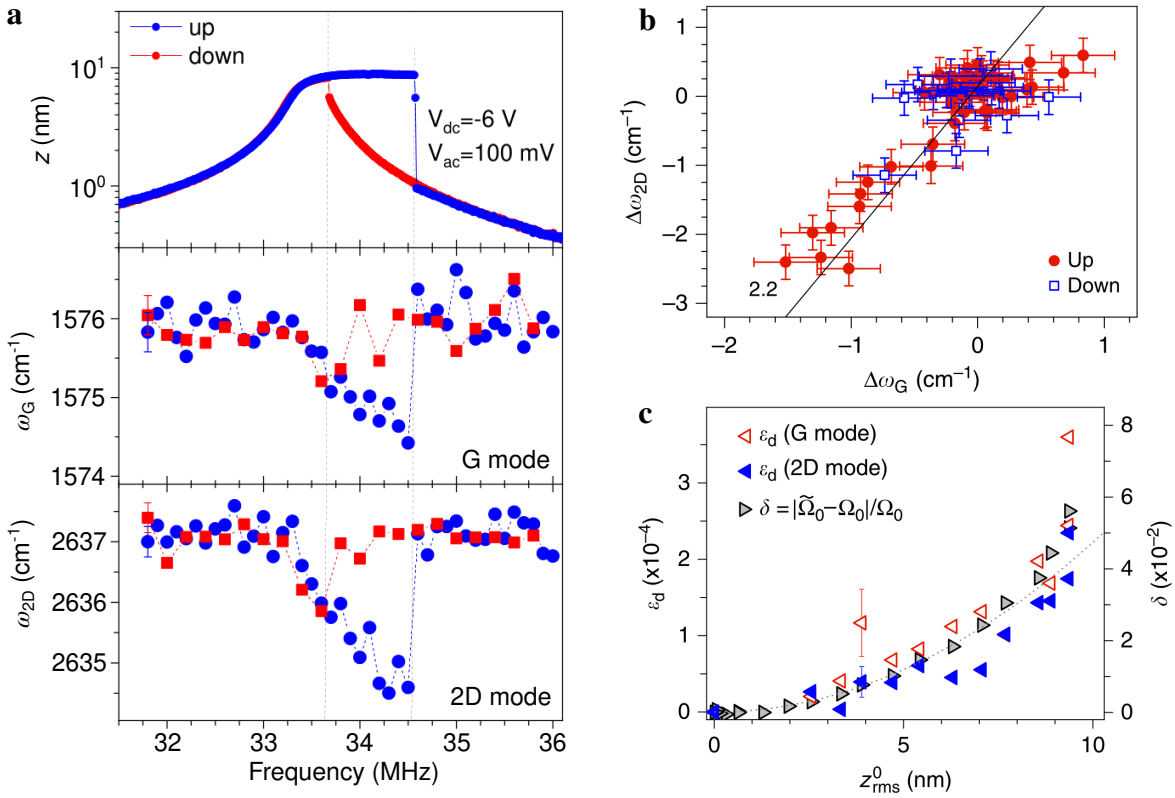

Figure 4.3: Dynamically induced strain in a monolayer graphene drum. **a**. Change in the G and 2D-mode frequency when the actuation frequency is sweeped up (blue) or down (red) through the non-linear mechanical resonance shown on the top panel. **b**. Correlation between the G and 2D-mode frequency shifts associated with the data points from a. **c**. Time averaged dynamical strain as a function of the maximum oscillation amplitude. All panels are adapted from [39].

graphene monolayers, D. Metten *et al.* demonstrated through Raman spectroscopy that doping induced non-adiabatic phonon softening is negligible with respect to strain induced phonon softening [161].

Thanks to an increasing sample quality, P. Hernández-López *et al.* recently demonstrated that the optical response of TMDs can be widely tuned by applying high DC voltages on the backgate of TMD-based 2D-NEMS [64]. Their work demonstrates that at low voltage the variation of the optical response of suspended monolayer WSe_2 is dominated by doping changes before attaining a strain dominated regime at higher voltages where a maximum strain value of 2.75 % is reached. In the process, the different strain dependences of free excitonic states and defect related states leads to a strong enhancement of the dark exciton emission thanks to a resonant hybridization of this last one with defect related states that do not shift with strain.

Even though the cited works give interesting perspectives on the strain tuning of the properties of 2D-materials, they rely on the static deflection of the suspended membrane and do not consider the dynamics of the system. However dynamical strain were highlighted by A. Reserbat-Plantey *et al.* in a multilayer graphene cantilever by probing the changes in the Raman features of graphene through the mechanical resonance of the system [162]. More

recently X. Zhang *et al.* showed that the high non-linearity of the mechanical response of graphene circular nanodrums can be used to dynamically enhance strains in graphene monolayers [39]. As shown figure 4.3a, the frequency of the G and 2D-mode features downshift accordingly to the spectrum of the mechanical vibration amplitude when the actuation frequency is sweeped through the non-linear mechanical resonance of the fundamental mode of the drum. Figure 4.3b presents the $\omega_G - \omega_{2D}$ correlation for the points of figure 4.3a with a slope around 2.2 in agreement with a strain dominated phenomenon. Furthermore, dynamically induced strain can reach anomalously high values with respect to statically induced strain. Figure 4.3c shows the time-averaged dynamically induced strain probed through Raman spectroscopy. Values up to $\varepsilon_d \approx 2.5 \times 10^{-2}$ % are reached for a peak oscillation amplitude $z^0_{rms} \approx 9$ nm that corresponds to the static strain value induced by a 60 nm static deflection.

This last result gives highly promising perspectives towards a strain induced modulation of the optical response in TMD based devices. It is reasonable to expect a similar kind of enhanced dynamical strain in the non-linear regime than observed with graphene that could give the possibility to induce an observable dynamical shift in the exciton energy with modulation frequencies in the 10-100 MHz range. This perspective has been explored in the framework of this PhD work and will be discussed in section 4.4.2.

Dynamical tuning of the Purcell-like effect

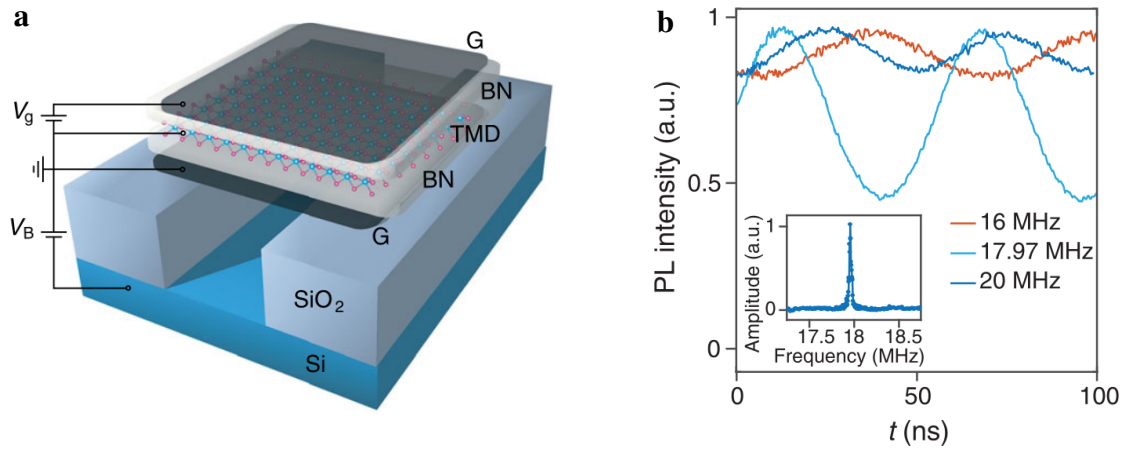

Figure 4.4: Dynamical tuning of the exciton resonance with a mirror. a. Sketch of the sample geometry used to achieve the modulation of the PL emission via a precise engineering of the cavity-like interferences. **b**. Time trace of the PL intensity when the sample is actuated off resonance (dark blue, orange) and exactly at resonance (light blue) with a 10 V AC amplitude. All panels are extracted from [163].

With a proper engineering of the optical interferences that occur in the sample, the mechanical degree of freedom can allow to control in a single sample the Purcell-like effect that we described in section 1.3.1. Such experiments where performed by Y. Zhou *et al.* [163]. They used a hBN-capped $MoSe_2$ monolayer with additional few-layer graphene as top and bottom electrodes, suspended over a trench in a Si/SiO_2 substrate (see figure 4.4a). The use of the graphene electrodes allow to ensure the neutrality of the $MoSe_2$ monolayer when

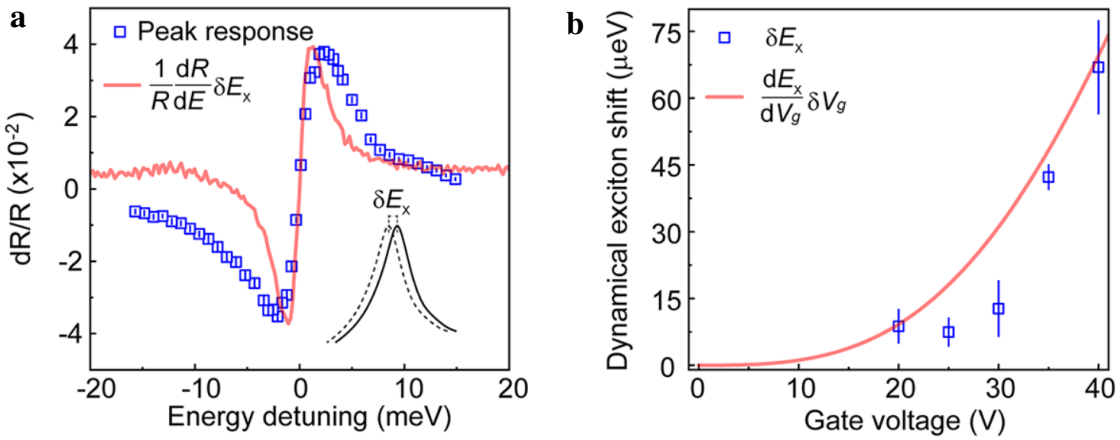

Figure 4.5: Exciton-optomechanical coupling in a suspended $MoSe_2$ monolayer. a. Peak response of the frequency dependent fractional change in the reflectance contrast as a function of the laser detuning (blue squares). The red line gives the energy derivative of the normalized reflectance contrast spectrum multiplied by the dynamical exciton shift δE_X. **b**. Gate voltage dependence of the dynamical shift. Adapted from [164].

a backgate is applied on the substrate to pull on the heterostructure. By depositing a gold layer at the bottom of the trench before suspending the heterostructure, they were able to strongly increase the interference effects in the sample to maximize the amplitude of the optical field oscillation as a function of the membrane position. With such samples, they demonstrated a 50% modulation of the PL intensity and a 60% modulation of the exciton radiative lifetime when the sample is actuated at resonance with a 10 V peak-to-peak AC voltage, corresponding to a maximum oscillation amplitude of 14 nm (see figure 4.4b).

Exciton-optomechanical coupling

Recently H. Xie *et al.* demonstrated a tunable exciton-optomechanical coupling at low temperature in a suspended monolayer $MoSe_2$ [164]. When actuated electrostatically, the oscillation of the $MoSe_2$ membrane induces a small dynamical shift of the exciton energy δE_X. If the sample is illuminated by a monochromatic light beam, it means that the reflectivity at this specific energy will be affected by the energy shift of the exciton. To experimentally highlight this effect, the authors probed the mechanical response at constant actuation of the system while changing the laser energy through the exciton resonance. With this procedure, it is possible to determine the fractional change in the reflectivity $dR/R = (R_{ac} - R_{dc})/R_{dc}$ as a function of the laser detuning $\Delta = E_L - E_X$. The evolution of the peak response of dR/R as a function of the detuning Δ is shown as blue empty squares in figure 4.5a and can then be compared to the fractional change in reflectivity that one would expect considering a dynamical shift of the exciton resonance δE_X. It can be estimated as

$$\frac{dR}{R} = \frac{1}{R}\frac{dR}{dE}\delta E_X \tag{4.26}$$

where $R^{-1}(dR/dE)$ corresponds to the derivative of the reflectance contrast spectrum. Thus, it is possible to determine δE_X by keeping it as a fitting parameter and use it to match the

optomechanically measured change of peak dR/R signal (blue markers in figure 4.5a) and the calculated one deduced from the reflectance contrast spectrum (red line in figure 4.5a).

The observed values of the dynamical exciton shift δE_X are shown figure 4.5b as a function of the DC backgate voltage. As shown with the continous red line in figure 4.5b the observed exciton shift δE_X agrees with the theoretically expected shift $\delta E_X = (dE_X/dV_g)\delta V_g$. The authors also show that the dynamical exciton shift can be used to detect thermal vibrations at cryogenic temperature and induces a periodic modulation of the photothermal force due to laser illumination. The modulation of the photothermal force is then producing a dynamical backaction on the vibration of the $MoSe_2$ membrane resulting in observable changes of the mechanical resonance frequency and line width as a function of both laser detuning and gate voltage.

Nanomechanical spectroscopy

The photothermal heating of a material depends on its absorption and is thus dependent on the energy of the incoming light. With this in mind, J. N. Kirchhof *et al.* developed an experimental way to mechanically measure the optical absorption of TMDs [165]. They used suspended few-layer TMDs over a fully crossing hole in a SiN membrane with a thin gold coating. The actuation is ensured by a transparent electrode situated below the sample. The mechanical response is then probed by a 633 nm laser focused on the SiN part of the vibrating membrane while the energy of a tunable laser focused on the center of the suspended MoS_2 area is varied from 1.24 to 3.1 eV. As the laser energy changes, so does the absorption of the MoS_2 flake that sees its temperature change accordingly. The energy dependent heating then translates as a frequency softening $\Delta f = f_0 - f$ of the mechanical resonance. The observed frequency shift is then normalized by the laser power to obtain the sample responsivity $\Delta f/\Delta P$ that is directly proportionnal to the sample absorption.

By measuring the changes in the mechanical frequency when the laser energy is varied, one can mechanically obtain the absorption spectrum of the material. It can then be combined with the reflection spectrum of a 2D-material measured with this nanomechanical spectroscopy technique to fully determine the dielectric function of the considered material in the accessible energy range of the excitation laser.

4.2 Actuation and readout of circular nanodrums

4.2.1 Optical readout

To probe the mechanical vibrations of a sample, we use an optical readout by detecting the reflection of a laser beam impinging on the sample. As described in figure 4.6 and C.3, the sample can be regarded as a low-finesse Fabry-Pérot cavity [1]. Multiple reflections within the cavity create an interference pattern in the sample that can be modelled numerically using a classical approach of the transfer matrix calculation [16, 166] that takes into account all the layers in the sample. The suspended van der Waals heterostructure takes the place of the top movable mirror and the total reflectance $\mathcal{R}$ of the system depends on its posi-

tion, as illustrated in figure 4.6 where the blue curve gives the reflectance of a suspended graphene/$MoSe_2$ sample for $\lambda = 632.8$ nm, being the wavelength of our He-Ne laser, as a function of the membrane deflection ξ. The sample geometry here is $d = 420$ nm and $d_b = 80$ nm.

Similar calculations can be used for a fixed membrane while tuning the d/d_b ratio to determine the optimal sample geometry. Since the interferences are modulating the total electomagnetic field inside the sample, absorption and emission are also affected and the calculation can be used to determine or optimise the exaltation factor $\mathcal{F}(\lambda) = I(\lambda)/I_0(\lambda)$ defined as the ratio between the emitted intensity in the considered drum-like geometry $I(\lambda)$ and the one of the bare unetched Si/SiO_2 geometry $I_0(\lambda)$, taken as a reference [16]. The black dashed line in figure 4.6 presents the variation of the exaltation factor $\mathcal{F}(\lambda_X)$ of the graphene/$MoSe_2$ sample at the exciton wavelength $\lambda_X \approx 750$ nm as a function of the deflection ξ.

Figure 4.6 illustrates how the interferences define the detection of mechanical oscillations. As the reflectance depends on the membrane deflection ξ, an oscillation $\delta\xi = z_0 \cos(\Omega t)$ of the membrane position is translated into an oscillation of the reflectance around its mean value $\mathcal{R} = \mathcal{R}(\xi_0) + \delta\mathcal{R}(\delta\xi)$. For $\delta\xi \ll \xi_0$ the oscillating term of the reflectance can be expanded in terms of $\delta\xi$ as

$$\delta\mathcal{R}(\delta\xi) \approx \left.\frac{\partial\mathcal{R}}{\partial\xi}\right|_{\xi_0} z_0 \cos(\Omega t) \tag{4.27}$$

by noting that $\delta\mathcal{R}(\xi_0) = 0$ and where $\left.\frac{\partial\mathcal{R}}{\partial\xi}\right|_{\xi_0}$ is the slope of the interference pattern at the equilibrium position.

The voltage measured by the detection photodiode can be written as

$$V_{APD} = AP_L\mathcal{R} + V^0_{APD} \tag{4.28}$$

where A is an experimental proportionnality factor, P_L is the incident laser power and V^0_{APD} is the offset voltage of the photodiode, acting as a simple offset. Inserting equation (4.27) in this expression gives

$$V_{APD} = AP_L\mathcal{R}(\xi_0) + \widetilde{V}_{APD}\cos(\Omega t) + V^0_{APD}. \tag{4.29}$$

By defining $\beta = AP_L\left.\frac{\partial\mathcal{R}}{\partial\xi}\right|_{\xi_0}$ as the *transduction factor* we get

$$\widetilde{V}_{APD}[\Omega] = \beta z_0[\Omega] \tag{4.30}$$

that links directly the amplitude of the membrane vibrations with the amplitude of the detected oscillating current at the same frequency. Note that equation (4.30) is valid only for oscillation amplitudes z_0 that are small with respect to the changes in $\left.\frac{\partial\mathcal{R}}{\partial\xi}\right|_{\xi_0}$. The determination of β is the key of the calibration of the experiment and can be done in different ways, some of them will be discussed later. The oscillations of the membrane can hen be measured thanks to a demodulation of the photodiode signal by a lock-in amplifier [167] or via the measure of the power spectral density of the membrane motion with a spectrum analyser.

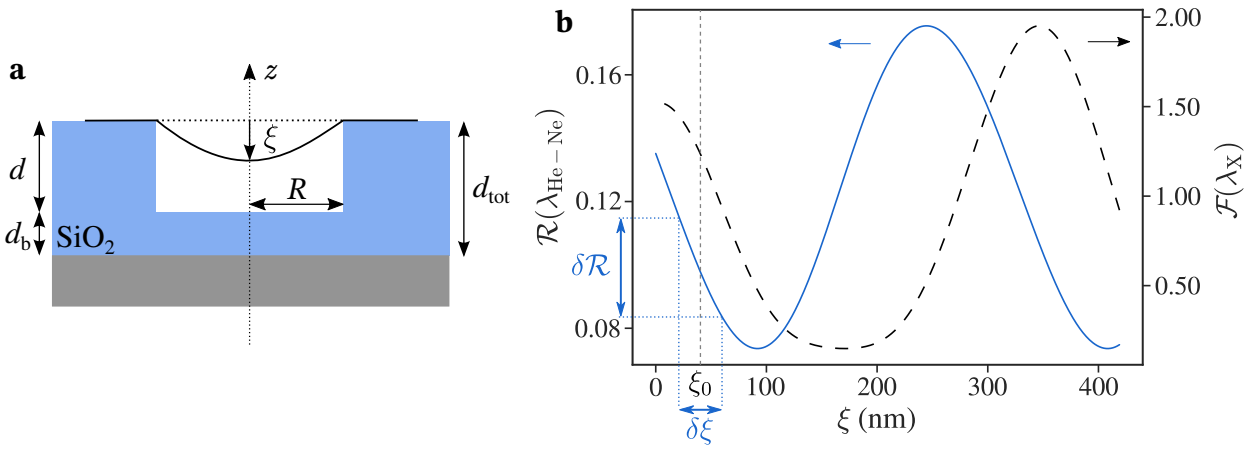

Figure 4.6: Interferences in a graphene/$MoSe_2$ nanodrum. The blue curve gives the variation of reflectance $\mathcal{R}$ at the laser wavelength $\lambda_{\mathrm{He-Ne}} = 632.8$ nm as a function of the membrane deflection ξ. The dashed black line is the exaltation factor at the exciton wavelength $\lambda_{\mathrm{X}} \approx 750$ nm.

4.2.2 Electrostatic actuation

I will describe here the electrostatic actuation of 2D-NEMS, that is the main actuation method used in this work. It relies on the use of the sample geometry as a plane capacitor with a capacitance C_{eq}. When a gate voltage $V_{\mathrm{g}}(t) = V_{\mathrm{dc}} + V_{\mathrm{ac}}\cos(\Omega t)$ is applied on the system, an attractive electrostatic force $F_{\mathrm{e}} = -\frac{1}{2}(\partial C_{\mathrm{eq}}/\partial z)V_{\mathrm{g}}^2$ is acting on the membrane. For small oscillations $V_{\mathrm{ac}} \ll V_{\mathrm{dc}}$ the electrostatic force can be expressed as

$$F_{\mathrm{e}} = F_{\mathrm{dc}} + F_0\cos(\Omega t) \tag{4.31}$$

with a constant term $F_{\mathrm{dc}} = -\frac{1}{2}(\partial C_{\mathrm{eq}}/\partial z)V_{\mathrm{dc}}^2$ and an oscillating force of amplitude $F_0 = -(\partial C_{\mathrm{eq}}/\partial z)V_{\mathrm{ac}}V_{\mathrm{dc}}$ with the same frequency Ω than the AC voltage. Thus, the electrostatic actuation has the benefits of providing control on the static deflection ξ_0 and inducing oscillations of the membrane. The descriptions given below follows the work of P. Weber *et al.* [168], inspired by references [169, 2].

Electrostatic pressure and static deflection

When a gate bias V_{g} is applied on a sample, an electrostatic pressure $p(\boldsymbol{r})$ acts on the membrane and dictates the shape of the deflection $\xi(\boldsymbol{r}, t)$ via the equilibrium condition[1] [168, 2]

$$\rho\frac{\partial^2\xi}{\partial t^2} = \sigma\nabla^2\xi + p(\boldsymbol{r}) \tag{4.32}$$

where ρ is the mass density of the membrane and σ its tensile stress. The pressure $p(\boldsymbol{r})$ can be deduced from $F_{\mathrm{e}} = \int p(\boldsymbol{r})\mathrm{d}^2\boldsymbol{r} = -(\partial U_{\mathrm{e}}/\partial z)$ with U_{e} the capacitive energy. Following the sketch of the sample figure 4.1a, the capacitance C_{eq} is the one of two capacitors in series

[1] This equation is the same as equation (4.20) for the case of a membrane ($\kappa \ll \sigma$) and with an additional external pressure $p(\boldsymbol{r})$.

$C_{\mathrm{eq}}^{-1} = C_{\mathrm{vac}}^{-1} + C_{\mathrm{SiO_2}}^{-1}$ that gives

$$C_{\mathrm{eq}}(\xi) = \frac{\epsilon_0}{d_{\mathrm{eq}} - \xi} \tag{4.33}$$

where we define $d_{\mathrm{eq}} = d + d_{\mathrm{b}}/\epsilon_{\mathrm{SiO_2}}$. The capacitive energy thus writes as an integral over the surface

$$U_{\mathrm{e}} = \frac{\epsilon_0 (V_{\mathrm{g}} - V_0)^2}{2} \int \frac{1}{d_{\mathrm{eq}} - \xi} \mathrm{d}^2\boldsymbol{r} \tag{4.34}$$

where V_0 stands for the neutrality point of the membrane.

For $\xi \ll d_{\mathrm{eq}}$ the integrand can be expanded as a series in powers of ξ/d_{eq}

$$U_{\mathrm{e}} = \frac{\epsilon_0 (V_{\mathrm{g}} - V_0)^2}{2} \int \sum_{n=0}^{\infty} \frac{\xi^n}{d_{\mathrm{eq}}^{n+1}} \mathrm{d}^2\boldsymbol{r}. \tag{4.35}$$

The electrostatic force F_{e} is then obtained by a differentiation of equation (4.35)

$$F_{\mathrm{e}} = -\frac{\partial U_{\mathrm{e}}}{\partial z} = \frac{\epsilon_0 (V_{\mathrm{g}} - V_0)^2}{2} \int \frac{1}{d_{\mathrm{eq}}^2} \sum_{n=0}^{\infty} (n+1) \left(\frac{\xi}{d_{\mathrm{eq}}}\right)^n \mathrm{d}^2\boldsymbol{r} \tag{4.36}$$

from which we deduce the electrostatic pressure to first order in ξ/d_{eq}

$$p(\boldsymbol{r}) \approx \frac{\epsilon_0 (V_{\mathrm{g}} - V_0)^2}{2 d_{\mathrm{eq}}^2} \left(1 + \frac{2\xi}{d_{\mathrm{eq}}}\right). \tag{4.37}$$

We now restrict ourselves to the static case and assume radial symmetry with respect to the center of the drum, such that (4.32) becomes to the lowest order in $2\xi_0/d_{\mathrm{eq}} \ll 1$

$$\frac{\sigma}{r} \frac{\partial}{\partial r} \left(r \frac{\partial \xi_0}{\partial r}\right) = -\frac{\epsilon_0 (V_{\mathrm{dc}} - V_0)^2}{2 d_{\mathrm{eq}}^2}. \tag{4.38}$$

This equation can be integrated by considering as boundary conditions that $\xi_0(R) = 0$ as no deflection can occur outside of the drum and $(\partial \xi_0/\partial r)(r = 0) = 0$ as the maximum deflection is reached at the center of the drum giving a flat profile at this specific point. The integration then yields a parabolic profile

$$\xi_0(r) = \xi_0(0) \left(1 - \frac{r^2}{R^2}\right) \tag{4.39}$$

with a maximal deflection at the center of the drum

$$\xi_0(0) = \frac{\epsilon_0 R^2 (V_{\mathrm{dc}} - V_0)^2}{8 \sigma d_{\mathrm{eq}}^2}. \tag{4.40}$$

Tuning of the resonance frequency

Considering equation (4.6), we can project the equilibrium condition of equation (4.32) on a specific mode $w(\boldsymbol{r},t)$ to obtain a modified version of (4.20)

$$\rho\frac{\partial^2}{\partial t^2}w(\boldsymbol{r},t) = \sigma\nabla^2 w(\boldsymbol{r},t) + \delta p(\boldsymbol{r},t) \tag{4.41}$$

where $\delta p(\boldsymbol{r},t)$ is the oscillating electrostatic pressure. From equation (4.37) and assuming $V_{\mathrm{ac}} \ll V_{\mathrm{dc}}$ we get

$$\delta p(\boldsymbol{r},t) \approx \frac{\epsilon_0(V_{\mathrm{dc}}-V_0)^2}{d_{\mathrm{eq}}^3}w(\boldsymbol{r},t) \tag{4.42}$$

that acts as an additional spring constant. Because of electrostatic elongation of the membrane, we have here an additional tension σ_{e} to the built-in tension σ_0 such that [170]

$$\sigma = \sigma_0 + \sigma_{\mathrm{e}}(V_{\mathrm{g}}) \tag{4.43}$$

where $\sigma_{\mathrm{e}}(V_{\mathrm{g}})$ is a non-trivial function of V_{g} and σ_0. For large V_{dc} when $\sigma_0 \ll \sigma_{\mathrm{e}}$, the gate dependence of the electrostatic tension follows $\sigma_{\mathrm{e}}(V_{\mathrm{g}}) \sim V_{\mathrm{dc}}^{4/3}$ [170].

By taking solutions of the form $w(\boldsymbol{r},t) \sim u(\boldsymbol{r})e^{i\Omega t}$ we recall similar solutions than in section 4.1.2 with mode profiles $u_{mn}(\boldsymbol{r})$ given by equation (4.21) and shifted eigenfrequencies [168, 171]

$$\Omega_{mn} = \sqrt{\frac{\alpha_{mn}}{\rho R^2}(\sigma_0 + \sigma_{\mathrm{e}}(V_{\mathrm{dc}})) - \frac{\epsilon_0}{\rho d_{\mathrm{eq}}^3}(V_{\mathrm{dc}}-V_0)^2}. \tag{4.44}$$

The behavior of the resonance frequency is then the result of a competition between the built-in tension σ_0 and the electrostatic tension σ_{e}:

- when $\sigma_0 \gg \sigma_{\mathrm{e}}$, the electrostatic pressure δp induces a *capacitive softening* that reduces the resonance frequency as V_{dc} increases.
- For $\sigma_0 \ll \sigma_{\mathrm{e}}$, that is always true for strong enough V_{dc}, the electrostatic tension overcomes the capacitive softening induced by the electrostatic pressure and leads to *capacitive hardening* that increases the resonance frequency as V_{dc} increases.

Since $\sigma_{\mathrm{e}}(V_{\mathrm{dc}}=0)=0$ at low bias the resonance frequency is dictated by the buit in tensile stress σ_0 and the variation of the resonance frequency can be fitted using equation (4.44) by setting $\sigma_{\mathrm{e}} = 0$ to determine both the neutrality point V_0 and the built-in stress σ_0. Furthermore, σ_0 also determines the overall shape of the curve by defining the size of the capacitive softening regime. For membranes with small built-in tension, this regime may be nonexistent or almost nonexistent, leading to a U-shaped curve as presented by the red curve in figure 4.7. Alternatively, for membranes with non negligible built-in tension, a W-shaped curve is observed as shown by the blue curve in figure 4.7.

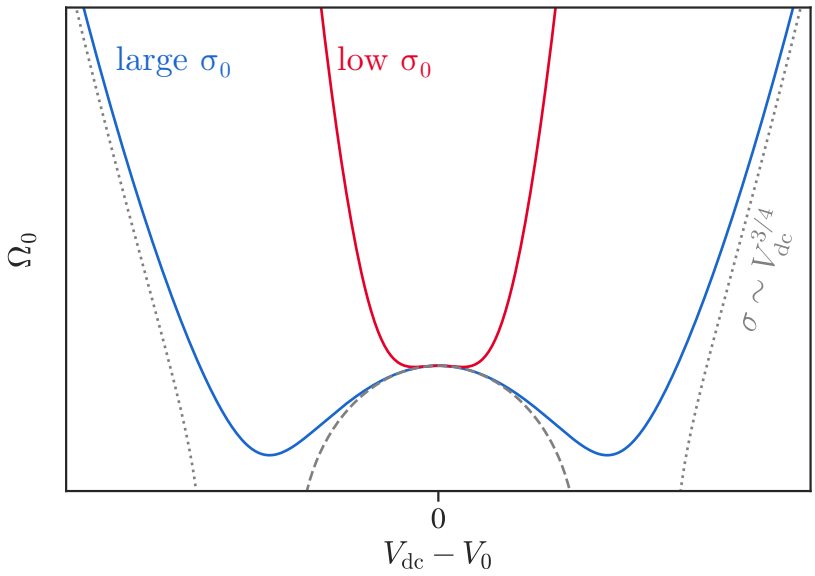

Figure 4.7: Electrostatic tuning of the resonance frequency. The blue and red curves give the variation of the resonance frequency $\Omega_0/2\pi$ with respect to the gate bias, for a membrane with non negligible built-in tension (blue) and negligible built-in tension (red). The grey dashed line gives the contribution from capacitive softening following equation (4.44) with $\sigma_e = 0$. The grey dotted lines are asymptotes for $\sigma_0 = 0$.

Transfer function and cut-off

When using electrostatic actuation one of the main parameters to consider is the efficiency of the electric gate, as it directly affects the amplitude of the actuation force. Even when disregarding potential losses of efficiency due to contact resistance [172] it is worth discussing the transfer function of the sample, acting as an RC low-pass filter [173].

Let us approximate the sample geometry by considering a rectangular flake of width L as the top electrode of a plane capacitor with a dielectric layer of thickness $d_{\rm eq}$. At a distance r from the electrode, its capacitance is $C(r) = Lr\epsilon_0/d_{\rm eq}$ and the resistance of the flake is $R = \varrho_{\rm s} r/L$, $\varrho_{\rm s}$ being the sheet resistance of the used material. The cut-off frequency of such a capacitor is then

$$\Omega_{\rm RC} = \frac{1}{RC} = \frac{d_{\rm eq}}{\varrho_{\rm s}\epsilon_0 r^2} \tag{4.45}$$

that scales as $1/r^2$. Thus, the further away the nanodrum is placed from the electrode, the more important the low pass filtering will be. Inserting equation (4.45) in the definition of the transfer function $\mathcal{T}(r) = [1 + (\Omega/\Omega_{\rm RC})^2]^{-1/2}$ allows to rewrite it as

$$\mathcal{T}(r) = \frac{1}{\sqrt{1 + (r/\Lambda)^4}} \tag{4.46}$$

where

$$\Lambda = \sqrt{\frac{d_{\rm eq}}{\varrho_{\rm s}\epsilon_0\Omega}} \tag{4.47}$$

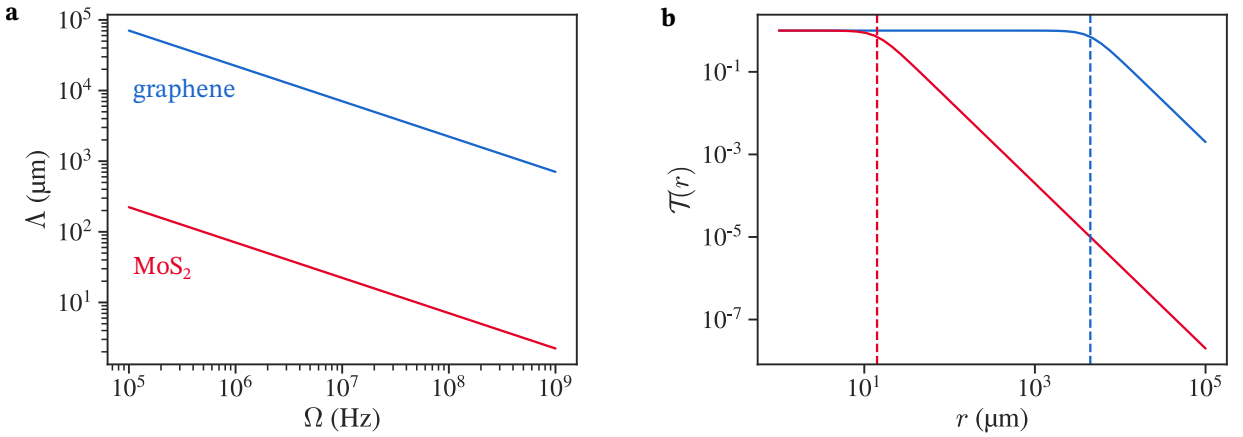

Figure 4.8: Distance dependent transfer function. a. Variation of the characteristic length Λ as a function of the actuation frequency $\Omega/2\pi$ following equation (4.47) for graphene (in blue) and MoS_2 (in red). **b.** Transfer function of the capacitor as a function of the distance from the electrode r, for graphene (in blue) and MoS_2 (in red). The frequency is $\Omega/2\pi = 25$ MHz. Vertical dashed lines gives the values of Λ associated to the different cases.

is a characteristic length acting as a skin depth and quantifying the range of the electrostatic gating. Equation (4.47) is plotted as a function of the frequency $\Omega/2\pi$ for graphene (in blue) and MoS_2 (in red) assuming approximated sheet resistances $\varrho_s \approx 10^2\ \Omega/\square$ for graphene [174] and $\varrho_s \approx 10^7\ \Omega/\square$ for MoS_2 [175]. Figure 4.8b shows the transfer function with respect to the distance to the electrode with the same parameters, for $\Omega = 25$ MHz that is typically in the range of operation of our samples. This specific example yields $\Lambda(25\text{ MHz}) \approx 4.5$ mm for graphene and $\Lambda(25\text{ MHz}) \approx 14$ µm for MoS_2. Considering the scale of our samples, we can conclude that this effect is irrelevant for graphene flakes, but of most importance in TMD ones.

This effect has to be kept in mind during the fabrication process, as nanodrums made with materials with a higher resistivity needs to be in the close vicinity of the electrode to be actuated efficiently. An other option is to use graphene at the bottom of the heterostructure to ensure the efficiency of the electrostatic actuation. In this work, all the presented contacted samples are based on graphene/TMD heterostructures where graphene ensures the electric contact with the gold pad. As such, the substrate design of the different samples presented in this chapter leaves a 10 µm space between the gold pad and the closest hole to it. Such substrates are meant to be used with the hybrid transfer technique discussed in appendix A even thought the closest holes from the electrodes might be usable for a TMD only resonator. However, different substrate designs (as the one represented in figure A.2) were also developed with smaller hole to pad distances in order to be used in samples involving nonconducting materials only.

4.2.3 Displacement calibration

We mentioned in section 4.2.1 that in order to translate the signal detected by our APD (in V) in a real oscillation amplitude (in nm), we need a way to determine the transduction parameter β. We will here advertise two different methods that can be used to achieve the calibration of the mechanical displacement of the sample. Both of them show different pros and cons and might be used jointly or independently depending on the experimental conditions or the precise sample configuration.

Thermal noise

The first calibration method uses the Brownian motion of the membrane that has a determined amplitude at a given temperature T. In the absence of external actuation forces, thermal fluctuations initiate a motion of the membrane. The thermal force F_{th} can be modelled as a Langevin force [1]. By definition, F_{th} respects the two following conditions [176]:

- the time-averaged amplitude of the force cancels out $\langle F_{\mathrm{th}}(t)\rangle = 0$,
- the autocorrelation function of the thermal force is the one for Brownian motion

$$g_{FF}(\tau) = \langle F_{\mathrm{th}}(t)F_{\mathrm{th}}(t+\tau)\rangle = 4m\gamma k_{\mathrm{B}}T\delta(\tau). \tag{4.48}$$

To understand how the thermal force F_{th} can actuate the resonant motion of the system and how to describe its corresponding spectrum as observed on a spectrum analyser, we follow the work of B. D. Hauer *et al.* [177]. The measurable quantity is the one sided power spectral density (PSD) of the membrane motion, defined as

$$S_{zz}[\Omega] = \int_0^\infty g_{zz}(\tau)e^{i\Omega\tau}\mathrm{d}\tau. \tag{4.49}$$

From this definition, the relation between the mean square amplitude of the motion $\langle z^2(t)\rangle$ and the PSD S_{zz} is obtained by noting that for a sufficiently long time window $T_0 \gg 2\pi/\Omega_0$

$$\langle z^2(t)\rangle = g_{zz}(0) = \frac{1}{2\pi}\int_0^\infty S_{zz}[\Omega]\mathrm{d}\Omega. \tag{4.50}$$

Thanks to this result, we can rewrite equation (4.8) in terms of the position and force PSDs

$$S_{zz}[\Omega] = |\chi_{\mathrm{m}}[\Omega]|^2 S_{FF}[\Omega] \tag{4.51}$$

with $S_{FF}[\Omega]$ being the PSD of the thermal force F_{th}. For Brownian motion this is a constant white noise $S_{FF}[\Omega] = S_{FF}^{\mathrm{th}}$, thus by applying an inverse Fourier transform on equation (4.51) and using equation (4.50) we get

$$\langle z^2(t)\rangle = \frac{S_{FF}^{\mathrm{th}}}{2\pi}\int_0^\infty \mathrm{d}\Omega|\chi_{\mathrm{m}}[\Omega]|^2 = \frac{QS_{FF}^{\mathrm{th}}}{4m^2\Omega_0^3} \tag{4.52}$$

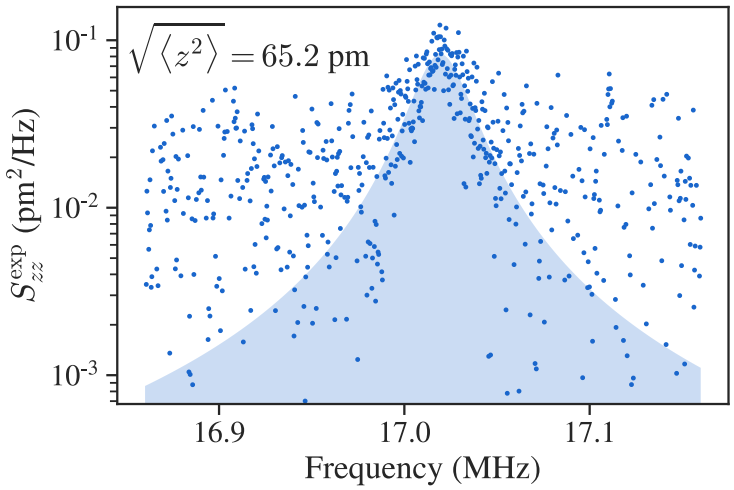

Figure 4.9: Thermal noise of a graphene/$MoSe_2$ sample. Blue dots are the experimentally measured power spectral density of the membrane displacement. The black line gives a lorentzian fit, and the colored blue area gives the square root of the time-averaged square displacement.

where we used the expression of $\chi_{\mathrm{m}}[\Omega]$ from equation (4.9). The mean square displacement $\langle z^2(t) \rangle$ is also related to the thermal energy of the system U via the equipartition theorem

$$\langle U \rangle = \frac{1}{2} m \Omega_0^2 \langle z^2(t) \rangle = \frac{1}{2} k_{\mathrm{B}} T. \tag{4.53}$$

Combining equations (4.52) and (4.53) gives an expression for the thermal white noise

$$S_{FF}^{\mathrm{th}} = \frac{4 m k_{\mathrm{B}} T \Omega_0}{Q} \tag{4.54}$$

and leads to the PSD of the motion amplitude that is peaked around the resonance frequency

$$S_{zz}[\Omega] = \frac{4 k_{\mathrm{B}} T \Omega_0}{m Q [(\Omega_0^2 - \Omega^2)^2 + (\Omega \Omega_0 / Q)^2]}. \tag{4.55}$$

Assuming that all the other sources of noise are white noises giving a constant background noise S_{VV}^{w}, the measured PSD at a given frequency f is written as

$$S_{VV}[f] = S_{VV}^{\mathrm{w}} + \eta S_{zz}[f] \tag{4.56}$$

where η is a transduction factor relating the theoretical displacement PSD S_{zz} to the measured one S_{VV}. In practice the PSD that is measured experimentally is $S_{VV}^{\mathrm{exp}} = V^2[f]/\Delta f$ with $V[f]$ the voltage spectrum and Δf the resolution bandwidth. This experimental data can be fitted using equation (4.56) to determine f_0, Q, S_{VV}^{w} and η. Once η is known, the displacement spectrum can be obtained and is given by $\sqrt{S_{zz}^{\mathrm{exp}}}$ in units of m/$\sqrt{\mathrm{Hz}}$. From equation (4.30) we can see that the link between the transduction factor η and the one introduced previously β is straightforward and gives $\eta = (\beta P_{\mathrm{L}})^2$ [178]. It is nonetheless important to remind here that those transduction coefficients are obviously valid only for a given device, as the thermal noise is usually measured on a spectrum analyser contrary

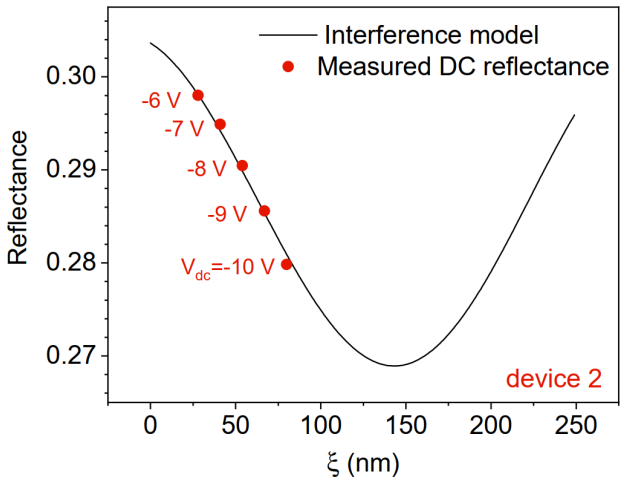

Figure 4.10: DC reflectance and interference model calibration. Matching of the DC reflectance of a graphene sample with the reflectivity calculated from an interference model. Taken from [39].

to the actuated mechanical response, measured with a lock-in amplifier or a vector network analyser. A link can be done to calibrate a different device using the thermal noise measured on a spectrum analyser by acquiring the same response at very low actuation on both devices at the same time [39].

Figure 4.9 shows the PSD of the displacement S_{zz}^{exp} for the graphene/$MoSe_2$ sample presented in chapter 4 obtained after fitting the voltage PSD S_{VV}^{exp} with equation (4.56). The temperature is $T = 100$ K, the laser power $P_{\text{L}} = 10$ µW and the DC voltage is $V_{\text{dc}} = -5$ V. The total mass of the drum is estimated as $m_{\text{tot}} = \pi R^2(\rho_{\text{Gr}} + \rho_{\text{MoSe}_2})$ where we take the sheet mass density of pristine graphene $\rho_{\text{Gr}} = 7.5 \times 10^{-7}$ kg.m^{-2} [39] and pristine $MoSe_2$ $\rho_{\text{MoSe}_2} = 4.6 \times 10^{-6}$ kg.m^{-2} [164], ignoring potential contamination from polymer residues due to the transfer process of $MoSe_2$. We then obtain an effective mass $m = 2.84 \times 10^{-17}$ kg for the fundamental mode. We thus determine a time-averaged RMS displacement $\sqrt{\langle z^2 \rangle} = 65.2$ pm from the equipartition theorem of equation (4.53).

However, while figure 4.9 demonstrates that this method can be used to calibrate the mechanical oscillations of 2D-NEMS for $T = 100$ K, measuring the thermal noise at cryogenic temperatures ($T = 4$ K) necessitates to amplify the Brownian motion [164, 179]. For this reason, we decided to use a different approach in this work, based on the knowledge of the interference pattern arising in our sample.

Interferometric calibration

Thanks to the ability to electrostatically tune the equilibrium position ξ_0 by applying a DC bias V_{dc}, the calibration of the membrane deflection can be done using the modelled interference pattern. Since the detected signal is directly related to the reflected intensity the correspondence can be done by rescaling the variation of the DC reflectance $\mathcal{R}_{\text{dc}}$ measured as a function of V_{dc} to match the shape of the interference pattern. In practice, the precise rescaling is not trivial and might be determined in a phenomenological way. This leads to

a determination of $\xi_0(V_{dc})$ that allows to obtain the experimental $\mathcal{R}_{dc}(\xi)$ curve, from which the slope at a given point ξ_0 is $P_L\beta$. Figure 4.10 presents such a calibration process for a graphene sample with $d_{tot} = 285$ nm and $d = 250$ nm [39].

This is the method that we apply in this work to calibrate the deflection of the suspended graphene/$MoSe_2$ and suspended graphene drums of device 1 in section 4.3. The detail of the phenomenological correspondance between the measured reflectance and the modelled one used in this case is detailed in section 4.3.2.

One of the advantages of this technique with respect to the one based on the thermal motion of the membrane is its ability to determine both the equilibrium position of the membrane ξ_0 at a given value of V_{dc} and the corresponding transduction coefficient, independently of the experimental conditions. Furthermore, the modelled interference pattern can also be used to determine the exaltation factor of the different spectroscopic features of the sample, that can then be used as a sanity check of the determined calibration.

However in order to properly model the interferences in the sample the exact geometry must be known, which can be difficult when non-monolayer flakes are involved.

4.3 Electromechanical tuning of the interlayer coupling in graphene/$MoSe_2$

In the previous chapter, we demonstrated that the optical phonons in monolayer graphene are affected differently by dielectric screening depending on their respective symmetries. This result offers the opportunity to probe variations of interlayer coupling in graphene/TMD heterostructures by a combined analysis of the G and 2D modes, where the G-mode is used to determine strain and/or doping contributions to the Raman response and isolate a change of the dielectric screening induced blueshift of the 2D-mode, signature of a modified coupling between the two layers.

We propose to apply this procedure in this section on a graphene/$MoSe_2$ nanodrum actuated electrostatically.

4.3.1 Sample characterization

Figure 4.11a shows an optical image of the studied sample (denoted device 1), formed by a graphene/$MoSe_2$ heterobilayer suspended over a 420 nm deep hole with a diameter of 5 µm. A mapping of the integrated PL intensity is shown in figure 4.11b together with typical PL spectra in figure 4.11c for SiO_2-supported $MoSe_2$ (blue), SiO_2-supported graphene/$MoSe_2$ (green) and suspended graphene/$MoSe_2$ (red). The strong PL quenching of a factor ~ 10 between SiO_2-supported $MoSe_2$ and graphene/$MoSe_2$ highlights the good coupling between the two layers [99]. As expected, a filtering of the PL spectrum is seen in both graphene/$MoSe_2$ parts of the sample, with negligible trion light emission with respect to the neutral exciton contribution (see section 1.3.2) [180]. In the three areas, the exciton PL feature presents a FWHM ~ 8 meV. The visible variation in the excitonic energies between the SiO_2-supported

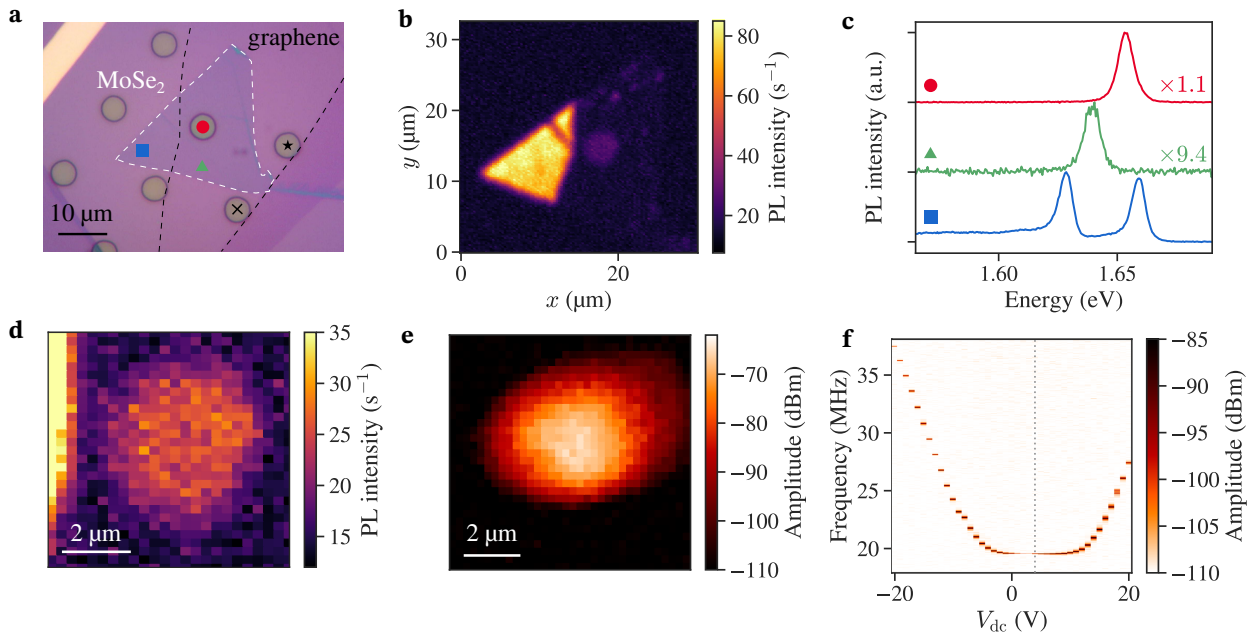

Figure 4.11: A graphene/$MoSe_2$ nanodrum. The used laser wavelength is 633 nm for both PL mapping and mechanical measurements. **a.** Optical image of the sample. Holes are 5 µm large in diameter. The markers define the spots of the spectra presented in **c**: Blue square for SiO_2-supported $MoSe_2$, green triangle for SiO_2-supported graphene/$MoSe_2$ and red circle for suspended graphene/$MoSe_2$. The black cross and star refer to two suspended graphene drums. **b.** Integrated PL intensity map. **c.** Example spectra for the three types of structures: SiO_2-supported $MoSe_2$ (blue), SiO_2-supported graphene/$MoSe_2$ (green) and suspended graphene/$MoSe_2$ (red). **d.** Zoom of the integrated PL intensity map on the suspended graphene/$MoSe_2$ part of the sample. **e.** Measured profile of the fundamental mechanical mode of the sample. Actuation is done electrostatically with $V_{dc} = 0$ V and $V_{ac} = 1$ mV. **f.** Variation of the mechanical response of the sample with respect to V_{dc}, for a AC bias $V_{ac} = 1$ mV. The grey dotted line indicates $V_0 = 4$ V. The laser power is 2 µW in b,c,d and 10 µW in e,f.

$MoSe_2$, suspended graphene/$MoSe_2$ and SiO_2-supported graphene/$MoSe_2$ (see figure 4.11c) can be assigned to changes in the dielectric environment and gives an additional demonstration of the quality of the coupling between the graphene and $MoSe_2$ monolayers [93].

Importantly, the PL is homogeneous over the suspended graphene/$MoSe_2$ membrane, with an increased exciton intensity compared to its SiO_2-supported counterpart thanks to constructive interferences in the cavity-like system (see section 4.2.1) that agrees with the expected enhancement factor around the exciton wavelength $\mathcal{F}(\lambda_X)$ for a well suspended heterostructure. The spatial homogeneity of the PL intensity over the nanodrum membrane suggests a flat membrane with no ripples and minimal contamination as no "bubble" with uncommon spectral signatures is visible.

A characterization of the mechanical response in the linear regime ($V_{ac} = 1$ mV) is shown figure 4.11e,f presenting respectively a mapping of the fundamental mode amplitude and the variation of the mechanical response with respect to V_{dc}. The fundamental mode frequency f_0 is highly tunable and follows a U-shaped behavior when the gate bias is varied, sign of an extremely reduced built-in stress σ_0 in the vibrating membrane (see section 4.2.2). From

the variation of f_0 with V_{dc}, we can get an estimation of the neutrality point V_0 that defines the symmetry axis of the U-shaped curve. In our case, we find $V_0 = 4$ V.

In addition to the suspended graphene/$MoSe_2$ drum that will focus most of our interest, two suspended graphene drums are identified by the black cross and star in figure 4.11a. Both of these drums are also connected and can be actuated electrostatically. Their Raman response will be compared with the one of the suspended graphene/$MoSe_2$ drum when we discuss potential doping contributions to our results.

4.3.2 Probing changes in interlayer coupling through Raman spectroscopy

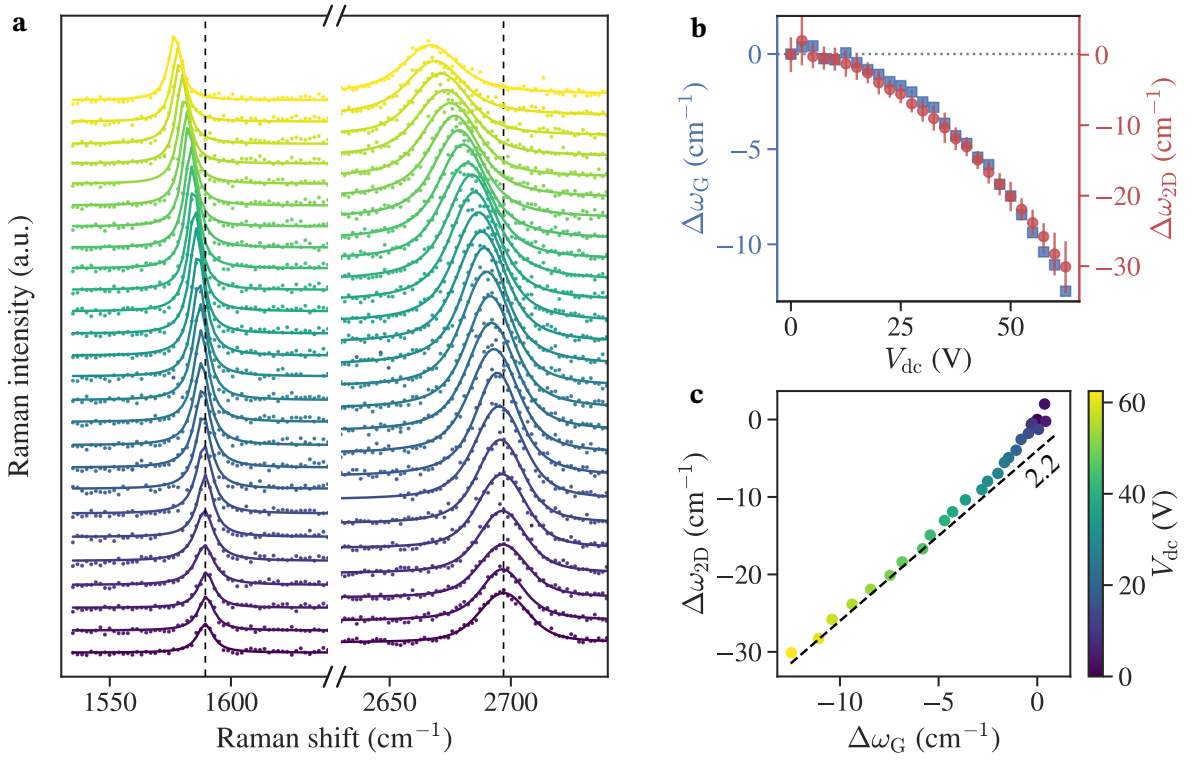

Figure 4.12: Gate dependent Raman spectroscopy of suspended graphene/$MoSe_2$. a. Gate dependent Raman spectra of graphene centered on the G and 2D modes of graphene. The colorscale is the same one as in **c**. **b.** Variation of the G-mode (blue) and 2D-mode (red) frequencies with respect to V_{dc}. **c.** G and 2D-mode frequency correlation. The slope of 2.2 corresponds to the one expected for strains.

To investigate potential changes in the interlayer coupling, we propose an application of the results presented in chapter 3. By electrostatically pulling on the suspended graphene/$MoSe_2$ heterostructure, we may expect to induce a very small change of the van der Waals gap as a consequence of the fact that the graphene layer is at the bottom of the heterostructure and may be more affected than the top TMD layer by the electrostatic force created by the backgate. Such a small change in the interlayer distance should translate as a reduction of the screening induced upshift of the 2D-mode frequency. As the G-mode frequency is not affected by screening, it can be used to determine contributions from strain or doping in the

Raman response in order to isolate a potential change of the 2D-mode frequency due to a decrease of the dielectric screening effect.

The Raman spectrum of graphene is measured at various V_{dc} using a laser wavelength of 532 nm at a fixed power of ~ 350 µW. The DC bias is provided by a Rohde & Schwartz NGP824 power supply. It is varied slowly (~ 25 mV/s) from $V_{dc} = 0$ V to $V_{dc} = 62.5$ V with 2.5 V steps between each measured spectrum. Figure 4.12a shows the measured Raman spectra at varying V_{dc}. Each spectrum is fitted using a Lorentzian profile for the G-mode and a Voigt profile for the 2D-mode. Figure 4.12b gives the variation of the G and 2D-mode frequencies, with a reference point taken at $V_{dc} = 0$ V. For both modes, a strong phonon softening is observed as V_{dc} is increased. From the $\Delta\omega_{2D} - \Delta\omega_G$ correlation presented figure 4.12c we deduce that this phonon softening is dominated at high bias by a progressive increase of tensile strain in the graphene layer, as the correlation qualitatively follows the 2.2 slope expected for strain (see section 1.1.3) [37]. At lower bias, the data seem to follow a slope that is higher than the 2.2 one expected for tensile strain. It is there that our discussion is focused and we will now test our hypothesis and investigate on a potential change in the dielectric environment of the graphene layer.

Calibration of static deflection

The DC reflectance $\mathcal{R}_{dc}$ of the sample is measured simultaneously to each Raman spectrum to ensure point to point coincidence between the two parameters. The variation of $\mathcal{R}_{dc}$ directly follows from the optical interferences in the sample and can be used to calibrate the membrane deflection as explained in section 4.2.3. Results of such a calibration process are shown figure 4.13, where the data points present the $\mathcal{R}_{dc}$ values renormalized to match the calculated reflectance $\mathcal{R}$ variation with the deflection ξ for a 532 nm laser wavelength. In practice, we first rescale the measured voltage V_{APD} to the total amplitude of the calculated ξ-dependent reflectivity $\mathcal{R}_{theory}$ and obtain $\bar{V}_{APD}$. Then, an additional scaling is used to match the experimental reflectivity $\mathcal{R}_{exp}$ with $\mathcal{R}_{theory}$. Since we know that $V_{APD} \propto \mathcal{R}$, we use a linear scaling $\mathcal{R}_{exp} = A\bar{V}_{APD} + B$. The intermediate scaling is not necessary but makes it easier to graphically match the theoretical and experimental curves.

On the x-axis (that links the gate bias V_{dc} to the deflection ξ), the theory suggests that the scaling should follow a $\xi \sim V_{dc}^2$ dependency (see equation (4.40)). However, it is impossible to obtain a matching of the theoretical and experimental curves with a purely quadratic scaling. We believe that this is a consequence of the breaking of the $2\xi_0/d_{eq} \ll 1$ condition. We thus decided to consider a more general scaling function by considering $\xi(V_{dc})$ as a polynomial function of order N

$$\xi(V_{dc}) = \sum_{n=0}^{N} a_n V_{dc}^n. \tag{4.57}$$

After multiple testing, a phenomenological agreement between the experimental $\mathcal{R}_{exp}$ and theoretical $\mathcal{R}_{theory}$ curves is reached for $N = 2$ with $a_2 = 10^{-3}$ nm.V^{-2}, $a_1 = 2.2$ nm.V^{-1} and $a_0 = 35$ nm.

However, it is important to note that such calibration is purely based on the graphical matching of the measured laser reflectance, giving $\mathcal{R}_{exp}$ and the calculated reflectivity $\mathcal{R}_{theory}$.

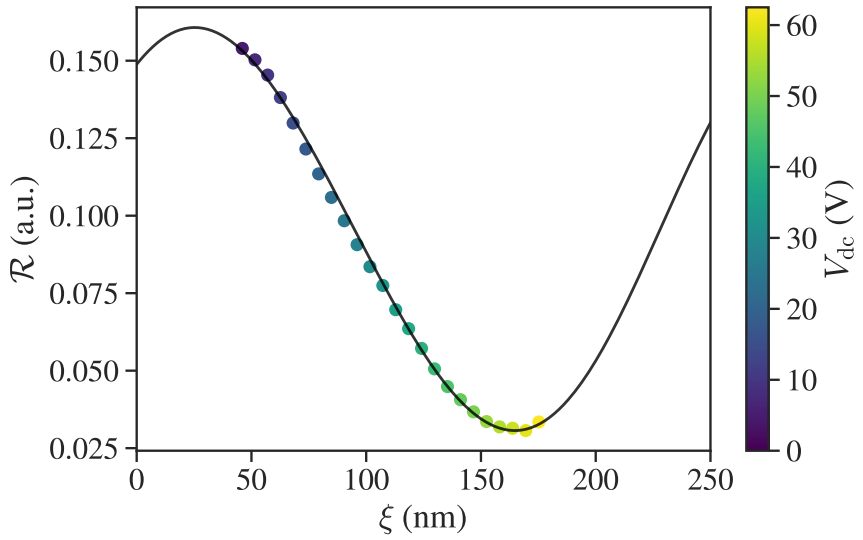

Figure 4.13: Calibration of the membrane deflection. Reflectance variation depending on the membrane deflection ξ for $\lambda = 532$ nm. The continuous line represents the calculated variation of the reflectance and markers represents the measured DC reflectance scaled to match the shape of the theoretical curve.

As it is based on the conservation of the general shape of the data, it is mandatory to have clear reference points in order to be consistent. In the present case, the calibration is possible thanks to the large range of ξ that is explored, approching two extrema of the reflectivity that have a clear and visible effect in the measured data. Note that in order to avoid any artifact in the process, experimental points corresponding to gate voltage values $V_{dc} < V_0$ are ignored.

Estimating doping in comparison with suspended graphene

As visible in figure 4.11a, the sample is also composed of two suspended graphene drums and comparing their behavior with our observations on suspended graphene/$MoSe_2$ can give us a better understanding of the underlying physics. We thus performed similar experiments as we did on the graphene/$MoSe_2$ drum on both suspended graphene drums. The gate dependent G and 2D modes frequencies of one of the graphene drums are shown figure 4.14. Analysis of the second graphene drum gives similar behaviors. Figure 4.15a shows the result of the calibration of $\xi(V_{dc})$ using equation (4.57). Matching of the scaled experimentally measured $\mathcal{R}_{dc}$ and the modeled variation of the reflectance $\mathcal{R}(\xi)$ is reached for $a_2 = 6 \times 10^{-3}$ nm.V^{-2}, $a_1 = 2.2$ nm.V^{-1} and $a_0 = 25$ nm. The ω_G - ω_{2D} correlation (see figure 4.15b) seems to change with the gate bias V_{dc}, roughly following the doping slopes (between 0.2-0.5) at low V_{dc} to gradually reach the strain correlation slope (around 2.2) at higher voltages. These observations suggest that doping cannot be neglected for graphene drums and is dominating the behavior of the Raman modes at low or moderate gate bias.

A clear reduction of the G-mode linewidth is observed (blue markers in figure 4.15c), reaching over 50% of reduction at higher voltage. Interestingly, the diminution of Γ_G occurs only after a certain critical value around $V_{dc} \approx 20$ V, suggesting minimal doping from the gate in this

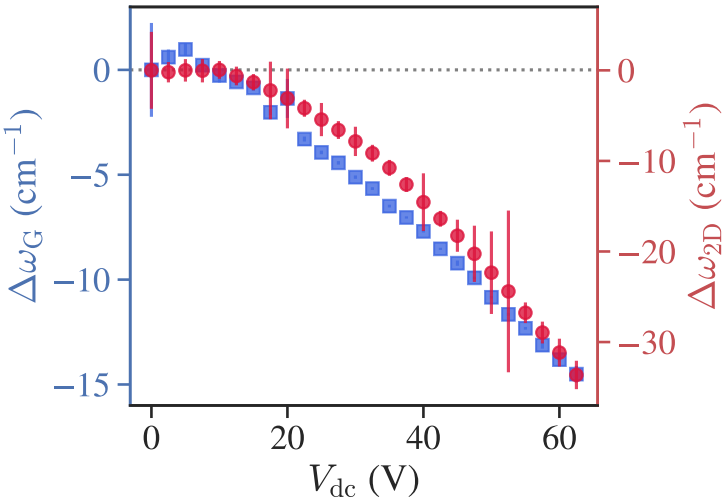

Figure 4.14: Gate dependent G-mode and 2D-mode frequencies in suspended graphene.

regime. Between $V_{dc} \approx 20$ V and $V_{dc} \approx 40$ V, Γ_G reduces continuously to reach a minimal value $\min(\Gamma_G) \approx 7$ cm^{-1} before remaining constant and rises again slightly only at the very highest values of V_{dc}. Such an evolution of Γ_G suggests that in the graphene drum case, the Fermi level of graphene varies between 0 and $|E_F| \approx 100 - 150$ meV in the explored range of V_{dc} [32].

A slight reduction of Γ_G is also observed in the suspended graphene/$MoSe_2$ case, but with considerably reduced amplitude (~ 2 cm^{-1} against ~ 9 cm^{-1} for suspended graphene). This observation together with the high unperturbed G-mode frequency $\omega_{G,0} = \omega_G(V_{dc} = 0) = 1589.4$ cm^{-1} and low initial G-mode width $\Gamma_{G,0} = \Gamma_G(V_{dc} = 0) = 7.9$ cm^{-1} suggest that the doping level of the graphene monolayer in this case is already non negligible at zero gate bias but that its sensitivity to the applied gate bias is strongly reduced. This high "native" doping could take its origin from photoinduced doping of graphene mediated by interlayer charge transfer from the $MoSe_2$ monolayer, as discussed in section 1.3.2 [99]. At room temperature, such process has been reported to be highly efficient under vacuum conditions and reach a saturation point at $|E_F| \approx 300$ meV even for moderate laser power. As our measurements were performed in cryogenic condition, the pressure is about 10^{-5} mbar, a range where our ~ 350 µW laser excitation is largely strong enough to reach the saturation regime.

In order to ensure that the gate induced change in the doping level of graphene is negligible with respect to the photodoping, we can estimate the maximum contribution from the gate as $\Delta n_{max} = C_{eq}(\xi)V_{dc}$, where $C_{eq}(\xi)$ is the deflection dependent capacitance of the sample given by equation (4.33) and compare it with the doping level that one could expect from a saturation of the photodoping. Figure 4.15d shows the result of such an estimation (blue dots). The maximum gate induced doping is expected to reach up to 1.3×10^{12} cm^{-2} when $V_{dc} = 62.5$ V if one assumes a perfect gate, while the doping level of graphene is known to reach 5×10^{12} cm^{-2} when the saturation of the photodoping is achieved (red line) [99]. Thus, we can be confident that the doping level may only be slightly affected by the applied gate in the case of the graphene/$MoSe_2$ drum.

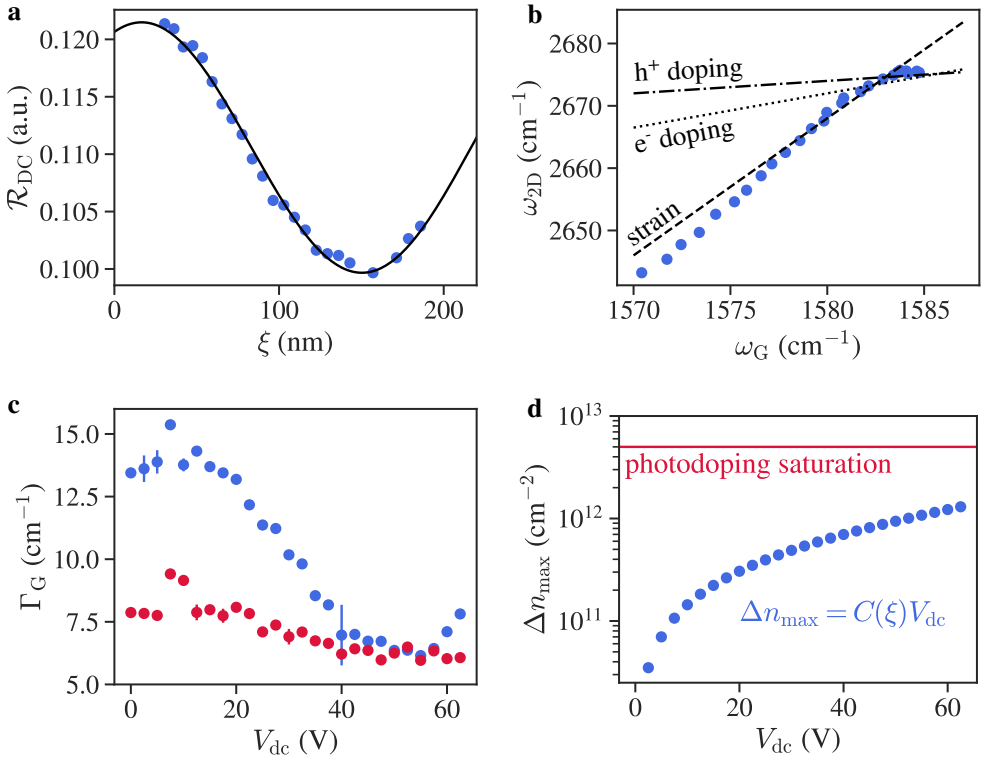

Figure 4.15: Gate dependent Raman spectroscopy of suspended graphene. **a.** Reflectance variation depending on the membrane deflection ξ for $\lambda = 532$ nm. The continuous line represents the calculated variation of the reflectance and markers represent the measured DC reflectance scaled to match the shape of the theoretical curve. **b.** Correlation between the 2D-mode and G-mode frequencies. Straight lines gives the expected correlation slopes for hole doping (dotted line), electron doping (dot-dashed line) and tensile strain (dashed line). **c.** Variation of the G-mode width Γ_G with respect to the gate bias V_{dc} for the suspended graphene drum (blue) and suspended graphene/$MoSe_2$ drum (red). **d.** Estimation of the maximum gate induced carrier density in graphene as a function of the gate bias.

Strain estimation

We then assume that the major contribution to changes of the G-mode frequency ω_G originates from a change of strain in graphene. For a change in biaxial strain $\Delta\varepsilon_s$ this shift in frequency with respect to the unpertubed value $\omega_{G,0}$ is given by

$$\Delta\omega_G = 2\gamma_G\omega_{G,0}\Delta\varepsilon_s \tag{4.58}$$

with the Grüneisen parameter $\gamma_G = 1.8$ [39, 146, 181]. The unperturbed value considered in our case is $\omega_{G,0} = \omega_G(V_{dc} = 0) = 1589.4$ cm^{-1}. The change in strain $\Delta\varepsilon_s$ determined using equation (4.58) is shown figure 4.16 and is in reasonable agreement with a simple estimation of strain variations from changes in the deflection $\Delta\xi$.

The theoretical estimation is obtained by considering the elongation of the membrane induced by a parabolic profile as described by equation (4.39) [182]. The elongation is given

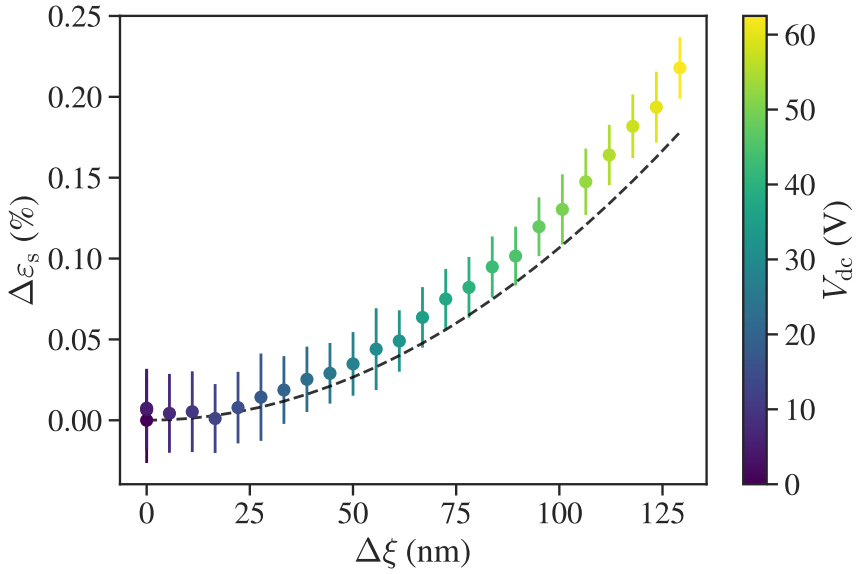

Figure 4.16: Strain estimation. Change of strain in the monolayer graphene with respect to the change in the membrane deflection. Markers are strain values estimated from the measured $\Delta\omega_G$, the dashed line corresponds to strain changes estimated from equation (4.60)

as [39]

$$\Delta L = \int_{-R}^{R} \mathrm{d}r \sqrt{1 + [\partial_r \xi(r)]^2} - 2R. \tag{4.59}$$

For small deflections $\xi \ll R$, it gives the static strain $\varepsilon_s = \Delta L/2R$. Applied to a parabolic profile, we determine the change of strain $\Delta\varepsilon_s$ as

$$\Delta\varepsilon_s = \frac{2}{3}\left(\frac{\Delta\xi}{R}\right)^2 \tag{4.60}$$

and use it to estimate the strain change as shown by the dashed line in figure 4.16.

However, this reasonable agreement is not a perfect agreement. The most probable explanation lies in the fact that equation (4.59) considers an averaged elongation over the whole suspended membrane. Since our laser spot is smaller than the 5 µm hole and focused on the center of the deflected membrane (i.e. at the maximum of deflection), we can reasonably expect to measure higher strain values than theoretically estimated. This explanation also agrees with the increasing missmatch between measured and modeled strain values as $\Delta\xi$ increases.

Estimation of the screening induced 2D-mode shift

From the shift of the G-mode $\Delta\omega_G$ and the estimations of static strain changes $\Delta\varepsilon_s$ we can determine the expected shift of the 2D-mode because of strain as

$$\Delta\omega_{2D}^{(\mathrm{strain})} = 2\gamma_{2D}\omega_{2D,0}\Delta\varepsilon_s \tag{4.61}$$

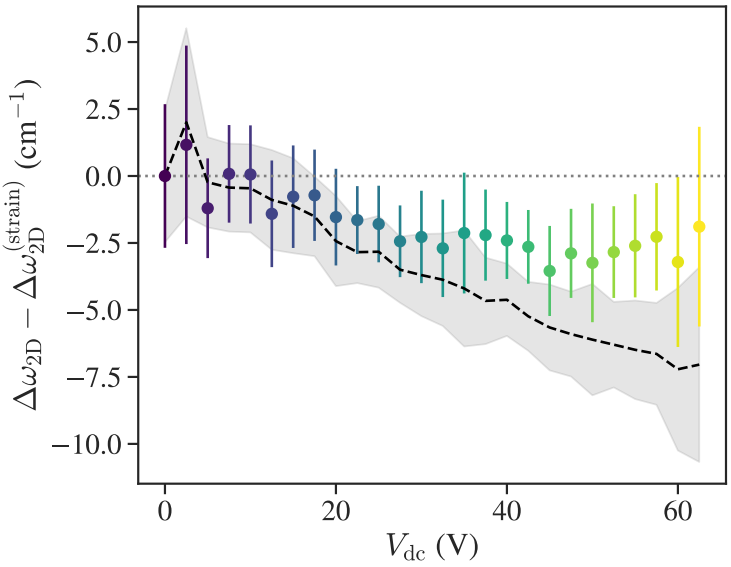

Figure 4.17: Deviation of the 2D-mode frequency from the expected strain behavior. Variation of the 2D-mode frequency shift $\Delta\omega_{2D}$ isolated from the strain contribution $\Delta\omega_{2D}^{(strain)}$ estimated from the G-mode shift $\Delta\omega_G$ (symbols) and from equation (4.60) (dashed line).

with the 2D-mode Grüneisen parameter $\gamma_{2D} = 2.4$ and unperturbed frequency $\omega_{2D,0} = \omega_{2D}(V_{dc} = 0) = 2697$ cm^{-1}. Assuming that the only other source of variation in ω_{2D} is due to dielectric screening, the observed 2D-mode shift is

$$\Delta\omega_{2D} = \Delta\omega_{2D}^{(strain)} + \Delta\omega_{2D}^{(screening)} \tag{4.62}$$

and the shift related to a change of dielectric screening can be isolated by taking the difference $\Delta\omega_{2D} - \Delta\omega_{2D}^{(strain)}$. The remaining 2D-mode shift is shown figure 4.17 where the markers corresponds to results obtained from strain estimations based on $\Delta\omega_G$ while the doted line is using strain estimations from equation (4.60). A small redshift of a few cm^{-1} is observed in both cases that could be assigned to a slight reduction of dielectric screening due to a small increase in the van der Waals gap, as the metallic graphene membrane at the bottom of the heterobilayer is electrostatically pulled more efficiently than the semiconducting $MoSe_2$ on top of it. However, further investigation are necessary as potential contributions from doping were neglected here.

Additional experiments

It is clearly visible from figure 4.17 that the effect that we attempt to observe here is extremely small. In order to be able to properly claim that the observed mismatch of the 2D-mode shift with the strain slope of the $\omega_G - \omega_{2D}$ correlation is really due to a change in the dielectric screening of the graphene layer, we need to ensure that no other contribution of any kind is involved. This implies to perform complementary experiments. We will there list a few of them.

First, the contribution from doping needs to be investigated in more details, by reproducing the same experiment with both gate polarities. Since the graphene/$MoSe_2$ drum is already

doped because of photoinduced doping of the graphene monolayer, we can expect to slightly increase or decrease the doping level of graphene depending on the sign of the applied gate voltage. Furthermore, the saturation of the photoinduced doping of graphene can be precisely probed by a simple power dependant study of the Raman response in the exact same experimental configuration as the work presented in this section and give enough insights to conclude on the role of photodoping [99, 100].

Secondly, our strain estimation would strongly benefit from a proper modeling and mapping of the strain field of the membrane and serve as a smoking gun to test our explanation of the slight mismatch between the strain measured from ω_G and the ones estimated with equation (4.60). This can be done by perfoming an hyperspectral mapping of the Raman response over the suspended area [146, 183] at various values of V_{dc}. A simultaneous mapping of the DC laser reflectance would then allow to directly correlate the local deflection of the membrane and the local strain that is applied on it.

4.4 Strain mediated tuning of light emission in graphene/TMD heterostructures

In this section, we focus on the influence of strain on the PL spectrum of the suspended graphene/$MoSe_2$ heterostructure in device 1. The data presented in this section were acquired in the same conditions as the one in the previous section on the same sample. Our goal here is to achieve a strain mediated tuning of the PL emission of the $MoSe_2$ neutral exciton. To this end, we first focus ourselves on the effect of static strain and attempt to determine the strain sensitivity of the exciton energy. Then, we attempt to use the non-linear mechanical response of the graphene/$MoSe_2$ resonator to dynamically modulate the exciton energy via strain.

4.4.1 Static strain tuning of the graphene/$MoSe_2$ PL spectrum

Strain dependent PL

Figure 4.18a shows a colormap that represents the PL spectrum as a function of the applied DC gate bias V_{dc} measured at the center of the suspended graphene/$MoSe_2$ drum of device 1 (see figure 4.11). The excitation is provided by a 532 nm laser at a fixed power of 10 µW. As expected, the exciton line redshifts progressively with the applied bias and the overall PL intensity diminishes. The behavior is symmetric with respect to the gate polarity and we choose here to focus on the positive side ($V_{dc} \geq 0$) to ensure the continuity with our Raman data from the previous section.

Typical PL spectra at different values of V_{dc} are shown in a semilog scale in figure 4.18b to evidence the fainter details of the spectrum. The shown spectra correspond to V_{dc} values of 0, 16, 32, 48 and 64 V respectively (from darker blue to yellow). Interestingly, we can note a very faint emission from the trion at low V_{dc} that was not present previously (i.e. on the PL map shown figure 4.11). While the main difference in terms of experimental configuration

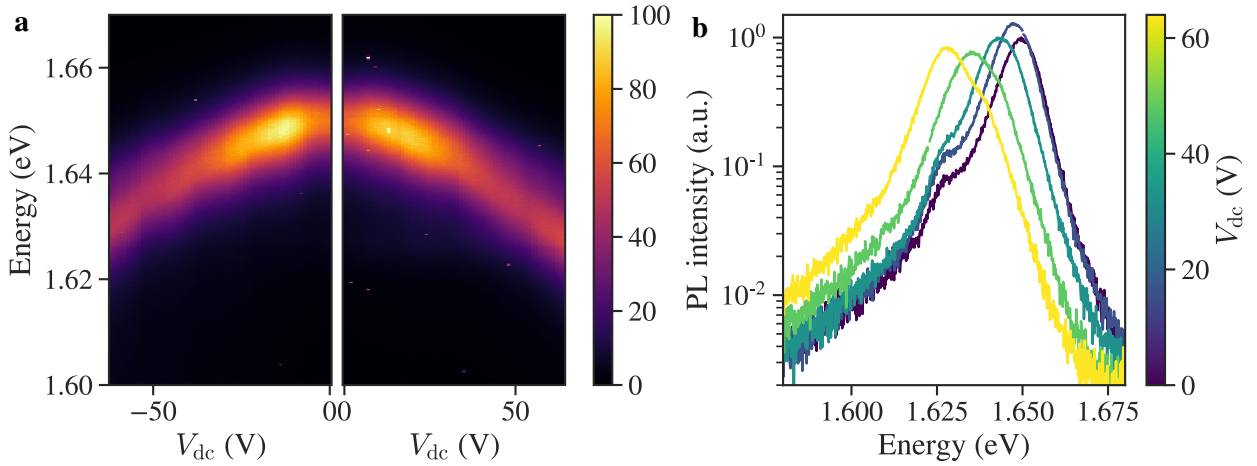

Figure 4.18: Gate dependent PL spectrum of suspended graphene/$MoSe_2$. a. Colormap of the PL spectrum of suspended graphene/$MoSe_2$ as a function of the DC gate bias V_{dc}. **b.** Examples of typical PL spectra (in semilog scale) for various values of V_{dc}. The corresponding DC bias (from darker blue to yellow) are V_{dc} = 0, 16, 32, 48 and 64 V. The laser power is fixed at 10 µW.

is the laser wavelength, that is now of 532 nm instead of 633 nm for the data presented figure 4.11, another plausible explanation would be a slight change in the doping level of the system. Indeed, the PL data of figure 4.18 was acquired after the Raman data presented in the previous section, that involved multiple cycles at high bias. The linewidth of the exciton feature is also larger than previously with a FWHM of 11 meV at zero bias, suggesting that membrane is strained even at zero gate bias.

At high values of V_{dc}, the exciton PL feature seems to be composed of multiple contributions. The trion feature seems to form a shoulder on the low energy tail while the main excitonic peak seems to split in two close lying contributions. However, the description of the fine structure of the neutral exciton feature under strain is out of the scope of this work and we will consider it as one single peak. We then proceed to fit the exciton feature with a single Voigt profile to determine its position E_{X^0}, linewidth and integrated intensity that are shown figure 4.19. In addition to the striking redshift of the exciton feature, that reaches 20.6 meV at the maximum voltage, a broadening of $\sim$ 5 meV is observed for $V_{dc} < 50$ V. Past this point, the FWHM reduces. However, we will focus ourself here on the position of the exciton line in order to establish its strain sensitivity, a parameter that will be of most importance in our futur interpretation of the dynamical behavior of the exciton line.

Estimation of the strain sensitivity

To obtain an estimation of the strain sensitivity of the exciton energy, we first proceed to a calibration of the static deflection using the same procedure as developed in section 4.3.2. The matching of the experimental and theoretical curves is shown figure 4.20a and is achieved for $a_2 = 2 \times 10^{-3}$ nm.V^{-2}, $a_1 = 1.9$ nm.V^{-1}, and $a_0 = 35$ nm. We then estimate the static strain $\Delta\varepsilon_s$ using equation (4.60) and determine the strain dependency of E_{X^0} presented figure 4.20b. In a similar way as the strain estimation of the previous section, we

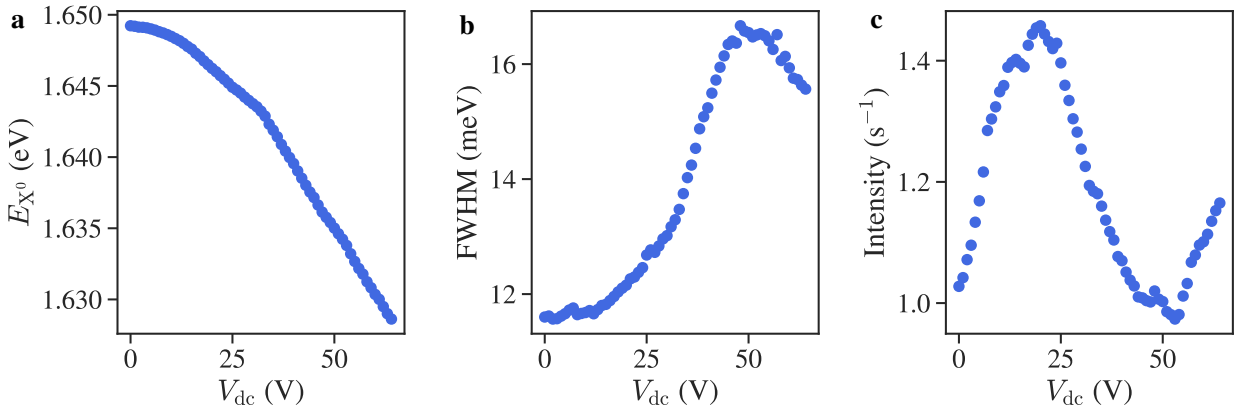

Figure 4.19: Fitted parameters of the gate dependant exciton peak. Position (**a**), linewidth (**b**) and intensity (**c**) of the neutral exciton X^0 emission line as a a function of the DC gate bias V_{dc}. Fit was done with a single Voigt profile.

may expect that our result becomes less precise at high V_{dc} since equation (4.60) considers an averaged elongation while we measure locally at the center of the deflected membrane.

However, we can expect our estimation to be more precise at low V_{dc}. Specifically, we can reasonably assume that it is true in the $V_{dc} \leq 20$ V range, that is the available range of the lock-in amplifier used to monitor the dynamical strain tuning of the exciton energy in the next section. A zoom in this range of the strain dependent exciton energy is shown in the inset of figure 4.20b. A linear fit restrained to this range is performed (see dashed orange line in the inset of figure 4.20b) and gives a strain sensitivity of -185 meV/%. We can note that this value is significantly higher than the ones reported in the literature that lies typically around $\sim 50 - 100$ meV/% for biaxail strain in monolayer $MoSe_2$ [164, 184, 185, 186]. However the commonly reported values does not consider suspended graphene/$MoSe_2$ heterostructures but isolated $MoSe_2$ layers. Further experiments are needed to understand the reason for this surprisingly high strain sensitivity, some of them are discussed in the paragraph below, as a measure of the strain via Raman spectroscopy to be correlated with strain sensitivity that we obtain from our PL data.

Discussion

As already mentioned, since our strain estimation is based on equation (4.60) we should expect it to underestimate the real strain value that we measure at the center of the circular drum, with increasing errors as V_{dc} increases. In the mean time we can also note a few potential contributions that are ignored in the present work.

A first one that might come to mind is the change of dielectric screening environment. Indeed, if the screening induced upshift of the 2D-mode frequency reduces because of a change in the van der Waals gap, then one could expect to see an equivalent change in the exciton energy [93]. A proper estimation of this effect would need a complete analysis of the influence of the dielectric environment on the exciton energy in $MoSe_2$ in analogy to the one performed for the Raman response of graphene in chapter 3. More precisely, such an analysis on a sample involving suspended $MoSe_2$ and suspended graphene/$MoSe_2$ areas would give precise

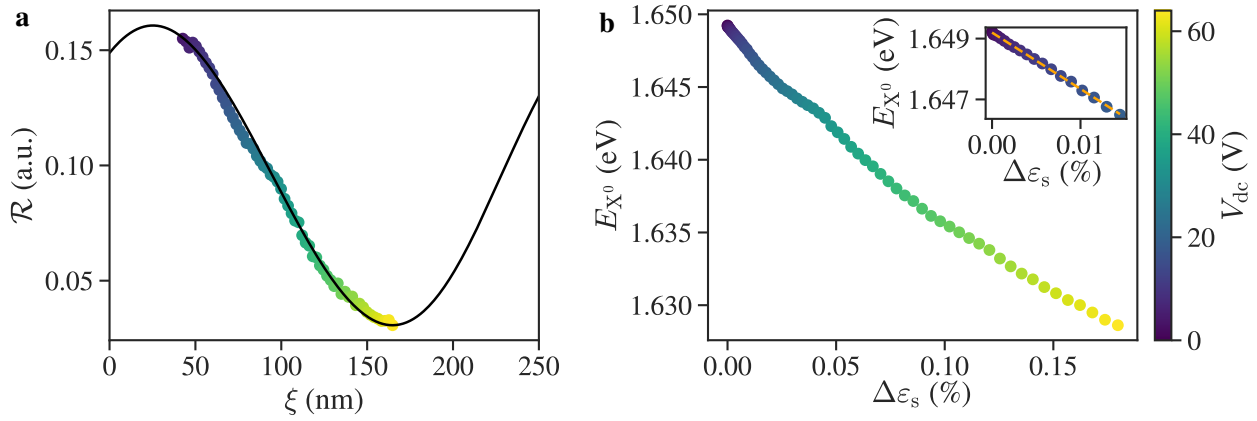

Figure 4.20: Displacement calibration and estimation of the strain sensitivity of suspended graphene/$MoSe_2$.
a. Reflectance variation depending on the membrane deflection ξ for $\lambda = 532$ nm. The continuous line represents the calculated variation of the reflectance and symbols represents the measured DC reflectance scaled to match the shape of the theoretical curve. **b.** Position of the exciton emission line E_{X^0} as a function of the applied static strain $\Delta\varepsilon_s$. The inset shows a zoom on the low bias region, for $V_{dc} \leq 20$ V together with a linear fit (orange dashed line).

insights on the energy change to expect. However, we might be able to get a first idea of the exciton shift that one can expect for this effect by comparing the observed change in the exciton energy in the PL map presented figure 4.11b,c with our spatially averaged data from chapter 3 and figure 3.5. For this we assume that the screening effects induced by $MoSe_2$ and WSe_2 are the same, and that the dielectric shift of E_{X^0} is the same for SiO_2-supported $MoSe_2$ versus graphene/$MoSe_2$ than for suspended $MoSe_2$ versus graphene/$MoSe_2$. A 16 cm^{-1} upshift of the 2D-mode frequency would then be related to a reduction of the exciton energy of 20 meV. As such, we could expect that if the screening induced upshift of ω_{2D} is reduced by 1 cm^{-1}, the exciton energy would increase accordingly by ~ 1.25 meV, provided that the two screening effects scales similarly with the interlayer distance.

These two points would benefit from the same type of precise mapping of the strain field of the suspended graphene/$MoSe_2$ flake, as already mentioned in section 4.3. A combined hyperspectral mapping of the PL response as well as both graphene and $MoSe_2$ Raman responses at different values of V_{dc} would enable a complete mapping of the strain distribution in the sample and allow to probe potential differences between the two close lying layers. However one has to note the extremely faint character of the E′ mode feature in the Raman spectrum of $MoSe_2$, especially for excitation wavelengths in the visible range [187, 99] that would make such work highly difficult. A simpler experiment that would already be of most usefulness would be a DC bias dependent study of the Raman response of the $MoSe_2$ flake to complete the work presented in this chapter. The evolution of the A_1' and E′ Raman features of $MoSe_2$ at the center of the suspended heterostructure would already give an additional probe of both strain and doping in the $MoSe_2$ layer and strongly strengthen our observations.

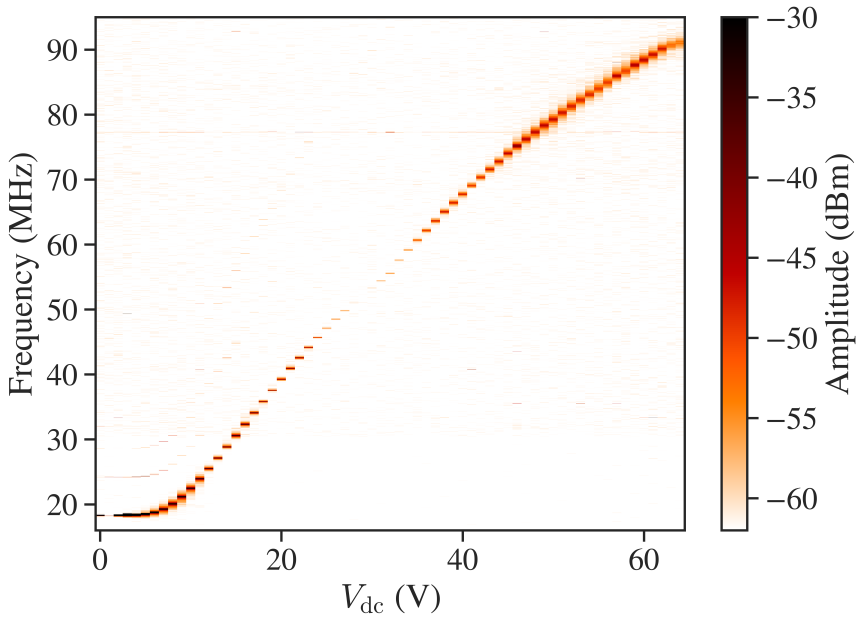

Figure 4.21: Mechanical response over a broad range of DC gate bias. Gate tunable mechanical response of device one in the 0 to 64 V range. The AC voltage amplitude is $V_{ac} = 10$ mV (peak-to-peak).

4.4.2 Dynamical strain-induced modulation of excitonic light emission in a graphene/$MoSe_2$ heterostructure

We now bring our attention to the dynamical regime and investigate the effect of dynamically induced strain when the sample is actuated at the mechanical resonance of the fundamental vibrational mode. We saw in the previous section that the exciton PL feature shifts with strain with a sensitivity of -185 meV/%, an effect that can easily be detected by a statically induced deflection of the membrane. In the dynamical regime, the oscillation amplitudes are rather small (of the order of one or a few nm) with respect to the static deflection that we induce with the backgate (up to $\Delta\xi \sim 150$ nm for $V_{dc} = 64$ V). Roughly, we can expect that the membrane's oscillation induces dynamical strain values in the 10^{-4} % range that would correspond to an exciton shift of approximately -100 µeV. Such small values are close from the limit of our spectral resolution but remains detectable.

The experimental procedure described below is largely inspired by the results from X. Zhang *et al.* [39] on graphene resonators, where it was shown that the non-linear mechanical resonance can induce enhanced dynamical strain in graphene (see section 4.1.3). Our objective in this section is to probe the effect of the non-linear mechanical resonance on the exciton energy and decipher a potential enhancement of the dynamically induced strain in device 1, in a similar fashion of the strain enhancement reported in [39]. All the data shown here were obtained with a 633 nm laser at a fixed power of 10 µW.

Figure 4.21 shows a DC gate bias dependence of the mechanical response measured with a vector network analyser with a fixed AC peak-to-peak amplitude $V_{ac} = 10$ mV. The explored DC range goes from $V_{dc} = 0$ to $V_{dc} = 64$ V and demonstrates the large tunability of the mechanical resonance frequency f_0, that scales from 18.5 MHz for $V_{dc} = 0$ to 91.4 MHz for

$V_{dc} = 64$ V. Similar tunability of the mechanical resonance in graphene/TMD membranes were already reported in reference [153]. In addition, we can note that the mechanical resonance disappears around $V_{dc} \approx 30$ V. It is the sign of a extremum of the deflection dependent reflectivity of the sample at this point and will be used as a reference point for our calibration in the next section. In the rest of the section, all mechanical responses are measured with a lock-in amplifier that also provides the electrostatic actuation.

Displacement calibration

If we want to compare the static and dynamic regimes, we need to calibrate the frequency dependent displacement of our resonator. As described in section 4.2.1, it means that we need to determine the transduction factor β. To this end, we apply once again the procedure developed in section 4.3.2, by scaling the deflection ξ as a second order polynomial function in terms of $|V_{dc} - V_0|$. However, the voltage range available from the lock-in amplifier is limited to $|V_{dc}| \leq 20$ V and we need to determine some specific reference point to perform our calibration. In all our static calibrations presented previously $a_0 = 35$ nm, suggesting that the equilibrium position of the membrane at zero bias is at a deflection $\xi = 35$ nm. We thus use this point as first reference point and fix $a_0 = 35$ nm.

A matching of the theoretical and experimental reflectivity curves is then achieved for $a_2 = 8.5 \times 10^{-2}$ nm.V^{-2}, $a_1 = 0.15$ nm.V^{-1} and $a_0 = 35$ nm. The result is presented figure 4.22a where the continuous line is the calculated reflectivity $\mathcal{R}_{theory}$ and the colored symbol the experimentally measured reflectivity $\mathcal{R}_{exp}$. The dashed line in figure 4.22a shows the derivative of the calculated reflectivity $d\mathcal{R}/d\xi$ that is directly related to the transduction coefficient β. Remarkably, the calibration implies that we reach the close vicinity of a minimum of the reflectivity pattern for $V_{dc} = -20$ V, in agreement with the observed diminution of the measured signal in the data shown figure 4.11f. Furthermore, we can note that with $V_0 = 4$ V, the effective applied voltage reaches $V_{dc} - V_0 = -24$ V, close from the disappearing of the mechanical signal observed in the bias values in the vicinity of $V_{dc} \approx 30$ V in figure 4.21. These two observations give us a strong confidence in the determined calibration.

We can thus determine β for each value of V_{dc} by inverting the scaling of the DC reflectivity introduced in section 4.3.2. The resulting values of β are shown figure 4.22b in µV/nm and will be used to calibrate the amplitude of the mechanical oscillations of our graphene/$MoSe_2$ resonator.

Strain induced modulation of the exciton energy

Figure 4.23a shows the evolution of the mechanical response of device 1 when the actuation amplitude V_{ac} is increased from 1 mV to 200 mV, at a fixed DC bias $V_{dc} = -5$ V. A backbone curve is forming as V_{ac} is increased. We can note that the non-linearity starts to appear already for $V_{ac} = 5$ mV.

In order to detect changes in the exciton energy due to strain induced by the non-linear vibration of the membrane, we measure the PL spectrum of our graphene/$MoSe_2$ heterostructure while actuating the sample at the peak frequency of the mechanical response f_p. We de-

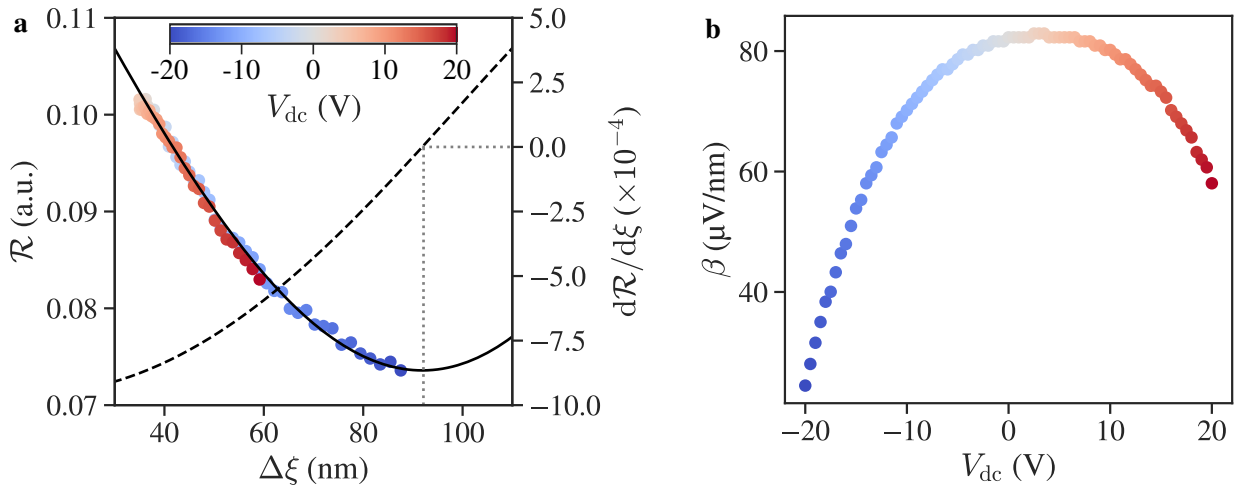

Figure 4.22: Displacement calibration and determination of the transduction coefficient. a. Calculated (continuous line) and experimentally measured (colored symbols) deflection dependent laser reflectivity $\mathcal{R}$. The dashed line gives the derivative of the calculated reflectivity $d\mathcal{R}/d\xi$ that is directly related to the transduction coefficient β. **b.** Transduction coefficient β as a function of the applied DC bias V_{dc}.

fine here the peak frequency f_p as the closest frequency from the jump frequency giving a non-linear oscillation that is stable enough to measure the PL spectrum before a drop in the vibration amplitude. The resulting shift of the exciton energy is shown figure 4.23b where we take as reference point the exciton energy measured out of resonance ($f = 21.5$ MHz, see red cross in figure 4.23a) with $V_{ac} = 1$ mV. The reference point is shown as a red symbol in figure 4.23b. The measured PL spectrum in the two extreme cases are shown figure 4.23c, where the red spectrum corresponds to the reference point (out-of-resonance actuation with $V_{ac} = 1$ mV, see red cross in figure 4.23a) and the blue one to the most strongly actuated one ($V_{ac} = 200$ mV, see blue cross in figure 4.23a). Figure 4.23d shows the difference of intensities between the two spectra from figure 4.23c.

A downshift of the exciton energy is observed, with an increasing amplitude as V_{ac} gets stronger. In the most strongly actuated case ($V_{ac} = 200$ mV), we determine a downshift of $\Delta E_{X^0} = -170 \pm 40$ μeV. Considering the strain sensitivity of -185 meV/% determined section 4.4.1, it corresponds to a dynamical strain value $\varepsilon_d = 9 \times 10^{-4} \pm 2 \times 10^{-4}$ %. It can be interesting to compare this result with a theoretical estimation based on the same idea as the model that gives us equation (4.60). We can thus estimate the dynamical strain value as

$$\varepsilon_d = \frac{2}{3}\left(\frac{z_0}{R}\right)^2. \tag{4.63}$$

In our case, for $V_{ac} = 200$ mV, the maximum amplitude measured at the peak frequency f_p is $z_0 = 5.9$ nm, that gives a dynamical strain estimation of $\varepsilon_d = 3.7 \times 10^{-4}$ %.

While this value is 2.4 times smaller than the one we measure in the PL response, this difference is not as striking as it was previously reported by X. Zhang *et al.* in graphene drums vibrating in the non-linear regime, where the measured value of the dynamical strain reaches 40 times the estimated value [39]. The high discrepancy reported in graphene was assigned to anharmonic oscillations and complex mode profiles [39]. Thus, we may consider that the

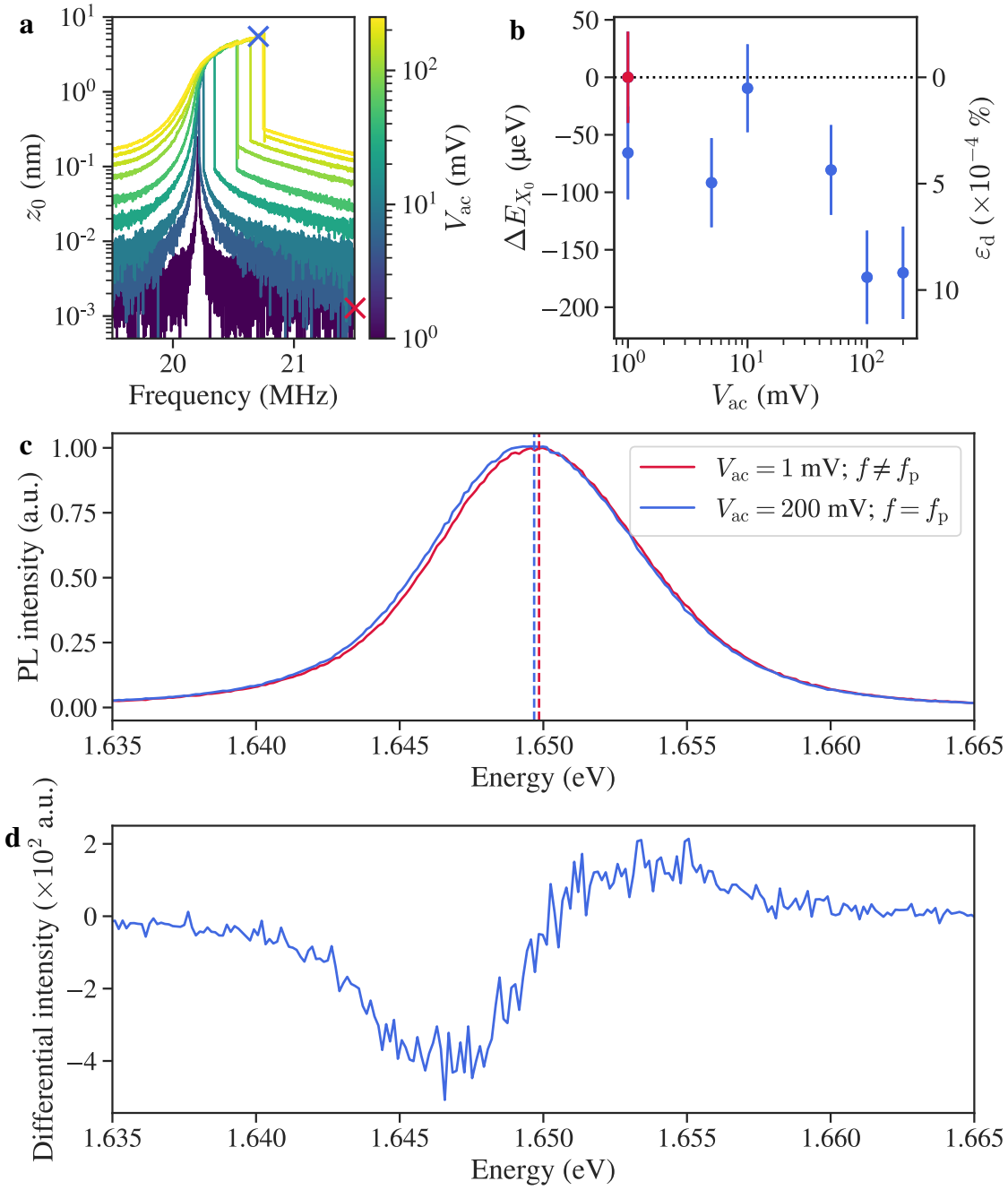

Figure 4.23: Dynamical strain modulation of light emission in graphene/$MoSe_2$. a. Variation of the mechanical response with increasing V_{ac} for a fixed $V_{dc} = -5$V. The presented data shows forward frequency sweeps. **b.** Energy shift of the exciton emission line as a function of V_{ac} measured by following the backbone curve. The actuation frequency is fixed at the closest stable value from the jump frequency. The energy reference is taken as the exciton energy measured out of resonance ($f = 21.5$ MHz, see red cross in a) at $V_{ac} = 1$ mV (red circle). The right axis gives the corresponding dynamical strain values ε_d determined using the strain sensitivity of -185 meV/% determined in section 4.4.1. **c.** PL spectrum of the neutral exciton feature in the two extreme cases being out-of-resonance actuation (see red cross in a) with $V_{ac} = 1$ mV (in red) and actuated at the peak frequency f_p (see blue cross in a) with $V_{ac} = 200$ mV (in blue). **d.** Intensity difference between the two spectra from c.

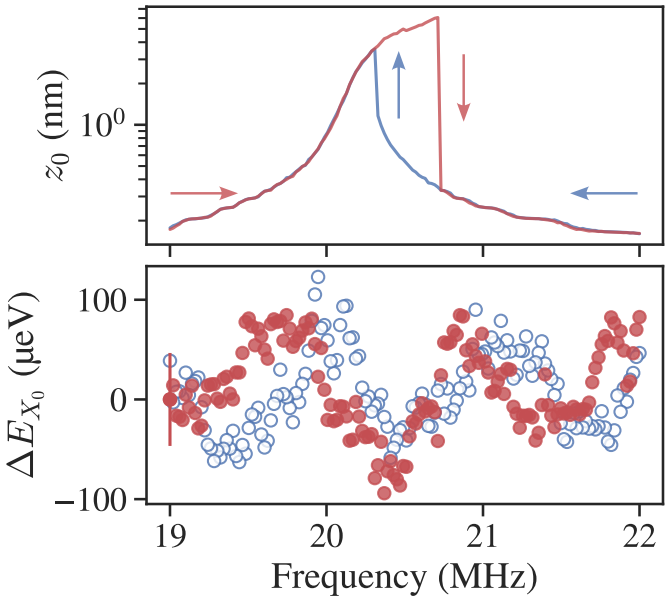

Figure 4.24: Frequency dependent modulation of the exciton energy. Nonlinear mechanical response in forward (red) and backward (blue) frequency sweeps (top) together with the associated frequency dependent shift of the exciton energy (bottom).

mode profile of our sample is only slightly altered by the non-linear regime. Noteworthy, the ratio between the RMS amplitude and the drum's radius z_0/R is comparable between device 1 ($z_0/R \sim 2.4$ ‰) and the graphene drum in reference [39] ($z_0/R \sim 3$ ‰). We could thus have expected to observe a similarly strong discrepancy and its absence might be a clue of the influence of the $MoSe_2$ layer on the mechanical properties of graphene.

Further experiments, notably consisting in a spatial mapping of the mode profiles in the non-linear regime could give us more informations to conclude on this point. In addition, not measuring the same high enhancement of the dynamical strain than reported in graphene drums strongly suggests us to reproduce the results of reference [39] on our graphene/$MoSe_2$ sample to see how the dynamical strain in graphene behave when the graphene layer is in contact with a TMD layers and if we measure similar strain values in both layer when the sample is actuated to resonance.

We can expect a higher precision by implementing a stroboscopic measurement scheme. One can see in figure 4.23c that the small redshift of the exciton PL feature is accompanied by a slight increase of its linewidth. The reason for this broadening comes from the continuous nature of our measure. As we probe the PL spectrum continuously while the strain changes with a frequency f, we detect the time-averaged PL spectrum of the sample that is composed of the sum of the time-dependent PL spectra that all shows different exciton energies depending on the real-time membrane deflection. The critical point for the implementation of such experiments is to temporally slice the laser beam used for the PL excitation using a time window $\Delta\tau_L$ that is shorter than half of the membrane's oscillation period $1/f_0$ in order to resolve changes in the PL spectrum in a single period of oscillation. Various difficulties can be identified toward this objective, as the light intensity needs to be modulated at the same frequency than the mechanical oscillation ($\gtrsim 20$ MHz in our case) with a short enough

duty cycle while still keeping enough PL signal.

We then attempted to measure the changes in the exciton energy as a function of the actuation frequency. Figure 4.24 shows the frequency dependent exciton shift when the sample is actuated through the non-linear mechanical resonance (bottom) together with the corresponding mechanical response (top). Red (blue) lines and symbols corresponds to forward (backward) frequency sweeps. However, we cannot observe any clear effect because of the quite low stability of the non-linear regime in this sample. Indeed, the data shown figure 4.24 were obtained in a fully automatized way with no procedure to ensure the stability of the mechanical oscillation during the acquisition time of the PL spectrum. A similar experiment was successfully performed on a different sample made of a few-layer graphene/WSe_2 heterostructure and is presented in appendix F.

Conclusion

In this chapter, we demonstrated on a graphene/$MoSe_2$ based sample the versatility of the circular drum geometry for the exploration of the properties of graphene/TMD heterostructures by a combination of techniques of optical spectroscopy and nanomechanics. Moreover, it is a sample geometry that already proved its viability as a strain engineering platform [14, 64, 39].

Thanks to a well established understanding of the Raman features of graphene towards strain and doping, we propose here a way to experimentally monitor proximity effects in graphene/TMD heterostructures based on the symmetry dependent screening of phonons in graphene that we reported in chapter 3. As the suspended heterostructure is deflected electrostatically, we use the frequency of the G-mode feature, that does not depend on screening, to determine strain in the graphene layer. We then use the determined strain value to estimate the corresponding strain induced shift of the 2D-mode frequency and isolate a small discrepancy between the measured 2D-mode frequency shift and the determined strain induced shift. Provided that the change in the doping level of graphene is negligible in the process, we suggest that the observed difference could arise from a diminution of the screening induced upshift of the 2D-mode due to a small change in the van der Waals gap. A comparison between our data on the suspended graphene/$MoSe_2$ heterostructure with a suspended graphene drum suggests that the doping contribution is negligible in the graphene/$MoSe_2$ case. However, we strongly insist on the preliminary character of those results that needs to be completed with additional experiments.

In addition, using the same sample, we demonstrate a strain induced modulation of the $MoSe_2$ exciton energy in both static and dynamic regimes. Using a simple modeling of the applied strain on the membrane, we use the measured PL spectra in the static regime to determine the strain sensitivity of the exciton energy in our sample. In the low deflection limit, we observe a linear strain dependence with a sensitivity of -185 meV/%. The determined strain sensitivity of the exciton energy is then used to estimate the dynamical strain induced on the heterostructure when the sample is actuated resonantly in the non-linear regime. We resolve a small redshift of the exciton PL feature up to -170 ± 40 µeV that we assign to time-averaged dynamical strain of $9 \times 10^{-4} \pm 2 \times 10^{-4}$ %. The results presented

in this chapter pave the way to the development of new experimental approaches for the investigation of light-matter interactions, proximity effects and strain induced phenomenons in van der Waals heterostructures.

Conclusion and perspectives

In this manuscript, we report on the properties of 2D-materials that can be greatly modified by the absence or change of underlying substrate and prove the versatility of the drum-like sample geometry to probe and control the properties of van der Waals heterostructures. The presented results can be separated in two parts.

The first one is composed of chapters 2 and 3. Chapter 2 presents room temperature results on suspended monolayer MoS_2 and WS_2. We show that in both materials, the absence of underlying substrate leads to a strong alteration of the PL spectrum when the laser excitation intensity is increased. In suspended MoS_2, our data shows an explosion of the PL intensity correlated with a strong redshift and broadening of the PL features. Our observations agree with previous reports of the formation of a dense electron-hole liquid phase mediated by an abrupt direct to indirect gap transition occuring in the material when the lattice temperature reaches about 550 K [110, 112]. In suspended WS_2, we observe once again a strong redshift and broadening of the emission feature, but with a reduced increase of the PL intensity. A unexpected enhancement of the A_1' Raman mode is also seen in correlation with the alteration of the PL spectrum. While further experiments are needed to properly conclude, we propose an interpretation based on the non-uniformity of the photoheating profile that favors an efficient exciton to trion conversion that may lead to the formation of an electron-hole plasma phase [73, 78]. However, we believe that the potential electron-hole plasma phase in suspended WS_2 is very unstable as a strong photobleaching is observed when the laser power is increased to higher powers.

In chapter 3 we report a symmetry dependent screening of the optical phonons in graphene. Using systematic hyperspectral mapping of the Raman response of graphene-based van der Waals heterostructures with different geometries, we show that the 2D-mode frequency ω_{2D} is highly sensitive to changes in the dielectric environment while the G-mode frequency ω_G remains constant in every situations. By measuring the 2D-mode dispersion on a sample with different configurations, we show that the upshift of ω_{2D} is related to a screening induced softening of the Kohn anomaly at the K point. In addition, a symmetry-based theoretical argument explains the absence of effect on ω_G thanks to a protection of the phonon frequencies at Γ that results from the degeneracy of the E_{2g} phonons at Γ. This theoretical argument is further supported by experimental data that shows the insensitivity of the 2D′-mode frequency with respect to dielectric screening. We thus demonstrate that the Raman response of graphene is a highly accurate gauge of dielectric screening and shed new light on Raman-based characterization of van der Waals heterostructures.

The second part corresponds to chapter 4, in which we exploit the newly build experimen-

tal setup detailed in appendix C and that was entirely developed in the scope of this PhD work. It is designed to perform automated experiments that combines optical spectroscopy and opto-electromechanics in drum-like samples, with a precise temperature control and enhanced mechanical stability. We use our results of chapter 3 to propose an experimental way to monitor changes in the interlayer coupling of a suspended graphene/$MoSe_2$ heterostructure deflected electrostatically. In this procedure, the G-mode Raman feature is used to characterize strain in the graphene layer and determine the associated shift of the 2D-mode feature. The estimated strain related shift of ω_{2D} is then removed from the measured value to isolate a potential change in the screening induces upshift of the 2D-mode feature. A comparative analysis on a suspended graphene drum is performed to ensure a negligible contribution from doping in the process. In a following section, the electrostatic actuation is used in the static regime to estimate the strain sensitivity of the exciton energy of our graphene/$MoSe_2$ heterostructure. The determined strain sensitivity is then used to probe dynamically induced strain in the sample when the membrane is brought to the non-linear mechanical regime. A time-averaged redshift of the exciton energy up to -170 ± 40 µeV is observed and assigned to time-averaged dynamical strain of $9 \times 10^{-4} \pm 2 \times 10^{-4}$ %.

Perspectives

In the following, we will present some of the perspectives related to the work presented in this manuscript.

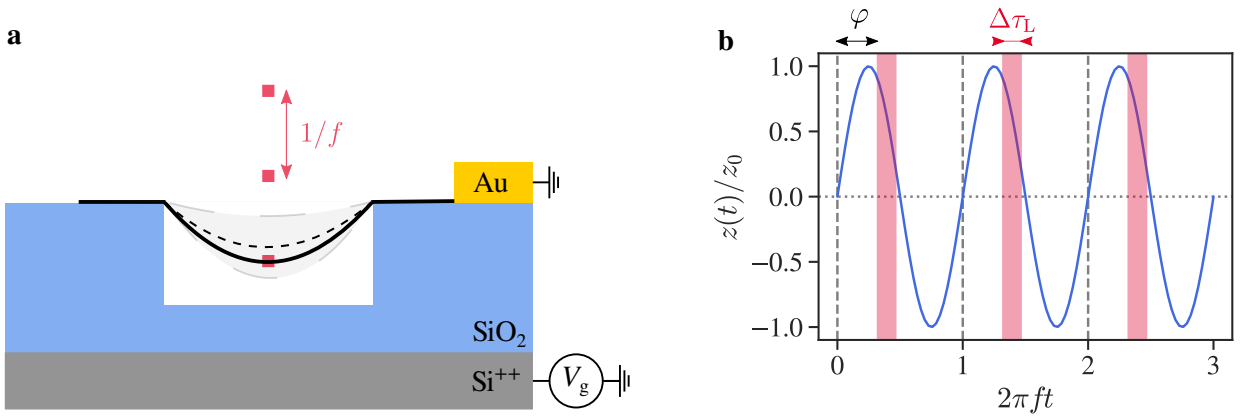

Figure 5.1: Stroboscopic experiment scheme. **a**. Simplified sketch of the stroboscopic measurement scheme. The grey dashed lines represent the maximum and minimum of the oscillating deflection, probed for $\varphi = \pm\pi/2$. The black dashed line gives the equilibrium position of the membrane, probed for $\varphi = 0, \pi$. **b**. Time-dependent amplitude of the mechanical oscillation normed by the maximum amplitude z_0. The vertical red thick lines represent the time window probed by the synchronous stroboscopic laser excitation.

Stroboscopic experiments

All of the results presented so far show time-averaged data. Notably, the observations reported in chapter 4 are obtained by measuring the optical response continuously over a large number of mechanical oscillations of the suspended membrane. By implementing a stroboscopic measurement scheme, we can add a temporal resolution and resolve the dynamical modulation of the optical features in a single oscillation period.

A simplified sketch of the stroboscopic measurement scheme is given figure 5.1. As the membrane oscillates following a sinusoidal function $z(t) = z_0 \sin(2\pi f t)$, the laser intensity is modulated by a square function at the same frequency f. The time window of the laser illumination $\Delta\tau_{\mathrm{L}}$ then defines the time resolution of the experiment. Thus, the temporal resolution increases as the duty cycle decreases and allows to probe the optical response during a single mechanical oscillation as a function of the phase difference φ between the mechanical oscillation and the laser excitation.

In practice, one needs to find a compromise between the temporal resolution and the total integrated time. Indeed, when $\Delta\tau_{\mathrm{L}}$ is reduced, the measured signal decreases as the effective integration time $\tau_{\mathrm{eff}} = D\tau_{\mathrm{tot}}$, where D is the duty cycle and τ_{tot} is the total acquisition time. A 10 % duty cycle seems as a good compromise in our case. However, the current acousto-optic modulator on our setup is not fast enough to ensure a clean and controllable modulation of the laser excitation at frequencies $f \gtrsim 10$ MHz, and thus does allow to implement the stroboscopic measurement scheme at the moment. The future acquisition of faster electro-optic modulators should increase the upper limit of the frequency modulation of the laser excitation and enable us to implement the stroboscopic experiment scheme and increase the precision of our results presented chapter 4.

Electromechanical control of the correlated phases in suspended TMDs

In chapter 2 we discussed on the formation of dense electron-hole phases in suspended monolayer TMDs. As stated before, the formation of an EHL phase in suspended monolayer MoS_2 is related to a transition from a direct electronic gap to an indirect gap due to thermal dilatation [110, 112]. Similar direct to indirect gap transitions may be reached through strain engineering [62, 63]. The drum-like geometry could thus be used to electrostatically induce strain in a suspended monolayer MoS_2 and control the phase transition by a combination of electromechanically induced strain and laser induced heating.

Electromechanical tuning of moiré patterns

Another interesting direction where the drum-like sample geometry could show its interest is the study of moiré physics. It has been shown that a precise control of the twist angle between the two monolayers in a TMD/TMD bilayer can form a moiré pattern that acts as a periodic superpotential felt by the electrons and that strongly affects the exciton features [85, 86]. Specifically, the band alignment in $MoSe_2/WS_2$ heterobilayers allows the electrons in the conduction bands of the two materials to hybridize (see figure 5.2a). The conduction band electron is then delocalized between the two layers and may couple to an electron

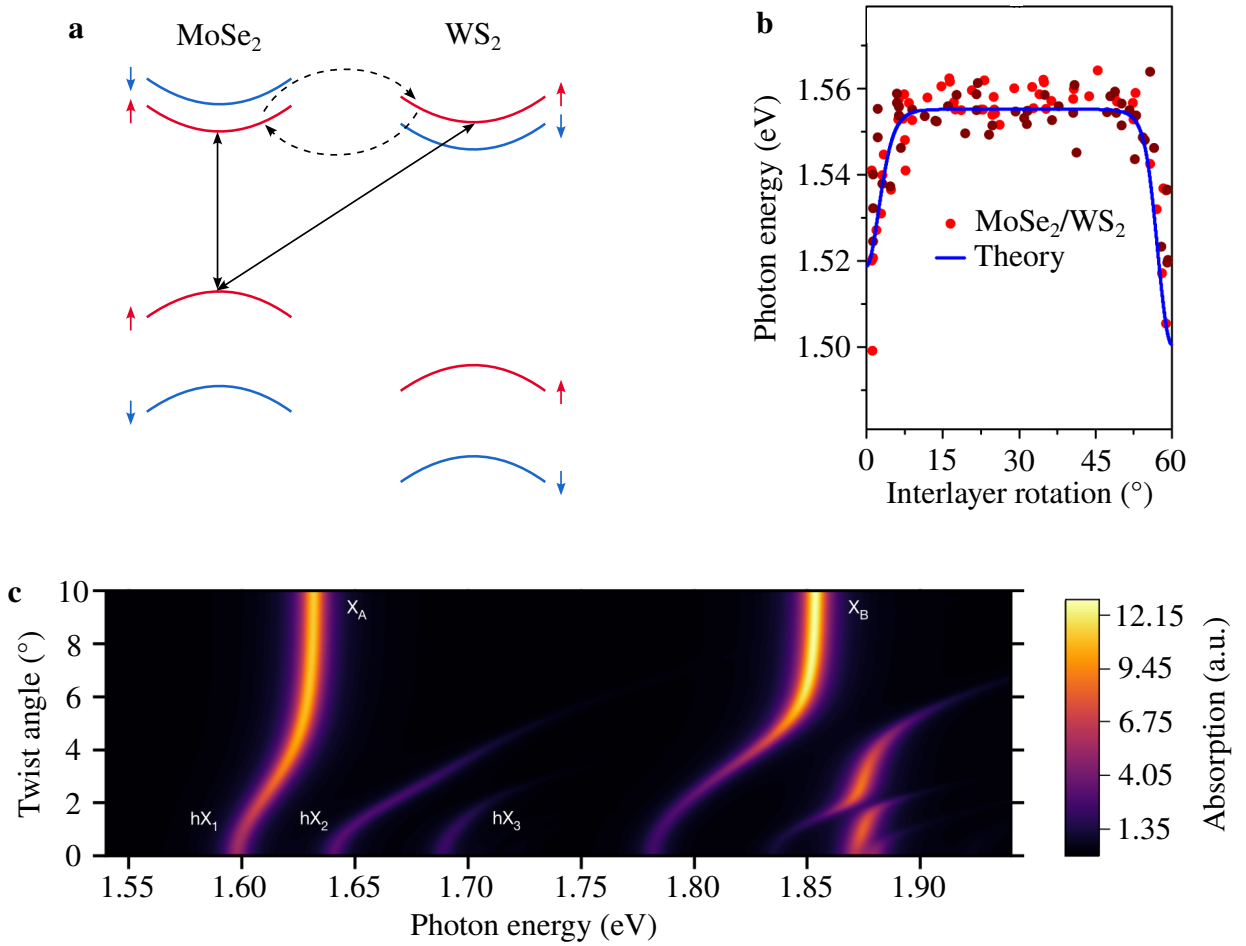

Figure 5.2: Hybridized excitons in $MoSe_2/WS_2$ heterobilayers. **a**. Band diagram of the $MoSe_2/WS_2$ heterobilayer. **b**. Energy of the room temperature PL feature of the hybridized exciton as a function of the interlayer twist angle. **c**. Calculated absorption spectra of the $MoSe_2/WS_2$ heterobilayer at low temperature as a function of the interlayer twist angle. b and c are adapted from [188].

in the $MoSe_2$ valence band. The result is an hybridization of the $MoSe_2$ exciton that is strongly dependent on the twist angle between the two layers [188, 189]. Figure 5.2b,c shows respectively the change of the hybrized exciton with the twist angle at room temperature, and the theoretically calculated absorption spectrum of the $MoSe_2/WS_2$ heterobilayer as a function of the twist angle at cryogenic temperatures [188].

Using the drum-like sample geometry, it might be possible to tune the interlayer twist angle of a $MoSe_2/WS_2$ heterobilayer using the electrostatic actuation and probe the resulting modification of the moiré pattern through the emission of the hybrized exciton states. The new experimental setup developed during this project would be perfectly fitted for such experiments as a precise control of the temperature and the applied voltage could allow a full investigation as a function of the membrane deflection (and consequently, strain and interlayer twist angle) and the temperature.

Opto-electro-mechanics of 2D-magnets

Recently, 2D magnetic materials were isolated and completed the 2D-materials toolkit [7, 190, 8]. The existence of a persistent magnetic order offers the perspective to embed a magnetic degree of freedom in van der Waals heterostructures. Interestingly, the magnetic phase transitions in 2D-magnets were observed both through Raman spectroscopy and optomechanics experiments. As an example, figure 5.3a presents a signature of the antiferromagnetic-paramagnetic phase transition of $FePS_3$ in the mechanical response of a drum-like sample where a $FePS_3$-based heterostructure is used as a vibrating membrane [191]. The decrease in resonance frequency with increasing temperature is due to a reduction in strain because of an increased thermal expansion of the $FePS_3$. As the phase transition occurs, the heat capacity of the material diverges in the vicinity of the Néel temperature T_N [192, 4]. This effect is directly translated as a peak in the frequency softening centered around T_N (see pink line in figure 5.3b,c). The data presented in figure 5.3 were measured by Joanna Wolff, PhD student in our team since october 2021, using the experimental setup built during my PhD work and detailed in appendix C. Similar experiments were reported in [191].

Additionally, it has been reported in reference [193] that changes in the interlayer magnetostriction in a suspended CrI_3 bilayer embedded in a van der Waals heterostructure that is submitted to an external magnetic field induces a clear jump in the mechanical resonance frequency. The jumps in the mechanical frequency were correlated to a measure of the out-of-plane magnetization via magnetic circular dichroism that allows to assign the changes in resonance frequency to magnetostriction effects due to the flip of the magnetization of one

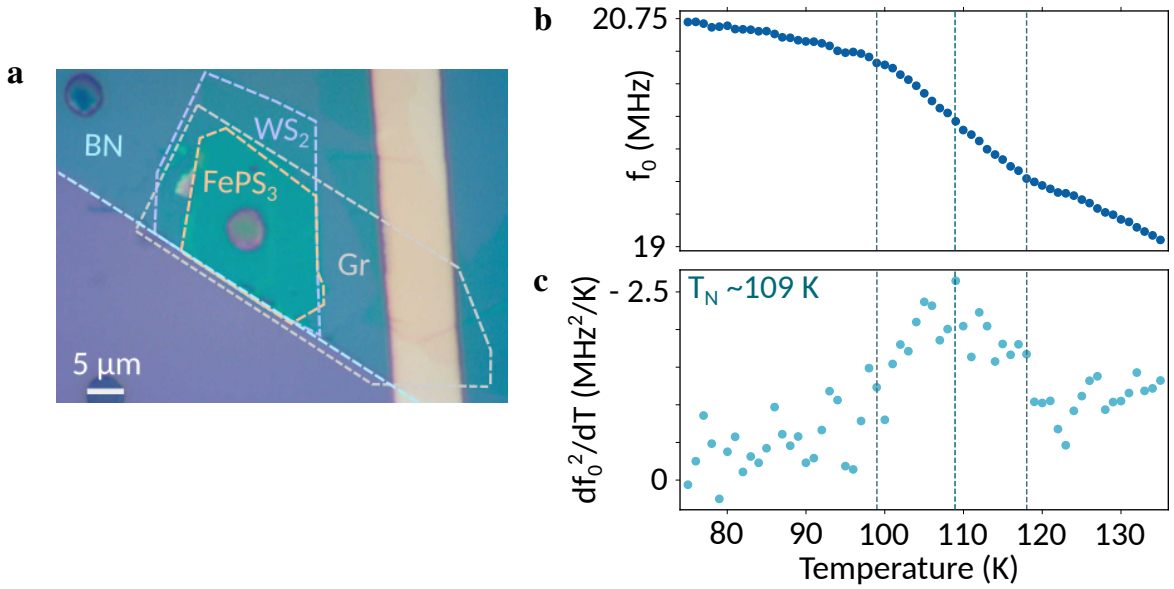

Figure 5.3: Examples of Optomechanical experiments on 2D-magnets. a. Optical image of a drum-like sample made of a suspended graphene/$FePS_3$/WS_2/hBN heterostructure. **b**. Change in the mechanical resonance frequency of the device shown in a with respect to temperature. **c**. Temperature derivative of the mechanical resonance frequency of the device shown in a with respect to temperature.

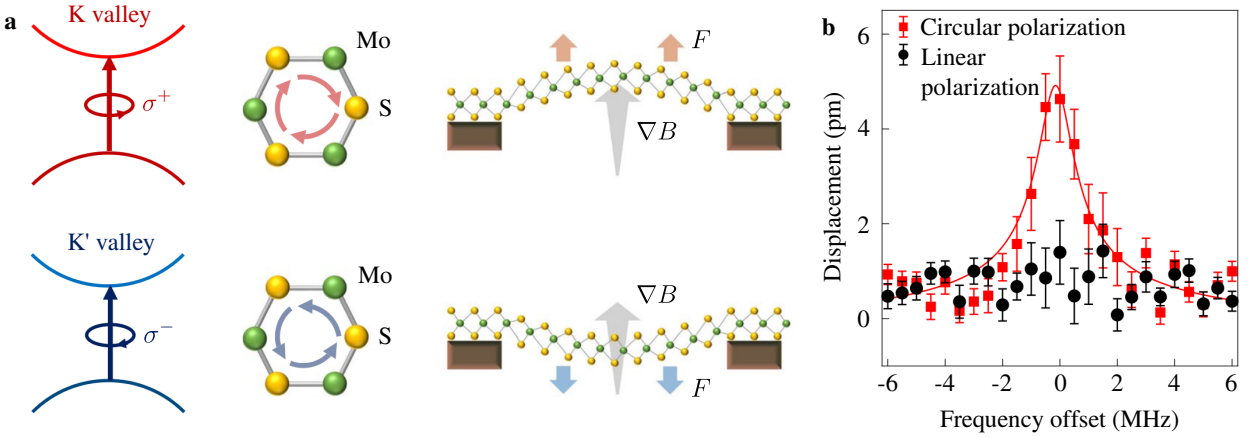

Figure 5.4: Valley-optomechanics on a suspended MoS_2 monolayer. **a**. Sketch of the valley-optomechanics principle. **b**. Measured mechanical response using a circularly polarized pump beam (red) and a linearly polarized pump beam (black). All panels are adapted from [194].

of the two layers [193].

The two presented examples demonstrates how the mechanical resonance frequency of a drum-like sample based on 2D-magnets can be used to probe the magnetic degree of freedom. In addition, the mechanical degree of freedom may be used to tune the magnetic properties via a modulation of strain in the vibrating membrane.

Valley-optomechanics

While most experiments on 2D-NEMS use either electrostatic or photothermal actuation, H. K. Li *et al.* demonstrated in 2019 the viability of an actuation technique based on the valley constrast in TMD monolayers [194]. This technique uses the fact that electrons in the K and K' valleys carry opposite magnetic moments with equivalent magnitudes. Thus if a magnetic gradient ∇B is present, a force with a magnitude

$$F = (N_{\mathrm{K}} - N_{\mathrm{K}'}) g \mu_{\mathrm{B}} \nabla B \tag{5.1}$$

is applied on the material. Here, N_{K} and $N_{\mathrm{K}'}$ stands for the population of electrons in the K and K' valleys, g for the Lande g-factor and μ_{B} for the Bohr magneton. This force can then be used to induce a mechanical displacement through the contrast in valley population that follows a circularly polarized excitation (see figure 5.4a for a sketch of the process).

In practice, the authors used a monolayer MoS_2 flake suspended over a square hole in a PMMA substrate coated with a Ni/Fe permalloy layer with a thin gold coating layer (inside and outside of the hole). When a magnetic field B is applied perpendicularly to the sample, the Ni/Fe permalloy layer creates a magnetic field gradient reaching up to 4000 $\mathrm{T.m^{-2}}$ at the center of the suspended MoS_2 flake for a magnetic field $B = 26$ mT, which creates the necessary conditions to induce a mechanical displacement when the flake is illuminated with circularly polarized light. The actuation of the mechanical motion of the membrane is then achieved by modulating the polarization of a 633 nm pump laser beam between σ^+ and σ^- polarized light with constant laser power. A linearly polarized laser beam at

654 nm is used to measure the resulting motion of the membrane. Figure 5.4b shows the measured mechanical response for a circularly polarized pump beam (red) compared to a linearly polarized pump beam (black).

With minimal changes in our setup, we could perform and improve this type of experiments based on an actuation of the mechanical motion via the contrast in the valley populations. An interesting direction on this topic would be to use a similar experimental configuration while varying the position of the actuation beam and use the electron spin transport to actuate the motion from the non-suspended part of the monolayer TMD and ensure the absence of photothermal effects.

APPENDIX A

Sample fabrication

This section is dedicated to the various fabrication techniques used in this work. All samples were made in the STnano cleanroom and 2D lab in IPCMS.

A.1 Designing substrates for 2D-NEMS

The very first step in the fabrication process is the design of substrates with prepatterned holes and electrodes using a combination of optical lithography, thin metal film deposition and reactive ion etching [195]. Patterns were designed with the open source software KLayout and drawn on standard Si/SiO_2 substrates with 500 nm thick oxide layers using the µPG101 UV laser lithography pattern generator from Heidelberg instrument available in the STnano cleanroom.

The processing of substrates is sketched in figure A.1:

- Steps 1-2: the lithographic photoresist is uniformly deposited on the Si/SiO_2 substrate with a spin coater.
- Step 3: the first layer of the pattern is drawn thanks to UV illumination locally activating the photoresist.
- Step 4: the development removes the activated parts of the photoresist layer.
- Steps 5-6: electrodes are deposited via metal evaporation. Cleaning of the sample removes the remaining photoresist and reveals the electrodes. In this work, all electrodes where formed of a 5 nm thick titanium film and 45 nm thick gold film.
- Steps 7-9: The same lithography process as steps 1-3 is repeated for the drawing of the second layer of the pattern.
- Steps 10-11: holes are etched in the uncovered parts of the substrate via reactive ion etching. All the Si/SiO_2 substrates used in this work where designed with 420 nm deep holes. The used gas mixture is composed of Ar (25 sccm) and CHF_3 (25 sccm) with an RF power of 130 W for 18 min at a pressure of 30 mTorr and temperature of 20 °C.

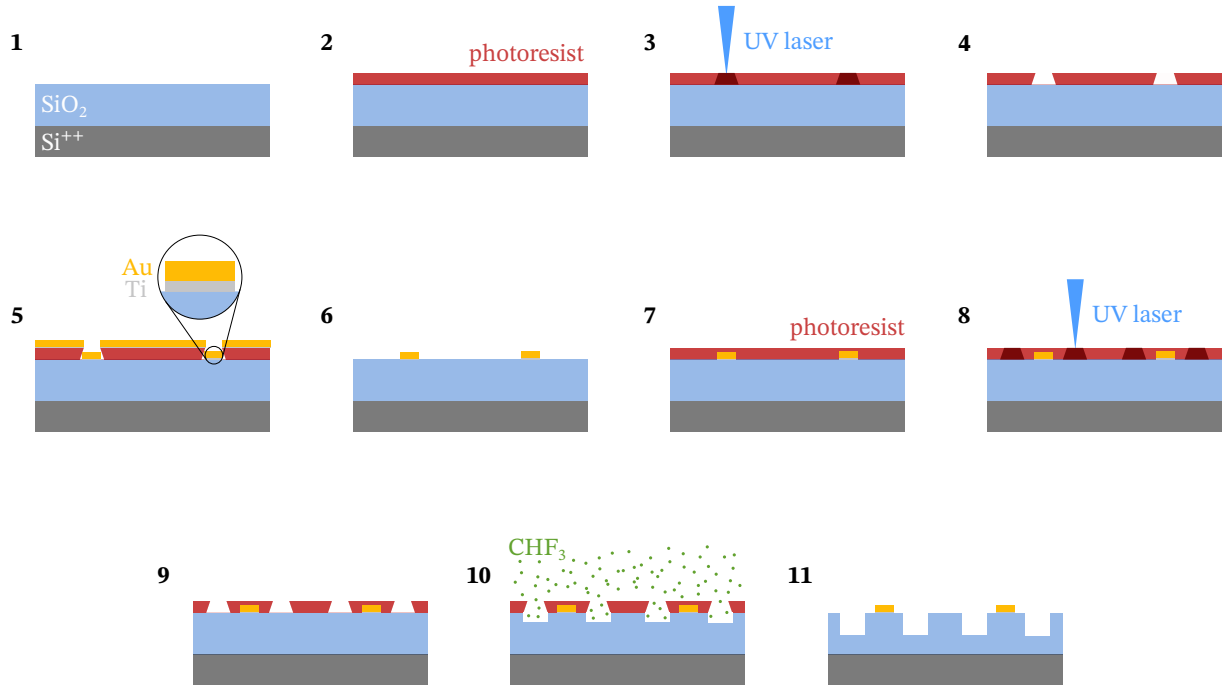

Figure A.1: Prepatterning electrodes and holes on Si/SiO_2 substrates. 1-6. Micropatterning electrodes with UV laser lithography and thin film deposition. **7-11**. Micropatterning holes with UV laser lithography and reactive ion etching.

For suspended samples without contacting electrodes (as the ones used in chapter 2), steps 2 to 6 can be ignored. A similar procedure can be applied to fully transparent quartz substrates for hole patterning.

Figure A.2 shows a typical substrate obtained from the described process. Different electrode geometries and hole repartitions where used during this PhD, with parameters varying depending on the used materials and the chosen transfer technique. Once the sample fully finished, the last step is the bonding of the sample. Classical wire bonding with gold bonds is used to connect the electrodes to the different pins of the chip carrier.

A.2 Mechanical exfoliation

Popularized by Geim and Novoselov in 2004 [13], the "scotch tape technique" [196] is a simple and efficient way to mechanically exfoliate 2D-materials down to the monolayer. Using scotch tape directly on the bulk material, this surprising technique allows to cleave the atomically thin layers and isolate mono and few layers of extremely high quality.

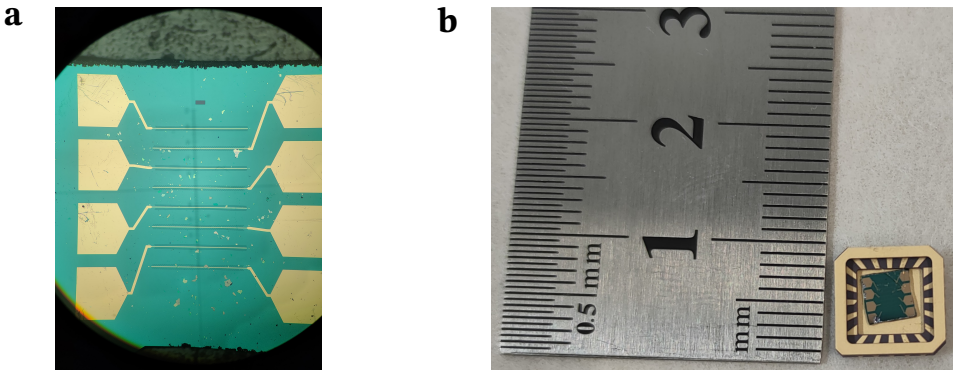

Figure A.2: Example of sample design. **a.** Optical image of a typical sample with prepatterned electrodes and holes. **b.** Real size of such a sample in its chip carrier.

Figure A.3 gives a summary of the process:

1. Place the bulk material on a piece of adhesive tape.
2. Fold the tape and peel of the crystal.
3. Stick a second piece of scotch tape onto the first one and apply a gentle pressure.
4. Peel off the second piece of adhesive tape. Repeat step 3 until obtaining semi-transparent areas of crystal.
5. Stick the tape with interesting areas on the target substrate or PDMS stamp and massage gently for a few minutes.
6. Peel off the adhesive tape from the substrate or PDMS stamp. For direct deposition on Si/SiO_2 substrates (used for graphene and hBN), the peel off needs to be slow and continuous. For deposition on a polydimethylsiloxane (PDMS) stamp (used for TMDs), the peel off needs to be done in one sharp and fast go.

Once exfoliated, mono and few layers thick flakes can be identified by optical contrast and, if needed, picked up and/or transferred using one of the techniques described below.

A.3 Transfer techniques and assembly of van der Waals heterostructures

In order to stack 2D-materials or place a flake or heterostructure on a precise location of a substrate, we need deterministic transfer techniques. I will now present the two techniques used in this work and discuss about the difficult task of efficiently suspend 2D-materials and heterostuctures.

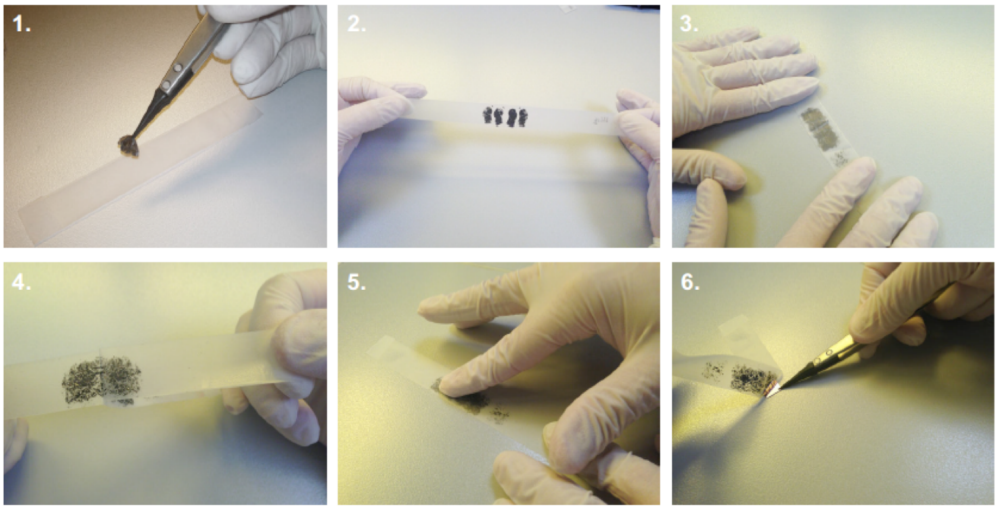

Figure A.3: Illustration of the steps of the mechanical exfoliation of 2D-materials. Adapted from [16].

A.3.1 Full dry transfer

This technique is based on the work of Castellanos-Gomez *et al.* [197] and is used to transfer monolayer TMDs. The point here is to deposit the exfoliated material on a film of PDMS on a glass slide as an intermediate step. Identification of thin flakes can be done directly on the polymer stamp. Once identified, the flake can be transferred deterministically thanks to the transfer station of the 2D lab shown figure A.4.

The transfer station is composed of a heating stage holding the target substrate with an integrated heater reaching 200°C, fixed on a rotating stage and embedded in an optical microscope. A stamp holder is positioned next to the heating stage with independent xyz positioning capabilities.

When the chosen flake and the target on the substrate are aligned, contact between the PDMS stamp and the substrate can be made. A contact line then appears and is generally brought mechanically to approximately a few tens of micrometers away from the area of interest, thanks to the z axis of the stamp holder positioning stage. We then use the heater to smoothly move the contact line through the flake by slowly increasing the temperature.

Once the whole flake is in contact, we can stop the heater and let the PDMS stamp to cool down and retract slowly from the substrate. The contact line will then follow the opposite path. This part is the most critical and needs to be done very slowly. As the PDMS will detach itself slowly from the substrate, the flake will remain on the substrate and transfer will be achieved.

This process can be iterated multiple times, but is more suited to the transfer of one single flake on a substrate or to complete simple heterostructures as every iteration has a non negligible risk of destroying already transfered materials.

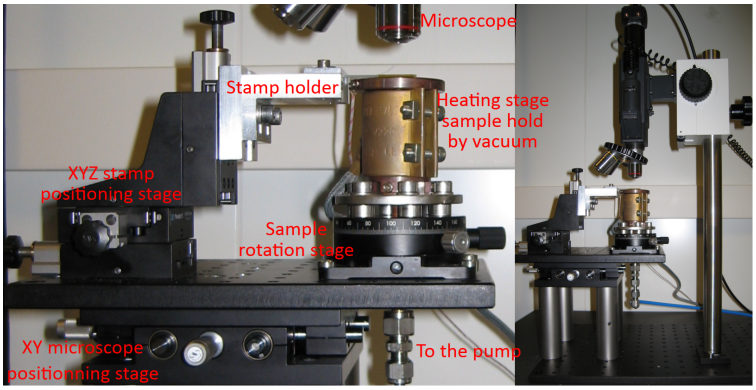

Figure A.4: Picture of the 2D lab transfer station. Adapted from [40].

A.3.2 PC-method

This technique uses a polycarbonate (PC) film as additional layer on top of a small PDMS stamp to create a "pick-up" stamp on which we will assemble the heterostructure before transfering it to the final substrate. Heating the stamp at 200°C for approximately 20 seconds is recommended to improve the adhesion of the PC film on the PDMS stamp. A thin hBN flake is then used on top of the PC film to complete the stamp (see figure A.5).

To pick-up a flake with such a stamp, we use the fact that adhesion between PC and hBN increases to overcome the adhesion of hBN on SiO_2 when the temperature reaches 80°C. For this, the substrates needs to be pre-heated to 40°C. Then contact between the stamp and the flake to pick-up can be made in a similar fashion as for the full dry technique. Once the contact has been fully achieved between the stamp and the flake to pick-up, the temperature can be increased to 80°C. The stamp can then be slowly withdrawn and the flake will be picked up. This procedure can be repeated to build complex heterostructures before deposition.

When the stacking is complete, the deposition on the target substrate is done by performing a similar procedure than for picking-up a flake, but with a temperature increased to 200°C instead of 80°C in order to melt the PC film. The sample needs to be cleaned afterwards in chloroform for at least one night to dissolve PC residues.

A.3.3 The art of suspending 2D-materials and heterostructures

All the different transfer techniques were tried for the suspension of 2D-materials and heterostructures over micrometric circular pits. Each of them are viable but more suited to different types of samples. Suspended monolayer TMD samples (see chapter 2) where done using the full dry transfer technique with extra care on substrates with low hole density in order to maximise the adhesion area. The PC method was succesfully tested for the suspension of few-layer graphene/TMD/hBN heterostructures and used later on to suspend more complex heterostructures. The main drawback is the mandatory hBN flake that highly increases the thickness of the suspended heterostructure. Samples made with this technique seem to exhibit larger built-in strain.

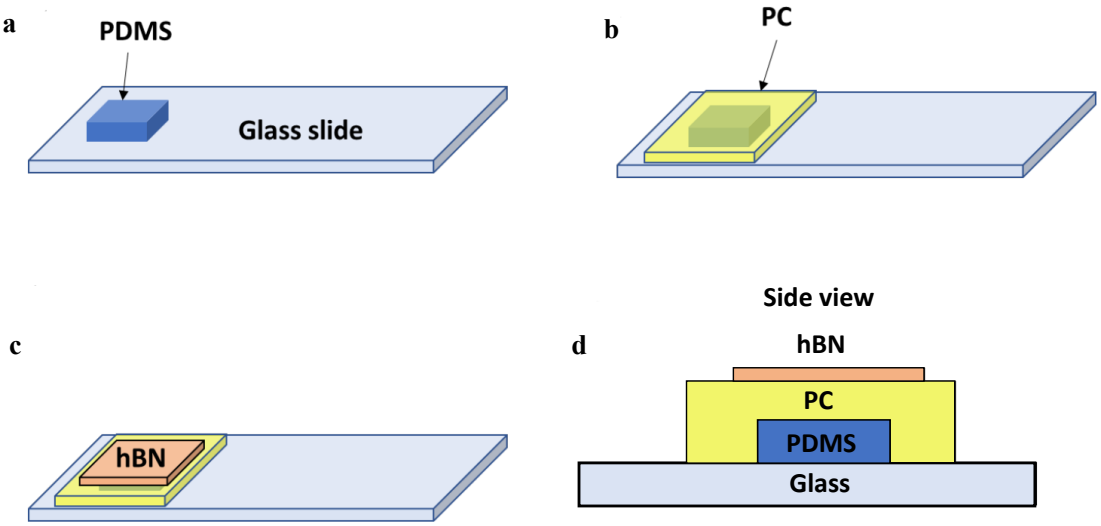

Figure A.5: The "pick-up" stamp. a. A piece of PDMS is put on a glass slide. **b.** The PDMS is covered by a PC film. **c.** A thin hBN flake is picked up to complete the stamp. **d.** Side view of the complete "pick-up" stamp. Adapted from [46].

An hybrid all dry method was used to suspend thin graphene/TMD heterostructures as presented in chapter 4. Graphene was first directly exfoliated on a substrate with high density of holes and electrodes, randomly giving large thin flakes of high quality. When a thin, if possible monolayer flake was identified to be at the same time suspended and connected to an electrode, a monolayer TMD flake was deposited on top of the suspended graphene via the all dry transfer method.

APPENDIX B

List of samples

Sample designation	Sample geometry
Sample A (MoS_2)	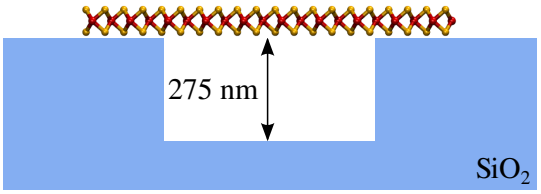
Sample B (WS_2)	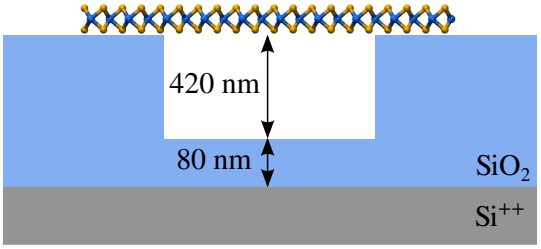

Figure B.1: Samples used to work on the dense electron-hole phases in suspended monolayer TMDs, presented in chapter 2.

Sample designation	Sample geometry
Sample 1 (hBN/Gr/WSe_2/hBN)	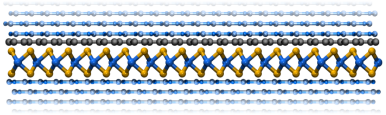
Sample 2 (Gr/WSe_2)	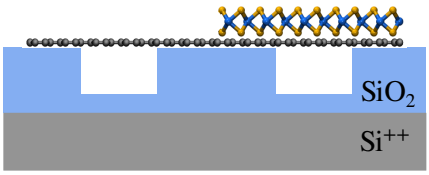
Sample 3 (hBN/$MoSe_2$/Gr)	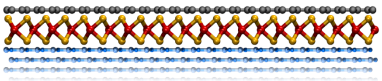
Sample 4 (Gr/WSe_2)	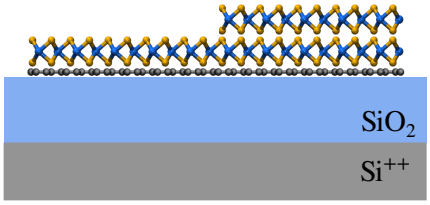

Figure B.2: Main samples used to work on symmetry dependent screening of the optical phonons in graphene, presented in chapter 3.

Sample designation	Sample geometry
Device 1 ($Gr/MoSe_2$)	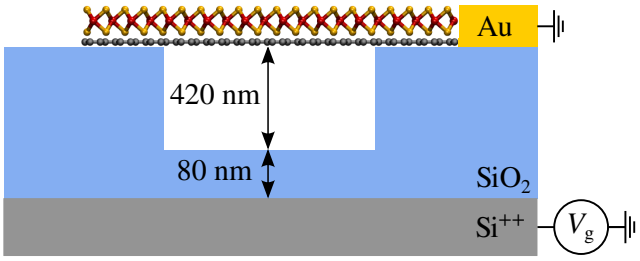
Device 2 ($FL\text{-}Gr/WSe_2$)	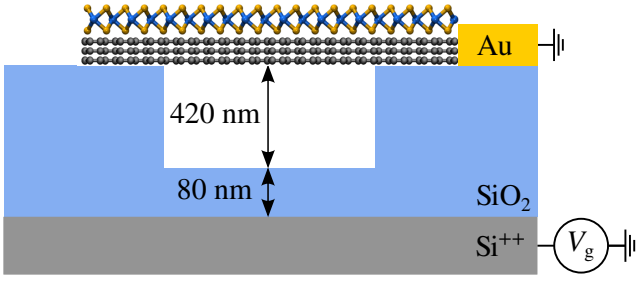

Figure B.3: Samples used to work on the electromechanical modulation of the optical properties of graphene/TMD heterostructures, presented in chapter 4.

APPENDIX C

Experimental setup

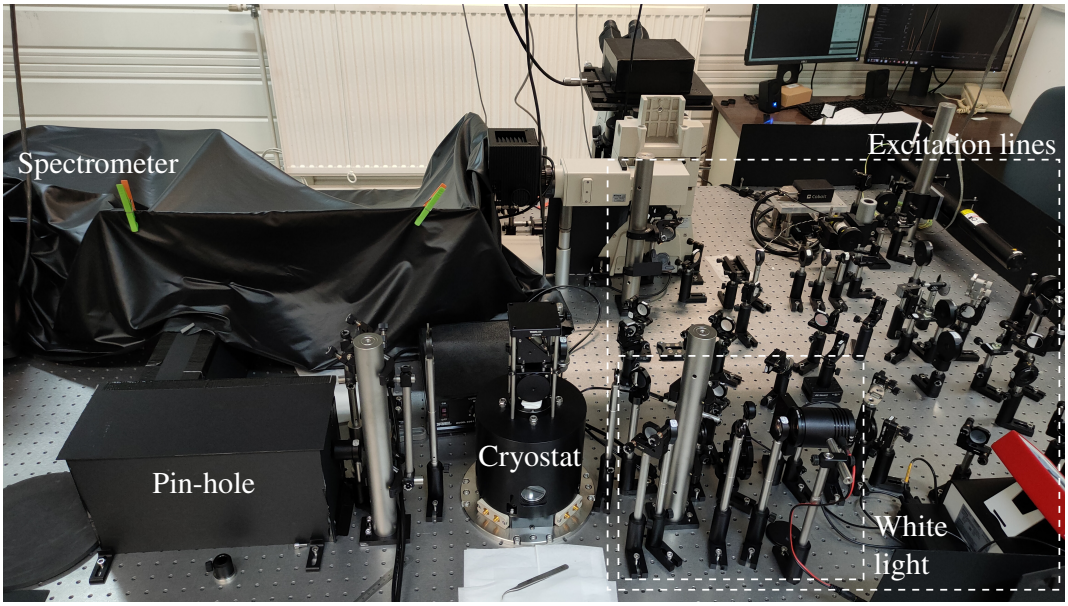

Figure C.1: A platform for opto-electro-mechanics.

In this section I will present the experimental setup developed during this thesis, with the aim of combining optical spectroscopy and nanomechanics of 2D-NEMS in a state-of-the-art cryo-compatible confocal microscope.

C.1 Helium free cryostat

This setup is built around a close-cycle Attocube Attodry 800 cryostat. The sample is cooled via thermal conduction: the cold head at the bottom of the sample chamber (see figure C.2a) is cooled down to a base temperature of 4 K thanks to a closed circuit of helium. The thermal link between the sample and the cold head is done by an Attocube Thermal Coupler (ATC), acting as a thermal bridge with incorporated thermal sensor and heater (see figure C.2b). This configuration allows to reach temperatures from 4 K to 320 K with a thermal stability that can reach < 10 mK and remain stable for hours.

The sample is mounted on top of a stack of cryo-compatible piezoelectric positionners and scanners. This piezo stack allows to move the sample in the 3 directions in space and perform high precision scans on a 2D plan. From bottom to top, it is composed of (see figure C.2b):

- an ANPz102 with resistive readout as z positionner. It has a travel range of 4.8 mm and a maximum resolution of 200 nm.
- Two ANPx101 with resistive readout as x and y positionners, with a travel range of 5 mm and a maximum resolution of 200 nm.
- An ANSxy100lr xy scanner with a 30 × 30 µm scanning range at 4 K (50 × 50 µm at 300 K) and sub-nm resolution.

To mount our samples, we use a modified sample holder with a home made PCB designed by Jérémy Thoraval, engineer at IPCMS (see figure C.2c). It is made to use samples in commercial chip carriers compatible with our second setup (see section C.3) and links the sample electrodes to the breakout box of the cryostat. Up to 8 electrodes can be contacted simultaneously.

Illumination and light collection are done thanks to a cryo-compatible microscope objective LT-APO with a 0.65 numerical aperture (NA) and long working distance (5 mm). The anti reflective coating allows more than 80% of transmitted light for wavelengths between 400 and 1000 nm, with an apochromatic range between 570 and 730 nm.

C.2 A cryo-compatible confocal microscope

The optical setup around the cryostat is set as a confocal microscope in backscattering geometry. Three different continuous lasers can be used and focused simultaneously onto the sample: a 633 nm He-Ne laser, a 532 nm diode laser and a 785 nm diode laser. Combinations

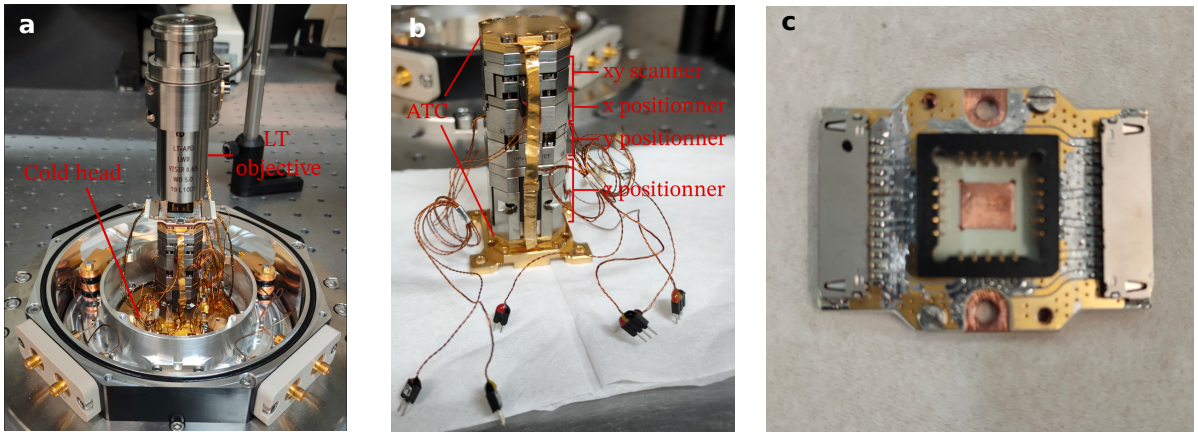

Figure C.2: Inside the sample chamber. a. Inside of the sample chamber once opened and the thermal shield removed. **b.** Details of the piezo stack. **c.** The home made PCB on a modified sample holder.

of half-wave plates ($\lambda/2$), polarising beamsplitters (PBS) and neutral density (ND) filters are used to change the incident power of the laser. A sketch of the setup is presented in figure C.3.

The 633 nm line is also used for the optical detection of mechanical motion of the 2D-NEMS (see section 4.2.1). A quarter wave plate ($\lambda/4$) is used to circularly polarize the light sent to the sample and linearise it back once reflected from the sample before reaching a PBS. Changing the angle of the quarter wave plate allows then to tune the intensity of the beam reaching the avalanche photodiode (APD) used to measure the reflected laser intensity in the reflective measurement of the mechanical motion (see section 4.2.1). The APD can be connected to the input of a HFLI Lock-in amplifier from Zurich Instrument (ZI-HFLI), a Vector Network Analyser (VNA) or a Spectrum Analyser (SA) to obtain the spectrum of the mechanical vibration.

Because of the far field nature of this configuration, our maximum resolution is limited by diffraction and the minimum lateral spotsize achievable Δx is given by the Abbe diffraction limit [103, 198]

$$\Delta x = 0.61 \frac{\lambda}{\mathrm{NA}} \tag{C.1}$$

with λ the wavelength of the light and NA the objective's numerical aperture. By applying this formula for the case of our 633 nm He-Ne laser and 0.65 NA objective we can reach an optimal spotsize of 595 nm.

The light focused in this diffraction limited spot is reflected by the sample and collected by the same objective together with scattered and emitted light at different wavelengths, before being transmitted through the beamsplitter. The collected light is then spatially filtered by being focused on a 75 µm pinhole. The bottom left corner of figure C.3 illustrates the confocal principle applied here [103]: the focal point on the sample is conjugated with the pinhole (green circle) to filter out collected contributions from points out of the diffraction limited spot (orange triangle). Furthermore, the pinhole is also strongly reducing the detection of out-of-focus points in the optical axis (red square), giving a better resolution along the z axis. This can be useful for different applications. In our case because of the small ratio between the thickness of our samples and the focal sensitivity of our long working distance objective, we cannot strictly achieve an out-of-plane resolution of our sample but the spatial filtering allows to strongly reduce unwanted contributions from the underlying substrate.

Once spatially filtered the light is collimated again and sent to an Acton SP2500 monochromator and a Pylon CCD camera from Princeton Instrument. Three different gratings can be used to diffract the incoming light: a 150 grooves/mm grating used for photoluminescence and reflectance contrast spectroscopy, a 600 grooves/mm grating used for Raman spectroscopy and precise low temperature photoluminescence, and a 1800 grooves/mm grating used for low frequency Raman spectroscopy. Finally, the diffracted light is focused on a 1340 × 100 PyLoN VIS/NIR CCD camera from Princeton Instrument.

Imaging of the sample is done thanks to a flippable lense placed just before the beamsplitter. This lens focuses the light at the bottom focal plane of the objective to obtain a large and uniform illumination of the sample. A flippable mirror placed before the pinhole allows to send the collected light to a webcam and image the sample.

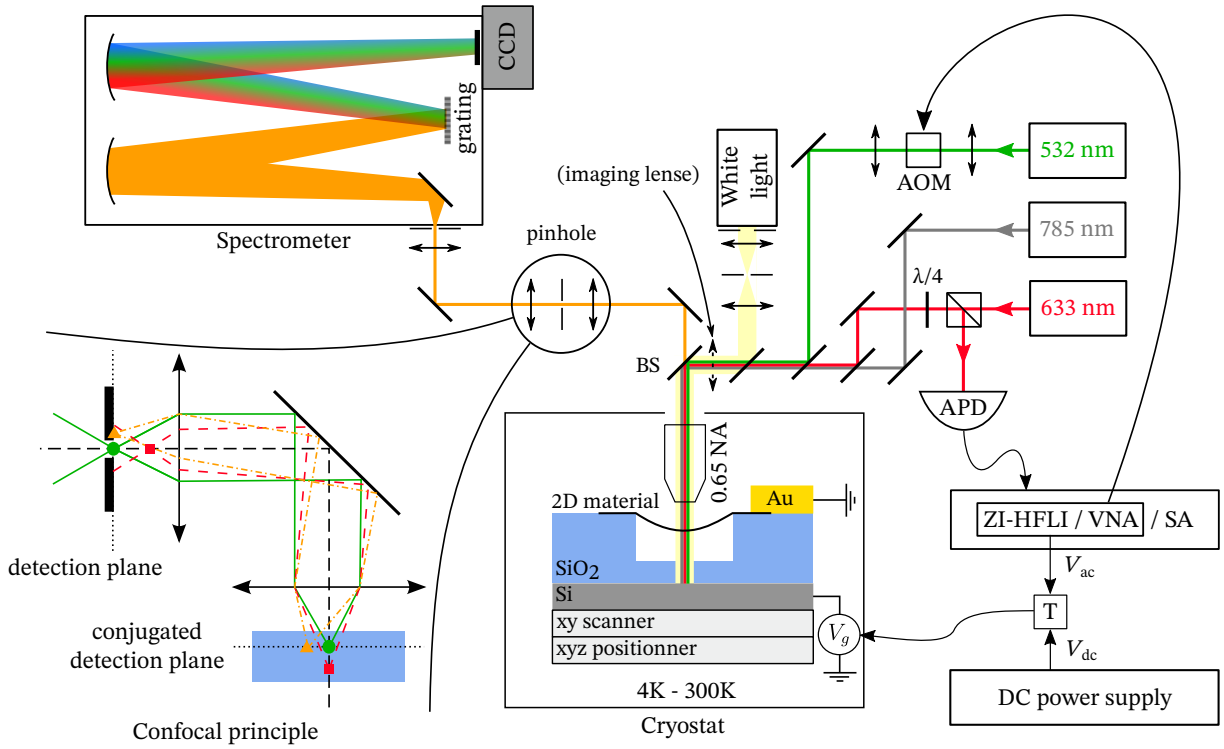

Figure C.3: Sketch of the setup. BS: Beamsplitter (Dichroic, 50/50 or 10/90), AOM: Acousto-optic modulator, APD: Avalanche photodiode, ZI-HFLI: Zurich Instrument High Frequency Lock-In, VNA: Vector Network Analyser, SA: Spectrum Analyser, T: Bias tee. Sketch of the confocal principle adapted from [103].

C.3 Room temperature setup

The room temperature experiments presented in chapter 2 and 3 where measured using a different setup that is described in this section. The room temperature setup consists in a confocal microscope in backscattering geometry built around a commercial optical microscope as visible in figure C.4. The reflected light is then sent to an Acton 2500 monochromator and a Spec10 CCD camera from Princeton Instrument with similar caracteristics as the Pylon camera of the setup presented in the previous section. Note that a similar commercial

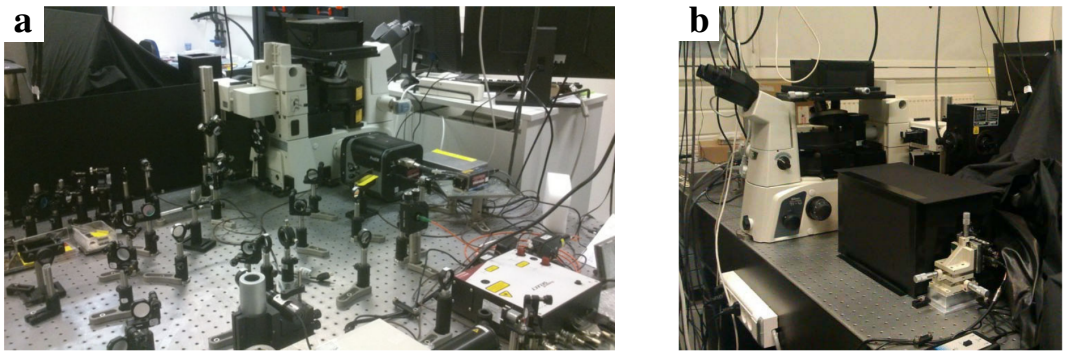

Figure C.4: Room temperature experimental setup.

microscope is included to the newly developed setup presented in the previous setup and can also be used for room temperature experiments.

A xyz piezo stage allows to map the optical response of the sample at room temperature with a maximum dimension of 200×200 µm and a 100 nm precision. A helium flow cryostat from Cryo Industry of America (CIA) with electrical access can be used to measure the optical response. However the poor stability of this setup when operating at low temperature makes optomechanical experiments quite difficult. In this project, the CIA cryostat was mostly used as a room temperature vacuum chamber and employed for the investigation of the high density regimes in suspended monolayer TMDs presented in chapter 2.

APPENDIX D

Optical spectroscopies

The optical properties of a material are set by the way excitations in this material couples to light. Despite their fundamentally different natures, all those excitations are described as oscillators that can be forced or driven by an electromagnetic field, and show resonances in the measured spectra. Optical spectroscopies exploit different light-matter coupling mechanisms to measure frequency-dependent susceptibilities.

Two types of excitations will be extensively studied in this work, using two different spectroscopic approaches that will be introduced in this section. The first ones are excitons [49, 4], that can be studied both in absorption and emission, via measurements of reflectance contrast or photoluminescence experiments. The second ones are phonons [4, 5] that will be probed by Raman spectroscopy.

D.1 Measuring absorption and emission spectra

D.1.1 Absorption and reflectance contrast

The absorption spectrum of a medium $\alpha(\omega)$ is directly related to its complex dielectric function $\epsilon(\omega)$ by [49]

$$\alpha(\omega) = 2\frac{\omega}{c}\mathrm{Im}\left[\epsilon^{1/2}(\omega)\right] \tag{D.1}$$

and can be modeled to first approximation by considering charged Lorentz oscillators [49]. Each mode is then related to a dipole moment leading to a net polarization that affects the dielectric function. In linear response theory, this model results in a sum of the resonances and gives

$$\epsilon(\omega) = 1 + \sum_j \frac{f_j}{\omega_j^2 - \omega^2 - i\omega\gamma_j} \tag{D.2}$$

with ω_j the j-th resonance frequency, γ_j the j-th damping rate and f_j the j-th oscillator strength. For dipole allowed transitions, such as bright excitons, the oscillator strength can be defined as

$$f_j = \frac{2N_j\omega_j}{\epsilon_0\hbar}|\langle f|\hat{\boldsymbol{d}}.\boldsymbol{e}|i\rangle|^2 \tag{D.3}$$

where N_j is the density of oscillators with resonance frequency ω_j, i and f the initial and final states of the involved transition, $\hat{\boldsymbol{d}}$ the dipole operator and $\boldsymbol{e} = \boldsymbol{E}/|\boldsymbol{E}|$ the unitary vector indicating the direction of the incoming light field.

In TMDs, absorption is strongly dominated by excitons (see section 1.2.3). Figure D.1a sketches the absorption process for the example of $MoSe_2$, the semiconducting TMD with the simplest optical spectrum. $|\text{fcc}\rangle$ represents the free carriers continuum such that $E_{\text{gap}} = \hbar\omega_{\text{fcc}}$, $|\text{X}\rangle$ and $|\text{X}^*\rangle$ represents the neutral exciton and trion (or charged exciton), and $|\text{D}\rangle$ represents excitons bound to local defects.

In practice, we do not directly measure the absorption spectrum of TMDs but a related quantity being the reflectance contrast

$$\frac{\Delta R}{R} = \frac{R_{\text{sample}} - R_{\text{substrate}}}{R_{\text{substrate}}} \tag{D.4}$$

obtained by shining white light on the sample and comparing the reflected spectrum of our sample with the one of the bare substrate. This quantity is directly related to the absorption spectrum $\alpha(\omega)$ but convoluted to interferences occuring in the sample, because of multiple reflexions at the interfaces of each dielectric medium. Complex modeling of the optical response is needed to predict the shape of the observed spectrum in this case [199]. Furthermore, the spectrum of the white light used in real life experiments may not be perfectly flat and increases even more the complexity of the reflectance contrast spectrum.

A typical reflectance contrast spectrum of $MoSe_2$ is shown figure D.1b. As expected, intrinsic excitonic states strongly dominates the absorption spectrum. It is worth noting that the defect states D are still absorbing despite the absence of observed feature in the spectrum. The reason for it being that their absorption is simply too low with respect to the ones of X and X^* to be detected.

D.1.2 Photoluminescence

While reflectance contrast is used to probe the absorption of excitons in TMDs, photoluminescence (PL) experiments measure the spontaneously emitted light. Laser excitation with an energy $\hbar\omega_{\text{in}} > E_{\text{gap}}$ is used to excite an electron-hole pair, and populate the $|\text{fcc}\rangle$ state. Strictly speaking, one can use an excitation with an energy $\hbar\omega$ lower than the lowest excitonic state and detect the emission of an excitonic population excited by upconversion, thanks to the interaction with phonons. Resonant excitation of a given state is also possible by matching the excitation energy with the energy of the given state. However in this work, the excitation is always non-resonant and at higher energy than the exciton state. This electron-hole pair can then recombine radiatively or thermalize non-radiatively to one of the excitonic states. Each involved state has a lifetime τ before it recombines. This lifetime is defined by the various decay paths available, that can be either radiative or non-radiative. One can separate those contributions by defining a state's decay rate as

$$\Gamma = \frac{1}{\tau} = \Gamma_{\text{r}} + \Gamma_{\text{nr}} \tag{D.5}$$

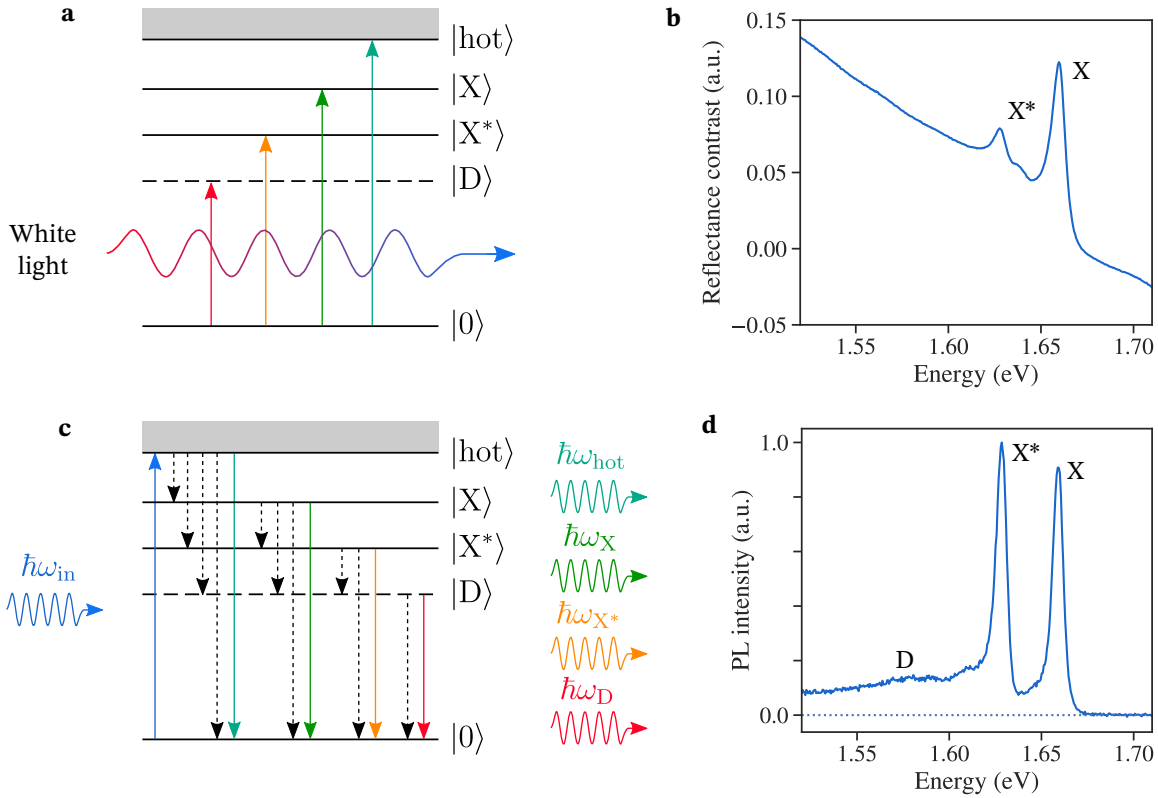

Figure D.1: Absorption and emission spectroscopy of $MoSe_2$ at low temperatures. Plain horizontal lines represents states visible in absorption, dashed horizontal lines are states that are not visible in absorption but may be detected by emission. Plain vertical arrows represent radiative decay or direct absorption while vertical dashed arrows represent non-radiative decay. **a.** Sketch of the absorption process in $MoSe_2$. **b.** Reflectance contrast spectrum of $MoSe_2$ with the neutral exciton X and trion X^* that dominates the absorption spectrum. **c.** Sketch of the photoluminescence process in $MoSe_2$. **d.** Photoluminescence spectrum of $MoSe_2$.

with Γ_r the radiative decay rate and Γ_{nr} the non-radiative decay rate. The efficiency of the radiative emission of a state is characterized by its quantum yield

$$\eta = \frac{\Gamma_r}{\Gamma_r + \Gamma_{nr}}. \tag{D.6}$$

Obviously, η is directly related to the emitted intensity and illustrates how non-radiative decay can quench the light emission if $\Gamma_{nr} \gg \Gamma_r$, independently of the underlying nature of the non-radiative decay path. Optimal emission efficiency is reached for $\Gamma_{nr} \ll \Gamma_r$.

Figure D.1c sketches the various possible decay paths between the different states in $MoSe_2$. Plain vertical arrows represents radiative decay while dashed arrows represents non-radiative decay. In the linear regime, the population of every state is determined by a complex interplay with the other states and the evolution of the population density N_j of the state $|j\rangle$ can be described with a differential equation of the form [200]

$$\frac{dN_j}{dt} = \sum_i \Gamma_{nr}^{i\to j} N_i - \sum_i \Gamma_{nr}^{j\to i} N_j - \Gamma_r^j N_j \tag{D.7}$$

where the first term of the right hand side describes contributions from non-radiative transitions from the other states to the state $|j\rangle$, the second term describes non-radiative decay towards the other states and the last term is related to radiative recombination from $|j\rangle$ to the ground state $|0\rangle$. Note that the two last terms in the right hand side are simply an expanded expression of $-\Gamma_j N_j$ that highlights the multiplicity of the possible decay paths. A pumping term might be included to describe the excitation of the $|\text{fcc}\rangle$ state at the origin of the recombination cascade. In continuous wave (CW) photoluminescence this pumping term is a constant directly related to the power of the incident laser, leading to a steady state situation with constant excitonic densities N_j. Experimentally that means that the density of population of all the excitonic states is affected by changes in the laser power. This will be important in chapter 2 when we will explore high density regimes in suspended TMDs.

Since the detected PL signal is composed of the emission features from all the states involved in the recombination cascade, more features are usually present in a PL spectrum than a reflectance contrast spectrum. A first example is visible in figure D.1d showing a PL spectrum of $MoSe_2$ where emission from defect states D is visible alongside the one from X and X*. This specific example can be explained by the fact that for sufficiently low laser power, the population of D states is comparable to the ones of X and X* leading to comparable emission intensities. This is not true anymore at high power because of saturation of defect states populations [103]. Another example is the charged biexciton XX^* visible in the PL spectrum of WS_2 [119]: this state is a composite state binding a dark exciton and a trion. Because the dark exciton transition is spin forbidden, it cannot be formed by the absorption of one photon and thus is not visible in reflectance contrast measurements. However, in PL experiments, the dark exciton state can be populated by the non-radiative relaxation of a state with higher energy and lead to the formation of the XX^* state that can recombine radiatively and be detected.

D.2 Introduction to Raman spectroscopy

D.2.1 Classical picture

Raman spectroscopy is based on the inelastic scattering of light with phonons. It was first reported by C. V. Raman in 1928 [201] and is now one of the main spectroscopic techniques to detects vibrations in molecules or solids. The description given here follows the one from P. Y. Yu and M. Cardona in ref. [5]. The main physical insights of Raman spectroscopy can be described classically by considering the polarization wave $\boldsymbol{P} = \epsilon_0 \bar{\boldsymbol{\chi}} \boldsymbol{E}$ induced by an electromagnetic wave $\boldsymbol{E}(\boldsymbol{r}, t) = \boldsymbol{E}_\text{i} \cos(\boldsymbol{k}_\text{i}.\boldsymbol{r} - \omega_\text{i} t)$ traveling through a medium with electric susceptibility $\bar{\boldsymbol{\chi}}$ [5].

At finite temperatures, thermally excited atomic vibrations in the medium induces fluctuations in the electric susceptibility $\bar{\boldsymbol{\chi}}$. The atomic displacement related to a phonon can be written as a plane wave $\boldsymbol{u}(\boldsymbol{r}, t) = \boldsymbol{u}_0 \cos(\boldsymbol{q}.\boldsymbol{r} - \Omega t)$ with frequency Ω and wavevector $\boldsymbol{q}$. In the quasistatic approximation[1] we can consider $\bar{\boldsymbol{\chi}}$ to be function of the atomic displacement

[1] We consider $\omega_e \gg \Omega$ with ω_e the characteristic electronic frequency of electrons, that determines $\bar{\boldsymbol{\chi}}$.

$\boldsymbol{u}$. As the amplitude of atomic vibrations is small with respect to the lattice constant in a solid, $\bar{\boldsymbol{\chi}}$ can be expanded as a Taylor series in $\boldsymbol{u}$ with respect to the equilibriuum position of atoms. To the first order, one obtains

$$\bar{\boldsymbol{\chi}} \approx \bar{\boldsymbol{\chi}}_0 + \left(\frac{\partial \bar{\boldsymbol{\chi}}}{\partial \boldsymbol{u}}\right)_0 .\boldsymbol{u} \tag{D.8}$$

with $\bar{\boldsymbol{\chi}}_0$ the electric susceptibility tensor without fluctuations, while the second term expresses the fluctuating part of the electric susceptibility due to lattice vibrations. Thanks to this expansion, we can rewrite the polarization wave as

$$\boldsymbol{P}(\boldsymbol{r}, t, \boldsymbol{u}) = \boldsymbol{P}_0(\boldsymbol{r}, t) + \boldsymbol{P}_{\text{ind}}(\boldsymbol{r}, t, \boldsymbol{u}) \tag{D.9}$$

where $\boldsymbol{P}_0$ is a polarization wave in phase with the excitation wave, related to Rayleigh scattering processes

$$\boldsymbol{P}_0(\boldsymbol{r}, t) = \epsilon_0 \bar{\boldsymbol{\chi}}_0 \boldsymbol{E}_{\text{i}} \cos(\boldsymbol{k}_{\text{i}}.\boldsymbol{r} - \omega_{\text{i}} t) \tag{D.10}$$

and $\boldsymbol{P}_{\text{ind}}$ is the polarization wave induced by the fluctuating electric susceptibility because of phonons, expressed as

$$\boldsymbol{P}_{\text{ind}}(\boldsymbol{r}, t, \boldsymbol{u}) = \epsilon_0 \left(\frac{\partial \bar{\boldsymbol{\chi}}}{\partial \boldsymbol{u}}\right)_0 .\boldsymbol{u}_0 \cos(\boldsymbol{q}.\boldsymbol{r} - \Omega t) \boldsymbol{E}_{\text{i}} \cos(\boldsymbol{k}_{\text{i}}.\boldsymbol{r} - \omega_{\text{i}} t). \tag{D.11}$$

The cosine product in equation D.11 can be linearised as

$$\begin{aligned} \boldsymbol{P}_{\text{ind}}(\boldsymbol{r}, t, \boldsymbol{u}) &= \frac{\epsilon_0}{2} \left(\frac{\partial \bar{\boldsymbol{\chi}}}{\partial \boldsymbol{u}}\right)_0 .\boldsymbol{u}_0 \boldsymbol{E}_{\text{i}} \left[\cos([\boldsymbol{k}_{\text{i}} + \boldsymbol{q}].\boldsymbol{r} - [\omega_{\text{i}} + \Omega]t) + \cos([\boldsymbol{k}_{\text{i}} - \boldsymbol{q}].\boldsymbol{r} - [\omega_{\text{i}} - \Omega]t)\right] \\ &= \boldsymbol{P}_{\text{AS}}(\boldsymbol{r}, t) + \boldsymbol{P}_{\text{S}}(\boldsymbol{r}, t) \end{aligned} \tag{D.12}$$

to reveal the two contributions that forms it with shifted frequencies. $\boldsymbol{P}_{\text{S}}$ and $\boldsymbol{P}_{\text{AS}}$ corresponds to *Stokes* and *Anti-Stokes* scattered waves, with respective frequencies $\omega_{\text{S}} = \omega_{\text{i}} - \Omega$ for the Stokes (S) wave and $\omega_{\text{AS}} = \omega_{\text{i}} + \Omega$ for the Anti-Stokes (AS) one. The total wavevector is conserved in this scattering process, with $\boldsymbol{k}_{\text{S}} = \boldsymbol{k}_{\text{i}} - \boldsymbol{q}$ and $\boldsymbol{k}_{\text{AS}} = \boldsymbol{k}_{\text{i}} + \boldsymbol{q}$. A numerical application of the wavevector conservation gives for visible light $k_{\text{i}} \sim 10^{-2}$ nm^{-1}, while a crystal lattice constant of around 1 Å corresponds to a wavevector $Q \sim 10^{1}$ nm^{-1}, giving the size of the associated first Brillouin zone. The ratio $k_{\text{i}}/Q \sim 10^{-3}$ gives us the portion of the Brillouin zone that we can explore and tells us that only phonons at Γ or in its very close neighbouring can be probed with Raman spectroscopy.

We define the *Raman shift* as the difference in energy of the scattered light with respect to the incident light $\Delta\omega = \omega_{\text{i}} - \omega$. This way of expressing the energy of the scattered light highlights the underlying microscopic process, that will be discussed in further details later, and gives the energy of the phonon induced in the scattering process. For Stokes and Anti-Stokes waves we have $\Delta\omega_{\text{S}} = \Omega$ and $\Delta\omega_{\text{AS}} = -\Omega$. In practice this quantity is usually given in wavenumbers as

$$\delta = \frac{\Delta\omega}{2\pi c} = \frac{1}{\lambda_{\text{i}}} - \frac{1}{\lambda} \tag{D.13}$$

and expressed in cm^{-1}.

Multiple phonon processes can be described by expanding equation (D.8) to higher order. Considering two phonons $\boldsymbol{u}_a$ and $\boldsymbol{u}_b$ with respective frequencies Ω_a and Ω_b and wavevectors $\boldsymbol{q}_a$ and $\boldsymbol{q}_b$ we can look at two-phonon processes by expanding up to the second order. The general form of the second order term of the Taylor expansion is

$$\bar{\boldsymbol{\chi}}^{(2)} = \left(\frac{\partial \bar{\boldsymbol{\chi}}}{\partial \boldsymbol{u}_a}\right)_0 .\boldsymbol{u}_a \left(\frac{\partial \bar{\boldsymbol{\chi}}}{\partial \boldsymbol{u}_b}\right)_0 .\boldsymbol{u}_b \tag{D.14}$$

and gives additional terms in the induced polarization $\boldsymbol{P}_{\mathrm{ind}}$ with frequencies shifted by $\Delta\omega = \pm(\Omega_a \pm \Omega_b)$. An interesting advantage of two phonon scattering is that phonons from any point of the Brillouin zone can be probed as long as $\boldsymbol{q}_a \pm \boldsymbol{q}_b \approx 0$. If the two phonons are identical, the obtained peak at $\Delta\omega = \pm 2\Omega$ is called an overtone and the involved process needs to respect $\boldsymbol{q}_a = -\boldsymbol{q}_b$. This is the case, for example, for the 2D-mode of graphene, being an overtone of D phonons close to the K point [28].

D.2.2 Raman tensor and peak intensities

Classically, the intensity $I(\omega)$ of a Raman peak should be proportionnal to the power radiated by its corresponding induced oscillating polarization, giving $I(\omega_s) \propto |\boldsymbol{P}_{\mathrm{ind}}.\boldsymbol{e}_{\mathrm{s}}|^2 \omega_{\mathrm{s}}^4$, with $\boldsymbol{e}_{\mathrm{s}}$ and ω_{s} the polarization and frequency of the scattered light [202, 203]. Following the previous results, we deduce that

$$I(\omega_{\mathrm{s}}) \propto |\boldsymbol{e}_{\mathrm{i}}.\bar{\boldsymbol{R}}.\boldsymbol{e}_{\mathrm{s}}|^2 |\boldsymbol{u}_0|^2 \omega_{\mathrm{s}}^4 \tag{D.15}$$

where $\boldsymbol{e}_{\mathrm{s}}$ is the polarization of the incident light field and we have defined the *Raman tensor*

$$\bar{\boldsymbol{R}} = \left(\frac{\partial \bar{\boldsymbol{\chi}}}{\partial \boldsymbol{u}}\right)_0 . \frac{\boldsymbol{u}_0}{|\boldsymbol{u}_0|}. \tag{D.16}$$

As $\bar{\boldsymbol{\chi}}$ is in the general case a rank 2 tensor, $\bar{\boldsymbol{R}}$ is also of rank 2, and has the same symmetries as the considered phonon mode. Equation (D.15) gives the selection rules for Raman spectroscopy:

- if the Raman tensor $\bar{\boldsymbol{R}}$ is null the phonon mode is not Raman active and is thus not visible via Raman spectroscopy. For centrosymmetric crystals or molecules, only vibrations that are symmetric with respect to the inversion center (G-modes) can be Raman active, while only antisymmetric vibrations (u modes) can be infrared active [204]. Note that inactive phonon modes might become visible through multimode Raman processes.

- Even if $\bar{\boldsymbol{R}}$ is not null, the intensity of the scattered light depends on the polarization of the incoming and scattered light and the mode may not be detectable in a specific experimental geometry. Since $\bar{\boldsymbol{R}}$ has the same symmetries than the phonon mode, this selection rule on polarization can also be used to measure the symmetries of the phonon by measuring the intensity of the scattered light for different polarization angles.

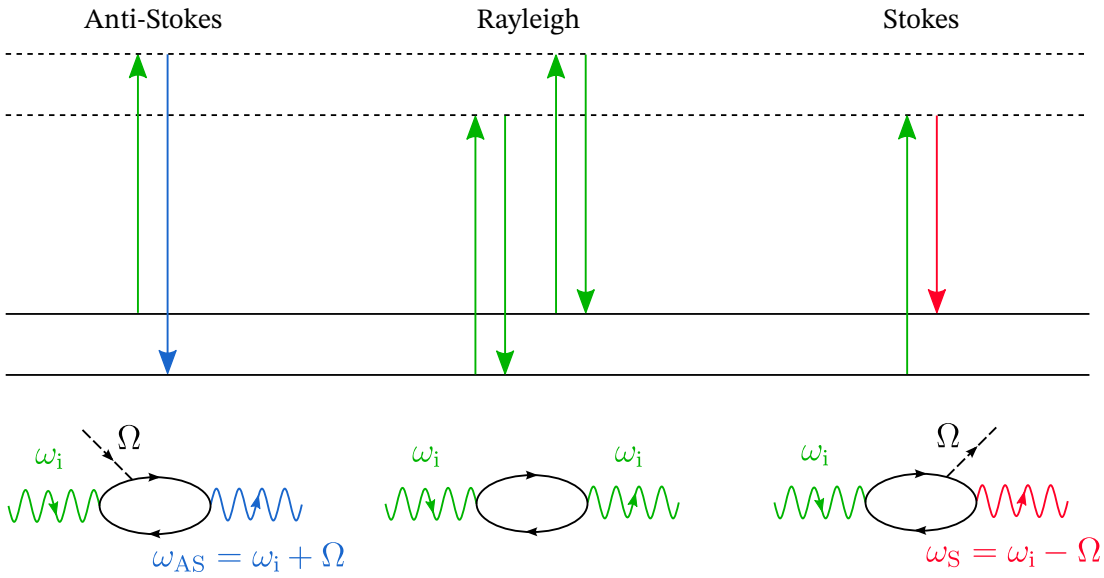

Figure D.2: Microscopic processes at play in one-phonon Raman spectroscopy. Top: energy diagram of the Anti-Stokes, Rayleigh and Stokes processes. Horizontal plain lines represent vibrationnal states, horizontal dashed lines are virtual states. Bottom: corresponding Feynman diagrams. Wavy lines represent photons, dashed lines phonons and closed loops represents electron-hole pairs.

Despite that equation (D.15) provides the selection rules for Raman spectroscopy, it also reaches the limits of the classical picture, as $I(\omega_s) \propto |\boldsymbol{u}_0|^2$ means that no light is scattered if no vibration is present, which is wrong. One has to go through a microscopic description of Raman scattering to go further. Figure D.2 describes the microscopic processes at play in one-phonon Raman scattering. First, the system is excited to a virtual state by creating an electro-hole pair via the interaction of the incoming light field with the electrons in the crystal. This electron-hole pair can either absorb a phonon (Anti-Stokes process), emit a phonon (Stokes process) or recombine without interactions with phonons (Rayleigh process). Finally, the electron-hole pair decays to the ground state by spontaneous emission of a photon.

The intensity of scattered light $I(\omega_s)$ is proportional to the scattering probability $\mathcal{P}(\omega_s)$ associated to the Feynman diagram of the considered process. This scattering probability is given by the Fermi Golden rule [5]

$$\mathcal{P}(\omega_s) = \frac{2\pi}{\hbar} \left| \sum_{n,m} \frac{\langle i|\hat{\mathcal{H}}_{e-l}(\omega_s)|m\rangle\langle m|\hat{\mathcal{H}}_{e-v}(\Omega)|n\rangle\langle n|\hat{\mathcal{H}}_{e-l}(\omega_i)|i\rangle}{[\hbar\omega_i - (E_n - E_i)][\hbar\omega_i - \hbar\Omega - (E_m - E_i)]} \right|^2 \delta(\hbar\omega_i - \hbar\Omega - \hbar\omega_s) \quad \text{(D.17)}$$

where $\hat{\mathcal{H}}_{e-l}$ is the electron-photon interaction hamiltonian, $\hat{\mathcal{H}}_{e-v}$ is the electron-phonon interaction hamiltonian, $|n\rangle$, $|m\rangle$ are the intermediate states with energies E_n and E_m. This probability can be strongly enhanced under resonant condition, meaning that one or more of the intermediate states is a real electronic state instead of a virtual state, leading to enhanced Raman intensities. Note that the electrons are unchanged after the scattering process, thus the time reversal of the Stokes process gives the Anti-Stokes process and vice-versa. For the

Rayleigh process, only one intermediate state is included and there is no contribution from the $\hat{\mathcal{H}}_{\mathrm{e-v}}$ term.

The differences between the Stokes and Anti-Stokes processes are included in the $\langle m|\hat{\mathcal{H}}_{\mathrm{e-v}}(\Omega)|n\rangle$ terms. For Stokes scattering, the number of phonons in the crystal is increased by one after the interaction, hence $\langle m|\hat{\mathcal{H}}_{\mathrm{e-v}}(\Omega)|n\rangle \propto \langle N_{\boldsymbol{q}}+1|\hat{a}^{\dagger}_{\boldsymbol{q}}|N_{\boldsymbol{q}}\rangle \propto \sqrt{N_{\boldsymbol{q}}+1}$, with $\hat{a}^{\dagger}_{\boldsymbol{q}}$ the phonon creation operator and $N_{\boldsymbol{q}}$ the number of phonons with wavenumber $\boldsymbol{q}$. Similarly, for the Anti-Stokes process $\langle m|\hat{\mathcal{H}}_{\mathrm{e-v}}(\Omega)|n\rangle \propto \langle N_{\boldsymbol{q}}|\hat{a}_{\boldsymbol{q}}|N_{\boldsymbol{q}}-1\rangle \propto \sqrt{N_{\boldsymbol{q}}}$. That way we obtain that the Stokes intensity I_{S} is proportional to $N_{\boldsymbol{q}}+1$ and the Anti-Stokes intensity is proportional to $N_{\boldsymbol{q}}$.

Phonons being bosons, they respect the Bose-Einstein statistics, giving that

$$N_{\boldsymbol{q}} = \frac{1}{e^{\hbar\Omega/k_{\mathrm{B}}T}-1} \tag{D.18}$$

with k_{B} the Boltzmann constant and T the temperature. Using this expression, we find that

$$\frac{I_{\mathrm{AS}}}{I_{\mathrm{S}}} \propto \frac{N_{\boldsymbol{q}}}{N_{\boldsymbol{q}}+1} \propto e^{-\hbar\Omega/k_{\mathrm{B}}T}. \tag{D.19}$$

Equation (D.19) tells us that the Anti-Stokes intensity is lower than the Stokes intensity by a factor which is exponentially increasing with the phonon frequency Ω and highlights the difficulty of measuring Anti-Stokes peaks for high energy modes. Provided that we have a reference point, it also gives us a way to estimate the temperature T of the phonons by comparing Stokes and Anti-Stokes intensities.

APPENDIX E

Spatial averaging of minimally doped and minimally strained samples

E.1 Defined samples areas

Spatial averages of the fitting parameters presented in the chapter 3 are obtained by considering a given region of interest. All the considered areas are depicted figure E.1. The regions of interest are first identified using the optical images of our samples. Graphene/TMD areas are further identified by examining the PL intensity of the TMD layer, which is strongly quenched due to near-field transfer of TMD excitons to graphene. To ensure that only well-coupled graphene/TMD heterostructures are considered, only regions displaying a PL quenching factor above 10 at room temperature are considered.

The error bars associated with the spatially averaged values are given by the standard deviation of each parameter in a specific area.

E.2 Built-in strain and unintentional doping

For each type of heterostructure, we examine the ω_{2D} versus ω_G and Γ_G versus ω_G correlations, as shown in figure E.2. As described in section 1.1.3 [37, 38, 146, 134, 32], such plots provide quantitative information on the residual charge carrier density (or non-intentional doping) and built-in strain field of the considered graphene area. First, the Γ_G-ω_G correlation allows to estimate the doping level based on robust models for doping induced zone-centre optical phonon renormalization [136, 205, 34]. For all cases, we find spatially averaged values $\langle\Gamma_G\rangle > 10$ cm^{-1} and no clear ω_G-Γ_G correlation (see figure E.2d-f and figure 3.7b). These observations indicate that unintentional doping leads to Fermi level shifts typically less than 100 meV away from the Dirac point [32].

The ω_{2D}-ω_G correlation allows us to separate the effect of doping and strain and hence resolve small variations of built-in strain in the studied hBN-based heterostructures (see figure E.2b,c). These variations leads to a scatter in the measured values of ω_{2D} and hence to slightly increased errorbars in the precise determination of the blueshift of ω_{2D} due to dielectric screening. However, despite these small variations, the ω_{2D}-ω_G correlations differs only

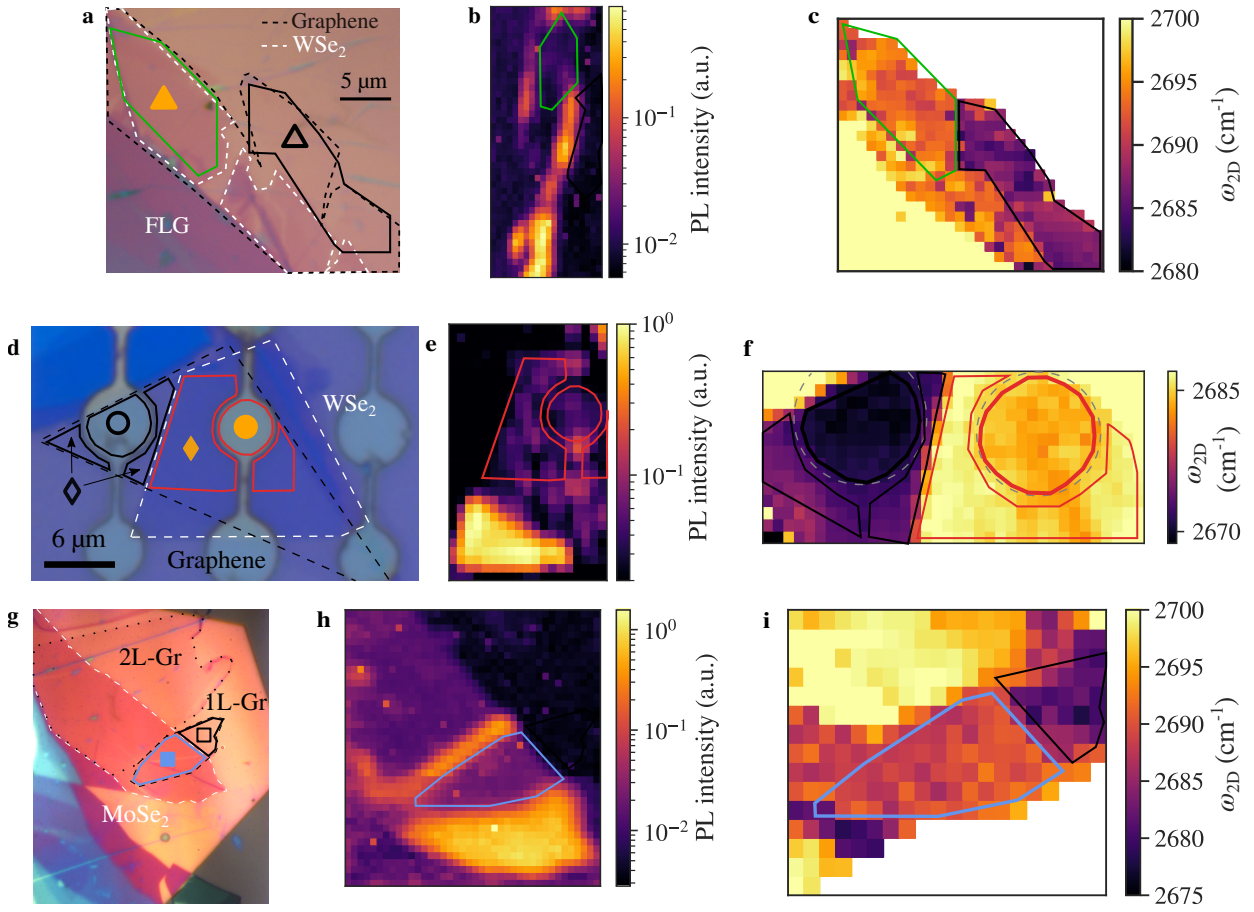

Figure E.1: Identification of the areas of interest. Top row: Optical image, PL intensity map and ω_{2D} map of Sample 1 with hBN-capped graphene and graphene/WSe_2 areas. Middle row: Optical image, PL intensity map and ω_{2D} map of Sample 2 with SiO_2-supported graphene and graphene/WSe_2 areas together with their suspended counterparts. Bottom row: Optical image, PL intensity map and ω_{2D} map of Sample 3 with hBN/graphene and hBN/$MoSe_2$/graphene areas.

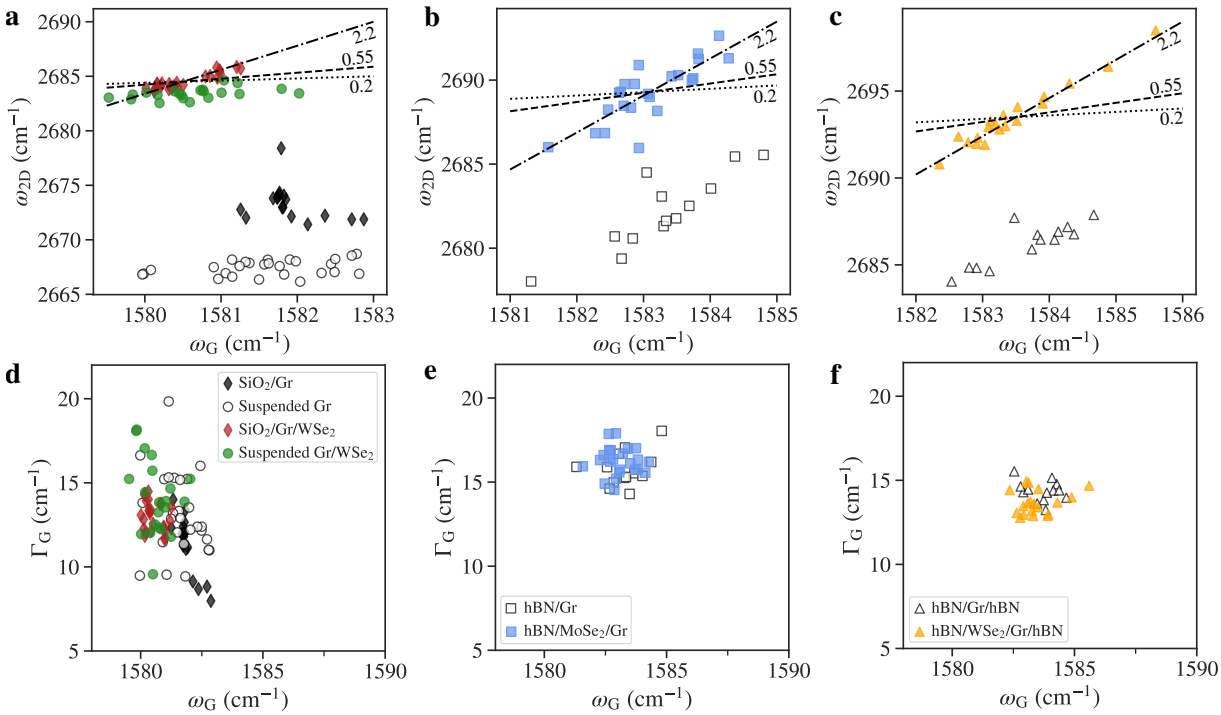

Figure E.2: Correlation plots. **a**, **b**, **c** ω_{2D} vs ω_G correlations for the three samples shown in Fig. 3 of the main text (Samples 2, 3 and 1 in Fig. E.1, respectively). The plotted lines give the expected correlation slopes for electron doping ($\partial\omega_{2D}/\partial\omega_G \approx 0.2$), hole doping ($\partial\omega_{2D}/\partial\omega_G \approx 0.55$) and strain ($\partial\omega_{2D}/\partial\omega_G \approx 2.2$). **d**, **e**, **f**. Γ_G versus ω_G correlations for the same samples.

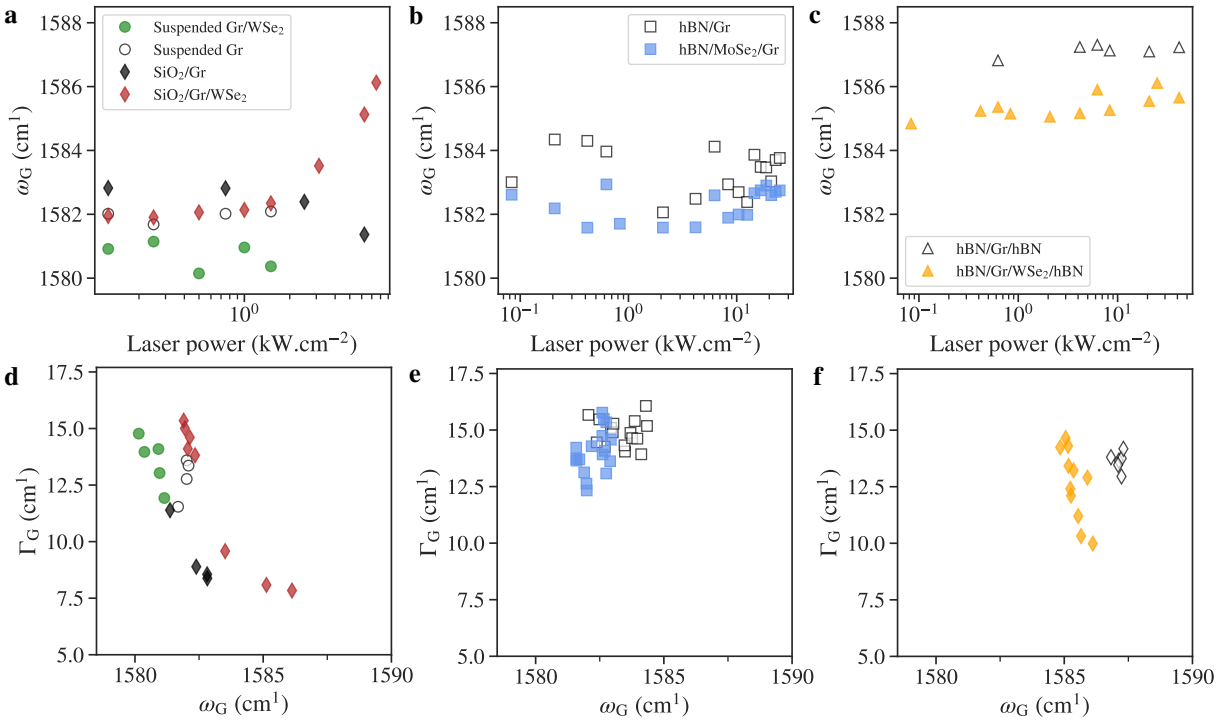

Figure E.3: Assessing photoinduced doping. Evolution of ω_G with increasing laser intensity (**a**, **b**, **c**) and Γ_G versus ω_G correlation under increasing laser intensity (**d**, **e**, **f**) for Sample 2, 3 and 1, respectively (see Fig. E.1). The laser photon energy is 2.33 eV.

by a rigid (screening-induced) shift of ω_{2D} when comparing bare graphene to graphene/TMD heterostructures, consolidating the hypothesis of low built-in strain (typically $\sim 10^{-2}\%$) in every situation.

E.3 Photoinduced doping

Interaction with polar substrates and molecular adsorbates [206] as well as interlayer charge transfer between TMD and graphene can lead to photoinduced doping of the graphene layer [99] and experimentally translate into a sizeable upshift and narrowing of the G-mode feature and may affect our results. Because of this, we performed laser power dependent measurements on our samples to determine the power threshold of such unwanted photoinduced doping. As shown in figure E.3, photodoping is observable in SiO_2-supported samples and is negligible in suspended graphene and in hBN-supported or hBN-capped samples [100]. To avoid any contribution from photoinduced doping of the graphene layer, all data presented in chapter 3 were acquired with laser powers below the threshold values observed in our power dependent analysis (typically $\sim 100\ \mu W/\mu m^2$).

APPENDIX F

Dynamical strain tuning of the light emission in a few-layer graphene/WSe_2 sample

In this section we present our observations on device 2, formed of a few-layer graphene (FLG) / WSe_2 heterostructure in a drum-like sample geometry. An optical image of the sample is presented figure F.1a together with the corresponding map of the integrated PL intensity around the exciton emission line in figure F.1c. Most of the SiO_2-supported FLG/WSe_2 part of the sample shows a highly quenched PL intensity, as well as a shifted and filtered emission spectrum, suggesting good coupling between the two composing materials (see figure F.1b). This is not so clear for the suspended FLG/WSe_2 drum: while the emission lines are clearly redshifted from the reference SiO_2-supported WSe_2, the PL intensity and PL spectrum is not homogeneous over the whole drum (see figure F.1c,d). This points towards a non optimal coupling of the two layers and imposes to carefully choose the spatial position to measure. All the following analysis focuses on the precise position indicated by the red point in figure F.1a.

Figure F.2a shows the changes of the mechanical response with respect to V_{dc}, with a slightly more W-shaped variation than our graphene/$MoSe_2$ sample (device 1) and a similar neutrality point $V_0 \approx 4$ V. That implies a higher level of built-in stress σ_0 that can be explained simply by the thicker nature of the membrane, being formed of a thicker graphene flake than device 1. The variation of the PL spectrum with respect to V_{dc} is presented figure F.2b with a focus on the neutral exciton in figure F.2c. As expected, a progressive strain induced redshift is observed when $|V_{dc}|$ is increased, reaching $\Delta E_{X_0} \approx -4.3 \pm 1.7$ meV for $V_{dc} = -15$ V. Assuming a strain sensitivity of the exciton energy of -94 meV/% for biaxial strain in WSe_2[1] [69, 64], we deduce a corresponding static strain change $\Delta\varepsilon_s \approx 5.6 \times 10^{-2} \pm 1.8 \times 10^{-2}$ %.

An analysis of the dynamical shift through the non-linear mechanical resonance is presented figure F.3 using the same automated measurement scheme as results from figure 4.24. The sample is actuated with $V_{dc} = 12$ V and $V_{ac} = 300$ mV. The non-linear regime is more stable than what was observed in device 1 and a small redshift is observed with values that follows the duffing response and present the same hysteresis: as visible in figure F.3b

[1] Note that this value was determined on suspended WSe_2 and not a graphene/WSe_2 heterostructure [69]. A similar analysis than performed on device 1 and presented in section 4.4.1 would give a more realistic estimation of the strain sensitivity.

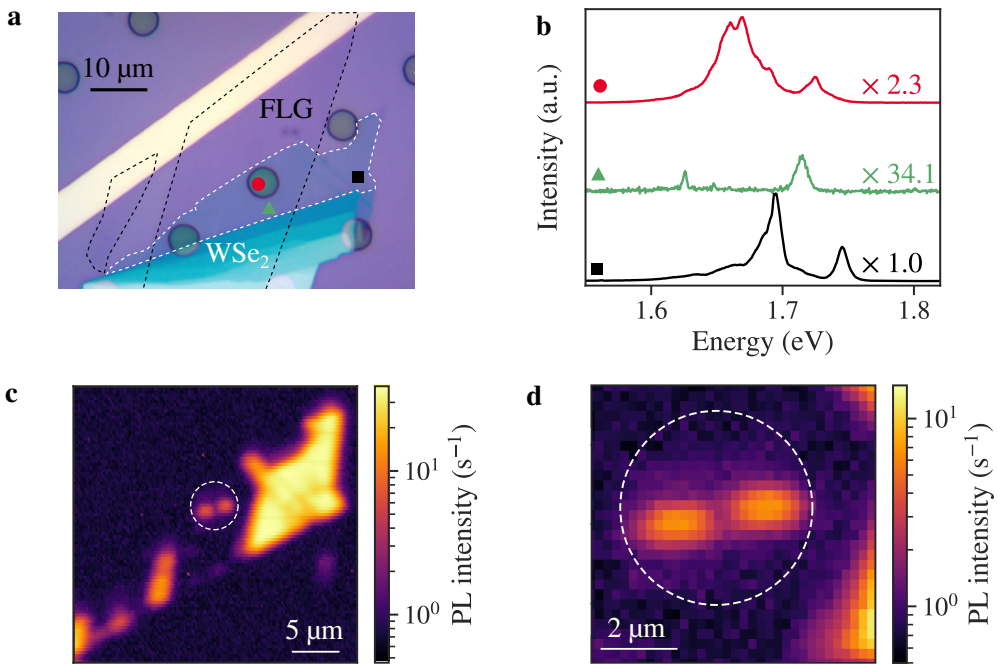

Figure F.1: Dynamical strain modulation of light emission in few-layer graphene/WSe_2. **a.** Optical image of device 2. The few-layer graphene (FLG) contours are defined by the dashed black line and the monolayer WSe2 contours by the white dashed line. **b.** Integrated PL intensity map. Integration limits are taken close to the neutral exciton to avoid contribution from other emission lines. The white dashed circle marks the resonator limits. **c.** Example PL spectra of SiO2 -supported WSe2 (black), SiO2 -supported graphene/WSe2 (green) and suspended graphene/WSe2 (red). Markers in a gives the precise points of the sample where the shown spectrum was obtained.

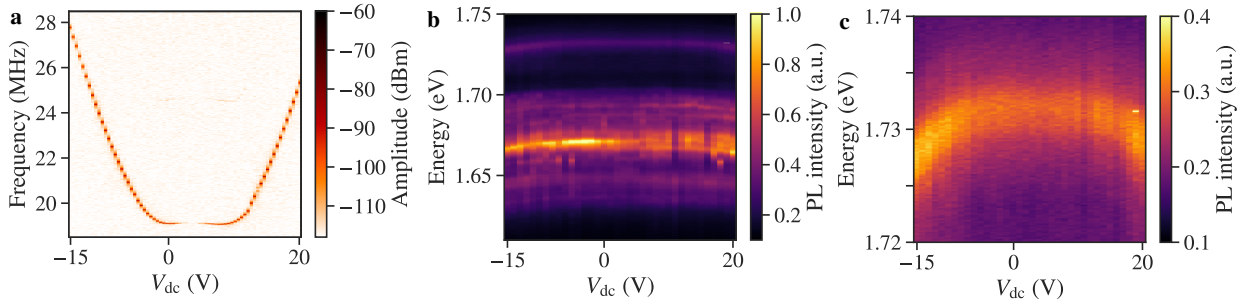

Figure F.2: DC bias dependent responses of device 2. **a.** Variation of the mechanical response of device 2 with respect to Vdc for an AC bias Vac = 1 mV. **b.** PL spectra of suspended FLG/WSe2 at varying Vdc. Measurement spot corresponds to the red dot in a. **c.** PL spectra from b zoomed on the neutral exciton.

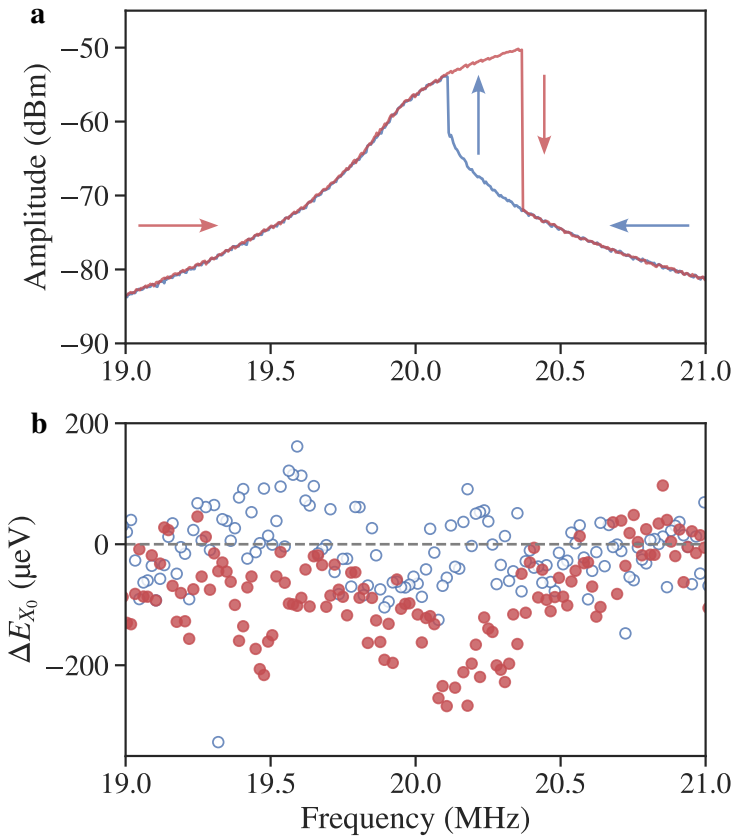

Figure F.3: Dynamical strain modulation of light emission in few-layer graphene/WSe_2. a. Duffing type non-linear mechanical response in the forward frequency direction (red) and backwards frequency direction (blue) for Vac = 300 mV and Vdc = 12 V. **b.** Frequency dependent shift of the exciton energy in the forward frequency direction (red) and backwards fre- quency direction (blue) for Vac = 300 mV and Vdc = 12 V.

the dynamical shift reaches $\Delta E_{X_0} \approx -192 \pm 76$ μeV at the maximum of the vibrational amplitude in the forward frequency direction, but no clear shift of the exciton line is observed when the frequency is sweeped in the backward direction. Assuming again a −94 meV/% linear strain sensitivity, this redshift is related to a dynamical variation of strain of $\Delta\varepsilon_d \approx 2 \times 10^{-3} \pm 8 \times 10^{-4}$ %.

Résumé en français

Introduction

Lorsque la dimensionnalité d'un système physique est réduite, les lois d'échelles sont modifiées, ce qui altère son comportement et ses propriétés physiques. A l'échelle macroscopique, le confinement spatial de l'une des trois dimensions mène à une optimisation du rapport entre surface et volume et à un premier effet intéressant : une diminution de la rigidité du matériaux considéré. Une fine feuille de matière peut alors être déformée puis éventuellement, si l'élasticité du matériau le permet, revenir à son état initial. Cette fine feuille de matière se comporte alors comme un oscillateur mécanique à deux dimensions dont les vibrations peuvent être entrainées de façon mécanique, comme pour la peau d'un tambour, ou de façon électrostatique, comme pour un haut-parleur. Les même règles physiques s'appliquent à plus petite échelle, jusqu'à l'ordre du µm et du nm dans les micro- et nano-systèmes électromécaniques (NEMS) [1, 2].

À l'échelle du nm, le confinement spatial conduit à la création d'états liés électroniques qui sont au cœur des principes de fonctionnement des technologies modernes [3, 4]. Le développement de méthodes de croissance de matériaux de haute précision a rendu possible la fabrication de nanostructures de plus en plus petites, dont les processus de fabrication sont désormais bien établis. En deux dimensions, des techniques telles que l'épitaxie par jet moléculaire ou le dépôt chimique en phase vapeur ont mené à la fabrication de puits quantiques faits d'hétérostructures semiconductrices, l'une des plus connues étant l'hétérostructure GaAs/AlGaAs, dont la couche confinée ne fait que quelques nm [5]. Le confinement bidimensionnel des électrons dans les puits quantiques a permis la création de dispositifs optiques aux performances et à l'efficacité décuplés.

Les matériaux bidimensionnels (2D) sont composés de feuillets d'atomes fortement liés entre eux par des liaisons covalentes dans le plan, empilés les uns sur les autres. Les différents feuillets sont liés entre eux par des forces de van der Waals qui sont bien plus faibles que les liaisons covalentes, ce qui permet d'isoler un feuillet unique du reste du cristal et pousser la physique à deux dimensions dans ses retranchements, à la frontière entre physique du solide et physique moléculaire. Ces matériaux atomiquement fins peuvent posséder une grande diversité de propriétés physiques, de semi-métallique comme le graphène à isolant comme le nitrure de bore hexagonal (hBN) ou semiconducteur comme les dichalcogénures de métaux de transition (TMD) [6]. Récemment, des matériaux 2D magnétiques ont été isolés et viennent compléter la famille des matériaux atomiquement fins [7, 8]. La finesse atomique des matériaux 2D les rends aussi fortement sensibles à leur environnement et

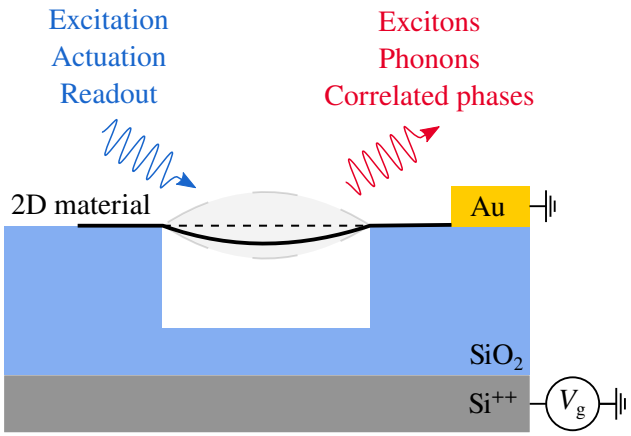

Figure F.4: L'architecture en micro-tambour comme nouvelle plateforme pour l'opto-électromécanique.

particulièrement accordables.

De plus, l'absence de liaisons libres à leur surface permet de combiner différents matériaux 2D et former des hétérostructures de van der Waals en empilant une séquence choisie de matériaux 2D les uns sur les autres [9]. Grâce au large éventail de propriétés des différents matériaux 2D existants, une quantité indénombrable d'architectures est réalisable en empilant divers matériaux. Les propriétés des hétérostructures formées sont alors définies par des mécanismes en champ proche prenant place à l'interface entre les matériaux.

Contrairement aux puits quantiques à base de semiconducteurs conventionnels qui sont par définition incorporés au sein d'un matériau plus épais, la structure cristalline bidimensionnelle des matériaux de van der Waals permet de créer des dispositifs avec des matériaux 2D suspendus, sans qu'ils ne soient en contact avec un substrat ou quelque matériau solide que ce soit. De cette façon, ils peuvent être utilisés comme des membranes vibrantes d'épaisseur atomique dont les vibrations sont régies par les mêmes règles physiques que les membranes macroscopiques [10]. Cette particularité nous donne une opportunité unique : celle de réaliser des dispositifs en forme de micro-tambours utilisant une hétérostructure de van der Waals comme membrane vibrante et ainsi utiliser son degré de liberté mécanique comme une sonde supplémentaire des propriétés des matériaux utilisés, ou encore comme une façon de les modifier.

Parmi les propriétés prometteuses des matériaux 2D, leurs propriétés optiques présentent un intérêt particulier. Par exemple, les TMD monocouches sont des semi-conducteurs à gap direct, qui peuvent donc efficacement absorber ou émettre de la lumière. Leur réponse optique est dominée par des excitons ayant une énergie de liaison qui dépasse l'énergie de l'agitation thermique à température ambiante [11]. Expérimentalement, la réponse optique des TMDs peut être étudiée avec des techniques de spectroscopie optique, telle que la photoluminescence, où la population d'excitons est créée grâce à une excitation laser [12]. La recombinaison des excitons se traduit alors par une raie d'émission bien définie dans le spectre de photoluminescence. Les caractéristiques de cette raie d'émission dépendent des diverses propriétés du matériau, telles que son niveau de dopage ou sa déformation, ainsi qu'à son environnement, à savoir son environnement diélectrique, la température ou le champ optique

[11].

Lorsque le matériau considéré est utilisé comme membrane vibrante dans un échantillon en forme de tambour, tous les paramètres qui affectent la réponse de l'exciton peuvent également être sensibles à la vibration mécanique du matériau en suspension et conduire à une interaction entre les propriétés optiques et mécaniques de la membrane vibrante utilisée. De plus, la réponse mécanique d'un tel micro-tambour peut être mesurée optiquement avec le même faisceau laser que celui utilisé pour exciter le matériau 2D suspendu. Grâce à sa configuration avantageuse, la géométrie d'échantillon en micro-tambour est une plate-forme prometteuse pour étudier le couplage de la réponse optique des hétérostructures de van der Waals suspendues avec leur degré de liberté mécanique, comme le montre la figure F.4. C'est dans le cadre de ce nouveau domaine de recherche que nous appellerons *opto-électro-mécanique* que s'inscrit ce travail de thèse.

Plus précisément, l'objectif général de cette thèse, démarrée en 2019, est de compléter une évolution thématique dans mon équipe d'accueil à l'IPCMS, initiée en 2016 suite à des travaux approfondis sur la physique des monocouches de graphène suspendues. L'idée est d'ajouter un degré de liberté mécanique à une méthodologie expérimentale basée principalement sur la spectroscopie optique de matériaux 2D et développer une activité de pointe en opto-électro-mécanique.

Ce manuscrit est divisé en 4 chapitres. Le premier est dédié à une présentation des principales propriétés des matériaux 2D étudiés durant cette thèse et leurs hétérostructures. Le deuxième présente des résultats sur l'étude de monocouches de TMD suspendues soumises à une forte excitation laser et s'intéresse à la formation potentielle de phases électroniques denses photoinduites. Le troisième chapitre est consacré à l'influence de l'écrantage diélectrique sur les différents phonons optiques du graphène, sondé par spectroscopie Raman. Finalement, dans le quatrième chapitre, un nouveau dispositif expérimental que j'ai développé spécifiquement dans le cadre de cette thèse est utilisé à son plein potentiel pour réaliser un contrôle électromécanique des propriétés d'une hétérostructure graphène/$MoSe_2$. Dans ce résumé, je vais présenter brièvement les principaux résultats détaillés dans les chapitres 2, 3 et 4.

Monocouches de TMD suspendues sous forte excitation laser

En illuminant un semiconducteur avec un faisceau laser, des paires électrons-trous sont créées, qui vont ensuite se lier par interaction coulombienne pour former des quasi-particules appelées excitons. En augmentant la densité d'excitons dans un matériau, il est possible de forcer ces excitons à interagir les uns avec les autres pour faire apparaitre de nouveaux états tels que les trions (des excitons chargés) ou les biexcitons (deux excitons liés). En augmentant encore la densité d'excitons, il est possible d'ioniser les différents états en une soupe de charges appelée un plasma d'électrons-trous (EHP). Ce plasma peut, si les porteurs de charges ont une durée de vie suffisante, atteindre une transition de phase et former une goutte macroscopique d'électrons et de trous ayant des propriétés semblables à celles d'un liquide et pouvant atteindre des dimensions de l'ordre de plusieurs µm [111].

De tels phénomènes ont été observés dans des dispositifs à base d'hétérostructures de van der Waals faisant profit de multicouches de $MoTe_2$ [111], le gap indirect de la multicouche permettant aux porteurs de charges d'avoir un temps de vie long, mais aussi dans des monocouches de MoS_2 suspendues [110, 112]. Dans le cas des monocouches de MoS_2 suspendues, qui ont un gap direct et ne devraient pas permettre une telle transition de phase en raison du court temps de vie des porteurs de charges, il a été démontré que l'excitation laser utilisée pour augmenter la densité d'excitons générait dans le même temps une dilatation thermique suffisamment importante pour modifier la structure de bande du matériau. Ces changements impliquent une transition de gap direct à gap indirect de la monocouche de MoS_2, autorisant alors la formation d'un liquide d'électrons et de trous. Cette transition se traduit par une abrupte augmentation de l'intensité et la largeur spectrale de la photoluminescence (PL) ainsi qu'un fort décalage vers le rouge de celle-ci, de l'ordre de plusieurs centaines de meV.

Dans cette section, les principaux résultats du chapitre 2 sont détaillés. L'étude décrite ici cherche en premier lieu à reproduire les résultats rapportés dans la littérature en observant la formation d'un liquide d'électrons et de trous (EHL) dans une monocouche de MoS_2 suspendue [110, 112]. Ensuite, le même protocole expérimental est appliqué sur une monocouche de WS_2 suspendue afin d'enquêter sur la présence ou non d'une transition de phase similaire dans ce matériau.

Phases électroniques denses dans une monocouche de MoS_2 suspendue

Notre première étape dans l'étude des monocouches de TMD suspendues soumises à une forte excitation laser consiste à reproduire des résultats rapportés dans la littérature, qui indiquent la formation d'une phase liquide d'électrons et de trous dans des monocouches de MoS_2 suspendues [110, 112]. Cette transition de phase se traduit par une forte et abrupte augmentation de l'intensité et de la largeur du spectre de photoluminescence, accompagnée d'un important décalage vers le rouge [110, 112]. La température critique de cette transition a été estimée à $T_c \approx 500$ K [110].

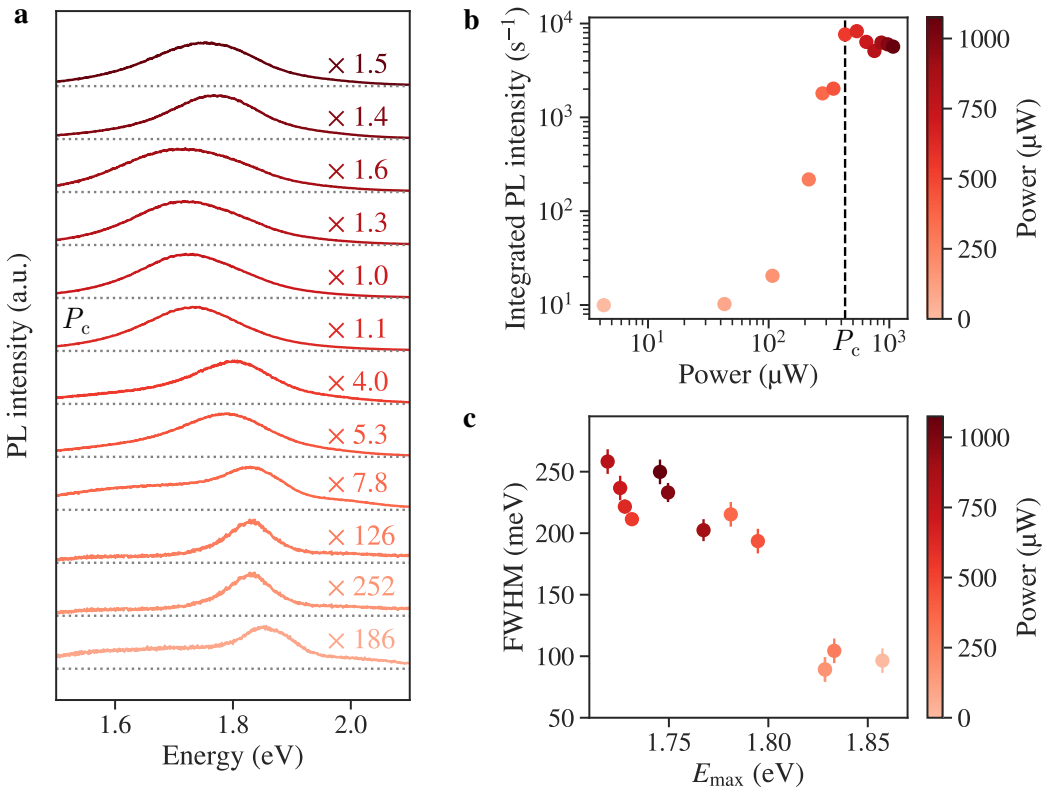

Figure F.5: Photoluminescence d'une monocouche de MoS_2 suspendue en fonction de la puissance laser. a. Evolution du spectre de PL d'une monocouche de MoS_2 suspendue lorsque la puissance est augmentée. **b.** Intensité de PL en fonction de la puissance laser. **c.** Corrélation entre la largeur et la position du pic de PL.

L'échantillon considéré est une monocouche de MoS_2 suspendue sur un trou de 4 µm de diamètre creusé dans un substrat de quartz pour éviter que de potentiels effets d'interférences optiques n'altèrent la forme du spectre détecté. Les spectres de photoluminescence et spectres Raman sont mesurés en fonction de la puissance, de façon consécutive afin d'assurer une corrélation point par point entre les deux types de mesures. Le laser utilisé est un laser continu d'une longueur d'onde de 532 nm focalisé sur un spot d'environ 1 µm de diamètre.

La figure F.5a montre les spectres de photoluminescence lorsque la puissance laser est augmentée progressivement. Chacun des spectres est ajusté par un profil de Voigt afin d'extraire l'intensité intégrée, la position du maximum d'intensité E_{max} et la largeur à mi-hauteur (FWHM). La figure F.5b,c montre une abrupte augmentation de l'intensité intégrée de PL de plus de 3 ordres de grandeurs lorsque la puissance est augmentée jusqu'à une valeur critique $P_c = 430$ µW. Au-delà de cette valeur, l'intensité intégrée reste globalement constante lorsque la puissance est augmentée. Cette soudaine augmentation de l'intensité d'émission est accompagnée d'un fort décalage vers le rouge de plus de 100 meV ainsi que d'un élargissement de la raie d'émission (voir figure F.5c). Ces observations sont en accord avec la formation d'une phase liquide d'électrons et de trous telle que rapportée dans la littérature [110, 112, 113].

Les spectres Raman associés à ces mesures de photoluminescence sont présentés figure F.6a et nous permettent d'estimer la température du cristal associée à chaque mesure du spectre de PL. En supposant que la dépendance en température de la position du pic E′ est linéaire

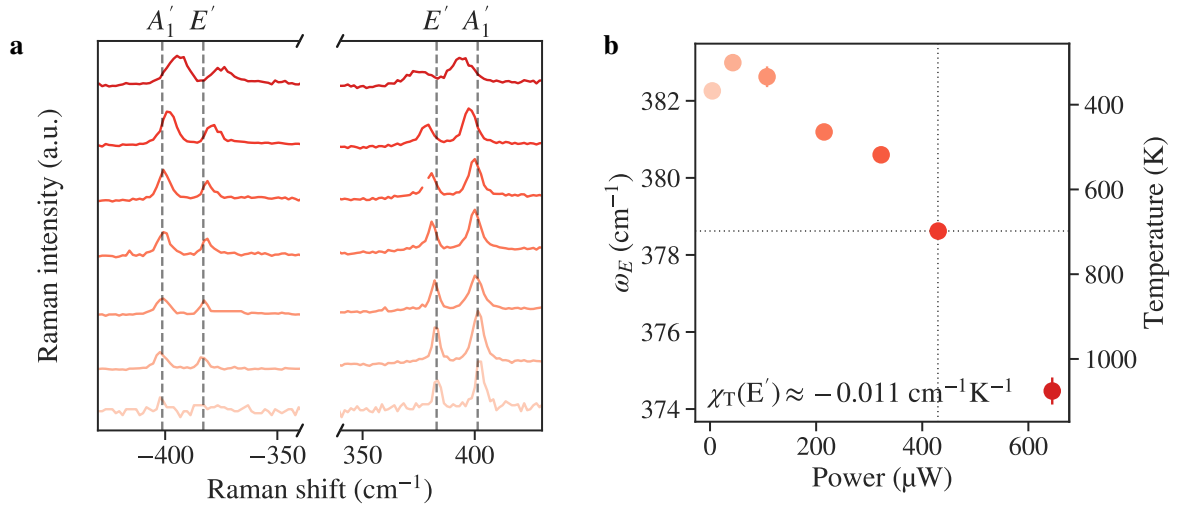

Figure F.6: Evolution de la réponse Raman d'une monocouche de MoS_2 suspendue en fonction de la puissance du laser. a. Evolution du spectre Raman d'une monocouche de MoS_2 suspendue lorsque la puissance est augmentée. **b.** Fréquence et température de phonons du mode E$'$ en fonction de la puissance laser.

$\omega_{E'}(T) - \omega_{E'}(T_0) = \chi_T(T - T_0)$ avec un coefficient thermique $\chi_T = -0.011$ cm^{-1} K^{-1} [78], une température critique $T_c \approx 700$ K est obtenue lorsque la puissance critique $P_c = 430$ µW est atteinte. De la même manière, une estimation de la température se basant sur le décalage en fréquence du mode A$'$ donne une température critique $T_c \approx 550$ K pour un coefficient thermique $\chi_T = -0.013$ cm^{-1} K^{-1} [78]. Une troisième estimation de la température peut être déduite du ratio entre les intensités des pics Stokes et Anti-Stokes en utilisant l'équation D.19 et en considérant le ratio à la plus faible puissance comme référence à température ambiante (300 K). De cette manière, une température critique $T_c \approx 700$ K est obtenue.

La combinaison de nos mesures de PL et de spectroscopie Raman est en accord avec les observations rapportées dans la littérature, qui attestent de la formation d'une phase liquide d'électrons et de trous dans des monocouches suspendues de MoS_2, rendue possible grâce à une transition de gap direct à indirect dans la structure électronique du matériau, elle-même induite de façon photothermique à une température $T_c \sim 500 - 700$ K.

Monocouche de WS_2 suspendue sous forte excitation laser

Le même protocole expérimental a été appliqué pour étudier une monocouche de WS_2 suspendue sur un trou de 6 µm de diamètre creusé dans un substrat de Si/SiO_2 afin d'étudier la possibilité d'atteindre un régime de phase dense électronique dans ce matériau. La figure F.7a présente l'évolution du spectre de PL lorsque la puissance laser est augmentée. Un net décalage vers le rouge ainsi qu'un élargissement du spectre est visible. Afin de mieux comprendre l'évolution du spectre de PL, tous les spectres ont été ajustés par un modèle composé de deux profils de Voigt qui, à faible puissance, peuvent être assignés respectivement à l'exciton neutre X^0 (en rouge) et le trion X^* (en bleu) [73, 127]. La dépendance en puissance de l'intensité des raies de PL ajustées est montrée figure F.7b. Deux régimes sont clairement identifiables, avec une transition à la puissance critique $P_c = 645$ µW. Le spectre

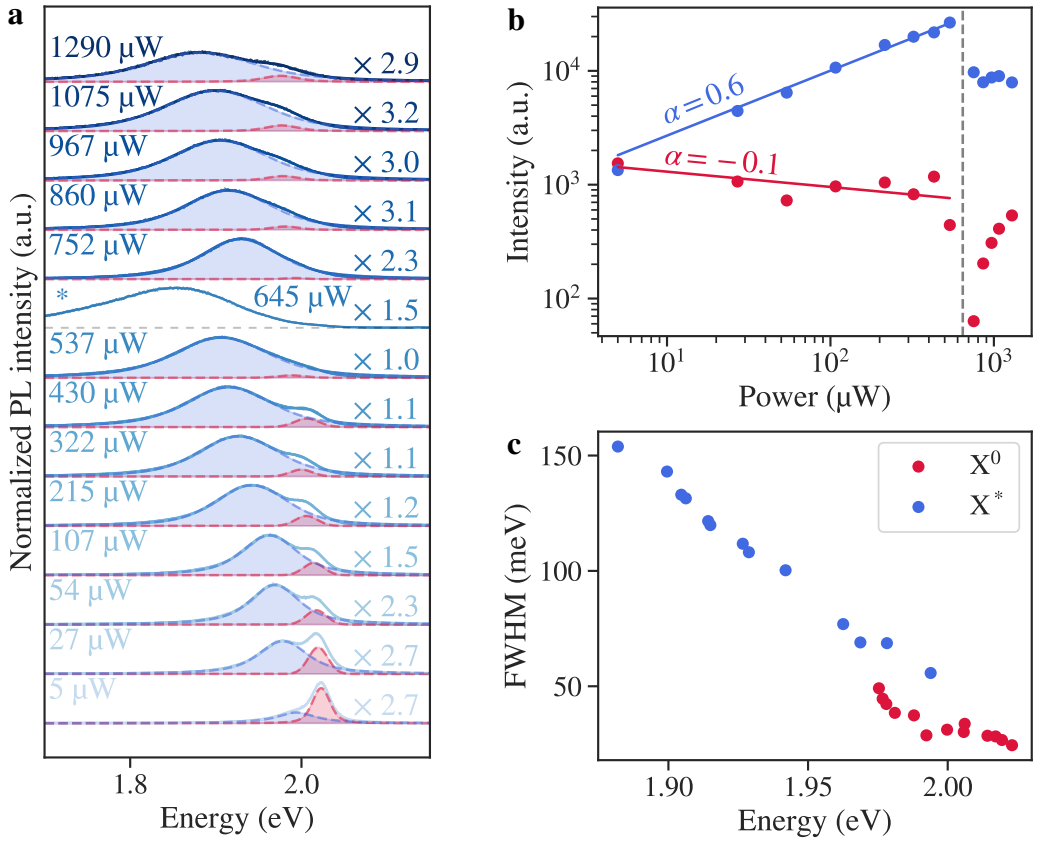

Figure F.7: Photoluminescence d'une monocouche de WS_2 suspendue en fonction de la puissance laser. a. Evolution du spectre de PL d'une monocouche de WS_2 suspendue lorsque la puissance est augmentée. Le spectre marqué d'une astérisque * indique le spectre à la puissance critique. **b.** Intensité intégrée des raie d'émission de l'exciton neutre (en rouge) et du trion (en bleu). La ligne pointillée indique la puissance critique. **c.** Corrélation entre la largeur (FWHM) et l'énergie des raies d'émission de l'exciton neutre (en rouge) et du trion (en bleu)

d'émission à la puissance critique est également différent des autres. C'est le seul spectre ne pouvant pas être ajusté par le modèle à double profil de Voigt. Ce cas particulier sera discuté plus loin.

Pour les puissances laser $P < P_c$, l'intensité de PL en fonction de la puissance laser suit une loi en puissance $I \sim P^\alpha$. Étonnamment, un ajustement de l'évolution de l'intensité d'émission de l'exciton neutre X^0 donne $\alpha = -0.1$, traduisant une densité excitonique au mieux constante lorsque la puissance laser augmente. L'intensité d'émission du trion X^* suit quant à elle une évolution sublinéaire avec $\alpha = 0.6$. La combinaison de ces évolutions mène à une rapide inversion de population entre exciton et trion avec un ratio $I_{X^*}/I_{X^0} \sim P^{0.7}$ qui suggère un fort taux de conversion exciton-trion ou une émission excitonique fortement réduite. Cet effet est associé à un progressif décalage vers le rouge et un élargissement des deux raies d'émission du spectre de PL (voir figure F.7c).

La figure F.8 présente les spectres Raman associés aux spectres de PL de la figure F.7. Contrairement au cas de MoS_2, le mode E' est ici indiscernable des pics Raman associés aux phonons 2LA(M) et ne peut pas être utilisé pour estimer la température du réseau. Nous nous concentrons donc sur le pic Stokes du mode A_1', le pic Anti-Stokes étant indétectable à

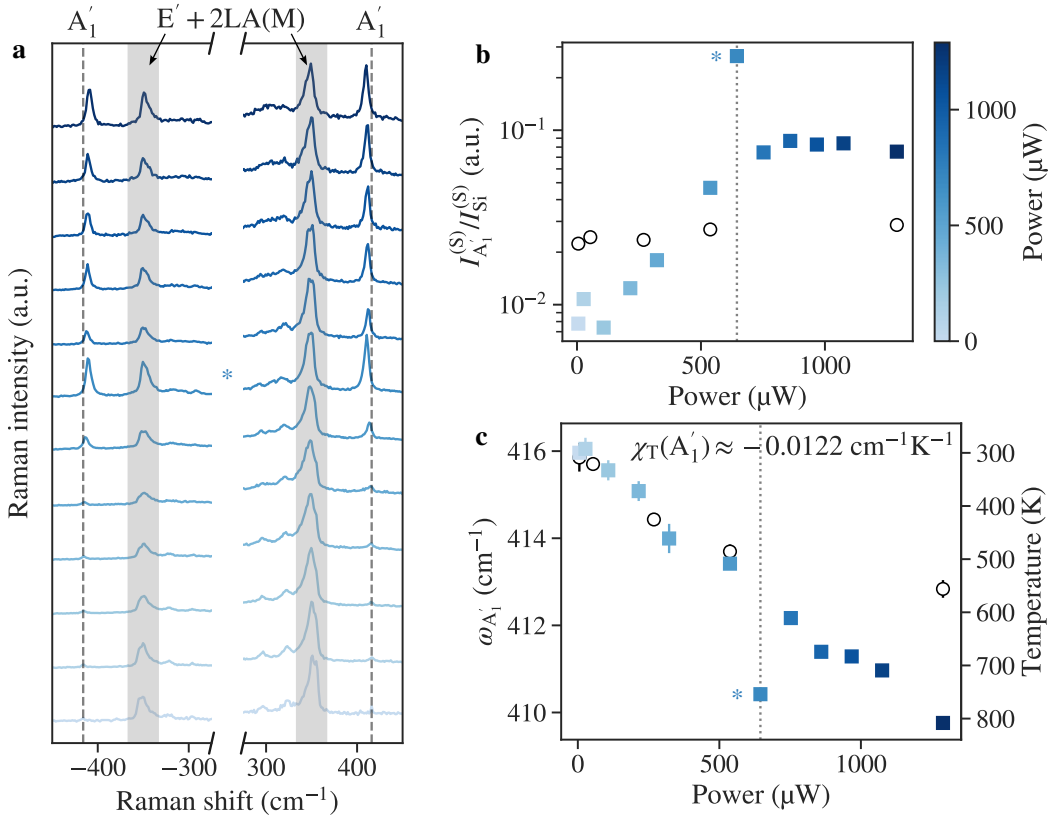

Figure F.8: Spectres Raman d'une monocouche de WS_2 suspendue en fonction de la puissance laser. a. Evolution du spectre Raman d'une monocouche de WS_2 suspendue lorsque la puissance est augmentée. Le spectre marqué d'une astérisque * indique le spectre à la puissance critique. **b.** Intensité du pic A_1' normalisé d'après celle du pic Raman du Si (à environ 520 cm^{-1}, non montré ici) en fonction de la puissance laser. **c.** Evolution de la fréquence du mode A_1' et de la température estimée d'après celui-ci en fonction de la puissance du laser.

faible puissance laser. L'intensité du pic A_1' augmente fortement avec la puissance et atteint un plateau lorsque $P > P_c$ (voir figure F.8b). Encore une fois, le point critique montre un résultat singulier, avec une intensité maximale du pic A_1'. Aucun effet n'est visible sur la partie supportée de l'échantillon (cercles noirs sur la figure F.8b).

De la même façon que précédemment, mous supposons que la fréquence du mode A_1' varie linéairement en fonction de la température afin de déterminer la température du cristal (voir figure F.8c). Un coefficient thermique $\chi_T = -0.0122$ $cm^{-1}K^{-1}$ est utilisé [82]. Une fois de plus le point à puissance critique donne une valeur singulière, avec une température $T_c \approx 750$ K, rompant avec la claire tendance linéaire du reste de la série de mesure. Une augmentation de température est aussi observée sur la zone supportée lorsque la puissance laser est augmentée (cercles noirs sur la figure F.7c) et atteint une température maximale de 550 K. Dans le cas suspendu, une importante augmentation de l'intensité du pic A_1' est déjà observée à ces températures alors qu'aucun effet n'est visible dans le cas supporté, ce qui est un indice supplémentaire mettant en évidence que l'exaltation du mode A_1' n'est pas simplement due à une augmentation de la température du réseau.

En analysant les résultats présentés jusqu'ici, on peut donc noter que le *régime intermédiaire*,

défini pour des puissances $P < P_c$, est notamment caractérisé par une forte conversion d'excitons en trions. Un scénario probable expliquant cet effet peut être imaginé en analogie aux résultats présentés dans la référence [73], qui montre qu'une distribution non-uniforme de contraintes appliquées par une pointe AFM sur une monocouche suspendue de WS_2 peut mener à un fort taux de conversion d'excitons en trions. Dans notre cas, la distribution non-uniforme des contraintes serait induite par le faisceau laser focalisé sur une surface plus petite que la zone suspendue et créant un profil de chaleur gaussien. La dilatation thermique résultante est alors non-uniforme, avec son maximum situé au centre de la membrane, qui canalise les charges et favorise la conversion d'excitons en trions, deux effets qui augmentent une densité de porteurs de charges déjà importante à cause de la forte excitation laser.

Au point critique $P = P_c$, l'extrême décalage vers le rouge et l'élargissement du spectre de PL qui ne peut plus être ajusté par un modèle à deux Voigt rends viable l'hypothèse de la formation d'un plasma d'électrons et de trous. Ainsi, la forte densité de porteurs de charges concentrés au centre de la membrane, combinée avec le fort taux de conversion d'excitons en trions, pourrait mener à la formation d'un EHP. Cependant, l'instabilité et la non reproductibilité de ces observations nous obligent à réaliser des mesures supplémentaires pour pouvoir conclure. Enfin, lorsque $P > P_c$, le décalage vers le rouge et l'élargissement du spectre de PL ainsi que l'exaltation du mode Raman A_1' atteignent tous des régimes de saturation. De plus, les intensités de PL diminuent ou saturent également (voir figure F.7b), ce qui suggère un effet de photoblanchiment et une destruction progressive de l'échantillon dû à une trop forte excitation laser.

Nos résultats valident donc les observations et interprétations de la littérature rapportant la formation d'une phase liquide d'électrons et de trous dans des monocouches suspendues de MoS_2 soumises à une forte excitation laser. En réalisant des expériences similaires sur une monocouche suspendue de WS_2, une importante conversion d'excitons en trions est observée menant à une progressive altération du spectre de photoluminescence qui pourrait être dû à la formation d'une phase dense d'électrons et de trous. Une forte éxaltation du mode Raman A_1' est également observée. Bien que ces résultats pourraient être expliqués par la combinaison d'une forte densité d'excitons et d'un profil non-uniforme de chauffage photoinduit qui favoriserait la conversion d'excitons en trions, il est nécessaire de reproduire ces résultats et réaliser des expériences complémentaires pour conclure.

Écrantage diélectrique des phonons optiques du graphène

Dans cette section, les principaux résultats du chapitre 3 sont résumés. Le graphène monocouche est considéré comme système modèle afin d'étudier l'impact de l'écrantage diélectrique sur les phonons optiques d'un métal. La spectroscopie Raman est utilisée sur différentes hétérostructures de van der Waals à base de graphène pour sonder les phonons optiques aux points Γ et K, K' et étudier l'effet de l'environnement diélectrique sur les anomalies de Kohn. Nos résultats mettent en évidence l'importance fondamentale de la symétrie des phonons sur leur sensibilité aux effets d'écrantage diélectrique.

La figure F.9 présente un exemple clair du phénomène. La figure F.9a montre une image optique d'un échantillon de graphène/WSe_2 encapsulé dans du nitrure de bore (hBN), avec des zones bien identifiées formées de graphène encapsulé (**i**) et de graphène/WSe_2 encapsulé (**ii**). Les cartes hyper-spectrales des fréquences du mode 2D et du mode G de cet échantillon sont présentées figure F.9b,c. Un net décalage du mode 2D vers le bleu, d'une valeur moyenne $\Delta\omega_{2D} = 7.3 \pm 3$ cm^{-1}, est visible sur toute la région de graphène/WSe_2 encapsulé par rapport à celle de graphène encapsulé, alors que dans le même temps la fréquence du mode G reste constante. Des spectres Raman typiques des deux régions considérées sont présentés figure F.9d.

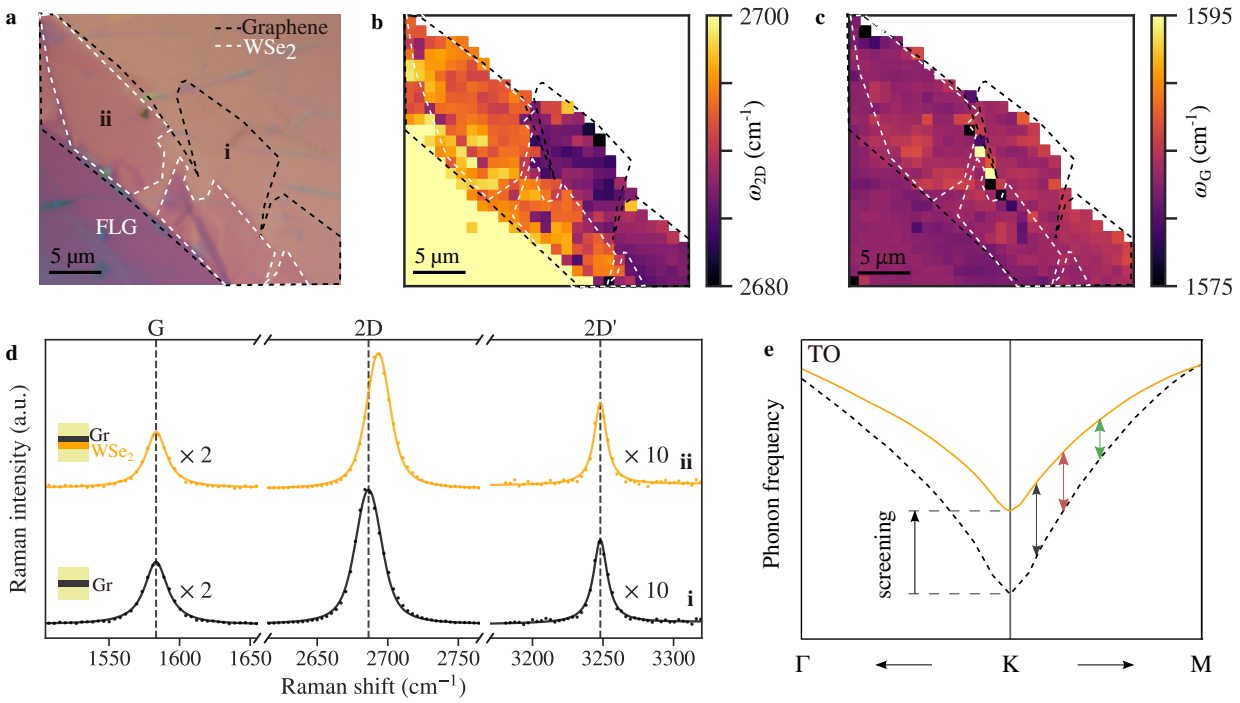

Figure F.9: Cartographie Raman d'un échantillon de graphène/WSe_2 encapsulé. a. Image optique de l'échantillon considéré. **b.** Cartographie de la fréquence du mode 2D. **c.** Cartographie de la fréquence du mode G. **d.** Spectres Raman typique de la zone de graphène encapsulé (**i**) et de graphène/WSe_2 encapsulé (**ii**). **e.** Schéma de l'effet d'adoucissement de l'anomalie de Kohn au point K,K' due à l'écrantage diélectrique.

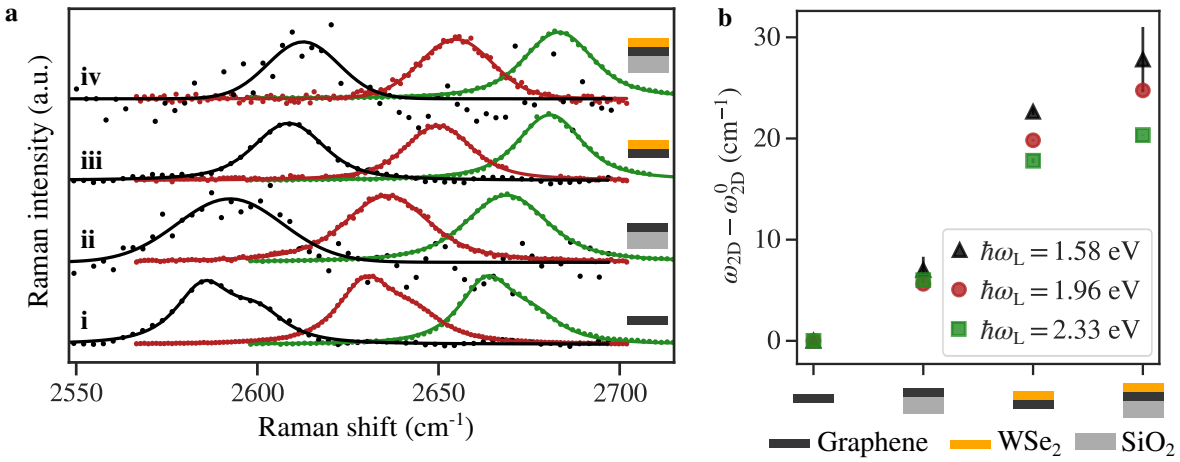

Figure F.10: Dispersion du mode 2D en fonction de l'énergie du laser. a. Spectres du mode 2D dans chacune des configurations considérées et pour les différentes énergies laser (noir pour 1.58 eV, rouge pour 1.96 eV et vert pour 2.33 eV). **b.** Fréquence du mode 2D ω_{2D} pour les différentes régions de l'échantillon et différentes énergies laser. Les données sont présentées par rapport à ω^0_{2D} la valeur de référence mesurée sur graphène suspendu.

Des comportements aussi différents ne peuvent pas être expliqués par des contraintes involontaires ou du dopage, car les deux impliqueraient un changement de la fréquence du mode G en concordance avec le décalage observé sur le mode 2D. Si l'augmentation en fréquence du mode 2D était dû à des contraintes, la fréquence du mode G devrait augmenter elle aussi d'environ 3 cm^{-1}. Dans le cas d'un effet dû au dopage, le mode G se décalerait de plus de 10 cm^{-1}. Une origine plus plausible est celle d'une différence de sensibilité à l'écrantage diélectrique des anomalies de Kohn à K, K' et à Γ.

Écrantage diélectrique de l'anomalie de Kohn au point K, K'

Des calculs de DFT cherchants à déterminer les énergies des phonons du graphène suggèrent qu'une augmentation de l'écrantage diélectrique dans le graphène provoque un adoucissement de l'anomalie de Kohn au point K, comme illustré sur la figure F.9e [130, 31, 27]. Cependant, modéliser des changements d'environnement diélectrique dans de tels calculs théoriques reste "artificielle" et une vérification expérimentale est nécessaire. Pour tester expérimentalement cette hypothèse, nous proposons de mesurer la dispersion de la fréquence du mode 2D en fonction de l'énergie du laser sur un échantillon donné avec différents types d'hétérostructures à base de graphène. En effet, à mesure que l'énergie du laser augmente, les phonons impliqués dans le processus Raman du mode 2D s'éloignent du point K, K'. Comme l'effet d'adoucissement dû à l'écrantage diélectrique diminue avec la distance relative au point K, K', on devrait s'attendre à une diminution du décalage vers le bleu induit par l'écrantage du mode 2D à mesure que l'énergie du laser augmente.

L'échantillon considéré est formé d'une hétérostructure graphène/WSe_2 déposée sur un substrat de Si/SiO_2 sur lequel des trous de 5 et 6 µm de diamètre ont été creusés. Il présente quatre zones d'intérêt : graphène suspendu (**i**), graphène sur SiO_2 (**ii**), graphène/WSe_2 suspendu (**iii**) et graphène/WSe_2 sur SiO_2 (**iv**). La réponse Raman du graphène a été mesurée

dans chacune des configurations avec trois lasers d'énergies différentes (1.58, 1.96 et 2.33 eV). Les spectres du mode 2D mesurés dans chaque cas sont présentés figure F.10a avec leurs ajustements respectifs.

Pour mettre en évidence l'effet de l'écrantage diélectrique, les différentes configurations sont ordonnées par ordre croissant d'écrantage diélectrique attendu et l'effet de l'environnement diélectrique est évalué en déterminant pour chaque énergie du laser le décalage $\omega_{2D} - \omega_{2D}^0$ par rapport à une valeur de référence ω_{2D}^0 correspondant à la fréquence du mode 2D dans le cas du graphène suspendu à cette même énergie laser, tel que présenté figure F.10b. De façon remarquable, le décalage vers le bleu du mode 2D dépend dans chaque cas de l'énergie du laser. Pour une énergie laser de 2.33 eV, le mode 2D se décale de 20 cm^{-1} entre la région **i** et la région **iv** alors qu'il se décale de 27 cm^{-1} pour une énergie laser de 1.58 eV. Nos observations montrent donc qu'une augmentation de l'écrantage diélectrique induit un décalage vers le bleu du mode 2D, décalage qui diminue avec l'énergie du laser, ce qui est en accord avec l'hypothèse d'un adoucissement de l'anomalie de Kohn au point K, K'.

Évolution de la fréquence des modes G et 2D dans différentes configurations d'hétérostructures

Pour obtenir une compréhension plus quantitative du phénomène observé, nous avons effectué une analyse systématique basée sur la cartographie hyper-spectrale de la réponse Raman d'un ensemble d'échantillons présentant différents types d'hétérostructures à base de graphène. L'ensemble considéré est composé des deux échantillons présentés figures F.9 et F.10 (respectivement appelés échantillon 1 et 2) et d'un échantillon supplémentaire formé d'une hétérostructure hBN/$MoSe_2$/graphène (voir appendice E et Ref. [100]), appelé échantillon 3. Désormais, toutes les données présentées dans cette section ont été acquises avec une énergie d'excitation de 2.33 eV.

Pour tous les échantillons, le mode G est ajusté par une lorentzienne pour extraire directement ω_G et Γ_G. Le mode 2D est quant à lui ajusté dans chaque cas par un profil de Voigt. Γ_{2D} est alors pris égal à la largeur à mi-hauteur du profil de Voigt. Sauf pour le cas du graphène suspendu, ω_{2D} est déterminé par la position centrale du profil de Voigt. Dans le cas particulier du graphène suspendu, un deuxième ajustement est effectué avec un double profil de Lorentz modifié basé sur l'équation (1.15), et nous prenons $\omega_{2D} = \omega_{2D\_}$.

Les différentes zones d'intérêt sont déterminées spatialement par une combinaison d'imagerie optique et de cartographie de PL. La réponse Raman de chaque zone définie est ensuite analysée pour garantir que les niveaux de dopage et de contrainte sont négligeables. Une étude de la réponse Raman en fonction de la puissance est également réalisée pour garantir que toutes les données sont acquises avec des puissances laser suffisamment faibles pour éviter tout photodopage parasite de la couche de graphène (généralement $\sim$ 100 $\mu W/\mu m^2$). Les détails sur la détermination préliminaire des zones d'intérêts et des potentielles contributions indésirables sont donnés en annexe E.

Les valeurs moyennes de ω_{2D} et ω_G sont rassemblées figure F.11a,b, où les hétérostructures sont présentées par ordre croissant d'écrantage diélectrique attendu. Les barres d'erreurs représentent l'écart-type des valeurs de ω_{2D} et ω_G moyennées spatialement. Une augmen-

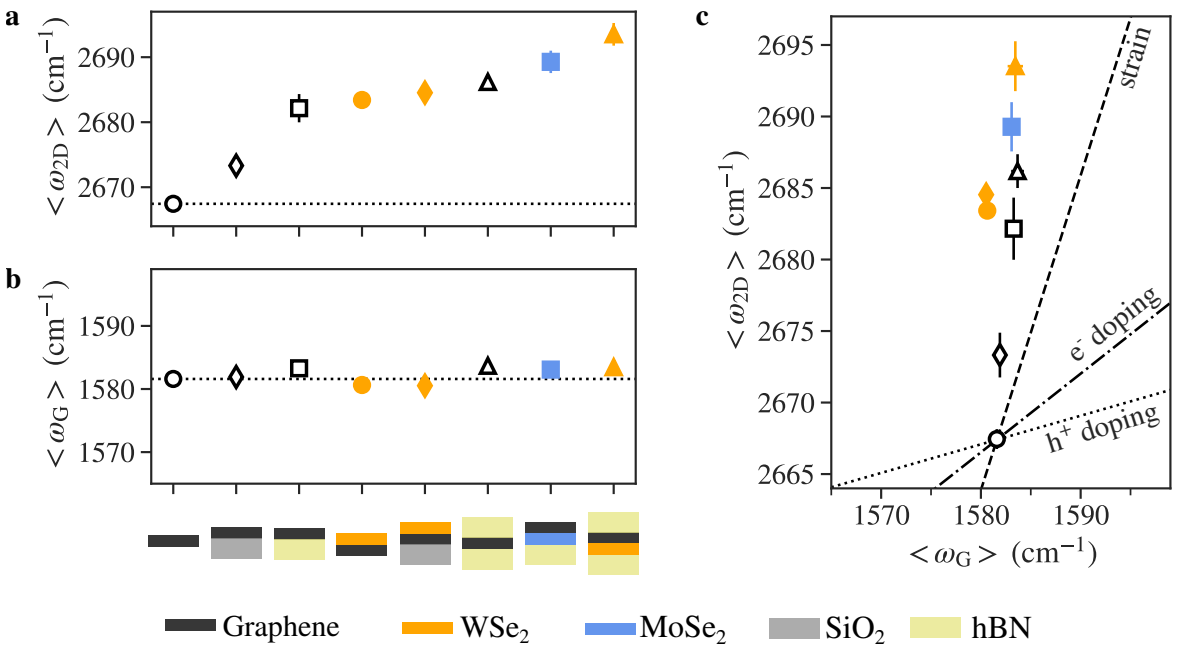

Figure F.11: Moyennes spatiales des fréquences des modes G et 2D a. Fréquence moyenne du mode 2D en fonction de l'hétérostructure considérée. **b.** Fréquence moyenne du mode G en fonction de l'hétérostructure considérée. **c.** Corrélation entre les fréquences moyennes du mode G et du mode 2D.

tation progressive de la fréquence du mode 2D est observée, atteignant un décalage de 26 ± 2.4 cm^{-1} dans le cas de graphène/WSe_2 encapsulé. Plusieurs informations intéressantes peuvent être extraites de la figure F.11a. Premièrement, alors que l'augmentation de ω_{2D} induite par un substrat de SiO_2 n'est que de 5.9 ± 2.3 cm^{-1}, des décalages bien plus prononcés de respectivement 14.8 ± 2.8 cm^{-1} et 16.0 ± 1.2 cm^{-1} sont mesurés lorsque le substrat est remplacé par du bulk de hBN ou une monocouche de WSe_2. Malgré leurs constantes diélectriques similaires, le hBN induit un décalage bien plus important que le SiO_2 [132, 133, 109], ce qui peut s'expliquer par la plus grande rugosité du SiO_2 par rapport à un matériau 2D [88] et suggère que le graphène reste partiellement découplé du substrat de SiO_2, alors qu'un substrat atomiquement plat assure un couplage optimal. Un tel résultat suggère également que le mode 2D est particulièrement sensible à l'environnement nanométrique du graphène [134] et que la correspondance directe entre la constante diélectrique d'un matériau couplé au graphène et l'augmentation de ω_{2D} induite par l'écrantage diélectrique est loin d'être triviale. De plus, le décalage du mode 2D est légèrement plus élevé dans le cas de graphène/WSe_2 suspendu que celui de graphène sur du bulk de hBN, ce qui illustre encore une fois la forte interaction entre monocouches de graphène et de TMD.

La figure F.11b montre que contrairement à la fréquence du mode 2D, la fréquence du mode G reste constante dans chacune des situations, avec une valeur moyenne de 1582 ± 2 cm^{-1}. L'invariance de ω_G est également visible figure F.11c, qui montre la corrélation $\omega_G - \omega_{2D}$ et présente un clair désaccord avec les pentes de corrélations attendues en présence de contraintes mécanique ou de dopage en électrons ou en trous, empêchant toute interprétation du phénomène se basant exclusivement sur des variations de contraintes ou de dopage.

Ce résultat peut paraître contre intuitif étant donné qu'une anomalie de Kohn est aussi présente au point Γ et que l'on pourrait donc s'attendre à un comportement similaire à celui des phonons au point K, K'. La différence de sensibilité à l'écrantage diélectrique entre mode G et mode 2D peut être comprise en considérant un argument théorique développé par nos collaborateurs de l'Université du Luxembourg, Sven Reichardt et Ludger Wirtz. Cet argument théorique stipule que les phonons optiques au point Γ sont décrits comme des quasiparticules vectorielles en raison de leur dégénérescence (liée à leur symétrie E_{2g}). Cela implique que l'Hamiltonien décrivant les interactions électron-phonon du système respecte l'identité de Ward, ce qui mène à une compensation des effets dû à l'environnement diélectrique et une indépendance des fréquences des phonons par rapport aux changements d'environnement diélectrique. Puisque les phonons au point K, K' ne sont pas dégénérés, cet argument n'est pas valable lorsque l'on considère des phonons en bord de zone de Brillouin, comme c'est le cas pour le mode 2D qui devient sensible à son environnement diélectrique.

Au cours des dernières années, l'analyse des caractéristiques des modes G et 2D a été largement utilisée pour la caractérisation d'échantillons à base de graphène, notamment en sondant les défauts, les contraintes et les niveaux de dopage. Nos résultats montrent que la variabilité observée dans la fréquence du mode 2D peut également provenir en grande partie de l'écrantage diélectrique alors que le mode G n'est quant à lui sensible qu'aux contraintes et au dopage. Ces résultats fournissent donc de nouvelles lignes directrices pour mieux comprendre les effets de proximité dans les hétérostructures. De plus, ils mettent en lumière l'importance de la symétrie des phonons dans leurs interactions avec leur environnement.

Modulation électromécanique des propriétés optiques d'une hétérostructure graphène/$MoSe_2$

Dans cette section, les principaux résultats du chapitre 4 sont détaillés. Tous les résultats présentés ont été mesurés à 4K, à l'aide du nouveau dispositif expérimental développé durant cette thèse et dont le but est de combiner des techniques de spectroscopie optique et de nanomécanique. L'échantillon considéré est présenté figure F.12. Il est formé d'une hétérostructure de graphène/$MoSe_2$ déposée sur un substrat de Si/SiO_2 avec un réseau de trous et des électrodes d'or. La figure F.12a montre une image optique de l'échantillon et met en évidence les différentes zones d'intérêt. Trois micro-tambours peuvent être identifiés, un avec une membrane de graphène/$MoSe_2$ (rond rouge) et deux avec une membrane de graphène (croix et étoile noires).

La figure F.12b,c présente une cartographie de PL de l'échantillon et des spectres typiques des zones de $MoSe_2$ supporté (carré bleu), graphène/$MoSe_2$ supporté (triangle vert) et graphène/$MoSe_2$ suspendue (rond rouge). L'hétérostructure de graphène/$MoSe_2$ présente une intensité de photoluminescence réduite par rapport à la monocouche de $MoSe_2$ ainsi qu'une absence d'émission du trion, deux signes caractéristiques d'un fort couplage inter-

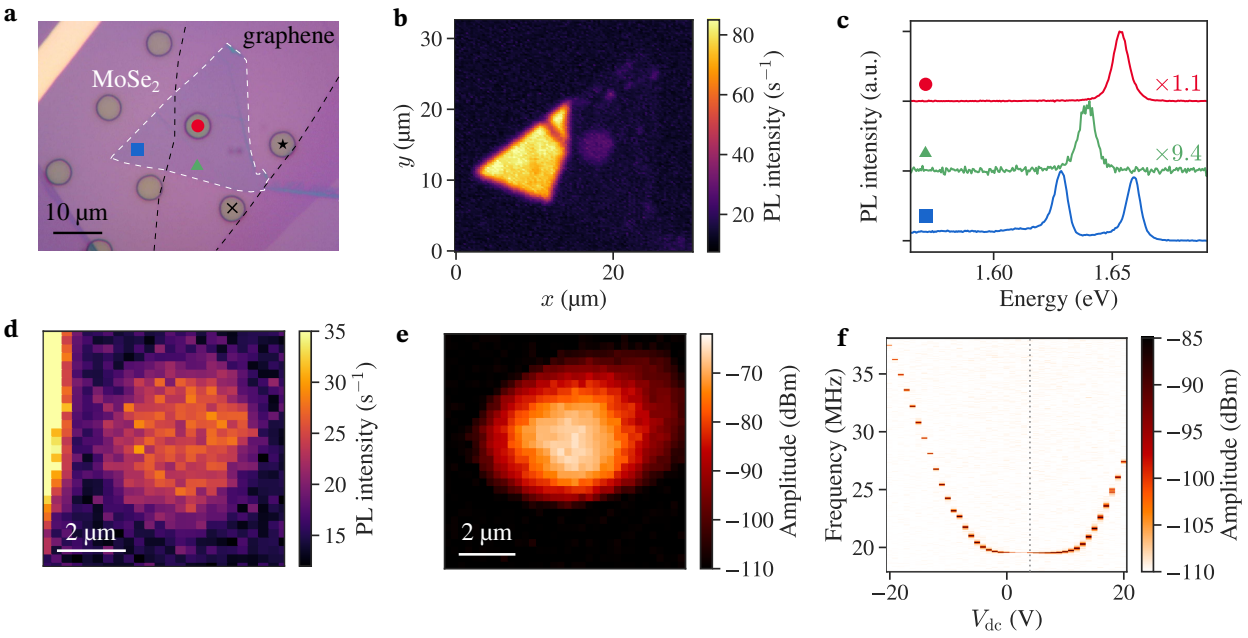

Figure F.12: Un micro-tambour de graphène/$MoSe_2$. **a.** Image optique de l'échantillon. Les symboles indiquent les points correspondants aux spectres présentés en c. **b.** Cartographie de l'intensité intégrée de PL. **c.** Exemples de spectres de PL de $MoSe_2$ supporté (carré bleu), graphène/$MoSe_2$ supporté (triangle vert) et graphène/$MoSe_2$ suspendu (rond rouge). **d.** Zoom de la carte de PL sur la zone de graphène/$MoSe_2$ suspendue. **e.** Profile mesuré du mode de vibration fondamentale du micro-tambour de graphène/$MoSe_2$. L'actuation est réalisée de façon électrostatique avec $V_{dc} = 0$ V et $V_{ac} = 1$ mV. **f.** Variation de la réponse mécanique de l'échantillon en fonction de V_{dc}, pour une tension alternative $V_{ac} = 1$ mV. La ligne pointillée grise indique $V_0 = 4$ V. La puissance laser est de 2 µW dans les panels b,c,d et de 10 µW dans les panels e,f. La longueur d'onde du laser est de 633 nm.

couche entre les deux matériaux [99, 98]. La figure F.12d, qui montre un zoom de la carte de PL centré sur le micro-tambour de graphène/$MoSe_2$, met en évidence l'homogénéité de la membrane suspendue de graphène/$MoSe_2$, ce qui suggère que la membrane ne présente aucun pli et n'a pas été contaminée par des résidus lors de la fabrication.

Une caractérisation de la réponse mécanique en régime linéaire ($V_{ac} = 1$ mV) est présentée figure F.12e,f présentant respectivement une cartographie du profil de vibration du mode fondamentale et la variation de la réponse mécanique en fonction de V_{dc}. La fréquence du mode fondamentale f_0 est hautement accordable et suit un comportement en forme de U lorsque la tension de grille varie, signe d'une contrainte native σ_0 faible dans la membrane vibrante [171]. La variation de f_0 avec la fréquence permet également d'estimer la valeur du point de neutralité à $V_0 = 4$ V, définissant l'axe de symétrie de la courbe en U.

Contrôle électromécanique du couplage intercouche dans une hétérostructure graphène/$MoSe_2$

Pour étudier les changements potentiels dans le couplage intercouche, nous proposons une application des résultats présentés dans le chapitre 3. En tirant électrostatiquement sur l'hétérostructure graphène/$MoSe_2$ suspendue, nous pouvons nous attendre à induire un très léger changement de l'espacement intercouche en raison du fait que la couche de graphène semi-métallique se trouve au bas de l'hétérostructure et peut être affecté plus fortement par la grille électrostatique que la couche supérieure de TMD semiconducteur. Ce léger changement de la distance intercouche devrait se traduire par une réduction du décalage du mode 2D dû à l'écrantage diélectrique. Comme la fréquence du mode G n'est pas affectée par l'environnement diélectrique, elle peut être utilisée pour déterminer les contributions des contraintes mécaniques ou du dopage dans la réponse Raman afin d'isoler un changement potentiel de la fréquence du mode 2D dû à une diminution de l'effet d'écrantage diélectrique.

Pour cela, la réponse Raman du micro-tambour est mesurée en fonction de la tension V_{dc} appliquée. Les spectres Raman correspondants sont montrés figure F.13a. Le mode G de chaque spectre est ajusté par une lorentzienne et le mode 2D par un profil de Voigt. La figure F.13b montre l'évolution des fréquences des modes G et 2D en fonction de la tension V_{dc} par rapport à leurs valeurs pour $V_{dc} = 0$ V. Pour les deux modes, un fort adoucissement des phonons est observé à mesure que V_{dc} augmente. La corrélation $\Delta\omega_G - \Delta\omega_{2D}$ présentée figure F.13c indique que les changements en fréquence des deux modes sont dominés par des effets de contraintes, étant donné que la corrélation suit globalement la pente de 2.2 attendue pour des contraintes mécaniques. On peut noter qu'à faible tension, les données semblent suivre une pente légèrement supérieure à celle attendue pour des contraintes mécaniques. C'est principalement ce régime que nous allons explorer plus en détail pour tester notre hypothèse et sonder un potentiel changement du couplage intercouche.

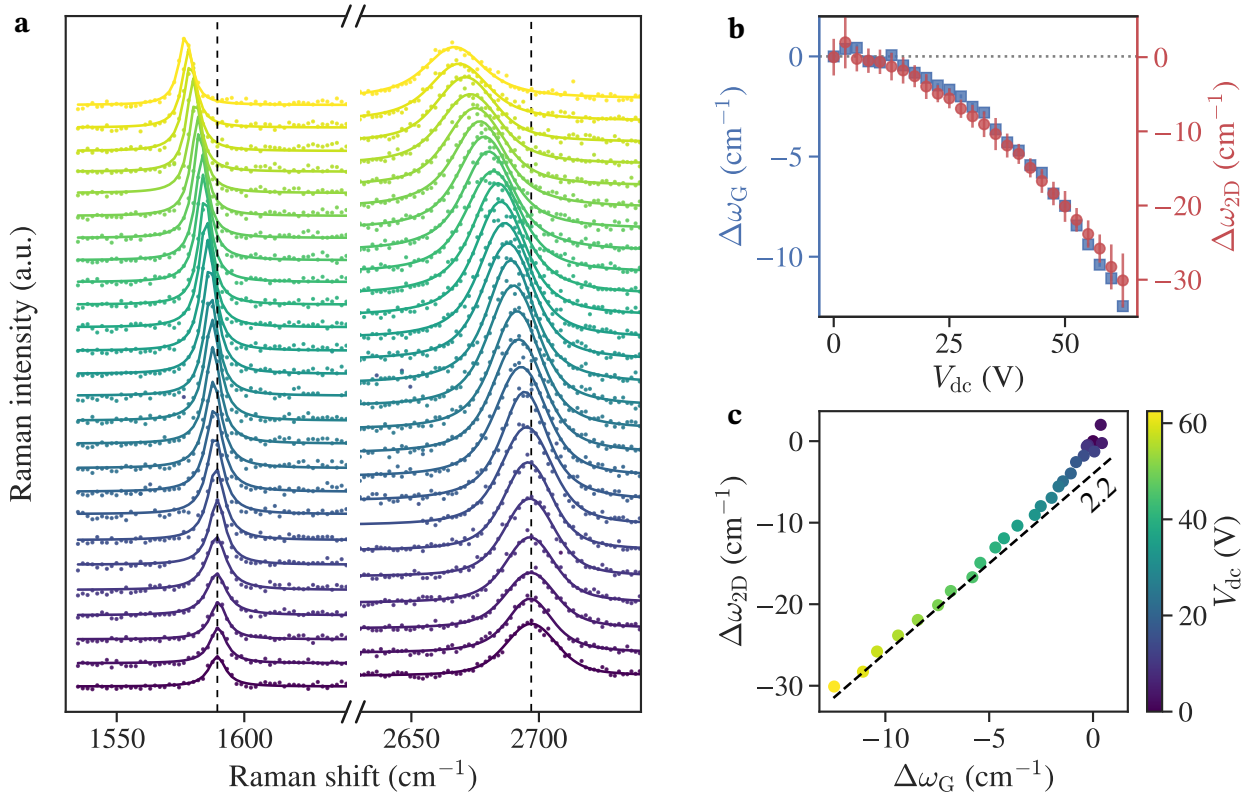

Figure F.13: Dépendance en tension de la réponse Raman du micro-tambour de graphène/$MoSe_2$. **a.** Spectres Raman en fonction de la tension de grille. **b.** Décalage en fréquence des modes G et 2D en fonction de la tension de grille. **c.** Corrélation entre les fréquences du mode G et du mode 2D.

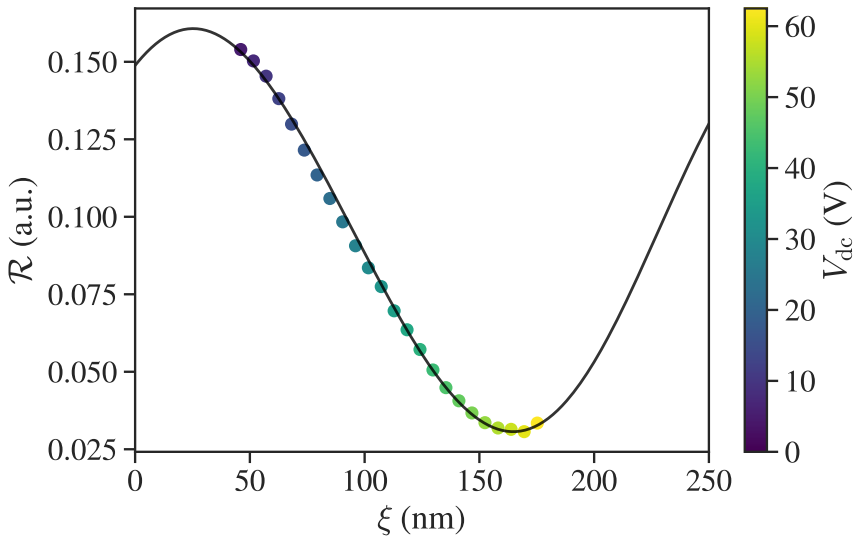

Figure F.14: Calibration de la déflection. Variation de la réflectance en fonction de la déflection. La ligne continue correspond au calcul théorique et les points colorés aux mesures expérimentales.

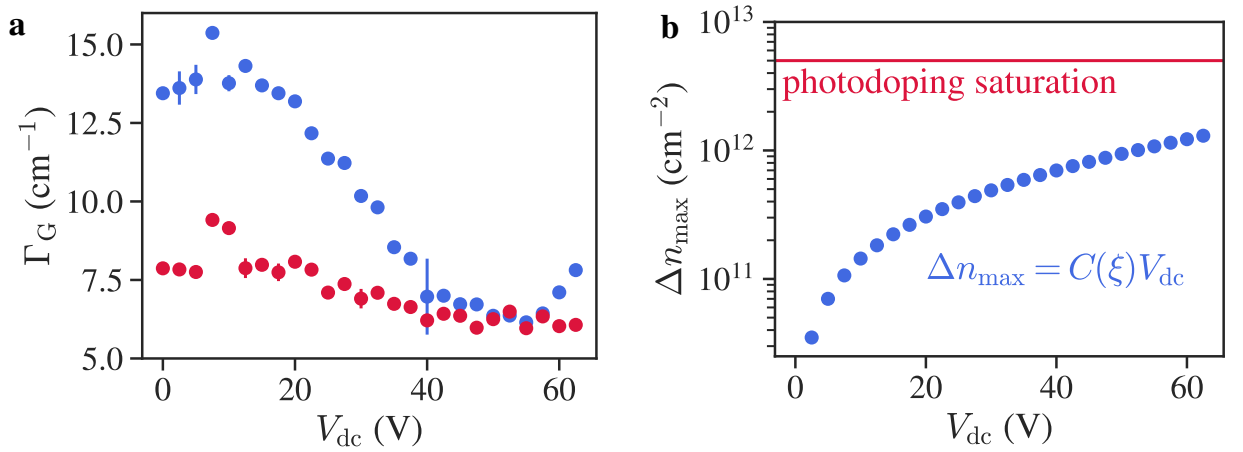

Figure F.15: Estimation du dopage par comparaison avec un micro-tambour de graphène. a. Variation de la largeur du pic G en fonction de la tension de grille appliquée V_{dc} dans le cas du micro-tambour de graphène (bleu) et de graphène/$MoSe_2$ (rouge). **b.** Estimation du niveau de dopage maximal pouvant être induit par la grille électrostatique (ronds bleus) en fonction de la tension de grille appliquée. La ligne rouge indique le niveau de dopage attendu dans le régime de saturation du photodopage.

Calibration de la déflection

La réflectance DC $\mathcal{R}_{dc}$ de l'échantillon est mesurée simultanément à chaque spectre Raman pour garantir une coïncidence point par point entre les deux paramètres. La variation de $\mathcal{R}_{dc}$ découle directement des interférences optiques dans l'échantillon et peut être utilisée pour calibrer la déflexion de la membrane. Pour cela, il suffit de faire correspondre les courbes de réflectance expérimentale et théorique (déterminée en considérant les réflexions, transmissions et absorptions de chaque constituant et interfaces de l'échantillon). Les résultats d'un tel processus de calibration sont présentés sur la figure F.14, où les points de données représentent les valeurs $\mathcal{R}_{dc}$ renormalisées pour correspondre à la variation de réflectance calculée $\mathcal{R}$ en fonction de la déflection ξ pour une longueur d'onde laser de 532 nm.

Estimation du dopage par comparaison avec un micro-tambour de graphène

Comme le montre la figure F.12a, l'échantillon est également composé de deux tambours de graphène suspendus. Comparer leur comportement avec nos observations sur graphène/$MoSe_2$ suspendu peut nous permettre de mieux comprendre la physique sous-jacente. Nous avons donc réalisé des expériences similaires à celles faites sur le micro-tambour de graphène/$MoSe_2$ sur les deux micro-tambours de graphène suspendus.

La figure F.15a présente l'évolution de largeur du pic G Γ_G pour l'un des deux micro-tambours de graphène (ronds bleus) et pour le micro-tambour de graphène/$MoSe_2$ (ronds rouges) en fonction de la tension de grille appliquée. Le second micro-tambour de graphène donne des résultats semblables. Une légère diminution de Γ_G peut être observée dans le cas du micro-tambour de graphène/$MoSe_2$, mais avec une amplitude moindre par rapport à celle observée sur le micro-tambour de graphène (~ 2 cm^{-1} pour graphène/$MoSe_2$ contre ~ 9 cm^{-1} pour la monocouche de graphène).

Cette observation combinée à la fréquence initiale du mode G étonnamment élevée dans le cas de graphène/$MoSe_2$ ($\omega_G(V_{dc} = 0) = 1589.4$ cm^{-1}), suggère que le niveau de dopage de la couche de graphène de l'hétérostructure est dès le départ supérieur à celui pouvant être induit par la grille électrostatique. Étant donné les puissances laser utilisées (~ 350 µW), il est fort probable que l'échantillon soit dans un régime de saturation du photodopage [99]. Ainsi, on peut donc s'attendre à ce que la grille n'affecte que faiblement le niveau de dopage de la couche de graphène de notre hétérostructure et que les effets observés soient dominés par les contraintes.

Afin de s'assurer que le changement du niveau de dopage du graphène induit par la grille électrostatique est faible par rapport au photodopage, nous pouvons estimer la contribution maximale de la grille comme $\Delta n_{max} = C_{eq}(\xi)V_{dc}$, où $C_{eq}(\xi)$ est la capacitance de l'échantillon et comparer le résultat avec le niveau de dopage attendu dans le régime de saturation du photodopage. La figure F.15b montre le résultat d'une telle estimation (points bleus). Le dopage maximal induit par la grille électrostatique devrait atteindre 1.3 $\times 10^{12}$ cm^{-2} lorsque $V_{dc} = 62.5$ V si l'on suppose une grille électrostatique parfaite, alors que le niveau de dopage attendu dans le régime de saturation du photodopage est de 5×10^{12} cm^{-2} (ligne rouge) [99].

Estimation de la contrainte

Nous pouvons donc considérer que les changements dans la fréquence du mode G sont majoritairement dominés par des effets de contraintes. En supposant que les variations de dopages soient trop faibles pour affecter la fréquence du mode G, nous pouvons en déduire la valeur de la contrainte mécanique appliquée par la grille électrostatique. Un changement $\Delta\varepsilon_s$ de contrainte biaxiale induira alors un décalage en fréquence par rapport à la valeur non perturbée $\omega_{G,0}$ de

$$\Delta\omega_G = 2\gamma_G\omega_{G,0}\Delta\varepsilon_s \tag{F.1}$$

avec le paramètre de Gruneisen $\gamma_G = 1.8$ [39, 146]. La valeur de référence utilisée ici est $\omega_{G,0} = \omega_G(V_{dc} = 0) = 1589.4$ cm^{-1}.

Les valeurs de contraintes déduites du décalage du mode G sont présentées figure F.16 et présentent un accord raisonnable avec une estimation théorique de la contrainte obtenue en considérant l'élongation de la membrane induite par la déflection $\Delta\xi$ de celle-ci. En considérant un profil parabolique et une faible déflection $\xi \ll R$, avec R le rayon du microtambour, la contrainte induite par la déflection de la membrane est donnée par [39, 182]

$$\Delta\varepsilon_s = \frac{2}{3}\left(\frac{\Delta\xi}{R}\right)^2. \tag{F.2}$$

Il est cependant important de noter que l'accord avec les données mesurées n'est pas parfait, notamment à fort V_{dc}. L'explication la plus probable vient du fait que l'équation (F.2) considère une élongation moyennée sur toute la surface de la membrane alors que les mesures expérimentales se concentrent sur le centre de la membrane, où l'élongation est maximale.

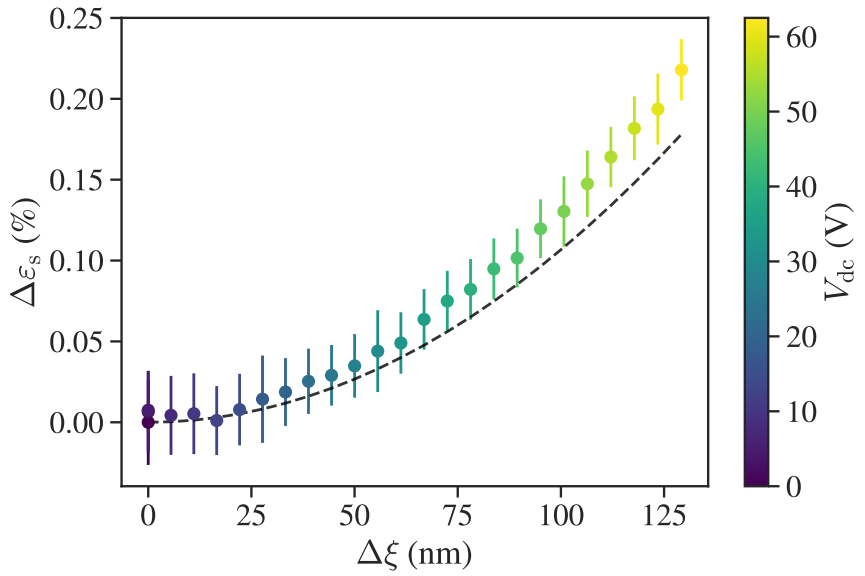

Figure F.16: Estimation de la contrainte. Changement dans le niveau de contrainte statique dans la couche de graphène en fonction de la déflection de la membrane. Les symboles sont estimés d'après le changement de fréquence du mode G et la ligne pointillée d'après l'équation (F.2).

Estimation du décalage du mode 2D dû à l'écrantage diélectrique

À partir du décalage du mode G $\Delta\omega_G$ et des estimations des changements de contrainte statique $\Delta\varepsilon_s$, nous pouvons déterminer le décalage attendu du mode 2D en raison de la contrainte comme

$$\Delta\omega_{2D}^{(strain)} = 2\gamma_{2D}\omega_{2D,0}\Delta\varepsilon_s \tag{F.3}$$

avec le paramètre de Grüneisen du mode 2D $\gamma_{2D} = 2.4$ et la fréquence non perturbée $\omega_{2D,0} = \omega_{2D}(V_{dc} = 0) = 2697$ cm^{-1}. En supposant que la seule autre source de variation de ω_{2D} soit due à l'écrantage diélectrique, le décalage du mode 2D observé est

$$\Delta\omega_{2D} = \Delta\omega_{2D}^{(strain)} + \Delta\omega_{2D}^{(screening)} \tag{F.4}$$

et le décalage lié à un changement d'écrantage diélectrique peut être isolé en prenant la différence $\Delta\omega_{2D} - \Delta\omega_{2D}^{(strain)}$.

Le décalage résiduel du mode 2D est présenté sur la figure F.17 où les marqueurs correspondent aux résultats obtenus à partir des estimations de contrainte basées sur la mesure de $\Delta\omega_G$ tandis que la ligne pointillée utilise les estimations de contrainte de l'équation (F.2). Un faible décalage vers le rouge de quelques cm^{-1} est observé dans les deux cas et pourrait être attribué à une légère réduction de l'écrantage diélectrique en raison d'une légère augmentation de l'espacement intercouches, car la membrane de graphène métallique au bas de l'hétérobicouche est tirée plus efficacement par la grille électrostatique que le $MoSe_2$ semi-conducteur au-dessus.

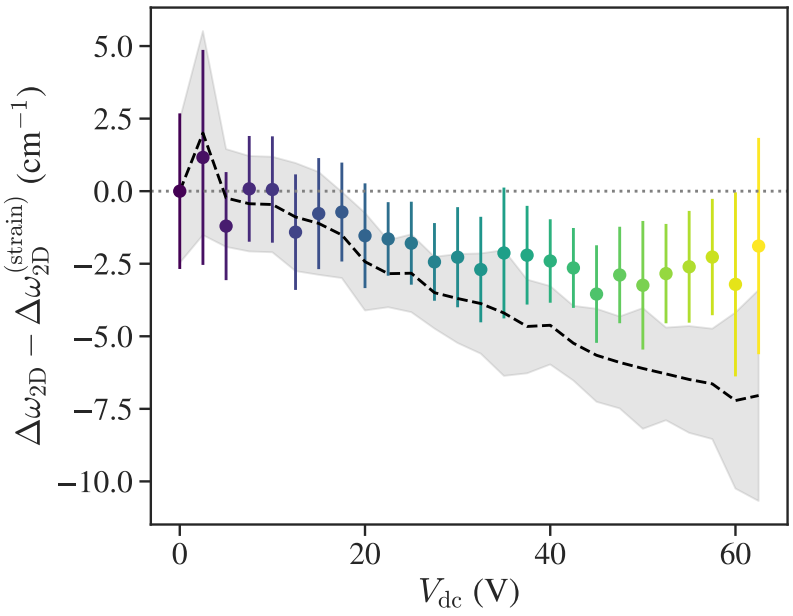

Figure F.17: Déviation du décalage du mode 2D par rapport au comportement attendu pour des contraintes. Les symboles représentent les valeurs basées sur l'estimation de la contrainte d'après le décalage du mode G et la ligne pointillée l'estimation théorique basée sur l'équation F.2.

Contrôle de l'émission de lumière d'une hétérostructure graphène/$MoSe_2$ par une modulation de la contrainte

Nous nous intéressons maintenant à l'influence des contraintes sur l'émission de lumière de notre micro-tambour de graphène/$MoSe_2$. L'objectif est ici de réaliser une modulation dynamique de la raie d'émission de l'exciton neutre du $MoSe_2$ via les contraintes mécaniques induites par la vibration de la membrane.

Estimation de la sensibilité aux contraintes

La figure F.18a montre une carte de couleurs qui représente le spectre de PL mesuré au centre du tambour de graphène/$MoSe_2$ en fonction de la tension de grille appliquée V_{dc}. L'excitation est assurée par un laser de 532 nm à une puissance fixe de 10 µW. Comme attendue, la raie de l'exciton se décale progressivement vers le rouge avec la tension appliquée et l'intensité totale diminue. Le comportement est symétrique par rapport à la polarité de la grille et nous choisissons ici de nous concentrer sur le côté positif ($V_{\mathrm{dc}} \geq 0$) pour assurer la continuité avec nos données Raman de la section précédente.

Les spectres sont ajustés par un profil de Voigt afin de déterminer la position en énergie de la raie excitonique. La déflection de la membrane en fonction de la tension de grille est déterminée de la même façon que dans la section précédente, en faisant coïncider la réflectance mesurée expérimentalement avec celle déterminée théoriquement. Nous estimons ensuite la valeur des contraintes statiques $\Delta\varepsilon_{\mathrm{s}}$ à l'aide de l'équation (F.2) et déterminons la dépendance en contrainte de E_{X^0} présentée dans la figure F.18b. De la même manière

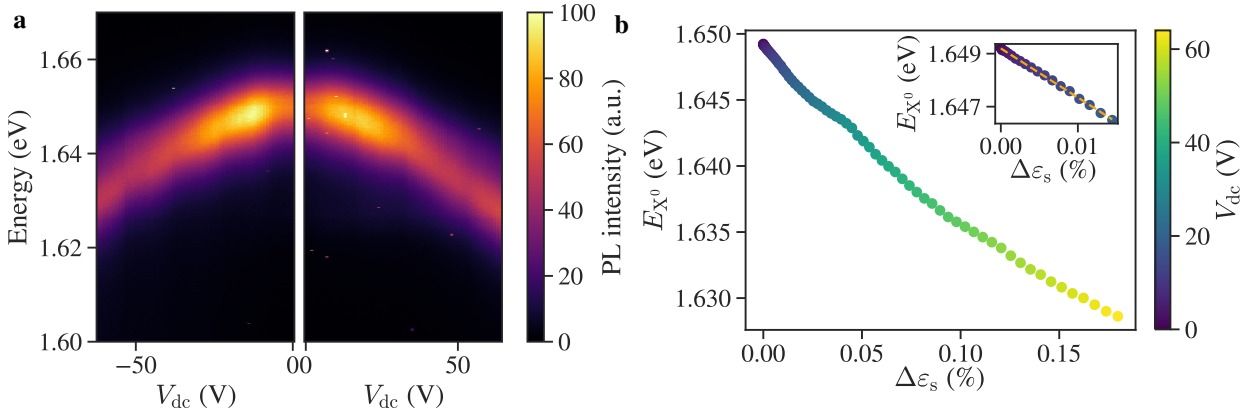

Figure F.18: Photoluminescence du micro-tambour de graphène/$MoSe_2$ en fonction de la tension. a. Évolution du spectre de PL en fonction de la tension de grille statique V_{dc} appliquée. **b.** Position en énergie de la raie excitonique en fonction de la contrainte statique induite par la grille électrostatique.

que l'estimation de la contrainte de la section précédente, nous pouvons nous attendre à ce que notre résultat devienne moins précis à fort V_{dc} puisque l'équation (F.2) considère un allongement moyen alors que nous mesurons localement au centre de la membrane.

Cependant, nous pouvons nous attendre à ce que notre estimation soit plus précise à faible V_{dc}. Plus précisément, nous pouvons raisonnablement supposer que cela est vrai pour $V_{dc} \leq 20$ V, c'est-à-dire la plage disponible de l'amplificateur lock-in utilisé pour l'actuation et la détection mécanique lors de nos mesures visant à contrôler dynamiquement la contrainte que nous présenterons dans la prochaine section. L'encadré de la figure F.18b se focalise sur cette plage de tensions. Un ajustement linéaire restreint à cette plage est effectué (voir la ligne pointillée orange dans l'encadré de la figure F.18b) et donne une sensibilité à la contrainte de -185 meV/%. Notons que cette valeur est nettement supérieure à celles rapportées dans la littérature qui se situe typiquement autour de $\sim 50 - 100$ meV/% pour des contraintes biaxialles dans une monocouche de $MoSe_2$ [164, 184, 185, 186]. Cependant, les valeurs communément rapportées ne prennent pas en compte des hétérostructures graphène/$MoSe_2$ suspendues mais des monocouches isolées de $MoSe_2$. D'autres expériences sont nécessaires pour comprendre la raison de cette sensibilité aux contraintes étonnamment élevée, telle qu'une étude de la dépendance en tension de la réponse Raman du $MoSe_2$, qui nous donnerait une mesure supplémentaire de la contrainte.

Modulation dynamique de l'énergie de l'exciton

Nous nous intéressons maintenant au régime dynamique en déterminant l'effet d'une modulation de la contrainte sur l'énergie de l'exciton neutre. D'après les résultats de la sous-section précédente, la raie excitonique se décale avec une sensibilité de -185 meV/% sous l'effet d'une contrainte statique. En régime dynamique, les amplitudes d'oscillation sont faibles (de l'ordre d'un ou quelques nm) par rapport à la déflexion statique induite par la grille électrostatique (jusqu'à $\Delta\xi \sim 150$ nm pour $V_{dc} = 64$ V). Qualitativement, on peut s'attendre à ce que l'oscillation de la membrane induise des valeurs de modulation de la

contrainte dynamique de l'ordre de 10^{-4} %, ce qui correspond à un décalage de la raie excitonique d'environ -100 µeV. Ces valeurs sont particulièrement faibles comparées à la largeur de la raie excitonique et sont proches de la limite de résolution spectrale, mais restent détectables.

La figure F.19a présente l'évolution de la réponse mécanique lorsque la tension d'actuation V_{ac} est augmentée de 1 mV à 200 mV, pour une tension continue fixe $V_{dc} = -5$ V. La courbe en aileron de requin caractéristique d'un résonateur de Duffing se forme à mesure que V_{ac} augmente [10, 156]. On peut noter que la non-linéarité commence déjà à apparaître pour $V_{ac} = 5$ mV.

Afin de détecter les changements dans l'énergie de l'exciton dus à la contrainte induite par la vibration non-linéaire de la membrane, nous mesurons le spectre de PL de notre hétérostructure graphène/$MoSe_2$ tout en entrainant l'échantillon à la fréquence maximale de la résonnance mécanique f_p. Nous définissons ici la fréquence maximale f_p comme la fréquence la plus proche de la fréquence de saut donnant une oscillation non-linéaire suffisamment stable pour mesurer le spectre de PL avant une chute de l'amplitude de vibration. Le décalage correspondant de l'énergie de l'exciton est représenté figure F.19b avec en point de référence l'énergie de l'exciton mesurée hors résonance ($f = 21.5$ MHz, voir croix rouge sur la figure F.19a) avec $V_{ac} = 1$ mV. Le point de référence est représenté par un symbole rouge sur la figure F.19b. Les spectres de PL mesurés dans les deux cas extrêmes sont montrés figure F.19c, où le spectre rouge correspond au point de référence (hors résonance avec $V_{ac} = 1$ mV, voir croix rouge sur la figure F.19a) et le bleu au point de forte vibration ($V_{ac} = 200$ mV, voir croix bleue sur la figure F.19a). La figure F.19d montre la différence d'intensité entre les deux spectres de la figure F.19c.

Une diminution de l'énergie de l'exciton est observée, avec une amplitude croissante à mesure que V_{ac} augmente. Dans le cas où la tension alternative est la plus forte ($V_{ac} = 200$ mV), un décalage de $\Delta E_{X^0} = -170 \pm 40$ µeV est observé. Considérant la sensibilité à la contrainte de -185 meV/% déterminée précédemment, cela correspond à une contrainte dynamique $\varepsilon_d = 9 \times 10^{-4} \pm 2 \times 10^{-4}$ %. Il peut être intéressant de comparer ce résultat avec une estimation théorique basée sur la même idée que le modèle qui nous donne l'équation (F.2). Nous pouvons ainsi estimer la valeur de la contrainte dynamique par

$$\varepsilon_d = \frac{2}{3}\left(\frac{z_0}{R}\right)^2. \tag{F.5}$$

Dans notre cas, pour $V_{ac} = 200$ mV, l'amplitude maximale mesurée à la fréquence maximale de résonance f_p est $z_0 = 5.9$ nm, ce qui donne une estimation de la contrainte dynamique de $\varepsilon_d = 3.7 \times 10^{-4}$ %.

Bien que cette valeur soit 2.4 fois inférieure à celle que nous mesurons dans la réponse en PL, cette différence n'est pas aussi importante que celle observée par X. Zhang *et al.* dans des tambours de graphène vibrant en régime non-linéaire, où la valeur mesurée de la contrainte dynamique atteint 40 fois la valeur estimée [39]. L'écart élevé signalé dans le graphène a été attribué aux oscillations anharmoniques et aux profils de modes complexes [39]. Ainsi, nous pouvons considérer que le mode de vibration de notre échantillon n'est que légèrement altéré par le régime non-linéaire. Il convient de noter que le rapport entre l'amplitude RMS et le rayon du micro-tambour z_0/R est comparable entre notre échantillon ($z_0/R \sim 2.4$ ‰)

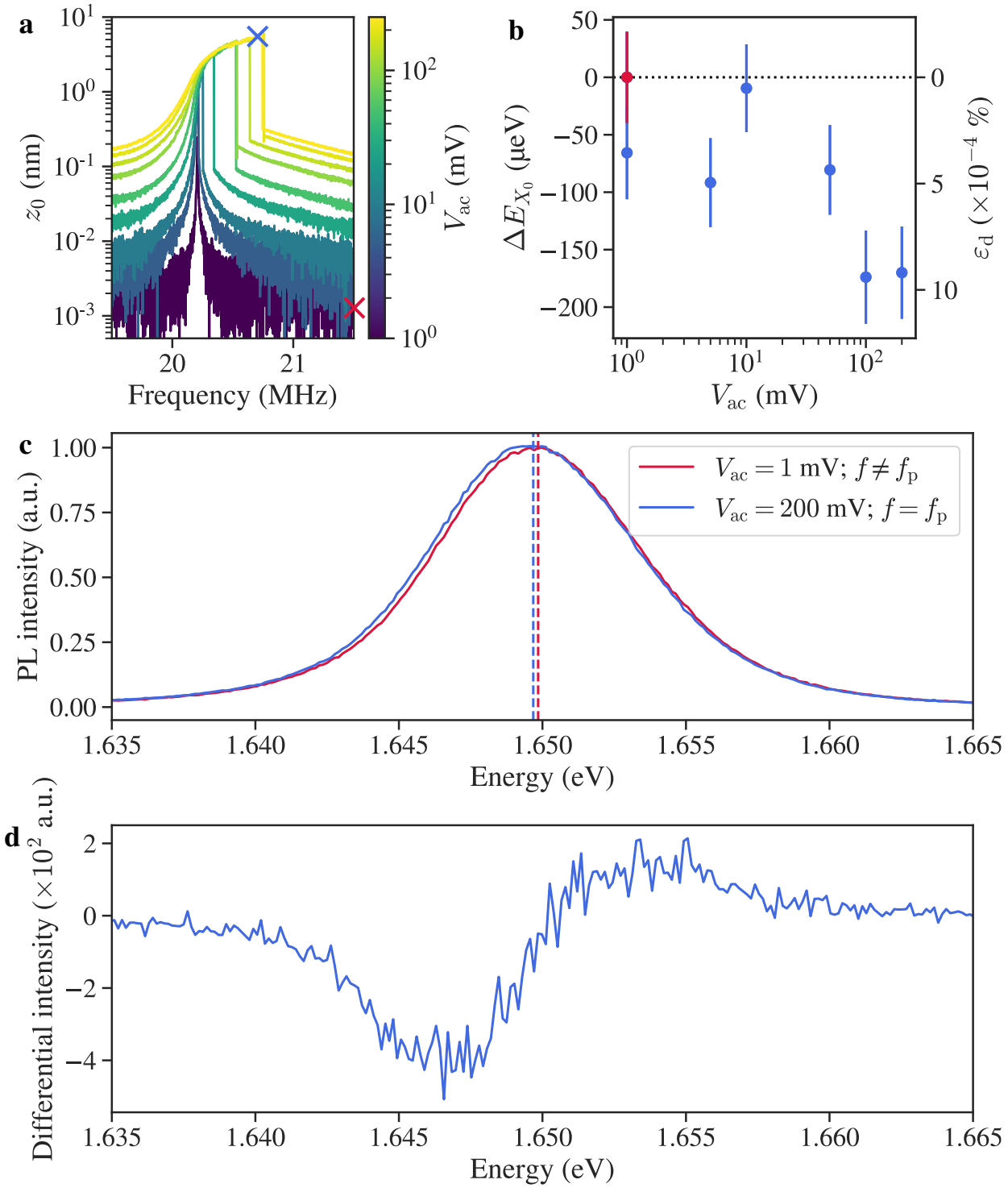

Figure F.19: Modulation dynamique de l'émission de lumière du micro-tambour de graphène/$MoSe_2$. **a.** Evolution de la réponse mécanique lorsque la tension alternative V_{ac} est augmentée, pour une tension continue fixée de $V_{dc} = -5$ V. **b.** Décalage en énergie de la raie d'émission de l'exciton en fonction de V_{ac}. L'énergie de référence est prise hors résonnance ($f = 21.5$ MHz, voir croix rouge dans a) pour $V_{ac} = 1$ mV (point rouge). **c.** Spectre de PL de la raie d'émission de l'exciton neutre dans les deux cas extrêmes, hors résonance à faible vibration (en rouge) et à forte vibration à la fréquence de résonance maximale f_p. **d.** Différence d'intensité entre les deux spectres de PL montrés en c.

et le tambour de graphène de la référence [39] ($z_0/R \sim 3$ ‰). On aurait donc pu s'attendre à observer un écart tout aussi important et son absence pourrait être un indice de l'influence de la couche de $MoSe_2$ sur les propriétés mécaniques du graphène.

D'autres expériences, consistant notamment en une cartographie spatiale des profils de modes en régime non-linéaire, pourraient nous donner plus d'informations pour conclure sur ce point. De plus, ne pas mesurer le même niveau de contrainte dynamique que rapporté dans des micro-tambours de graphène nous suggère fortement de reproduire les résultats de la référence [39] sur notre échantillon de graphène/$MoSe_2$ pour voir comment se comporte la contrainte dynamique dans le graphène lorsque la couche de graphène est en contact avec une couche de TMD et si des valeurs de contrainte similaires sont mesurées dans les deux couches lorsque l'échantillon entre en résonance.

Les résultats présentés dans cette section qui résume le chapitre 4 de ce manuscrit met en lumière le potentiel des échantillons en micro-tambour pour l'étude des hétérostructures de van der Waals. Dans un premier temps, nous avons montré que le degré de liberté mécanique apporté par la géométrie en micro-tambour donne la possibilité de contrôler le couplage intercouche au sein d'un même échantillon. Dans un deuxième temps, nous avons démontré la possibilité d'utiliser la résonance mécanique d'un micro-tambour de graphène/$MoSe_2$ pour moduler dynamiquement son émission de lumière via un contrôle dynamique de la contrainte.

Conclusion

Dans ce manuscrit, nous avons présenté une étude des propriétés de matériaux 2D pouvant être considérablement modifiées par l'absence ou le changement du substrat sous-jacent et avons démontré la polyvalence de la géométrie d'échantillon en forme de micro-tambour pour sonder et contrôler les propriétés des hétérostructures de van der Waals. Les résultats présentés peuvent être séparés en deux parties.

La première partie est composée des chapitres 2 et 3. Dans le chapitre 2, nous avons présenté des résultats à température ambiante sur des monocouches suspendues de MoS_2 et WS_2. Nous avons montré que dans les deux matériaux, l'absence de substrat sous-jacent entraîne une forte altération du spectre de PL lorsque l'intensité de l'excitation laser augmente.

Dans le cas de MoS_2 suspendu, nos données montrent une explosion de l'intensité de PL corrélée à un fort décalage vers le rouge et à un élargissement du spectre de PL. Nos observations concordent avec des résultats de la littérature rapportant la formation d'une phase liquide d'électrons et de trous médiée par une transition abrupte dans la structure des bandes électroniques, passant d'un gap direct à un gap indirect lorsque la température du réseau atteint environ 550 K [110, 112]. Dans le cas de WS_2 suspendu, un fort décalage vers le rouge est à nouveau observé, combiné à un élargissement de la PL, mais avec une augmentation réduite de son intensité. Une augmentation inattendue de l'intensité du mode Raman A_1' est également observée en corrélation avec l'altération du spectre de PL. Bien que d'autres expériences soient nécessaires pour conclure correctement, nous proposons une interprétation basée sur la non-uniformité du profil de chauffage photo-induit qui favorise une conversion efficace des excitons en trions pouvant conduire à la formation d'un plasma d'électrons et de

trous [73, 78]. Cependant, nous pensons que la potentielle phase de plasma électrons-trous dans le WS_2 suspendu est très instable, car un fort photoblanchiment est observé lorsque la puissance du laser est augmentée à des puissances plus élevées.

Dans le chapitre 3, nous avons présenté des résultats démontrant que la symétrie des phonons optiques du graphène détermine leur sensibilité aux effets d'écrantage diélectrique. En se basant sur la cartographie hyperspectrale de la réponse Raman d'hétérostructures de van der Waals à base de graphène avec différentes géométries, nous avons montré que la fréquence du mode 2D ω_{2D} est très sensible aux changements de l'environnement diélectrique tandis que la fréquence du mode G ω_G reste constante dans toutes les situations. En mesurant la dispersion du mode 2D sur un échantillon avec différentes configurations, nous avons démontré que l'augmentation de ω_{2D} est liée à un adoucissement de l'anomalie de Kohn au point K provoqué par l'écrantage diélectrique. De plus, un argument théorique explique l'absence d'effet sur ω_G grâce à une protection des fréquences des phonons à Γ qui résulte de la dégénérescence des phonons E_{2g} à Γ. Ainsi, nous avons montré que la réponse Raman du graphène est une sonde très précise des effets d'écrantage diélectrique, ce qui élargit la déjà grande utilité de cette technique pour la caractérisation d'hétérostructures de van der Waals.

La deuxième partie correspond au chapitre 4, dans lequel nous avons exploité le nouveau dispositif expérimental détaillé en annexe C et qui a été entièrement développé dans le cadre de ce travail de thèse. Il est conçu pour réaliser des expériences automatisées combinant spectroscopie optique et optoélectromécanique dans des échantillons en forme de micro-tambour, avec un contrôle précis de la température et une grande stabilité mécanique.

En utilisant nos résultats du chapitre 3, une nouvelle façon de sonder les changements dans le couplage intercouche dans une hétérostructure graphène/$MoSe_2$ suspendue a été proposée. Le mode G du graphène est alors utilisé pour déterminer la contrainte induite par une grille électrostatique et déterminer le décalage associé du mode 2D. Le décalage estimé de ω_{2D} dû à la contrainte est ensuite soustrait à la valeur mesurée pour isoler un changement potentiel dans le décalage du mode 2D dû à l'écrantage diélectrique.

Dans la section suivante, la grille électrostatique a été utilisée en régime statique pour estimer la sensibilité à la contrainte de l'énergie de l'exciton de notre hétérostructure graphène/$MoSe_2$. La sensibilité à la contrainte déterminée a ensuite quant à elle été utilisée pour sonder la contrainte induite dynamiquement dans l'échantillon lorsque la membrane atteint le régime de vibration non-linéaire. Un décalage vers le rouge de l'énergie de l'exciton atteignant jusqu'à -170 ± 40 µeV a été observé et attribué à une contrainte dynamique de $9 \times 10^{-4} \pm 2 \times 10^{-4}$%.

Bibliography

[1] Silvan Schmid, Luis Guillermo Villanueva, and Michael Lee Roukes. *Fundamentals of Nanomechanical Resonators*. Springer, 1st edition, 2016.

[2] L. D. Landau, E. Lifshitz, J. Sykes, W. Reid, and E. H. Dill. *Theory of elasticity: Vol. 7 of course of theoretical physics*. Pergamon Press, 2nd edition, 1970.

[3] David J. Griffiths. *Introduction to Quantum Mechanics*. Cambridge University Press, 1 edition, 1995.

[4] Giuseppe Grosso and Giuseppe Pastori Parravicini. *Solid State Physics*. Academic Press, London, 2000.

[5] Peter Y. Yu and Manuel Cardona. *Fundamentals of Semiconductors*. Springer, 3rd edition, 2001.

[6] Pulickel Ajayan, Philip Kim, and Kaustav Banerjee. Two-dimensional van der waals materials. *Physics Today*, 69(9):38–44, 2016.

[7] M. Gibertini, M. Koperski, A. F. Morpurgo, and K. S. Novoselov. Magnetic 2D materials and heterostructures. *Nature Nanotechnology*, 14(5):408–419, May 2019.

[8] Qing Hua Wang, Amilcar Bedoya-Pinto, Mark Blei, Avalon H. Dismukes, Assaf Hamo, Sarah Jenkins, Maciej Koperski, Yu Liu, Qi-Chao Sun, Evan J. Telford, Hyun Ho Kim, Mathias Augustin, Uri Vool, Jia-Xin Yin, Lu Hua Li, Alexey Falin, Cory R. Dean, Fèlix Casanova, Richard F. L. Evans, Mairbek Chshiev, Artem Mishchenko, Cedomir Petrovic, Rui He, Liuyan Zhao, Adam W. Tsen, Brian D. Gerardot, Mauro Brotons-Gisbert, Zurab Guguchia, Xavier Roy, Sefaattin Tongay, Ziwei Wang, M. Zahid Hasan, Joerg Wrachtrup, Amir Yacoby, Albert Fert, Stuart Parkin, Kostya S. Novoselov, Pengcheng Dai, Luis Balicas, and Elton J. G. Santos. The magnetic genome of two-dimensional van der waals materials. *ACS Nano*, 16(5):6960–7079, 2022.

[9] A. K. Geim and I. V. Grigorieva. Van der waals heterostructures. *Nature*, 499(7459):419–425, Jul 2013.

[10] Peter G Steeneken, Robin J Dolleman, Dejan Davidovikj, Farbod Alijani, and Herre S J van der Zant. Dynamics of 2D material membranes. *2D Materials*, 8(4):042001, aug 2021.

[11] G. Wang, Alexey Chernikov, Mikhail Glazov, Tony Heinz, Xavier Marie, Thierry Amand, and Bernhard Urbaszek. Excitons in atomically thin transition metal dichalcogenides. *Reviews of Modern Physics*, 90, 07 2017.

[12] Shivangi Shree, Ioannis Paradisanos, Xavier Marie, Cedric Robert, and Bernhard Urbaszek. Guide to optical spectroscopy of layered semiconductors. *Nature Reviews Physics*, 3(1):39–54, Jan 2021.

[13] K. S. Novoselov, A. K. Geim, S. V. Morozov, D. Jiang, Y. Zhang, S. V. Dubonos, I. V. Grigorieva, and A. A. Firsov. Electric field effect in atomically thin carbon films. *Science*, 306(5696):666–669, 2004.

[14] Dominik Metten. *Probing the opto-electronic and mechanical properties of suspended graphene membranes by Raman spectroscopy.* PhD thesis, Université de Strasbourg, 2016.

[15] A. H. Castro Neto, F. Guinea, N. M. R. Peres, K. S. Novoselov, and A. K. Geim. The electronic properties of graphene. *Rev. Mod. Phys.*, 81:109–162, Jan 2009.

[16] Guillaume Froehlicher. *Optical spectroscopy of two-dimensional materials : graphene, transition metal dichalcogenides and Van der Waals heterostructures.* PhD thesis, Université de Strasbourg, 2016.

[17] J N Fuchs and Mark Oliver Goerbig. Introduction to the physical properties of graphene. 2008.

[18] P. R. Wallace. The band theory of graphite. *Phys. Rev.*, 71:622–634, May 1947.

[19] S. Reich, J. Maultzsch, C. Thomsen, and P. Ordejón. Tight-binding description of graphene. *Phys. Rev. B*, 66:035412, Jul 2002.

[20] R. R. Nair, P. Blake, A. N. Grigorenko, K. S. Novoselov, T. J. Booth, T. Stauber, N. M. R. Peres, and A. K. Geim. Fine structure constant defines visual transparency of graphene. *Science*, 320(5881):1308–1308, 2008.

[21] M. S. Dresselhaus and G. Dresselhaus. Intercalation compounds of graphite. *Advances in Physics*, 51(1):1–186, 2002.

[22] Stéphane Berciaud, Xianglong Li, Han Htoon, Louis E. Brus, Stephen K. Doorn, and Tony F. Heinz. Intrinsic line shape of the raman 2D-mode in freestanding graphene monolayers. *Nano Letters*, 13(8):3517–3523, 2013.

[23] W. Kohn. Image of the fermi surface in the vibration spectrum of a metal. *Phys. Rev. Lett.*, 2:393–394, May 1959.

[24] Sven Reichardt. *Many-Body Perturbation Theory Approach to Raman Spectroscopy and Its Application to 2D Materials.* PhD thesis, RWTH Aachen University & University of Luxembourg, 2018.

[25] S. Piscanec, M. Lazzeri, Francesco Mauri, A. C. Ferrari, and J. Robertson. Kohn anomalies and electron-phonon interactions in graphite. *Phys. Rev. Lett.*, 93:185503, Oct 2004.

[26] Stefano Piscanec, Michele Lazzeri, J. Robertson, Andrea C. Ferrari, and Francesco Mauri. Optical phonons in carbon nanotubes: Kohn anomalies, peierls distortions, and dynamic effects. *Phys. Rev. B*, 75:035427, Jan 2007.

[27] Michele Lazzeri, Claudio Attaccalite, Ludger Wirtz, and Francesco Mauri. Impact of the electron-electron correlation on phonon dispersion: Failure of lda and gga dft functionals in graphene and graphite. *Phys. Rev. B*, 78:081406, Aug 2008.

[28] Andrea C. Ferrari and Denis M. Basko. Raman spectroscopy as a versatile tool for studying the properties of graphene. *Nature Nanotechnology*, 8:235–246, 04 2013.

[29] D. M. Basko. Theory of resonant multiphonon raman scattering in graphene. *Phys. Rev. B*, 78:125418, Sep 2008.

[30] D. L. Mafra, G. Samsonidze, L. M. Malard, D. C. Elias, J. C. Brant, F. Plentz, E. S. Alves, and M. A. Pimenta. Determination of LA and TO phonon dispersion relations of graphene near the dirac point by double resonance raman scattering. *Phys. Rev. B*, 76:233407, Dec 2007.

[31] Pedro Venezuela, Michele Lazzeri, and Francesco Mauri. Theory of double-resonant raman spectra in graphene: Intensity and line shape of defect-induced and two-phonon bands. *Phys. Rev. B*, 84:035433, Jul 2011.

[32] Guillaume Froehlicher and Stéphane Berciaud. Raman spectroscopy of electrochemically gated graphene transistors: Geometrical capacitance, electron-phonon, electron-electron, and electron-defect scattering. *Phys. Rev. B*, 91:205413, May 2015.

[33] Michele Lazzeri and Francesco Mauri. Nonadiabatic Kohn anomaly in a doped graphene monolayer. *Phys. Rev. Lett.*, 97:266407, Dec 2006.

[34] Simone Pisana, Michele Lazzeri, Cinzia Casiraghi, Kostya S. Novoselov, A. K. Geim, Andrea C. Ferrari, and Francesco Mauri. Breakdown of the adiabatic born–oppenheimer approximation in graphene. *Nature Materials*, 6(3):198–201, Mar 2007.

[35] J. Martin, N. Akerman, G. Ulbricht, T. Lohmann, J. H. Smet, K. von Klitzing, and A. Yacoby. Observation of electron–hole puddles in graphene using a scanning single-electron transistor. *Nature Physics*, 4(2):144–148, Feb 2008.

[36] Qiuzi Li, E. H. Hwang, and S. Das Sarma. Disorder-induced temperature-dependent transport in graphene: Puddles, impurities, activation, and diffusion. *Phys. Rev. B*, 84:115442, Sep 2011.

[37] Ji Eun Lee, Gwanghyun Ahn, Jihye Shim, Young Sik Lee, and Sunmin Ryu. Optical separation of mechanical strain from charge doping in graphene. *Nature Communications*, 3(1):1024, Aug 2012.

[38] Dominik Metten, François Federspiel, Michelangelo Romeo, and Stéphane Berciaud. Probing built-in strain in freestanding graphene monolayers by Raman spectroscopy. *physica status solidi (b)*, 250(12):2681–2686, 2013.

[39] Xin Zhang, Kevin Makles, Léo Colombier, Dominik Metten, Hicham Majjad, Pierre Verlot, and Stéphane Berciaud. Dynamically-enhanced strain in atomically thin resonators. *Nature Communications*, 11:5526, 2020.

[40] Etienne Lorchat. *Optical spectroscopy of heterostructures based on atomically-thin semiconductors*. PhD thesis, Université de Strasbourg, 05 2019.

[41] J. Ribeiro-Soares, R. M. Almeida, E. B. Barros, P. T. Araujo, M. S. Dresselhaus, L. G. Cançado, and A. Jorio. Group theory analysis of phonons in two-dimensional transition metal dichalcogenides. *Phys. Rev. B*, 90:115438, Sep 2014.

[42] Andrea Splendiani, Liang Sun, Yuanbo Zhang, Tianshu Li, Jonghwan Kim, Chi-Yung Chim, Giulia Galli, and Feng Wang. Emerging photoluminescence in monolayer MoS_2. *Nano Letters*, 10(4):1271–1275, 2010.

[43] Kin Fai Mak, Changgu Lee, James Hone, Jie Shan, and Tony F. Heinz. Atomically thin MoS_2: A new direct-gap semiconductor. *Phys. Rev. Lett.*, 105:136805, Sep 2010.

[44] Kin Mak and Jie Shan. Photonics and optoelectronics of 2D semiconductor transition metal dichalcogenides. *Nature Photonics*, 10:216–226, 03 2016.

[45] Xiaodong Xu, Wang Yao, Di Xiao, and Tony F. Heinz. Spin and pseudospins in layered transition metal dichalcogenides. *Nature Physics*, 10(5):343–350, May 2014.

[46] Luis Enrique Parra Lòpez. *Tailoring the luminescence of atomically-thin semiconductors at the sub-nanometer scale.* PhD thesis, Université de Strasbourg, 07 2021.

[47] M R Molas, C Faugeras, A O Slobodeniuk, K Nogajewski, M Bartos, D M Basko, and M Potemski. Brightening of dark excitons in monolayers of semiconducting transition metal dichalcogenides. *2D Materials*, 4(2):021003, jan 2017.

[48] C. Robert, B. Han, P. Kapuscinski, A. Delhomme, C. Faugeras, T. Amand, M. R. Molas, M. Bartos, K. Watanabe, T. Taniguchi, B. Urbaszek, M. Potemski, and X. Marie. Measurement of the spin-forbidden dark excitons in MoS_2 and $MoSe_2$ monolayers. *Nature Communications*, 11(1):4037, Aug 2020.

[49] Claus F. Klingshirn. *Semiconductor Optics*. Springer, 4th edition, 2012.

[50] Alexey Chernikov, Timothy C. Berkelbach, Heather M. Hill, Albert Rigosi, Yilei Li, Burak Aslan, David R. Reichman, Mark S. Hybertsen, and Tony F. Heinz. Exciton binding energy and nonhydrogenic rydberg series in monolayer WS_2. *Phys. Rev. Lett.*, 113:076802, Aug 2014.

[51] A. Molina-Sánchez and L. Wirtz. Phonons in single-layer and few-layer MoS_2 and WS_2. *Phys. Rev. B*, 84:155413, Oct 2011.

[52] Timothy C. Berkelbach, Mark S. Hybertsen, and David R. Reichman. Theory of neutral and charged excitons in monolayer transition metal dichalcogenides. *Phys. Rev. B*, 88:045318, Jul 2013.

[53] J. S. Blakemore. Semiconducting and other major properties of gallium arsenide. *Journal of Applied Physics*, 53(10):R123–R181, 1982.

[54] Pierluigi Cudazzo, Ilya V. Tokatly, and Angel Rubio. Dielectric screening in two-dimensional insulators: Implications for excitonic and impurity states in graphane. *Phys. Rev. B*, 84:085406, Aug 2011.

[55] L. V. Keldysh. Coulomb interaction in thin semiconductor and semimetal films. *ZhETF Pisma Redaktsiiu*, 29:716, June 1979.

[56] Jason S. Ross, Sanfeng Wu, Hongyi Yu, Nirmal J. Ghimire, Aaron M. Jones, Grant Aivazian, Jiaqiang Yan, David G. Mandrus, Di Xiao, Wang Yao, and Xiaodong Xu. Electrical control of neutral and charged excitons in a monolayer semiconductor. *Nature Communications*, 4(1474), 2 2013.

[57] Kin Fai Mak, Keliang He, Changgu Lee, Gwan Hyoung Lee, James Hone, Tony F. Heinz, and Jie Shan. Tightly bound trions in monolayer MoS_2. *Nature Materials*, 12(3):207–211, Mar 2013.

[58] Kevin O'Donnell and X Chen. Temperature dependence of semiconductor band gaps. *Applied Physics Letters*, 58:2924 – 2926, 07 1991.

[59] Y.P. Varshni. Temperature dependence of the energy gap in semiconductors. *Physica*, 34(1):149 – 154, 1967.

[60] C. Robert, D. Lagarde, F. Cadiz, G. Wang, B. Lassagne, T. Amand, A. Balocchi, P. Renucci, S. Tongay, B. Urbaszek, and X. Marie. Exciton radiative lifetime in transition metal dichalcogenide monolayers. *Phys. Rev. B*, 93:205423, May 2016.

[61] F. Cadiz, E. Courtade, C. Robert, G. Wang, Y. Shen, H. Cai, T. Taniguchi, K. Watanabe, H. Carrere, D. Lagarde, M. Manca, T. Amand, P. Renucci, S. Tongay, X. Marie, and B. Urbaszek. Excitonic linewidth approaching the homogeneous limit in MoS_2-based van der waals heterostructures. *Phys. Rev. X*, 7:021026, May 2017.

[62] Hiram J. Conley, Bin Wang, Jed I. Ziegler, Richard F. Jr. Haglund, Sokrates T. Pantelides, and Kirill I. Bolotin. Bandgap engineering of strained monolayer and bilayer MoS_2. *Nano Letters*, 13(8):3626–3630, 2013.

[63] E. Blundo, M. Felici, T. Yildirim, G. Pettinari, D. Tedeschi, A. Miriametro, B. Liu, W. Ma, Y. Lu, and A. Polimeni. Evidence of the direct-to-indirect band gap transition in strained two-dimensional WS_2, MoS_2, and WSe_2. *Phys. Rev. Res.*, 2:012024, Jan 2020.

[64] Pablo Hernández López, Sebastian Heeg, Christoph Schattauer, Sviatoslav Kovalchuk, Abhijeet Kumar, Douglas J. Bock, Jan N. Kirchhof, Bianca Höfer, Kyrylo Greben,

Denis Yagodkin, Lukas Linhart, Florian Libisch, and Kirill I. Bolotin. Strain control of hybridization between dark and localized excitons in a 2D semiconductor. *Nature Communications*, 13(1):7691, Dec 2022.

[65] M. M. Glazov, Florian Dirnberger, Vinod M. Menon, Takashi Taniguchi, Kenji Watanabe, Dominique Bougeard, Jonas D. Ziegler, and Alexey Chernikov. Exciton fine structure splitting and linearly polarized emission in strained transition-metal dichalcogenide monolayers. *Phys. Rev. B*, 106:125303, Sep 2022.

[66] Sefaattin Tongay, Jian Zhou, Can Ataca, Kelvin Lo, Tyler S. Matthews, Jingbo Li, Jeffrey C. Grossman, and Junqiao Wu. Thermally driven crossover from indirect toward direct bandgap in 2D semiconductors: $MoSe_2$ versus MoS_2. *Nano Letters*, 12(11):5576–5580, 2012.

[67] Iris Niehues, Robert Schmidt, Matthias Drüppel, Philipp Marauhn, Dominik Christiansen, Malte Selig, Gunnar Berghäuser, Daniel Wigger, Robert Schneider, Lisa Braasch, Rouven Koch, Andres Castellanos-Gomez, Tilmann Kuhn, Andreas Knorr, Ermin Malic, Michael Rohlfing, Steffen Michaelis de Vasconcellos, and Rudolf Bratschitsch. Strain control of exciton–phonon coupling in atomically thin semiconductors. *Nano Letters*, 18(3):1751–1757, 2018.

[68] Zahra Khatibi, Maja Feierabend, Malte Selig, Samuel Brem, Christopher Linderälv, Paul Erhart, and Ermin Malic. Impact of strain on the excitonic linewidth in transition metal dichalcogenides. *2D Materials*, 6(1):015015, nov 2018.

[69] Burak Aslan, Colin Yule, Yifei Yu, Yan Joe Lee, Tony F Heinz, Linyou Cao, and Mark L Brongersma. Excitons in strained and suspended monolayer WSe_2. *2D Materials*, 9(1):015002, oct 2021.

[70] Marvin Kulig, Jonas Zipfel, Philipp Nagler, Sofia Blanter, Christian Schüller, Tobias Korn, Nicola Paradiso, Mikhail Glazov, and Alexey Chernikov. Exciton diffusion and halo effects in monolayer semiconductors. *Physical Review Letters*, 120, 05 2018.

[71] Jonas Zipfel, Marvin Kulig, Raül Perea-Causín, Samuel Brem, Jonas D. Ziegler, Roberto Rosati, Takashi Taniguchi, Kenji Watanabe, Mikhail M. Glazov, Ermin Malic, and Alexey Chernikov. Exciton diffusion in monolayer semiconductors with suppressed disorder. *Phys. Rev. B*, 101:115430, Mar 2020.

[72] Luis E. Parra López, Anna Rosławska, Fabrice Scheurer, Stéphane Berciaud, and Guillaume Schull. Tip-induced excitonic luminescence nanoscopy of an atomically-resolved van der waals heterostructure, 2022.

[73] Moshe G. Harats, Jan N. Kirchhof, Mengxiong Qiao, Kyrylo Greben, and Kirill I. Bolotin. Dynamics and efficient conversion of excitons to trions in non-uniformly strained monolayer WS_2. *Nature Photonics*, 14(5):324–329, May 2020.

[74] S. Lazić, A. Violante, K. Cohen, R. Hey, R. Rapaport, and P. V. Santos. Scalable interconnections for remote indirect exciton systems based on acoustic transport. *Phys. Rev. B*, 89:085313, Feb 2014.

[75] Andres Castellanos-Gomez, Rafael Roldán, Emmanuele Cappelluti, Michele Buscema, Francisco Guinea, Herre S. J. van der Zant, and Gary A. Steele. Local strain engineering in atomically thin MoS_2. *Nano Letters*, 13(11):5361–5366, 2013.

[76] Ji Feng, Xiaofeng Qian, Cheng-Wei Huang, and Ju Li. Strain-engineered artificial atom as a broad-spectrum solar energy funnel. *Nature Photonics*, 6(12):866–872, Dec 2012.

[77] Carmen Palacios-Berraquero, Dhiren M. Kara, Alejandro R.-P. Montblanch, Matteo Barbone, Pawel Latawiec, Duhee Yoon, Anna K. Ott, Marko Loncar, Andrea C. Ferrari, and Mete Atatüre. Large-scale quantum-emitter arrays in atomically thin semiconductors. *Nature Communications*, 8(1):15093, May 2017.

[78] Rusen Yan, Jeffrey R. Simpson, Simone Bertolazzi, Jacopo Brivio, Michael Watson, Xufei Wu, Andras Kis, Tengfei Luo, Angela R. Hight Walker, and Huili Grace Xing. Thermal conductivity of monolayer molybdenum disulfide obtained from temperature-dependent Raman spectroscopy. *ACS Nano*, 8(1):986–993, 2014.

[79] Xin Zhang, Xiao-Fen Qiao, Wei Shi, Jiang-Bin Wu, De-Sheng Jiang, and Ping-Heng Tan. Phonon and Raman scattering of two-dimensional transition metal dichalcogenides from monolayer, multilayer to bulk material. *Chem. Soc. Rev.*, 44:2757–2785, 2015.

[80] C. R. Zhu, G. Wang, B. L. Liu, X. Marie, X. F. Qiao, X. Zhang, X. X. Wu, H. Fan, P. H. Tan, T. Amand, and B. Urbaszek. Strain tuning of optical emission energy and polarization in monolayer and bilayer MoS_2. *Phys. Rev. B*, 88:121301, Sep 2013.

[81] Biswanath Chakraborty, Achintya Bera, D. V. S. Muthu, Somnath Bhowmick, U. V. Waghmare, and A. K. Sood. Symmetry-dependent phonon renormalization in monolayer MoS_2 transistor. *Phys. Rev. B*, 85:161403, Apr 2012.

[82] Xiaoting Huang, Yang Gao, Tianqi Yang, Wencai Ren, Hui-Ming Cheng, and Tianshu Lai. Quantitative analysis of temperature dependence of Raman shift of monolayer WS_2. *Scientific Reports*, 6(1):32236, Aug 2016.

[83] L. Wang, I. Meric, P. Y. Huang, Q. Gao, Y. Gao, H. Tran, T. Taniguchi, K. Watanabe, L. M. Campos, D. A. Muller, J. Guo, P. Kim, J. Hone, K. L. Shepard, and C. R. Dean. One-dimensional electrical contact to a two-dimensional material. *Science*, 342(6158):614–617, 2013.

[84] Yuan Cao, Valla Fatemi, Shiang Fang, Kenji Watanabe, Takashi Taniguchi, Efthimios Kaxiras, and Pablo Jarillo-Herrero. Unconventional superconductivity in magic-angle graphene superlattices. *Nature*, 556(7699):43–50, Apr 2018.

[85] Nathan P. Wilson, Wang Yao, Jie Shan, and Xiaodong Xu. Excitons and emergent quantum phenomena in stacked 2d semiconductors. *Nature*, 599(7885):383–392, Nov 2021.

[86] Di Huang, Junho Choi, Chih-Kang Shih, and Xiaoqin Li. Excitons in semiconductor Moiré superlattices. *Nature Nanotechnology*, 17(3):227–238, Mar 2022.

[87] C. E. Ekuma, V. Dobrosavljević, and D. Gunlycke. First-principles-based method for electron localization: Application to monolayer hexagonal boron nitride. *Phys. Rev. Lett.*, 118:106404, Mar 2017.

[88] Jiamin Xue, Javier Sanchez-Yamagishi, Danny Bulmash, Philippe Jacquod, Aparna Deshpande, K. Watanabe, T. Taniguchi, Pablo Jarillo-Herrero, and Brian J. LeRoy. Scanning tunnelling microscopy and spectroscopy of ultra-flat graphene on hexagonal boron nitride. *Nature Materials*, 10(4):282–285, Apr 2011.

[89] Darshana Wickramaratne, Leigh Weston, and Chris G. Van de Walle. Monolayer to bulk properties of hexagonal boron nitride. *The Journal of Physical Chemistry C*, 122(44):25524–25529, 2018.

[90] G. Cassabois, P. Valvin, and B. Gil. Hexagonal boron nitride is an indirect bandgap semiconductor. *Nature Photonics*, 10(4):262–266, Apr 2016.

[91] Igor Aharonovich, Jean-Philippe Tetienne, and Milos Toth. Quantum emitters in hexagonal boron nitride. *Nano Letters*, 22(23):9227–9235, 2022.

[92] Akbar Basha Dhu-al-jalali-wal-ikram Shaik and Penchalaiah Palla. Optical quantum technologies with hexagonal boron nitride single photon sources. *Scientific Reports*, 11(1):12285, Jun 2021.

[93] Archana Raja, Andrey Chaves, Jaeeun Yu, Ghidewon Arefe, Heather M. Hill, Albert F. Rigosi, Timothy C. Berkelbach, Philipp Nagler, Christian Schüller, Tobias Korn, Colin Nuckolls, James Hone, Louis E. Brus, Tony F. Heinz, David R. Reichman, and Alexey Chernikov. Coulomb engineering of the bandgap and excitons in two-dimensional materials. *Nature Communications*, 8(1):15251, May 2017.

[94] Archana Raja, Lutz Waldecker, Jonas Zipfel, Yeongsu Cho, Samuel Brem, Jonas D. Ziegler, Marvin Kulig, Takashi Taniguchi, Kenji Watanabe, Ermin Malic, Tony F. Heinz, Timothy C. Berkelbach, and Alexey Chernikov. Dielectric disorder in two-dimensional materials. *Nature Nanotechnology*, 14(9):832–837, Sep 2019.

[95] H. H. Fang, B. Han, C. Robert, M. A. Semina, D. Lagarde, E. Courtade, T. Taniguchi, K. Watanabe, T. Amand, B. Urbaszek, M. M. Glazov, and X. Marie. Control of the exciton radiative lifetime in van der waals heterostructures. *Phys. Rev. Lett.*, 123:067401, Aug 2019.

[96] Jiaqi He, Nardeep Kumar, Matthew Z. Bellus, Hsin-Ying Chiu, Dawei He, Yongsheng Wang, and Hui Zhao. Electron transfer and coupling in graphene–tungsten disulfide van der waals heterostructures. *Nature Communications*, 5(1):5622, Nov 2014.

[97] M. Massicotte, P. Schmidt, F. Vialla, K. G. Schädler, A. Reserbat-Plantey, K. Watanabe, T. Taniguchi, K. J. Tielrooij, and F. H. L. Koppens. Picosecond photoresponse in van der waals heterostructures. *Nature Nanotechnology*, 11(1):42–46, Jan 2016.

[98] Etienne Lorchat, Luis E. Parra López, Cédric Robert, Delphine Lagarde, Guillaume Froehlicher, Takashi Taniguchi, Kenji Watanabe, Xavier Marie, and Stéphane Berciaud. Filtering the photoluminescence spectra of atomically thin semiconductors with graphene. *Nature Nanotechnology*, 15(4):283–288, Apr 2020.

[99] Guillaume Froehlicher, Etienne Lorchat, and Stéphane Berciaud. Charge versus energy transfer in atomically thin graphene-transition metal dichalcogenide van der waals heterostructures. *Physical Review X*, 8, 01 2018.

[100] Luis Enrique Parra López, Loïc Moczko, Joanna Wolff, Aditya Singh, Etienne Lorchat, Michelangelo Romeo, Takashi Taniguchi, Kenji Watanabe, and Stéphane Berciaud. Single- and narrow-line photoluminescence in a boron nitride-supported $MoSe_2$/graphene heterostructure. *Comptes Rendus. Physique*, 22(S4):77–88, 2021.

[101] P. L. Hernández Martínez A. Govorov. *Understanding and Modeling Förster-type Resonance Energy Transfer (FRET).*

[102] Th. Förster. Zwischenmolekulare energiewanderung und fluoreszenz. *Annalen der Physik*, 437(1-2):55–75, 1948.

[103] Lukas Novotny and Bert Hecht. *Principles of Nano-Optics*. Cambridge University Press, 2nd edition, 2012.

[104] R. S. Swathi and K. L. Sebastian. Resonance energy transfer from a dye molecule to graphene. *The Journal of Chemical Physics*, 129(5):054703, 2008.

[105] Ermin Malic, Heiko Appel, Oliver T. Hofmann, and Angel Rubio. Förster-induced energy transfer in functionalized graphene. *The Journal of Physical Chemistry C*, 118(17):9283–9289, 2014.

[106] D. L. Dexter. A theory of sensitized luminescence in solids. *The Journal of Chemical Physics*, 21(5):836–850, 1953.

[107] Andres Castellanos-Gomez, Vibhor Singh, Herre S. J. van der Zant, and Gary A. Steele. Mechanics of freely-suspended ultrathin layered materials. *Annalen der Physik*, 527(1-2):27–44, 2015.

[108] D. C. Elias, R. V. Gorbachev, A. S. Mayorov, S. V. Morozov, A. A. Zhukov, P. Blake, L. A. Ponomarenko, I. V. Grigorieva, K. S. Novoselov, F. Guinea, and A. K. Geim. Dirac cones reshaped by interaction effects in suspended graphene. *Nature Physics*, 7(9):701–704, Sep 2011.

[109] Choongyu Hwang, David A. Siegel, Sung-Kwan Mo, William Regan, Ariel Ismach, Yuegang Zhang, Alex Zettl, and Alessandra Lanzara. Fermi velocity engineering in graphene by substrate modification. *Scientific Reports*, 2(1):590, Aug 2012.

[110] Alexander W. Bataller, Robert A. Younts, Avinash Rustagi, Yiling Yu, Hossein Ardekani, Alexander Kemper, Linyou Cao, and Kenan Gundogdu. Dense electron–hole plasma formation and ultralong charge lifetime in monolayer MoS_2 via material tuning. *Nano Letters*, 19(2):1104–1111, 2019.

[111] Trevor B. Arp, Dennis Pleskot, Vivek Aji, and Nathaniel Gabor. Electron–hole liquid in a van der waals heterostructure photocell at room temperature. *Nature Photonics*, 13, 02 2019.

[112] Yiling Yu, Alexander W. Bataller, Robert Younts, Yifei Yu, Guoqing Li, Alexander A. Puretzky, David B. Geohegan, Kenan Gundogdu, and Linyou Cao. Room-temperature electron–hole liquid in monolayer MoS_2. *ACS Nano*, 13(9):10351–10358, 2019.

[113] Robert Younts, Alexander Bataller, Hossein Ardekani, Yiling Yu, Linyou Cao, and Kenan Gundogdu. Near band-edge optical excitation leading to catastrophic ionization and electron–hole liquid in room-temperature monolayer MoS_2. *physica status solidi (b)*, 256(11):1900223, 2019.

[114] Guillaume Froehlicher, Etienne Lorchat, and Stéphane Berciaud. Direct versus indirect band gap emission and exciton-exciton annihilation in atomically thin molybdenum ditelluride $MoTe_2$. *Physical Review B*, 94, 02 2016.

[115] Nardeep Kumar, Qiannan Cui, Frank Ceballos, Dawei He, Yongsheng Wang, and Hui Zhao. Exciton-exciton annihilation in $MoSe_2$ monolayers. *Phys. Rev. B*, 89:125427, Mar 2014.

[116] Shinichiro Mouri, Yuhei Miyauchi, Minglin Toh, Weijie Zhao, Goki Eda, and Kazunari Matsuda. Nonlinear photoluminescence in atomically thin layered WSe_2 arising from diffusion-assisted exciton-exciton annihilation. *Phys. Rev. B*, 90:155449, Oct 2014.

[117] Yiling Yu, Yifei Yu, Chao Xu, Andy Barrette, Kenan Gundogdu, and Linyou Cao. Fundamental limits of exciton-exciton annihilation for light emission in transition metal dichalcogenide monolayers. *Phys. Rev. B*, 93:201111, May 2016.

[118] A. Suna. Kinematics of exciton-exciton annihilation in molecular crystals. *Phys. Rev. B*, 1:1716–1739, Feb 1970.

[119] Philipp Nagler, Mariana V. Ballottin, Anatolie A. Mitioglu, Mikhail V. Durnev, Takashi Taniguchi, Kenji Watanabe, Alexey Chernikov, Christian Schüller, Mikhail M. Glazov, Peter C. M. Christianen, and Tobias Korn. Zeeman splitting and inverted polarization of biexciton emission in monolayer WS_2. *Phys. Rev. Lett.*, 121:057402, Aug 2018.

[120] Yumeng You, Xiao-Xiao Zhang, Timothy C. Berkelbach, Mark S. Hybertsen, David R. Reichman, and Tony F. Heinz. Observation of biexcitons in monolayer WSe_2. *Nature Physics*, 11(6):477–481, Jun 2015.

[121] Matteo Barbone, Alejandro R.-P. Montblanch, Dhiren M. Kara, Carmen Palacios-Berraquero, Alisson R. Cadore, Domenico De Fazio, Benjamin Pingault, Elaheh Mostaani, Han Li, Bin Chen, Kenji Watanabe, Takashi Taniguchi, Sefaattin Tongay, Gang Wang, Andrea C. Ferrari, and Mete Atatüre. Charge-tuneable biexciton complexes in monolayer WSe_2. *Nature Communications*, 9(1):3721, Sep 2018.

[122] Alexey Chernikov, Claudia Ruppert, Heather M. Hill, Albert F. Rigosi, and Tony F. Heinz. Population inversion and giant bandgap renormalization in atomically thin WS_2 layers. *Nature Photonics*, 9(7):466–470, Jul 2015.

[123] L. V. Keldysh. The electron-hole liquid in semiconductors. *Contemporary Physics*, 27(5):395–428, 1986.

[124] N N Sibeldin. Electron–hole liquid in semiconductors and low-dimensional structures. *Physics-Uspekhi*, 60(11):1147, nov 2017.

[125] S. W. Koch. *Dynamics of First-Order Phase Transitions in Equilibrium and Nonequilibrium Systems*. Springer-Verlag, 1984.

[126] F. Lohof, A. Steinhoff, M. Florian, M. Lorke, D. Erben, F. Jahnke, and C. Gies. Prospects and limitations of transition metal dichalcogenide laser gain materials. *Nano Letters*, 19(1):210–217, 2019.

[127] Kathleen M. McCreary, Aubrey T. Hanbicki, Simranjeet Singh, Roland K. Kawakami, Glenn G. Jernigan, Masa Ishigami, Amy Ng, Todd H. Brintlinger, Rhonda M. Stroud, and Berend T. Jonker. The effect of preparation conditions on Raman and photoluminescence of monolayer WS_2. *Scientific Reports*, 6(1):35154, Oct 2016.

[128] Kazuro Murayama, Ryo Natsui, and Hikari Koami. Exponential tail in the luminescence spectrum from electron–hole liquid and electron–hole plasma in diamond. *Journal of the Physical Society of Japan*, 82(4):043701, 2013.

[129] E. del Corro, A. Botello-Méndez, Y. Gillet, A. L. Elias, H. Terrones, S. Feng, C. Fantini, Daniel Rhodes, N. Pradhan, L. Balicas, X. Gonze, J.-C. Charlier, M. Terrones, and M. A. Pimenta. Atypical exciton–phonon interactions in ws2 and wse2 monolayers revealed by resonance raman spectroscopy. *Nano Letters*, 16(4):2363–2368, 2016.

[130] F. Forster, A. Molina-Sanchez, S. Engels, A. Epping, K. Watanabe, T. Taniguchi, L. Wirtz, and C. Stampfer. Dielectric screening of the Kohn anomaly of graphene on hexagonal boron nitride. *Phys. Rev. B*, 88:085419, Aug 2013.

[131] C. Faugeras, S. Berciaud, P. Leszczynski, Y. Henni, K. Nogajewski, M. Orlita, T. Taniguchi, K. Watanabe, C. Forsythe, P. Kim, R. Jalil, A. K. Geim, D. M. Basko, and M. Potemski. Landau level spectroscopy of electron-electron interactions in graphene. *Phys. Rev. Lett.*, 114:126804, Mar 2015.

[132] Willi Volksen, Robert D. Miller, and Geraud Dubois. Low dielectric constant materials. *Chemical Reviews*, 110(1):56–110, 2010.

[133] R. Geick, C. H. Perry, and G. Rupprecht. Normal modes in hexagonal boron nitride. *Phys. Rev.*, 146:543–547, Jun 1966.

[134] C. Neumann, S. Reichardt, P. Venezuela, M. Drögeler, L. Banszerus, M. Schmitz, K. Watanabe, T. Taniguchi, F. Mauri, B. Beschoten, S. V. Rotkin, and C. Stampfer. Raman spectroscopy as probe of nanometre-scale strain variations in graphene. *Nature Communications*, 6(1):8429, Sep 2015.

[135] Feliciano Giustino. Electron-phonon interactions from first principles. *Rev. Mod. Phys.*, 89:015003, Feb 2017.

[136] Tsuneya Ando. Anomaly of optical phonon in monolayer graphene. *Journal of the Physical Society of Japan*, 75(12):124701, 2006.

[137] J. L. Mañes. Symmetry-based approach to electron-phonon interactions in graphene. *Phys. Rev. B*, 76:045430, Jul 2007.

[138] Michael E Peskin and Daniel V Schroeder. *An Introduction to Quantum Field Theory*. Westview Press, Boulder, 1995.

[139] Christoph Neumann, Luca Banszerus, Michael Schmitz, Sven Reichardt, Jens Sonntag, Takashi Taniguchi, Kenji Watanabe, Bernd Beschoten, and Christoph Stampfer. Line shape of the raman 2D peak of graphene in van der waals heterostructures. *physica status solidi (b)*, 253(12):2326–2330, 2016.

[140] Weijie Zhao, Zohreh Ghorannevis, Leiqiang Chu, Minglin Toh, Christian Kloc, Ping-Heng Tan, and Goki Eda. Evolution of electronic structure in atomically thin sheets of WS_2 and WSe_2. *ACS Nano*, 7(1):791–797, 2013.

[141] S. Timoshenko and J. N. Goodier. *Theory of elasticity*. McGraw-Hill Book Company, Inc., 2nd edition, 1951.

[142] Cornelia Schwarz. *Optomechanical, vibrational and thermal properties of suspended graphene membranes*. PhD thesis, Université Grenoble Alpes, 2016.

[143] Ryan C. Cooper, Changgu Lee, Chris A. Marianetti, Xiaoding Wei, James Hone, and Jeffrey W. Kysar. Nonlinear elastic behavior of two-dimensional molybdenum disulfide. *Phys. Rev. B*, 87:035423, Jan 2013.

[144] Li Song, Lijie Ci, Hao Lu, Pavel B. Sorokin, Chuanhong Jin, Jie Ni, Alexander G. Kvashnin, Dmitry G. Kvashnin, Jun Lou, Boris I. Yakobson, and Pulickel M. Ajayan. Large scale growth and characterization of atomic hexagonal boron nitride layers. *Nano Letters*, 10(8):3209–3215, 2010.

[145] M Annamalai, S Mathew, M Jamali, D Zhan, and M Palaniapan. Elastic and non-linear response of nanomechanical graphene devices. *Journal of Micromechanics and Microengineering*, 22(10):105024, sep 2012.

[146] Dominik Metten, Fran çois Federspiel, Michelangelo Romeo, and Stéphane Berciaud. All-optical blister test of suspended graphene using micro-raman spectroscopy. *Phys. Rev. Applied*, 2:054008, Nov 2014.

[147] Changgu Lee, Xiaoding Wei, Jeffrey W. Kysar, and James Hone. Measurement of the elastic properties and intrinsic strength of monolayer graphene. *Science*, 321(5887):385–388, 2008.

[148] J. Scott Bunch, Arend M. van der Zande, Scott S. Verbridge, Ian W. Frank, David M. Tanenbaum, Jeevak M. Parpia, Harold G. Craighead, and Paul L. McEuen. Electromechanical resonators from graphene sheets. *Science*, 315(5811):490–493, 2007.

[149] Andres Castellanos-Gomez, Ronald van Leeuwen, Michele Buscema, Herre S. J. van der Zant, Gary A. Steele, and Warner J. Venstra. Single-layer MoS_2 mechanical resonators. *Advanced Materials*, 25(46):6719–6723, 2013.

[150] Jaesung Lee, Zenghui Wang, Keliang He, Jie Shan, and Philip X.-L. Feng. High frequency MoS_2 nanomechanical resonators. *ACS Nano*, 7(7):6086–6091, 2013.

[151] Fan Ye, Jaesung Lee, and Philip X.-L. Feng. Atomic layer MoS_2-graphene van der waals heterostructure nanomechanical resonators. *Nanoscale*, 9:18208–18215, 2017.

[152] Nicolas Morell, Antoine Reserbat-Plantey, Ioannis Tsioutsios, Kevin G. Schädler, François Dubin, Frank H. L. Koppens, and Adrian Bachtold. High quality factor mechanical resonators based on WSe_2 monolayers. *Nano Letters*, 16(8):5102–5108, 2016. PMID: 27459399.

[153] Fan Ye, Arnob Islam, Teng Zhang, and Philip X.-L. Feng. Ultrawide frequency tuning of atomic layer van der waals heterostructure electromechanical resonators. *Nano Letters*, 21(13):5508–5515, 2021.

[154] P. Weber, J. Güttinger, A. Noury, J. Vergara-Cruz, and A. Bachtold. Force sensitivity of multilayer graphene optomechanical devices. *Nature Communications*, 7(1):12496, Aug 2016.

[155] Dejan Davidovikj, Farbod Alijani, Santiago José Cartamil Bueno, H S. J. van der Zant, Marco Amabili, and P.G. Steeneken. Nonlinear dynamic characterization of two-dimensional materials. *Nature Communications*, 8, 12 2017.

[156] Ali Hasan Nayfeh and Dean T. Mook. *Nonlinear oscillations*. John Wiley & Sons, Ltd, 1979.

[157] A. Fartash, Ivan K. Schuller, and M. Grimsditch. Thin-film modeling for mechanical measurements: Should membranes be used or plates? *Journal of Applied Physics*, 71(9):4244–4248, 1992.

[158] Dejan Davidovikj, Jesse J. Slim, Santiago J. Cartamil-Bueno, Herre S. J. van der Zant, Peter G. Steeneken, and Warner J. Venstra. Visualizing the motion of graphene nanodrums. *Nano Letters*, 16(4):2768–2773, 2016.

[159] Nicolas Morell, Slaven Tepsic, Antoine Reserbat-Plantey, Andrea Cepellotti, Marco Manca, Itai Epstein, Andreas Isacsson, Xavier Marie, Francesco Mauri, and Adrian Bachtold. Optomechanical measurement of thermal transport in two-dimensional $MoSe_2$ lattices. *Nano Letters*, 19(5):3143–3150, 2019.

[160] K. L. Ekinci and M. L. Roukes. Nanoelectromechanical systems. *Review of Scientific Instruments*, 76(6):061101, 2005.

[161] Dominik Metten, Guillaume Froehlicher, and Stéphane Berciaud. Monitoring electrostatically-induced deflection, strain and doping in suspended graphene using Raman spectroscopy. *2D Materials*, 4(1):014004, dec 2016.

[162] Antoine Reserbat-plantey, Laëtitia Marty, Olivier Arcizet, Nedjma Bendiab, and Vincent Bouchiat. A local optical probe for measuring motion and stress in a nanoelectromechanical system. *Nature nanotechnology*, 7:151–5, 03 2012.

[163] You Zhou, Giovanni Scuri, Jiho Sung, Ryan J. Gelly, Dominik S. Wild, Kristiaan De Greve, Andrew Y. Joe, Takashi Taniguchi, Kenji Watanabe, Philip Kim, Mikhail D. Lukin, and Hongkun Park. Controlling excitons in an atomically thin membrane with a mirror. *Phys. Rev. Lett.*, 124:027401, Jan 2020.

[164] Hongchao Xie, Shengwei Jiang, Daniel A. Rhodes, James C. Hone, Jie Shan, and Kin Fai Mak. Tunable exciton-optomechanical coupling in suspended monolayer $MoSe_2$. *Nano Letters*, 21(6):2538–2543, 2021.

[165] Jan N. Kirchhof, Yuefeng Yu, Gabriel Antheaume, Georgy Gordeev, Denis Yagodkin, Peter Elliott, Daniel B. de Araújo, Sangeeta Sharma, Stephanie Reich, and Kirill I. Bolotin. Nanomechanical spectroscopy of 2D materials. *Nano Letters*, 22(20):8037–8044, 2022.

[166] Hong-Hua Fang, Bo Han, C Robert, M A. Semina, D Lagarde, E Courtade, T Taniguchi, K Watanabe, Thierry Amand, Bernhard Urbaszek, Mikhail Glazov, and Xavier Marie. Control of the exciton radiative lifetime in van der waals heterostructures. *Physical Review Letters*, 123:067401, 02 2019.

[167] Zurich Instruments. White paper: Principles of lock-in detection and the state of the art. 11 2016.

[168] P. Weber, J. Güttinger, I. Tsioutsios, D. E. Chang, and A. Bachtold. Coupling graphene mechanical resonators to superconducting microwave cavities. *Nano Letters*, 14(5):2854–2860, 2014.

[169] S. Timoshenko. *Vibration Problems in Engineering*. Read Books, 2008.

[170] Changyao Chen, Sami Rosenblatt, Kirill I. Bolotin, William alb, Philip Kim, Ioannis Kymissis, Horst L. Stormer, Tony F. Heinz, and James Hone. Performance of monolayer graphene nanomechanical resonators with electrical readout. *Nature Nanotechnology*, 4:861–867, 12 2009.

[171] Jaesung Lee, Zenghui Wang, Keliang He, Rui Yang, Jie Shan, and Philip X.-L. Feng. Electrically tunable single- and few-layer MoS_2 nanoelectromechanical systems with broad dynamic range. *Science Advances*, 4(3):eaao6653, 2018.

[172] Adrien Allain, Jiahao Kang, Kaustav Banerjee, and Andras Kis. Electrical contacts to two-dimensional semiconductors. *Nature Materials*, 14:1195–1205, 12 2015.

[173] Kevin G. Schädler, Carlotta Ciancico, Sofia Pazzagli, Pietro Lombardi, Adrian Bachtold, Costanza Toninelli, Antoine Reserbat-Plantey, and Frank H. L. Koppens. Electrical control of lifetime-limited quantum emitters using 2D materials. *Nano Letters*, 19(6):3789–3795, 2019.

[174] F. Bonaccorso, Z. Sun, T. Hasan, and A. C. Ferrari. Graphene photonics and optoelectronics. *Nature Photonics*, 4(9):611622, 2010.

[175] Britton W. H. Baugher, Hugh O. H. Churchill, Yafang Yang, and Pablo Jarillo-Herrero. Intrinsic electronic transport properties of high-quality monolayer and bilayer MoS_2. *Nano Letters*, 13(9):4212–4216, 2013.

[176] Noëlle Pottier. *Physique statistique hors d'équilibre : Processus irréversibles linéaires*. EDP Sciences, 2007.

[177] B.D. Hauer, C. Doolin, K.S.D. Beach, and J.P. Davis. A general procedure for thermomechanical calibration of nano/micro-mechanical resonators. *Annals of Physics*, 339:181–207, 2013.

[178] Kevin G. Schädler. *Single quantum emitter manipulation with 2D materials*. PhD thesis, Universitat politècnica de Catalunya & Università degli studi Firenze, 2018.

[179] Jaesung Lee, Steven W. Shaw, and Philip X.-L. Feng. Giant parametric amplification and spectral narrowing in atomically thin MoS_2 nanomechanical resonators. *Applied Physics Reviews*, 9(1):011404, 2022.

[180] Etienne Lorchat, Luis E. Parra López, Cédric Robert, Delphine Lagarde, Guillaume Froehlicher, Takashi Taniguchi, Kenji Watanabe, Xavier Marie, and Stéphane Berciaud. Filtering the photoluminescence spectra of atomically thin semiconductors with graphene. *Nature Nanotechnology*, 15:283–288, 04 2020.

[181] Charalampos Androulidakis, Emmanuel N. Koukaras, John Parthenios, George Kalosakas, Konstantinos Papagelis, and Costas Galiotis. Graphene flakes under controlled biaxial deformation. *Scientific Reports*, 5(1):18219, Dec 2015.

[182] D. Cattiaux, S. Kumar, X. Zhou, A. Fefferman, and E. Collin. Geometrical nonlinearity of circular plates and membranes: An alternative method. *Journal of Applied Physics*, 128(10):104501, 2020.

[183] Jae-Ung Lee, Duhee Yoon, and Hyeonsik Cheong. Estimation of young's modulus of graphene by Raman spectroscopy. *Nano Letters*, 12(9):4444–4448, 2012.

[184] Riccardo Frisenda, Matthias Drüppel, Robert Schmidt, Steffen Michaelis de Vasconcellos, David Perez de Lara, Rudolf Bratschitsch, Michael Rohlfing, and Andres Castellanos-Gomez. Biaxial strain tuning of the optical properties of single-layer transition metal dichalcogenides. *npj 2D Materials and Applications*, 1(1):10, May 2017.

[185] Shahnaz Aas and Ceyhun Bulutay. Strain dependence of photoluminescence and circular dichroism in transition metal dichalcogenides: a k · p analysis. *Opt. Express*, 26(22):28672–28681, Oct 2018.

[186] Lukas Mennel, Matthias Paur, and Thomas Mueller. Second harmonic generation in strained transition metal dichalcogenide monolayers: Mos2, mose2, ws2, and wse2. *APL Photonics*, 4(3):034404, 2019.

[187] P. Soubelet, A. E. Bruchhausen, A. Fainstein, K. Nogajewski, and C. Faugeras. Resonance effects in the Raman scattering of monolayer and few-layer mose$_2$. *Phys. Rev. B*, 93:155407, Apr 2016.

[188] Evgeny M. Alexeev, David A. Ruiz-Tijerina, Mark Danovich, Matthew J. Hamer, Daniel J. Terry, Pramoda K. Nayak, Seongjoon Ahn, Sangyeon Pak, Juwon Lee, Jung Inn Sohn, Maciej R. Molas, Maciej Koperski, Kenji Watanabe, Takashi Taniguchi, Kostya S. Novoselov, Roman V. Gorbachev, Hyeon Suk Shin, Vladimir I. Fal'ko, and Alexander I. Tartakovskii. Resonantly hybridized excitons in Moiré superlattices in van der waals heterostructures. *Nature*, 567(7746):81–86, Mar 2019.

[189] Long Zhang, Zhe Zhang, Fengcheng Wu, Danqing Wang, Rahul Gogna, Shaocong Hou, Kenji Watanabe, Takashi Taniguchi, Krishnamurthy Kulkarni, Thomas Kuo, Stephen R. Forrest, and Hui Deng. Twist-angle dependence of Moiré excitons in $WS_2/MoSe_2$ heterobilayers. *Nature Communications*, 11(1):5888, Nov 2020.

[190] Bevin Huang, Michael A. McGuire, Andrew F. May, Di Xiao, Pablo Jarillo-Herrero, and Xiaodong Xu. Emergent phenomena and proximity effects in two-dimensional magnets and heterostructures. *Nature Materials*, 19(12):1276–1289, Dec 2020.

[191] Makars Šiškins, Martin Lee, Samuel Mañas-Valero, Eugenio Coronado, Yaroslav M. Blanter, Herre S. J. van der Zant, and Peter G. Steeneken. Magnetic and electronic phase transitions probed by nanomechanical resonators. *Nature Communications*, 11(1):2698, Jun 2020.

[192] B. Diu, C. Guthmann, and B Roulet. *Physique Statistique*. Hermann, 1 edition, 1997.

[193] Shengwei Jiang, Hongchao Xie, Jie Shan, and Kin Fai Mak. Exchange magnetostriction in two-dimensional antiferromagnets. *Nature Materials*, 19(12):1295–1299, Dec 2020.

[194] Hao-Kun Li, King Yan Fong, Hanyu Zhu, Quanwei Li, Siqi Wang, Sui Yang, Yuan Wang, and Xiang Zhang. Valley optomechanics in a monolayer semiconductor. *Nature Photonics*, 13(6):397–401, Jun 2019.

[195] Richard C. Jaeger. *Introduction to microelectronic fabrication*. Prentice Hall, 2nd edition, 2002.

[196] R. F. Frindt. Single crystals of MoS_2 several molecular layers thick. *Journal of Applied Physics*, 37(4):1928, 1966.

[197] Andres Castellanos-Gomez, Michele Buscema, Rianda Molenaar, Vibhor Singh, Laurens Janssen, Herre S J van der Zant, and Gary A Steele. Deterministic transfer of two-dimensional materials by all-dry viscoelastic stamping. *2D Materials*, 1(1):011002, apr 2014.

[198] E. Abbe. Beiträge zur theorie des mikroskops und der mikroskopischen wahrnehmung. *Archiv für Mikroskopische Anatomie*, 9:413–468, 1873.

[199] Yilei Li and Tony F. Heinz. Two-dimensional models for the optical response of thin films. *2D Materials*, 5:025021, 2018.

[200] Alain Aspect Gilbert Grynberg and Claude Fabre. *Introduction aux lasers et à l'optique quantique*. Ellipses, 1997.

[201] C. V. Raman and K. S. Krishnan. A new type of secondary radiation. *Nature*, 121(3048):501–502, Mar 1928.

[202] David J. Griffiths. *Introduction to electrodynamics*. Prentice Hall, 3rd edition, 1999.

[203] Andrew Zangwill. *Modern electrodynamics*. Cambridge University Press, 1st edition, 2012.

[204] Ewen Smith and Geoffrey Dent. *Modern Raman Spectroscopy*. John Wiley & Sons, Ltd, 1st edition, 2005.

[205] Jun Yan, Yuanbo Zhang, Philip Kim, and Aron Pinczuk. Electric field effect tuning of electron-phonon coupling in graphene. *Phys. Rev. Lett.*, 98:166802, Apr 2007.

[206] Sunmin Ryu, Li Liu, Stephane Berciaud, Young-Jun Yu, Haitao Liu, Philip Kim, George W. Flynn, and Louis E. Brus. Atmospheric oxygen binding and hole doping in deformed graphene on a SiO_2 substrate. *Nano Letters*, 10(12):4944–4951, 2010.

Université de Strasbourg

Loïc MOCZKO

Suspended van der Waals heterostructures: from optical spectroscopy to opto-electro-mechanics

ECOLE DOCTORALE pcp

Résumé

Dans cette thèse, nous présentons une étude des propriétés physiques de matériaux bidimensionnels et d'hétérostructures de van der Waals en combinant des techniques de spectroscopie optique et de nanomécanique. En premier lieu, nous nous intéressons à l'influence de l'environnement sur la réponse optique de matériaux bidimensionnels. Nous étudions la réponse en photoluminescence et le spectre Raman de monocouches de dichalcogénures de métaux de transition (TMD) suspendues et soumises à une forte excitation laser. Nos résultats mettent en évidence la formation d'une phase dense d'électrons et de trous sur une monocouche de disulfure de molybdène (MoS_2) ainsi qu'une forte conversion d'excitons en trions sur une monocouche de disulfure de tungstène (WS_2).
Le cas de monocouches de graphène est étudié en analysant l'évolution des fréquences des phonons optiques, obtenues par micro-spectroscopie Raman, en fonction de l'environnement diélectrique. Cette étude démontre que la sensibilité d'un mode de phonon du graphène vis-à-vis de l'écrantage diélectrique dépend de sa symétrie.
Enfin, nous démontrons sur un nano-résonateur mécanique en forme de tambour dont la membrane vibrante est constituée d'une hétérostructure de van der Waals, qu'il est possible de modifier et contrôler électro-mécaniquement la réponse optique de l'hétérostructure utilisée. Ce travail montre que l'architecture en nanotambours permet d'appliquer une contrainte ajustable tout en modifiant le niveau de dopage et ouvre la voie vers le développement de dispositifs opto-électro-mécaniques dont les caractéristiques sont contrôlables avec une grande précision.

Mots-clés : matériaux bidimensionnels, hétérostructures de van der Waals, spectroscopie Raman, spectroscopie de photoluminescence, nanomécanique, opto-électro-mécanique, effets diélectriques, effets de contraintes.

Résumé en anglais

In this thesis, we present an investigation of the physical properties of two-dimensional materials and van der Waals heterostructures by combining optical spectroscopy and nanomechanical measurements. First, we investigate how the environment surrounding the material affects its optical properties. We study the photoluminescence and Raman spectra of suspended semiconducting transition metal dichalcogenides (TMD) monolayers submitted to a strong laser excitation. We show that a dense electron-hole phase can be formed in monolayers of molybdenum disulfide (MoS_2) and observe a strong excitons to trions conversion in tungsten disulfide (WS_2).
The case of graphene is investigated through a systematic analysis of the evolution of the optical phonon frequencies in monolayer graphene by the means of micro-Raman spectroscopy in order to understand the role of dielectric screening. Our results demonstrate that the sensitivity of a phonon mode in graphene towards dielectric screening is determined by its symmetry.
Finally, we use a drum-like mechanical resonator where a van der Waals heterostructure acts as a vibrating membrane, to study the interplay between the mechanical degrees of freedom of the resonator and the optical response of the used heterostructure. This work demonstrates that the drum-like sample architecture allows to control the strain and doping levels and paves the way to the development of finely tunable opto-electro-mechanical systems such as light sources and detectors.

Keywords: two-dimensional materials, van der Waals heterostructures, Raman spectroscopy, photoluminescence spectroscopy, nanomechanics, opto-electro-mechanics, dielectric screening, strain.